Coupling and stochasticity in mesoscopic brain dynamics

Maciej Jedynak

Universitat Politècnica de Catalunya

Doctoral Thesis

Coupling and stochasticity in mesoscopic brain dynamics

Author:
Maciej Jedynak

Supervisors:
Prof. Jordi Garcia-Ojalvo
Prof. Antonio J. Pons

A thesis submitted in fulfilment of the requirements for the degree of Doctor of Philosophy in the

Department of Physics

February 2017

To my Family

Acknowledgements

Writing this Thesis took a little bit of work and a lot of learning. I am therefore grateful to all those who taught me and let me learn, starting from my first teachers –my parents– all the way to the supervisors of this Thesis. I feel truly fortunate that I could work under the guidance of Jordi Garcia-Ojalvo and Antonio J. Pons. It was essential to have their support combined with freedom to pursue my own ideas and research. Their passion for science was inspiring me the whole time.

This Thesis would have not been possible without the Neural Engineering Transformative Technologies initiative, supported by the Marie Skłodowska-Curie Initial Training Network scheme. I am grateful to all those who brought that initiative to life, especially to its coordinator, Stephen Coombes. The three months I spent working under his supervision at the University of Nottingham enriched my studies immensely. That is also thanks to Sid Visser, who was generous with his time and helpful explanations. I thank Ingo Bojak from the University of Reading for his valuable advice. I also thank Karen Mullinger from the University of Nottingham for sharing her experimental data. It was a pleasure to work with Marc Goodfellow from the University of Exeter, who contributed to the work presented in this Thesis. I am also grateful to Axel Hutt and Laurent Bougrain for their hospitality during my secondment in Nancy.

I thank the members of the Dynamical Systems Biology laboratory, the Centre for Genomic Regulation, and the Nonlinear Dynamics, Nonlinear Optics and Lasers laboratory. It was great to work, share scientific ideas, and spend time with them. I thank all my friends, who helped me in one way or another to accomplish this Thesis, and made my time spent in Barcelona a wonderful and unforgettable experience.

Finally, a very special 'thank you' goes to my wife Paulina. Without her encouragement, I might have not started this PhD at all. Without her support, I might have not finished it.

"Never let knowledge stand in the way of truth"

Anonymous

Summary

The brain is known to operate under the constant influence of noise arising from a variety of sources. It also organises its activity into rhythms spanning multiple frequency bands. These rhythms originate from neuronal oscillations which can be detected via measurements such as electroencephalography (EEG) and functional magnetic resonance (fMRI). Experimental evidence suggests that interactions between rhythms from distinct frequency bands play a key role in brain processing, but the dynamical mechanisms underlying this cross-frequency interactions are still under investigation. Some rhythms are pathological and harmful to brain function. Such is the case of *epileptiform* rhythms characterising epileptic seizures.

Much has been learnt about the dynamics of the brain from computational modelling. Particularly relevant is *mesoscopic* scale modelling, which is concerned with spatial scales exceeding those of individual neurons and corresponding to processes and structures underlying the generation of signals registered in the EEG and fMRI recordings. Such modelling usually involves assumptions regarding the characteristics of the background noise, which represents afferents from remote, non-modelled brain areas. To this end, Gaussian white noise, characterised by a flat power spectrum, is often used. In contrast, macroscopic fluctuations in the brain typically follow a '$1/f^b$' spectrum, which is a characteristic feature of temporally correlated, coloured noise.

In Chapters 3-5 of this Thesis we address by means of a stochastically driven mesoscopic neuronal model, the three following questions. First, in Chapter 3 we ask about the significance of deviations from the assumption of white noise in the context of brain dynamics, and in particular we study the role that temporally correlated noise plays in eliciting aberrant rhythms in the model of an epileptic brain. We find that the generation of epileptiform dynamics in the model depends non-monotonically on the noise correlation time. We show that this is due to the maximisation of the spectral content of epileptogenic rhythms in the noise. These rhythms fall into frequency bands that indeed were experimentally shown to increase in power prior to epileptic seizures. We explain these effects in terms of the

interplay between specific driving frequencies and bifurcation structure of the model.

Second, in Chapter 4 we show how coupling between cortical modules leads to complex activity patterns and to the emergence of a phenomenon that we term *collective excitability*. Temporal patterns generated by this model bear resemblance to clinically observed characteristics of epileptic seizures. In that chapter we also introduce a fast method of tracking a loss of stability caused by excessive inter-modular coupling in a neuronal network. Third, in Chapter 5 we focus on cross-frequency interactions occurring in a network of cortical modules, in the presence of coloured noise. We suggest a mechanism that underlies the increase of power in a fast rhythm due to driving with a slow rhythm, and we find the noise parameters that best recapitulate experimental power spectra. Finally, in Chapter 6, we examine models of haemodynamic and metabolic brain processes, we test them on experimental data, and we consider the consequences of coupling them with mesoscopic neuronal models.

Taken together, our results show the combined influence of noise and coupling in computational models of neuronal activity. Moreover, they demonstrate the relevance of dynamical properties of neuronal systems to specific physiological phenomena, in particular related to cross-frequency interactions and epilepsy. Insights from this Thesis could in the future empower studies of epilepsy as a *dynamic disease*, and could contribute to the development of treatment methods applicable to drug-resistant epileptic patients.

Resum

El cervell opera sota la influiència de sorolls amb diversos orígens. També organitza la seva activitat en una sèrie de ritmes que s'expandeixen en diverses bandes de freqüència. Aquests ritmes tenen el seu origen en les oscil·lacions neuronals i poden detectar-se via mesures com les electroencefalogràfiques (EEG) o la ressonància magnètica funcional (fMRI). Les evidències experimentals suggereixen que les interaccions entre ritmes operant en bandes de freqüència diferents juguen un paper central en el processat cerebral però els mecanismes dinàmics subjacents a les interaccions inter-freqüència encara estan investigant-se. Alguns ritmes són patològics, com és el cas dels ritmes *epileptiformes* que caracteritzen les convulsions epilèptiques.

Fent servir el modelatge computacional s'ha après molt sobre la dinàmica del cervell. Especialment rellevant és el modelatge a l'escala *mesoscòpica*, que té a veure amb les escales espacials superiors a les de les neurones individuals i que correspon als processos que generen EEG i fMRI. Tal modelatge, en general, implica supòsits relatius a les característiques del soroll de fons que representa zones remotes del cervell no modelades. Amb aquesta finalitat s'utiliza sovint el soroll blanc gaussià, que es caracteritza per un espectre de potència pla. Les fluctuacions macroscòpiques en el cervell, però, normalment segueixen un espectre '$1/f^b$', que és un tret característic de les correlacions temporals i el soroll de color.

Als Capítols 3-5 d'aquesta Tesi abordem mitjançant un model neuronal mesoscòpic forçat estocàsticament, les tres preguntes següents. En primer lloc, en el Capítol 3 ens preguntem sobre la importància de les desviacions de l'assumpció de soroll blanc en el context de la dinàmica del cervell i, en particular, estudiem el paper que juga el soroll amb correlació temporal en l'obtenció de ritmes aberrants d'un cervell epilèptic. Trobem que la generació de les dinàmiques epileptiformes depèn de forma no monòtona del temps de correlació del soroll. Aquests ritmes es divideixen en bandes de freqüència que, segons, s'ha mostrat experimentalment, augmenten la

seva potència espectral abans de les crisis epilèptiques. Expliquem aquests efectes en termes de la interacció entre les freqüències específiques del forçament i l'estructura de bifurcació del model.

En segon lloc, en el Capítol 4 es mostra com l'acoblament entre mòduls corticals condueix a patrons d'activitat complexes i a l'aparició d'un fenomen que anomenem *excitabilitat col·lectiva*. Els patrons temporals generats per aquest model s'assemblen a les observacions clíniques de les convulsions epilèptiques. En aquest capítol també introduïm un mètode d'anàlisi de la pèrdua d'estabilitat causada per l'acoblament inter-modular excessiu en les xarxes neuronals. En tercer lloc, en el Capítol 5 ens centrem en les interaccions inter-freqüència que es produeixen en una xarxa de mòduls corticals en presència de soroll de color. Suggerim un mecanisme subjacent a l'augment de la potència spectral de ritmes ràpids a causa del forçament amb un ritme lent, i veiem quins paràmetres del soroll descriuen millor els espectres de potència experimental. Finalment, en el Capítol 6, estudiem models dels processos hemodinàmics i metabòlics del cervell, els comparem amb dades experimentals i considerem les conseqüències del seu acoblament amb models neuronals mesoscopics.

En conjunt, els nostres resultats mostren la influència combinada del soroll i l'acoblament en models computacionals de l'activitat neuronal. D'altra banda, també demostren la importància de les propietats dinàmiques dels sistemes neuronals en fenòmens fisiològics especfics com les interaccions inter-frequència i l'epilèpsia. Els resultats d'aquesta Tesi contribueixen a potenciar l'estudi de l'epilèpsia com una *malaltia dinàmica*, i el desenvolupament de mètodes de tractament aplicables a pacients epilèptics resistents als fàrmacs.

Contents

Abbreviations

BOLD	**B**lood **O**xygen **L**evel **D**ependent
CMRO2	**C**erebral **M**etabolic **R**ate of **O**xygen
CTC	**C**ommunication **T**hrough **C**oherence
DCM	**D**ynamic **C**ausal **M**odelling
ECoG	**E**lectro**co**rtico**g**raphy
EEG	**E**lectro**e**ncephalo**g**raphy
fMRI	**f**unctional **M**agnetic **R**esonance **I**maging
LFP	**L**ocal **F**ield **P**otential
LTI	**L**inear **T**ime-**I**nvariance
MEG	**M**agneto**e**ncephalo**g**raphy
MRI	**M**agnetic **R**esonance **I**maging
NMM	**N**eural **M**ass **M**odel
OM	**O**rnstein-**U**hlenbeck
PERS	**P**oststimulus **E**vent-**R**elated **S**ynchronisation
PSD	**P**ower **S**pectral **D**ensity
PSP	**P**ost**s**ynaptic **P**otential
SDE	**S**tochastic **D**ifferential **E**quation
SN	**S**addle-**N**ode
SNIC	**S**addle-**N**ode on **I**nvariant **C**ircle
SR	**S**tochastic **R**esonance
SW	**S**pike-and-**W**ave

CHAPTER 1

INTRODUCTION

The brain is the most complex organ in the human body. It contains about 86 billion neurons – cells that process, store, and transfer information (Azevedo et al., 2009). The interaction between neurons involves passing signals from *axons* in a neuron to *dendrites* in another neuron via *synapses* (see Figure 1.1). It has been estimated that a neocortical[1] neuron establishes 7000 synaptic contacts on average (Pakkenberg et al., 2003; Tang et al., 2001). The neuronal structure is supported by blood vessels and non-neuronal glia cells, occurring in a number similar to the number of neurons (Azevedo et al., 2009). These cells additionally increase the enormous complexity of the neuronal network, e.g. glial astrocytes affect and respond to neuronal activity as well as interact with each other (Khakh and McCarthy, 2015). The human brain provides functionalities crucial to life, such as sensation, perception, cognition, learning, memory, sleep-wake cycle, language, motor control, and behaviour. It gives rise to self-awareness and consciousness. Understanding how the brain works, and in particular how its functionalities emerge from its anatomy and physiology, is one of the greatest modern intellectual challenges and the Holy Grail of modern neuroscience. One of the ways of undertaking this quest is by means of mathematical models and computational simulations of brain processes. These are the methods employed in this Thesis.

The way in which modern science deals with issues such as memory and decision making led to the invention of computers. But the brain defies a naive parallel to them. Unlike computers it utilises both analogue and digital communication (Sarpeshkar, 1998) and it works in a redundant, parallel and asynchronous manner with a varying processing speed. Although this speed is much lower than of computers, the human brain outperforms the latter on tasks such as intuition, creativity, abstract thinking, and improvisation. And it does so consuming less power than computers

[1] *Neocortex* – the part of the brain with most of the recent evolutionary changes.

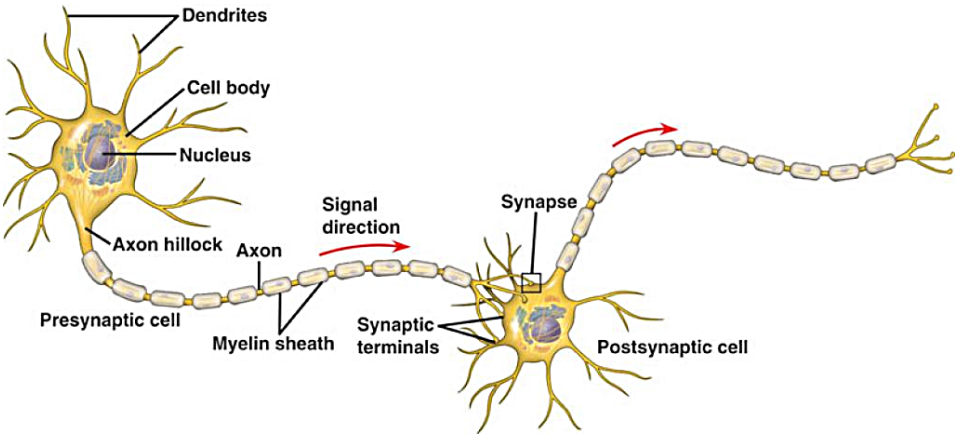

Figure 1.1: Neuronal communication. An action potential (pulse of membrane depolarisation current) travels from left to right (red arrow) through a synapse - connection point between the postsynaptic neuron axon and the postsynaptic dendrite or soma (in this case). The potential arising from incoming signals is summed in the soma (axon hillock, in particular). If this potential exceeds a threshold, the signal is propagated down the axon. Myelin sheath accelerates the signal propagation speed (http://www.anatomylibrary.us).

(Herculano-Houzel, 2011; Sarpeshkar, 1998). Furthermore, the brain does not follow the von Neumann architecture, but rather integrates memory and processing in the same structures. Finally, it self-organises (Abbott and Nelson, 2000), can become spontaneously active (Fox and Raichle, 2007) and operates in a significantly noisy environment (Faisal et al., 2008).

The role of noise in shaping activity of the brain is one of the main interests of this Thesis. In order to study this subject we represent the brain as a stochastic nonlinear dynamical system and we examine it using mathematics and physics approaches. We abstract the brain activity from its functionalities, thereby avoiding the abovementioned complications, solely focusing on the time evolution of its state. We interpret this in terms of brain rhythms, which can take the form of healthy or unhealthy patterns. We relate these patterns to experimental recordings of the brain's activity, in particular to electroencephalographic (EEG) recordings. This approach allows us to propose explanations of empirically known phenomena related to epilepsy and cross-frequency transfer, to make predictions, and to evaluate usability of mathematical models. The model used

in this Thesis is not concerned with the activity of individual neurons, but rather with activity of neuronal patches that loosely correspond to spatial scales typical to mechanisms underlying EEG or functional magnetic resonance (fMRI) recordings. Before discussing in detail the mathematical formulation of this model, we introduce in this chapter structures of the brain and the processes that are the subjects of modelling.

The reminder of the Introduction is organised as follows. In Section 1.1 we briefly introduce brain anatomy, narrowing the description down from the whole brain to neuronal structures. We describe forebrain (Section 1.1.1), cortex and cortical neurons (Section 1.1.2), and cortical columns (Section 1.1.3). We focus on the latter structures because they are the objects of the mathematical modelling performed in this Thesis. Therefore, we discuss them in details, including historical background and open questions. Then, from the anatomical and functional description of cortical columns, we move on to principles underlying generation of electrophysiological signals (Section 1.2) and their simulation in mathematical models (Section 1.3). Next, in Section 1.4 we introduce a whole variety of applications of models considering the brain a dynamical system. We discuss studies on rhythmic and arrhythmic activity of the brain, chaos, noise, brain networks and applications of dynamical systems in empowering medical research. We particularly focus on epilepsy, which is in the foci of this Thesis.

1.1 Anatomical and physiological foundations of mathematical brain modelling

The brain is anatomically divided in four main structures: cerebral hemispheres, diencephalon, brain stem, and cerebellum. The cerebral hemispheres host the neuronal circuits responsible for sensory, motor, and higher cognitive functions. Moreover, since it is the most outer part of the brain, it is accessible by means of non-invasive probing techniques such as EEG and fMRI. Measurements performed with these techniques can be related to results obtained from mathematical models, which in majority of cases are concerned with modelling neuronal tissue. The diencephalon, in turn, is involved in regulating cortical activity, therefore it is often taken

into account in modelling. For these reasons we introduce briefly the anatomy of the cerebral hemispheres and diencephalon (together called the *forebrain*), and above all, we thoroughly discuss the concept of *cortical column*, which is fundamental for the modelling used in this Thesis.

1.1.1 Forebrain

The cerebral hemispheres (called together *cerebrum*) account for most of the mass of the brain (83% according to Marieb and Hoehn, 2007). Each hemisphere is composed of (1) an outer layer of *cortex* – grey matter that consists of neuronal cells bodies, (2) white matter, situated deeper and embodying tracts of neuronal connections, and (3) the most deeply placed *basal nuclei (ganglia)*. The surface of the hemispheres (*the cortex*) is folded, forming elevations of tissue –*gyri*– and grooves –*sulci*– (the deepest of which are called fissures). The most elaborated modelling approaches (Bojak et al., 2010) include this folding, which brings the simulated EEG/fMRI signals closer to the real ones. In simplified approaches, the two-dimensional cortex may be approximated by an infinite medium (e.g. periodic boundary conditions) or a sphere (Robinson et al., 2006).

The hemispheres are conceptually divided by arbitrarily chosen *sulci* into five lobes: four of them located directly underneath the skull (frontal, parietal, occipital and temporal, Figure 1.2) and one located deeper in the brain (insula). These lobes are further divided into functional areas, which are specialised in certain types of processing (e.g. sensory or motor). Realisation of complex tasks requires integration of information from different areas, which is realised by axonal tracts in the white matter. The white matter fibres are classified into three groups: commissure fibres that connect homologous cortical areas located in different hemispheres (whose thick tract is called *corpus callosum*), association fibres that connect areas within the same hemisphere, and projection fibres that run radially and connect the cortex to lower brain areas.

The diencephalon is such an area; it is situated inside the hemispheres, from which it derives its Greek name, meaning 'through brain'. It is made of grey matter and is composed of three key structures known as thalamus, hypothalamus and epithalamus. The main role of thalamus is to shape cortical activity, acting as a gateway to the cortex that mediates, sorts, and

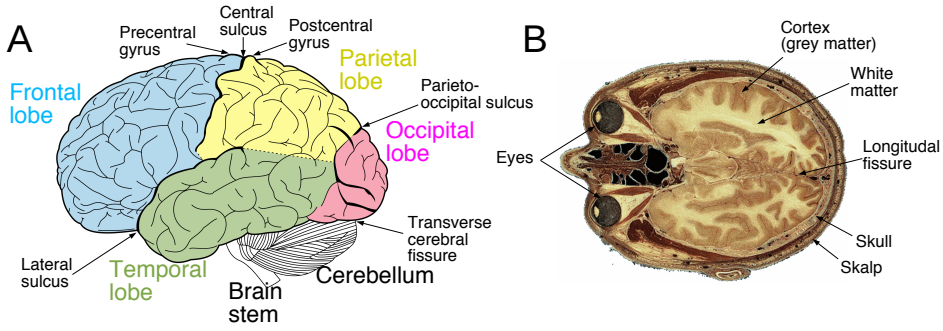

Figure 1.2: Structure of the human brain. Panel A shows a drawn schematic longitudinal view of the human brain (adapted from https://commons.wikimedia.org). Panel B shows a post-mortem performed transversal section through the human skull (U.S. National Library of Medicine, 2001-2015).

standarises afferent signals. Moreover, thalamic neurons establish reciprocal connections with their cortical counterparts, effectively creating feedback loops which further sculpt cortical activity. The thalamus consists of functionally specialised nuclei connected with specific areas of the cortex (Marieb and Hoehn, 2007). The hypothalamus plays a central role in maintaining homeostasis of the body. It regulates the body temperature, hunger, thirst, the sleep-wake cycle (together with the epithalamus), and the endocrine system, and it is a centre for emotional response.

1.1.2 Cerebral cortex

The cerebral cortex is the outer layer of the cerebrum, and consists of grey matter (neuronal cells bodies). Only 20% of the brain neurons are located in the cerebral cortex (Azevedo et al., 2009). These neurons are much more highly connected than the remaining 80%, which is the reason why the cortex (along with the white matter) occupies $\sim 80\%$ of the total brain mass or volume (Hofman, 1988; Marieb and Hoehn, 2007; Rilling and Insel, 1999). Without the white matter the cortex is 2-4 mm thick (Marieb and Hoehn, 2007) and has a laminar structure, consisting of six layers[2], by convention referred to as I-VI, with the numbering starting from the most superficial

[2]Six layers are present in the *neocortex*, which accounts for 90%-95% of all cortical neurons (Karlsen and Pakkenberg, 2011). There are also less evolutionary developed parts of the cortex with less than six layers.

layer. Before characterising neuronal content, connectivity and functionality of these layers, we briefly introduce a rough taxonomy of cortical neurons.

Cortical neurons

Neuronal cells are very diverse. They are characterised by different morphologies, gene expression patterns, neurotransmitters, and firing patters. The most broad classification of cortical neurons is between spiny and aspiny non-pyramidal neurons (DeFelipe and Fariñas, 1992). Dendritic branches of the spiny cells have heterogeneously distributed spines that facilitate synaptic contacts (see Figure 1.3A). Axons of the spiny cells connect mostly to the spines of other cells of the same type. The spiny cells can be further subdivided into pyramidal and stellate neurons (DeFelipe and Fariñas, 1992).

Pyramidal neurons owe their name to the triangular shape of their soma and account for 60%-85% of all cortical neurons (Liley et al., 2012). They are furnished with a long descending axon and two dendritic structures: apical and basal (see Figure 1.3A). The axons allow for the formation of connections extending out for centimetres through the white matter. They connect to dendrites and somata of interneurons and dendrites of other pyramidal cells. Basal dendrites are horizontally, branching arbours originating at the base of the soma. Apical dendrites start as single branches originating at the top apex of the pyramidal soma and reaching out, towards the cortical surface (*pia*), up to layer I, where they form a wide tuft. The configuration of dendritic arbours tends to be different, depending on the cortical layer in which the neuron is located (Spruston, 2008).

Spiny stellate cells lack the long axon and the apical dendrite. They are classified as *interneurons* that do not directly conduct signals to far distances, but rather form local circuits via their star-shaped dendrites, from which the 'stellate' name is derived. All spiny neurons act in an excitatory manner on their downstream associates. The majority of non-spiny (smooth) interneurons, constituting anywhere between 10%-25% of cerebral neurons (Buxhoeveden and Casanova, 2002), operate in the opposite way, inhibiting their efferent contacts. It is estimated that there is around ten non-spiny neuronal types in the cerebral cortex (Markram et al.,

2004). The inhibitory interneurons may target axons, dendrites or somas (Markram et al., 2004). Somatic connections exhibit the strongest inhibitory effect, which is called *perisomatic*.

Cortical connectivity and laminar structure

Although cortical connectivity involves an enormous number of elements and connections, some repetitive schemes of circuitry can be distinguished. In this Thesis, we use a mathematical model of such a brain circuit and we relate conclusions drawn from computational simulations to (patho)physiology. In general, the brain circuits are species-dependent and brain area-dependent. For instance, cortico-cortical and thalamo-cortical connectivity patterns may strongly vary (e.g. barrel cortex of rodents, discussed later). Also phenotypes of neurons change between species; for example more types of inhibitory neurons are found in the brains of primates than in the brains of other mammals (DeFelipe et al., 2002). Therefore, although we review below cortical connectivity patterns in a fairly general way, one needs to bear in mind that neural circuits are not governed by absolute rules.

Pyramidal neurons are mostly found in layers III and V, although they are present in all layers with the exception of layer I, where their apical dendrites extend and where in general only few (mostly inhibitory) neurons are present. Spiny stellate neurons are present only in layer IV, where (along with other neurons) they receive sensory thalamo-cortical afferents (Jones, 1998; Liley et al., 2012). Their partial apical dendrites only reach layer III (Markram et al., 2004). Connections from the cortex to subcortical regions originate in layers V and VI. For example, voluntary motor control connections that run through the cortico-spinal tract originate in layer V (Meyer, 1987), whereas connections to the thalamus extend from layer VI (Lam and Sherman, 2010). Reciprocal connections from the thalamus to the cortex terminate in layer I (Rubio-Garrido et al., 2009) or IV (Jones, 1998), depending on the type of the source thalamic cells thereby forming thalamo-cortical feedback loops. Commisure and associational cortico-cortical long-range efferents arise mostly in layers II, III (Buxhoeveden and Casanova, 2002; Mountcastle, 1997) (some also in layers V, VI)

and they in general might terminate in all layers, but mostly II, III, IV (Buxhoeveden and Casanova, 2002), with an ending preference depending on their origin (Rockland and Pandya, 1979). In general, long-range connections are organised in discrete tracts penetrating the white matter, whereas the short-range intrinsic cortical connectivity is uniform.

This connectivity across all layers interconnects neurons of the same type. It also involves pyramidal collaterals that feed to local inhibitory interneurons, which in turn feed back to the pyramidal neurons and inhibit them. A similar, but excitatory, feedback loop involves spiny stellate neurons. The intrinsic connectivity is also strongly arranged in a vertical manner: e.g. information descends through the layers via apical dendrites of the pyramidal neurons and is passed up by the spiny stellate cells from layer IV. This leads to a high degree of correlation in the activity of vertically co-aligned neurons. Furthermore, horizontal ranges of various neuronal structures set boundaries of the neuronal assemblies whose activity tends to correlate. This gives rise to a notion of a 'cortical column' that we discuss in the next section.

1.1.3 Cortical columns

Apart from the symmetry arising from the laminar arrangement of the cortex, one can also - arguably, as we show later - distinguish cylindrical repetitive neuronal structures going through all the layers: so-called cortical columns. These columns correspond to building blocks of the model used in this Thesis. Therefore, we discuss them thoroughly, in order to set the scene for the interpretation of the mathematical results.

Origins

The concept of these columns can be dated back to Lorente de No (1938) who studied mice and proposed that the cortex is organised in unitary 'vertical chains'. The term 'cortical column' was first used by Mountcastle (1957) who performed electrophysiological measurements on the cat primary somatic sensory cortex and observed that stimulation of same peripheral receptive fields led to almost simultaneous arousals of vertically arranged neurons belonging to different layers. Mountcastle concluded

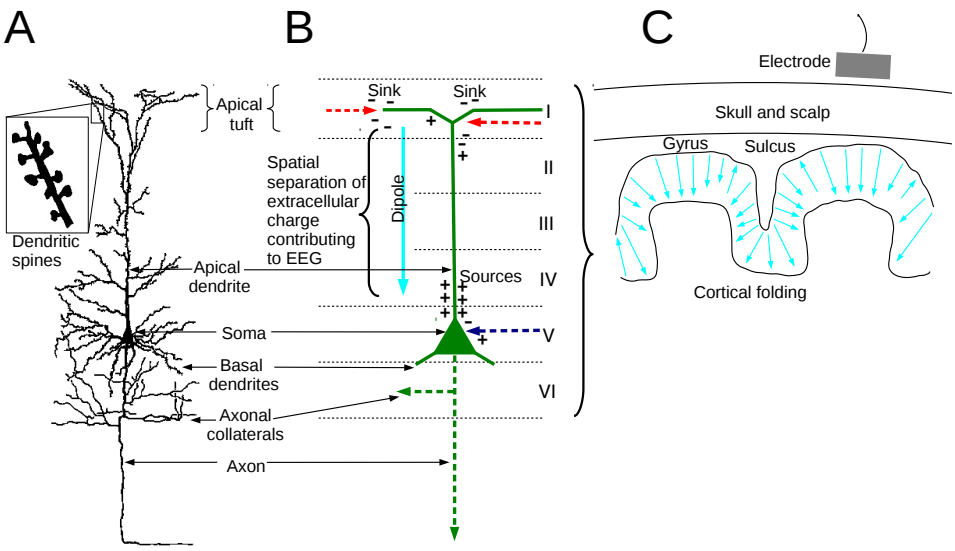

Figure 1.3: Neuronal morphology and electrical activity. Panel A (adapted from https://grey.colorado.edu/CompCogNeuro) shows tracing of a cortical pyramidal neuron, with a region of dendritic spines shown in the inset. The cortical layers in panel B are denoted with Roman numerals and a scheme of a pyramidal neuron from layer V is shown in green. Panel B also shows spatial charge separation resulting from the synaptic activity; '+/-' denote electrical charge in the extracellular medium. Dashed lines symbolise axons and continuous lines stand for dendrites. Incoming excitatory (red) and inhibitory (blue) connections create sinks and sources of charge which from distance can be approximated by a dipole (cyan). The cortical folding and the perpendicular alignment (with respect to the cortical layers) of pyramidal neurons create a folded sheet of such dipoles (panel C, based on Nunez and Srinivasan, 2006). Electric field generated by this sheet can be measured by an electrode placed on the scalp (grey), as it is done in EEG recordings. In the example shown in panel C, the antiparallel dipoles close to the *sulcus* counteract and diminish the signal. In general, this signal is strongest over the *gyri*, due to the vertical alignment of the dipoles, and closest distance between them and the EEG electrode (grey). The figure is schematic and does not hold anatomical proportions (the thickness of cortex is in reality 2 mm-4 mm and the thickness of the scalp and skull is ~ 1 cm, Marieb and Hoehn, 2007).

that the vertical organisation of the cortex has also a *functional* character and he estimated that the diameter of these functional columns is not greater than 0.5 mm. Later Woolsey and Van der Loos (1970) observed a barrel-like organisation of neurons in layer IV of the mouse somatosensory cerebral cortex. This is due to the somatotopic construction of that layer, which Woolsey and Van der Loos (1970) described as a field of 'discrete cytoarchitectonic units' organised around afferents coming from individual whiskers in a way resembling their spatial alignment. Woolsey and Van der Loos (1970) refer to the observed barrels as morphological manifestations of the functional columns described previously by Mountcastle (1957).

In 1981 the Nobel Prize in Physiology and Medicine was awarded to David H. Hubel and Tornsten Wiesel for their discoveries concerning information processing in the visual system. The laureates had observed a columnar organisation of the cat (Hubel and Wiesel, 1963) and macaque (Hubel and Wiesel, 1977) visual cortices. They noted that columns of neurons (of diameter ~ 0.4 mm) were exhibiting *ocular dominance*, i.e. they were reacting to visual input from one eye or the other. Moreover, columns of diameter ~ 20 μm-50 μm were related functionally, that is, they would respond most readily to visual stimulation with moving bars of similar angular orientations. The orientation preference was changing in a smooth manner along the cortex, and the groups of columns covering the full 180° range of stimulation angles were found to be organised in 'hypercolumns', which in turn were engrafted upon topographic representation of the visual field (Hubel and Wiesel, 1977). These observations showed that columnar organisation of the cortex involves compound structures and spans various spatial scales.

Spatial classification

The cerebral structures can be considered in at least three spatial scales: *microscopic*, *mesoscopic* and *macroscopic*. We define the microscopic scale in the range of tens of micrometers, on the order of the size of the neuronal soma (5 to 140 μm, Marieb and Hoehn, 2007). The macroscopic scale is of the order of centimetres, and on the order of the size of the whole brain or brain areas, as defined for example in the Brodmann's (Zilles and Amunts, 2010)

or Montreal (Mazziotta et al., 1995) brain maps. In between those two limits there is a range of spatial scales often termed *mesoscopic* (English: 'middle', 'medial'). The size of cortical columns falls into this range. There is no single neuronal structure that categorically determines a cortical column, but rather we can distinguish a number of anatomical formations that in one way or another organise neurons in vertically oriented assemblies, and therefore give rise to the notion of a cortical column. As a consequence, we can speak of cortical columns of various sizes (and thus types).

The mathematical modelling employed in this Thesis relies on assumptions that are valid in the mesoscopic scale (see Section 1.3 and Chapter 2), but it is not limited to a specific spatial dimension. To the contrary, it has been used to describe the activity of neuronal structures ranging from the smallest *minicolumn* (Babajani and Soltanian-Zadeh, 2006) up to a brain area (Breakspear et al., 2006). Often this modelling method is associated generally with 'cortical columns' without specifying their exact type. This is justified because granularity and the mathematical description of this method is not concerned with subtleties distinguishing various types of cortical columns. In what follows, we review these types of cortical columns briefly (and in a very simplified way).

The notion of a *minicolumn*[3] follows mostly from the range of the lateral extent of inhibitory connections, which roughly coincides with the size of vertically co-aligned assemblies of cells and with the size of the axonal and dendritic bundles of pyramidal neurons. Without discussing details of these structures, we associate a minicolumn with a spatial extent of ~ 50 μm in diameter, with the corresponding numbers of neurons being in range $80 - 200$ (for details see Buxhoeveden and Casanova, 2002). The lateral extents of cortico-cortical and thalamo-cortical afferent fibres are characterised by diameters ~ 0.3 mm and ~ 0.5 mm, respectively, and they accentuate mesoscopic columns that contain $\sim 10^4$ neurons (Liley et al., 2012). Moreover, the horizontal axonal ramifications of cortical pyramidal neurons (axonal collaterals) bind together thousands of minicolumns

[3]Some sources use interchangeably 'minicolumn' and 'microcolumn' (Buxhoeveden and Casanova, 2002; Mountcastle, 1997), while others reserve the latter for structures as small as a single row of ~ 20 neurons (Liley et al., 2012).

and form *macrocolumns*[4]. These columns are ~ 1.5 mm wide in diameter and they contain $\sim 2 \cdot 10^5$ neurons (Liley et al., 2012).

Functionality

The columnar structure differentiates the cortex from subcortical areas, which are organised into a set of specialised nuclei and ganglia (see Section 1.1.1). The importance of the cortical architecture may be the reason why evolution favoured to develop rather cortical folding (that increases the number of columns) over thickness (that would increase the number of neurons per column). Various different explanations for the emergence of folding have been proposed (Bullmore and Sporns, 2012). Apart from introducing computational organisation, the columnar structure of the cortex brings about a number of advantages. It is favourable for connectivity, which only needs to concern columns, not the contained individual neurons, which due to the columnar structure share information. Furthermore, the columnar solution increases adaptability because it empowers development due to plasticity. Since it is columns rather than neurons that implement elementary functionalities, the individual neurons lose their importance and may undergo plastic rewiring without causing abrupt losses of functionality. Finally, redundancy within the columns enhances reliability and tolerance to noise.

Cortical columns - structural or functional

The aforementioned spatial classification of cortical columns, albeit systematic, leaves ambiguous which anatomical structure is really represented by the minicolumn. This column can be identified with vertical rows of cell bodies or with formations of axons or dendrites. None of these structures, however, is comparable with the size of an individual pyramidal cell. This mismatch between the size of the majority of the cortical neurons and the regularity of the orientation map was already realised by Hubel and Wiesel (1974) and is being reiterated nowadays. For example, Narayanan et al. (2015) found that in the vibrisal rat cortex the majority of intracortical axons reach out far outside of the somatotopic cortical column. Another difficulty arises from the fact that the columnar structure is

[4]Note that these columns, according to our classification, fall in the *mesoscopic* scale.

not perfectly regular. Minicolumns are not uniform across the cortical layers, they do not take shapes of regular cylinders, but rather 'swirling slabs' (Costa and Martin, 2010) and they may fork (Rockland and Ichinohe, 2004). For these reasons the notion of an anatomical cortical minicolumn is still under debate (Costa and Martin, 2010).

Despite these perplexities related to anatomy, the concept of a *functional column* is well established. The functional modularity of the cortex seems to be a versatile solution: between species whose brains vary in size by three orders of magnitude, the mesoscopic column only change in size between 300 μm and 600 μm (Mountcastle, 1997). Furthermore, although the different cortical areas process a variety of information types (visual, auditory, somatic sensation, cognitive, etc.), the columns engaged in these processings are remarkably alike. Still, they can develop some differences and specialisations. For instance, functional columns sensitive to orientation preference found by Hubel and Wiesel in cats and monkeys were not found in the visual cortex of rodents (Costa and Martin, 2010). Similarly, coding methods in the somatosensory and visual cortices are different. For instance, only in the latter case the same neurons participate in two orthogonal codings at a time (orientation preference and ocularity).

Cortical connectivity is still under intensive research (Shepherd and Sten, 2010). For instance, thorough anatomical studies on mapping of the cortical circuitry led to the founding of the Blue Brain Project (Markram, 2006) which attempted to simulate *in silico* the rat cortical column. Nevertheless, for computational simulations focused on phenomenological dynamical modelling, anatomical details may not be crucial. One could, for example, model intra- and inter- layer connectivity between groups of neurons without determining their exact spatial arrangement, but rather on the basis of their average interconnectivity (Shepherd and Sten, 2010). Such approach led to a notion of modelling functional *canonical circuits* (Douglas and Martin, 1991) rather than anatomical cortical columns. This idea is not entirely new, but rather dates back to the concept of *neural mass* or *population* modelling that was introduced in order to simulate the generation of electrophysiological signals (Freeman, 1975).

1.2 EEG AND PHYSIOLOGY OF NEURONAL OSCILLATIONS

Having discussed the basic anatomy of the cortex, we proceed to the physiology of the neuronal oscillations detectable in electrical recordings, such as EEG. In this Thesis we use a computational model that simulates such oscillations, therefore we introduce their origins and the measurement methods prior to discussing the computational results.

'EEG' stands for 'electroencephalography' (English: 'electrical-brain-recording') - a term introduced by Hans Berger, who was the first to detect and record the electrical activity of the brain (Berger, 1933). In principle, the EEG recordings capture electric potentials generated by the charge arising from the synaptic activity of pyramidal neurons in the cortex. The EEG recordings are performed via electrodes placed non-invasively on the scalp, therefore at some distance from the neurons (see Figure 1.3C). For this reason, and due to attenuating effects of the tissue, the EEG is not correlated with firing patterns of spikes (Logothetis, 2003; Nunez and Srinivasan, 2006). Furthermore, for the same reason, a single electrode registers a signal that is generated by a large number of neurons.

Neurotransmitters, released by the arrival of a presynaptic spike, bind to receptors on the postsynaptic dendrite and change conductivity of its membrane. In consequence, a local 'sink' of current is created (see Figure 1.3C), which leads to imbalance of charges between the inside and the outside of the neuron (Bojak and Breakspear, 2015). The charge inside the dendrite is conducted towards the neuronal soma, leaking through the passive membrane on the way and creating 'sources' of charge. Dendrites of interneurons are short and lack directional preference, therefore 'sources' and 'sinks' (when measured from a distance) cancel each other. In contrast, the long apical dendrites of pyramidal neurons (see Figure 1.3A,B) provide a systematic separation of these charges, which far from the neuron can be approximated by a dipole (Buzsáki et al., 2012). This effect is depicted in Figure 1.3B. Red arrows in cortical layer I stand for afferents synaptically acting in an excitatory manner and thereby creating 'sinks' for positive charge (surging into the neuron) which are spatially separated from 'sources' appearing closer to the soma.

The dipoles arising from excitatory synaptic activity are not totally counterbalanced by dipoles caused by inhibitory synaptic activity, because in the case of pyramidal neurons, the excitatory synapses tend to be located on the apical dendrites (e.g. on the apical tuft, receiving excitatory input from remote brain areas, as shown in Figure 1.3A,B), whereas the inhibitory synapses tend to be located on the basal dendrites (due to local circuitry with inhibitory interneurons, see Spruston, 2008) or even directly on the soma (the *perisomatic* effect mentioned in Section 1.1.2), as shown in Figure 1.3B. Moreover, because apical dendrites of different pyramidal neurons are parallel, dipoles can sum up and create a distribution of charges on the cortical sheet. Because of the folding of the cortex (see Section 1.1.1), the dipoles aligned horizontally to the skull surface (located close to the *sulci*) may partially cancel out. The dipoles located at the *gyri*, in contrast, are vertically oriented and are closer to the skull surface (and therefore to the measuring electrodes); thus they are the ones that mainly contribute to the EEG signal (Figure 1.3C). Furthermore, the signal is strongest when the activity of the dipoles is temporally coherent.

In Section 1.1.3 we mentioned that neurons aligned vertically in the cortex tend to exhibit correlated activity, which can be explained by the strong local connectivity. Indeed, experimental studies showed that coherence in the EEG generation occurs in the millimetre domain (Bojak and Breakspear, 2015; Bullock et al., 1995). This means that the activity of closely situated and strongly coupled neurons is to a certain extent synchronous, where 'synchrony' is used with respect to slowly decaying synaptic activity, rather than rapid spiking. The observation that the amplitude of the signal generated by N harmonic sources grows with N when they are coherent, and with $\sqrt{N}$ when their phases are distribute randomly (Bojak and Breakspear, 2015; Nunez and Srinivasan, 2006) leads to an important conclusion: EEG recordings are mainly influenced by signals generated by coherent groups of neurons, which greatly dominate over signals from incoherent, albeit larger groups. In the next section we introduce concepts underlying the computational modelling of activity of neuronal groups, often termed *neural masses* or *populations*.

1.3 POPULATION MODELLING

Mathematical modelling of physical or physiological systems requires a choice of the level of accuracy. A faithful computational simulation of a biological neuronal system could consider the geometry of individual cellular bodies and the dynamics of ions, neurotransmitters, ion channels, etc. When the system has the complexity of the human brain (see the introduction of this chapter), however, such level of accuracy could be compared to an attempt to model the trajectories of all molecules of gas in a vast chamber. The impracticability of this approach follows from at least two facts: its enormous computational complexity and the overabundance of the resulting data. In practice, one is not interested in the motion of each molecule, but rather in phenomenological measures of the whole system, such as temperature and pressure. Similar dimension reductions are often performed in theoretical neuroscience (Pang et al., 2016). For example, when relating computational modelling results of the activity of neuronal tissue with EEG or fMRI recordings, one is not concerned with the spatial and temporal scales typical to the activity of individual neurons, but rather with the scale set by the resolution of these signals, and - depending on the modelling method - with the scale typical to processes responsible for the generation of these signals.

In this Thesis we are interested in the behaviour of populations of neurons that are interconnected and therefore synchronised to an extent which gives rise to occurrence of electric dipoles registered in the recordings, or to observable changes in metabolic activity reflected in the blood-oxygen-level dependent (BOLD) signals measured in fMRI (details of BOLD and fMRI are discussed in Chapter 6). From an anatomical viewpoint, these neuronal populations can be identified with the columns described in Section 1.1.3, in particular with mesoscopic-scale columns, the dimensions of which do not exceed the spatial resolution of the EEG and fMRI recordings ($> 1\,\text{cm}$ and $> 0.5\,\text{mm}$, respectively, Bojak and Breakspear, 2015).

As explained in Section 1.1.3, cortical columns have internal structures, e.g. they comprise different types of neurons. Groups of neurons sharing physiological properties are mathematically modelled as *neuronal populations* or *neural masses*. These groups can be then interconnected to resemble

the internal structure of a cortical column, with a degree of fidelity that depends on the model. Populations are dimensionless, but the modelled columns can be arranged in a way resembling the geometry of the cortex. These point populations may model groups of neurons of various sizes, as long as the intrapopulation coherence is sufficiently high and invariant. This requirement follows from the aforementioned fact that groups of synchronously firing pyramidal neurons produce a signal highly exceeding the signal produced by groups of unsynchronised neurons, and thus the former are the dominant source of activity in the overall EEG. As discussed in Section 1.1.3, the internal activity of cortical columns have been shown to exhibit a high degree of correlation which makes them good candidates for population modelling. This approach is one of many that enables theoretical studies of brain dynamics.

1.4 The brain as a dynamical complex system

The human brain is one of the most complex systems under study in modern science. It exhibits the arguably most fascinating phenomenon known to humankind, that is self-consciousness. The functionalities of the brain are believed to emerge from the collective activity of large-scale brain networks (Park and Friston, 2013). This activity is shaped by structural connectivity of the brain (described in the previous Sections) and by local neuronal dynamics, which are in focus of this Thesis. These dynamics are strongly nonlinear (Friston et al., 2000) in both microscopic (Hodgkin and Huxley, 1990) and mesoscopic (Deco et al., 2008) scales, and are inherently noisy (Faisal et al., 2008). Nonlinearity gives rise to occurrence of phenomena such as multistability, oscillations and bifurcations, all of which are dealt with in this Thesis.

Both experimental and theoretical studies of the brain dynamics *in vivo* can be performed according to one of the following paradigms. (1) First, the brain might be studied in its *resting state*, i.e. in the absence of external stimulation. (2) When stimulation is applied, one can map characteristics of the stimulation and the response, to infer brain's internal mechanisms. (3) Finally, studying neuronal diseases allows to relate aberrant dynamical patterns of the brain to structural defects. This approach permits to map

brain mechanisms to functions. In this Thesis we are interested in the effects of rhythmic and stochastic driving on a neuronal model of a cortical column (and interconnected columns). This driving may be attributed to external stimulation, but also to natural background activity of brain areas encompassing the considered neuronal patch. This links our results to the first two paradigms. The third paradigm is referred to in Chapters 3 and 4 where we computationally model effects related to epilepsy.

In the reminder of Section 1.4 we first introduce rhythmic dynamics of the brain, then we proceed to arrhythmic, broadband chaotic and stochastic activity. We discuss potential functions of these mechanisms. Next, we introduce concepts of metastability and transitions in the brain, and we discuss spectral properties of mesoscopic-scale neuronal activity. We close this section with an introduction of brain networks and diseases.

1.4.1 Rhythms of the brain

The brain is known to operate in a wide range of frequencies, occupied by rhythms spanning over four orders of magnitude (Buzsáki and Draguhn, 2004). These rhythms are generated by internal neuronal mechanisms, i.e. are self-sustained in the absence of external driving. Remarkably, the same temporal order of rhythms is present in brains of different mammalian species, although the volume of these brains changes by more than four orders of magnitude (Buzsáki et al., 2013). This suggests universality of fundamental mechanisms responsible for generation of neuronal oscillations. Biological studies revealed that even an individual neuron can exhibit oscillations and resonate at specific frequencies (Hutcheon and Yarom, 2000). Nevertheless, the macroscopic brain rhythms are not only a reflection of frequency characteristics of individual neurons, but rather arise as collective phenomena from specific mechanisms, e.g. from circuitry such as feedback loops.

Neuronal oscillations are believed to correspond to different internal brain processes and to reflect different brain states (Engel et al., 2001; Klimesch, 1999). In numerous experiments it has been shown that different mental tasks are associated with changes in power in different brain rhythms (Babiloni et al., 2014; Cannon et al., 2014; Harmony, 2013; Harmony et al., 1999). This separation of bands in the frequency domain

allows different processes to operate simultaneously and independently. Nevertheless, this frequency-based separation of processes in the brain is not strict. Due to the nonlinear character of the brain dynamics, these processes can interact in a number of ways (Buzsáki, 2006) resulting in phenomena such as rhythms adjustment - various types of synchronisation (Pikovsky et al., 2001), quenching, phase precession, and a number of inter-frequency modulations, so-called 'cross-frequency couplings' (Jirsa and Müller, 2013). These include phase-to-power coupling, which occurs when the power (amplitude) of one rhythm (the faster one) is modulated by the phase of the second rhythm (the slower one). In Chapter 5 we suggest a potential dynamical scenario underlying this phenomenon.

In general, brain rhythms can be linked to a variety of perceptual, cognitive and sensorimotor functionalities (Baar et al., 2001). A classification of rhythms along with their associated brain states and processes is as follows. The slowest neuronal oscillations with frequencies < 1 Hz are most often associated with *slow wave sleep* activity (Steriade and McCarley, 2005) and the *UP-DOWN* states (Compte et al., 2003). The delta rhythm spans, depending on the author, from 0.5 Hz or 1 Hz to 4 Hz. It has been linked to performance of mental tasks (Harmony, 2013) and to sleep. The theta rhythm is generated in the cortex and hippocampus. It corresponds to the 4 - 8 Hz frequency range, and it has been linked to navigation, planning and memory (Buzsáki and Moser, 2013; Osipova et al., 2006). The rhythm falling within 8 - 12 Hz band is termed 'alpha'. It is the dominant oscillation in the human brain, strongest on the occipital lobe (site of the visual cortex) and increasing during relaxed wakefulness. These rhythms are linked to visual processing (Babiloni et al., 2005; Dijk et al., 2008), attention (Ray and Cole, 1985) and retrieval of long-term memory (Klimesch, 2012). It is currently believed that at least two mechanisms may be responsible for the generation of alpha oscillations: intrinsic properties of cortical neurons and a thalamo-cortical interaction (Liley et al., 2010). Beta oscillations span frequencies from 12 Hz to 30 Hz and are related to altered states, mental and emotional activities (Ray and Cole, 1985), and motor control (Pfurtscheller et al., 2005). Finally, the fastest, gamma oscillations correspond to the range above 30 Hz. They have been linked to attention, and

encoding and retrieval of declarative memory (Jensen et al., 2007). They have also been hypothesised to be crucial for cortical computation (Fries, 2009).

The above classification should be considered a guideline rather than rigid or complete because there is much we do not know about functionalities and generating mechanisms of neuronal oscillations. Moreover, many different processes may be associated with the same rhythm. For example *sleep spindles* generated in the reticular nucleus of the thalamus (Bonjean et al., 2012) and sensorimotor mu rhythms (Pfurtscheller et al., 1997) overlap with the alpha band.

This classification might suggest that due to the distinction of sources, the overall power spectrum of the whole brain would be a collection of separated peaks. But although spectral peaks indeed do appear, their height might be transient and dependent on the current brain state. According to the 'labile brain' theory (Friston et al., 2000), due to nonlinear interactions, dynamics of the brain are on the transient move between stable complex incoherence and predictable synchrony. We focus on long transient dynamical states exhibited by mesoscopic neuronal models in Chapter 4. The dynamically varying spectral peaks are embedded in a background exhibiting $1/f^b$ power law scaling. This peculiar shape of the background power spectrum can stem from a number of different mechanisms (discussed in Section 1.4.5). In Chapter 5 we perform spectral analysis of simulated neuronal signals revealing peaks embedded in a realistic background.

The rhythmic activity of the brain might only reflect undergoing processes, but it also might play a crucial role on its own (Buzsáki, 2006). For example, the mechanism of 'communication through coherence' (CTC) proposed by Fries (2005) assumes that efficient transmission of information between neuronal assemblies requires coherence of their oscillations, assuring temporal adjustment between input and output of the information flow. This adjustment could be provided by a slow rhythm, coordinating

activity of the communicating populations, e.g. by synchronously modulating their activeness, as in the 'phase-to-amplitude' cross-frequency coupling scenario (discussed broadly in Chapter 5). A hierarchy of such nesting rhythms could also serve as a communication protocol allowing to transfer composite meanings and representations (Buzsáki et al., 2013).

CTC is capable not only of establishing but also disestablishing communication routes between remote neuronal populations. Therefore, it can support one of the fundamental functionalities of the brain, so called 'segregation-integration'. By diminishing communication capabilities CTC may functionally separate distributed neuronal populations, thereby providing them with operational independence. This is important for local computations in specialised brain areas (see Section 1.1), e.g. simultaneous processing of visual and auditory stimuli, their interpretation, and motor control. On the other hand, by establishing connections, CTC may allow for mediation of a solution consistent across the areas, which is necessary for solving complex tasks that involve various sensory inputs, cognition, control of output, etc.

In reality, the synchronisation task is additionally hampered by the fact that signals in the brain propagate with a finite velocity. The CTC concept embraces the resulting delays (Barardi et al., 2014; Bastos et al., 2015). In general, delays can seriously affect the mesoscopic dynamics, e.g. leading to bifurcations (Coombes and Laing, 2009), or even stabilising the (mesoscopic) dynamics (Atay and Hutt, 2006). A phenomenal property of the mammalian brains is that communication over greater distances tends to be realised with higher velocity than on short distances (Buzsáki et al., 2013). This effectively diminishes communication dissimilarities between closely and remotely located brain areas, empowering integrative capabilities of the brain (Vicente et al., 2008). This feature might be the reason for the aforementioned preservation of rhythms across different mammalian species, in spite of significant differences between their brain sizes. Apart from rhythmicity, brain dynamics exhibit a certain degree of apparent randomness that we discuss in the following section.

1.4.2 Chaos and noise

In theoretical and experimental studies alike, the neuronal dynamics appear highly complex and to a certain degree random, reflecting perhaps the fact that the behaviour of organisms is not fully foreseeable. Since chaos theory showed that unpredictable activity can arise from purely deterministic systems, it became ambiguous whether the apparent disorder and irregularity stem from noise or from chaoticity. In neuronal dynamics both types of behaviour are relevant, which prompted Freeman (2000) to propose the term 'stochastic chaos'. It is important to keep in mind, however, that although stochastic and chaotic systems may appear alike because noise and chaos share similarities (Sapienza et al., 2000), the origins and properties of these two phenomena are fundamentally different (Rabinovich and Abarbanel, 1998). Chaos has a well-determined structure in phase space, which can be used for control (Schöll and Schuster, 2008), synchronisation (Boccaletti et al., 2002) and information transmission (Hayes et al., 1993), whereas noise lacks such structure. *In vitro* analysis of hipoccampal activity (Slutzky et al., 2001) suggests that neuronal systems, although globally stochastic, contain local 'pockets of determinism', where chaos control methods may be applied. Following that observation, dedicated methods of identification of determinism in neuronal systems have been proposed (Slutzky et al., 2002). Nevertheless, also noise is known to be utilised in a constructive way in the nervous system (McDonnell and Ward, 2011). In what follows, we discuss the role of chaos and stochasticity in neuronal processing.

Chaotic brain

A suggestion that the brain displays chaotic behaviour was arguably first put forward by Kaczmarek and Babloyantz (1977) in the context of a theoretical model of focal epilepsy. Later Babloyantz et al. (1985) found chaotic attractors in experimental EEG time series recorded in sleeping humans. Shortly afterwards Skarda and Freeman (1987) introduced a neural mass model of the olfactory bulb, and suggested that chaos plays a crucial role in neuronal processing. According to their proposal chaos precedes emergence of ordered states, which correspond to the recognition of known

patterns (odours), and at the same time allows for learning of new patterns. Rabinovich and Abarbanel (1998) constructed a model of a central pattern generator of the lobster heart beat. They observed that an assembly of Hindmarsh-Rose spiking neurons coupled in an inhibitory way was able to generate regular bursts, although individual neurons were capable of displaying chaos. Such an increase of regularity with complexity is uncommon in dynamical systems, e.g. it is contrary to what is observed during turbulence. Rabinovich and Abarbanel suggested that chaotic behaviour allows a broad exploration of phase space and that it provides adaptability, since unstable chaotic orbits can be easily escaped. Finally, they showed that rhythms generated by their model were robust against changes to parameters, thereby demonstrating chaos-generated reliability.

So far many theoretical works have shown the occurrence of chaos in both micro- and mesoscopic neuronal models. Sompolinsky et al. (1988) found chaos in a neuronal network of nonlinear elements interconnected in a random, asymmetric manner. Schiff et al. (1994) and Slutzky et al. (2003) observed *in vitro* chaotic behaviour in rat hippocampal brain slices and they implemented methods of chaos control to suppress epileptic-like neuronal activity. Recently stimulus-induced suppression of chaos was studied theoretically by Rajan et al. (2010). Vreeswijk and Sompolinsky (1996) showed that excitatory-inhibitory balance in neuronal networks may result in chaotic behaviour. Liley et al. (2002) found chaos in a spatially extended mean field model of electrocortical activity. Also in mesoscopic-scale models chaos was observed by Coombes and Laing (2009), Roberts and Robinson (2012) and many others. In summary, these studies have shown that the capability of displaying chaos is an innate feature of neuronal systems.

Noisy brain

The results presented in this Thesis focus particularly on the impact of stochasticity on neuronal dynamics. Therefore, in what follows we briefly introduce potential sources and roles of noise relevant to functioning of the brain. The apparent randomness in the nervous system is present on many levels: from the variability of external stimuli, through neuronal processing, to motor response (Faisal et al., 2008). On the level of single neuron, stochasticity manifests as thermal noise affecting molecular diffusion, the

kinetics of neurotransmitters, and the dynamics of synapses and individual ion channels (McDonnell and Ward, 2011). Dynamical variability also arises from the morphological diversity of neurons (Padmanabhan and Urban, 2010) and the stochasticity of their gene expression (Kærn et al., 2005). Furthermore, randomness might arise from the irregularity of neuronal networks (Torcini and Angulo-Garcia, 2014), and from the fact that they recurrently couple many nonlinear elements (McDonnell et al., 2016). Also, the representation, processing, and transfer of information in the brain are subject to noise (Faisal et al., 2008). Since the brain has evolved under the influence of these inevitable stochastic factors, it has developed means of reducing their destructive effects. For example, redundancy (see Section 1.1.3) allows to increase signal-to-noise ratio by averaging over time and over many neurons (Faisal et al., 2008). Using prior-knowledge (Eddy, 2004; Knill and Pouget, 2004) and making predictions (Kalman, 1960) allow to further mitigate the influence of noise.

Studies of stochastic dynamical systems have shown that noise may not only blur the deterministic solution, but might also play a constructive role, leading to qualitatively new phenomena: noise-induced oscillations, state transitions, synchronisation, breaking and restoring of symmetry, and – in case of spatially extended systems – pattern formation and wave propagation (Lindner et al., 2004; San Miguel and Toral, 1997). Similarly, the nervous system has learnt not only to minimise effects of noise, but also to benefit from them. The brain adopts strategies such as stochastic optimal control (Todorov and Jordan, 2002) to maximise the desired result of undertaken tasks. Spontaneous releases of neurotransmitters, previously thought of to be erratic, help to establish synaptic connections in early brain development and thus control growth of the dendritic arbours (Andreae and Burrone, 2015). Furthermore, noise-induced transitions between attractors allow to explore the brain's dynamical repertoire (Ghosh et al., 2008). Variability in neuronal activations naturally allows for population coding (Ma et al., 2006) and facilitates Bayesian inference (Knill and Pouget, 2004). Moreover, not only randomness in dynamics, but also diversity of the system itself may increase performance (Tessone et al., 2006).

Another constructive action of noise in the nervous system is via *stochastic resonance* (SR) (Gluckman et al., 1996; McDonnell and Abbott, 2009; Moss, 2004). In classical stochastic resonance a moderate noisy enhancement of otherwise sub-threshold stimuli improves the detection performance (signal-to-noise ratio) of a nonlinear system. Later studies showed how coupling of many units to compound systems ('arrays') leads to enhancement of SR (Lindner et al., 1995; Wiesenfeld, 1991), coining the notion of an *array-enhanced* SR. This coupling may even abolish the sub-threshold condition, giving rise to *suprathreshold* SR (Stocks, 2000). Finally, *aperiodic* SR concerns broadband (aperiodic) signals. It has been observed experimentally in rats (Collins et al., 1996b) and in various theoretical neuronal models (Collins et al., 1996a). Often SR phenomena in neuronal systems are revealed by driving these systems with signals that combine (a)periodic components and (temporally correlated) noise (Chialvo et al., 1997; Gai et al., 2010; Longtin, 1993). We adopt a similar approach in Chapters 3 and 5 where we employ periodic driving and a temporally correlated noise. We show how varying noise parameters other than intensity, leads to maximisation of certain properties of the driven neuronal system.

Counterintuitively and similarly to chaos, noise was found in some cases to increase synchrony and reliability in neuronal systems (Ermentrout et al., 2008). When intensity of noise is tuned, an excitable compound system affected by this noise may exhibit an enhancement in the coherence of neuronal oscillations. This phenomenon is called *coherence resonance* and was observed in theoretical neuronal models (Pikovsky and Kurths, 1997) and recently in cortical tissue of ferrets (Sancristóbal et al., 2016) *in vitro*. Robust control over coherence might play a fundamental role for communication between neuronal assemblies in the brain, performed in multiple coexisting frequency bands, as discussed in Section 1.4.1.

1.4.3 Metastability

In the absence of external stimuli (i.e. in the resting state), the dynamics of the brain do not converge to some kind of a well defined low-energy 'ground state of idleness', but instead explore a repertoire of states (Deco et al., 2013). Such exploration can be the result of a series of stochastic perturbations inducing transitions between states (Deco et al., 2009). We

study this scenario throughout this Thesis. Other scenarios may involve the aforementioned chaos, neuronal fatigue (Duch et al., 2013) or metastability (Shanahan, 2010), which refers to a state that is not, strictly speaking, stable, but that may still persist for an extended period of time.

Metastability has been recently shown to support efficient CTC transmission between remote brain areas (Deco and Kringelbach, 2016). It may take the form of *chimera states* (Shanahan, 2010), i.e. states in which both synchrony and asynchrony coexist (Abrams et al., 2008). This allows to benefit from both at a time. A similar effect is achieved when the system operates between the two phases (e.g. synchronous and asynchronous). Indeed, regardless of whether the abovementioned exploration of the repertoire of brain states is driven by noise and/or metastability, it is most easily realised when the dynamical system representing the brain operates close to a transition, often referred to as a 'critical point'. In what follows we elaborate on interpretation and meaning of 'criticality'.

1.4.4 Criticality and the verge of transition

The brain can be studied in spatial scales ranging from the *microscopic* scale, which concerns the activity of individual neurons, up to the *macroscopic* scale, where collective effects are observed. In statistical physics, the gap between phenomena at different spatial scales can be bridged in the *critical* state, where two phases separated by a *second-order phase transition* meet. In this state, an arbitrarily small perturbation can grow up to system's boundaries. It is due to the diverging susceptibility of the system, a behaviour characteristic of *critical phenomena*, which also involve self-similarities and power law scaling of temporal and spatial correlations. These effects concern not only classically understood thermodynamical systems; in their seminal paper Bak et al. (1987) illustrate critical effects on a model system of a pile of sand, where adding a single grain may cause a large avalanche, if the slope is steep enough. This system is driven towards the critical slope steepness by its own dynamics: a slope that is too steep tends to produce avalanches and thereby lowers its steepness, while a shallower one accumulates dropped sand and becomes steeper. In such cases we talk of *self-organised* criticality (Pruessner, 2012). Signatures of criticality have

been found in a broad class of systems ranging from artificial (e.g. traffic jams, financial markets) to environmental and biological systems (Bak, 1996; Marković and Gros, 2013; Valverde et al., 2015). It has been conjectured that the brain is one of such systems (Chialvo et al., 2008; Hesse and Gross, 2014; Plenz, 2013).

In the natural sciences, the term 'critical' is also used in the context of abrupt, discontinuous transitions, sometimes also termed 'catastrophic' (Scheffer et al., 2001). These transitions are found in a variety of systems, including ecological, social and biological (Scheffer, 2009). In the context of the brain, traits of catastrophic transitions are betrayed by onsets (Milanowski and Suffczyński, 2016) and offsets (Kramer et al., 2012) of epileptic seizures. Due to the dramatic consequences of critical transitions, their early detection is of high interest (Scheffer et al., 2009). One of the signatures allowing for such a detection is *critical slowing down*, which is also expected to occur at the critical state associated with the second-order phase transitions (due to diverging temporal correlations). In nonlinear dynamical models – such as the one used in this Thesis – transitions correspond to bifurcations. At a bifurcation where the force of the vector field changes from attractive to repulsive, the time of return to the steady state and the susceptibility to external perturbations are maximised. The model used in this Thesis operates close to a bifurcation, in particular close to a catastrophic transition in our studies of epilepsy (Chapters 3 and 4).

Criticality in the brain

The concept that the brain self-organises towards criticality can be based on the following reasoning. At criticality, high susceptibility would render the brain most responsive to external stimuli and would cause spatial and temporal correlations to diverge, which in turn would bolster long-range communication and memory (Chialvo et al., 2008). Furthermore, operating close to a phase transition would allow the brain to 'take the best out of all realms' separated by the transition and as a result could satisfy both the 'segregation' and the 'integration' demands (Chialvo et al., 2008). These realms separated by a transition may refer e.g. to order and chaos, synchrony and asynchrony, activity and quiescence. In general, the brain might be critical with respect to one such transition, but not critical

with respect to the other. Critical dynamics would lead to optimal processing, understood as maximised adaptability (Bak and Chialvo, 2001), widest accessible dynamic range, and highest information transmission and capacity (Shew and Plenz, 2013). This critical hypothesis, although very appealing, has yet not been unambiguously proven.

In physical systems criticality can be found when a slow variation of a control parameter is accompanied by a measurement of an order parameter. In practice, such approach is not feasible in the brain. This limitation was partially overcome by computational modelling, which in several studies has shown that experimental observations are best resembled by models operating close to criticality (Haimovici et al., 2013; Meisel et al., 2012; Millman et al., 2010; Tetzlaff et al., 2010), or in a slightly subcritical regime (Priesemann et al., 2014), which can be understood as a safety self-regulation and readiness for critical processing of stimuli. Bonachela et al. (2010) suggested that since neuronal dynamics are non-conservative, they do not, strictly speaking, operate on the critical point, but rather 'hover over' it (drifting back and forth during firing and neuronal recharging). Computational modelling studies have shown that experimental data is best replicated when the system operates slightly below a bifurcation, thus not necessarily criticality (Deco et al., 2013, 2015).

Experimental evidence considered supportive for the existence of the critical dynamics in the brain include divergence of spatial correlations found in fMRI recordings (Haimovici et al., 2013), power law scaling in synchronisation metrics of fMRI and magnetoencephalography (MEG) data (Kitzbichler et al., 2009), and power law scaling indicating self-similarity in amplitude fluctuations of alpha band EEG and MEG recordings (Linkenkaer-Hansen et al., 2001). Power laws have been found in scaling of neuronal avalanches observed *in vitro* in rat cortical neurons (Beggs and Plenz, 2003), and *in vivo* in monkey (Petermann et al., 2009) and human (Shriki et al., 2013) cortices. Other experiments (Dehghani et al., 2012) do not confirm power law scaling of neuronal avalanches, or show that the apparent power laws may result solely from stochastic processes, not self-organised criticality (Bonachela et al., 2010; Miller et al., 2009; Touboul and Destexhe, 2010). Furthermore, Benayoun et al. (2010) showed that

the power law scaling of avalanches may arise from properties of non-critical neuronal networks, which amplify small stochastic perturbations to large bursts. Finally, Botcharova et al. (2012) noted fallibility of the previously used signature of criticality, namely power law distribution of phase-locking. For these reasons, the matter of self-organised criticality in the brain is a subject of an ongoing debate (Beggs and Timme, 2012).

1.4.5 $1/f^b$ power spectra

In this Thesis, we study the dynamics of a neuronal model embedded in a realistic background characterised by a $1/f^b$-like power spectral density (PSD or 'power spectrum'). We motivate this research by the fact that a number of measurements related to neuronal activity exhibits a $1/f^b$ shape of the PSD. These measurements include (He, 2014): voltage of the neuronal subthreshold membrane potential (El Boustani et al., 2009), local field potential (LFP) (Milstein et al., 2009), electrocorticography (ECoG) (Freeman and Zhai, 2009; He et al., 2010; Miller et al., 2009), EEG and MEG (Dehghani et al., 2010), and fMRI (He, 2011). The $1/f^b$ PSD dependence has been also found in time series of fluctuations of alpha activity amplitude in EEG and MEG recordings (Linkenkaer-Hansen et al., 2001). In these cases the exponent b often takes values between 2 and 3 (Freeman et al., 2000; He et al., 2010; Miller et al., 2009; Milstein et al., 2009), but generally may vary between 0 and 4 (Freeman and Zhai, 2009), and it depends on the type of measurement, frequency range, brain region, task performed during recording, and finally on brain state and condition of the subject. The $1/f^b$ PSD dependence is a sign of an arrhythmic activity (He, 2014) that lacks a characteristic temporal scale and thus contrasts with brain oscillations (see Section 1.4.1) with narrowly defined frequencies. Both arrhythmic activity and oscillations are believed to be present in the brain (Miller et al., 2009), and therefore the resulting PSD often has a form of peaks embedded in the $1/f^b$ background.

The $1/f^b$ dependence on the frequency f of the PSD of temporal fluctuations indicates that these fluctuations are characterised by long-range correlations (also following power laws). In this Thesis we focus solely on temporal fluctuations, therefore in the remainder of the Introduction we refer to them, if not stated otherwise. Signals yielding the $1/f^b$ PSD

are often referred to as '$1/f$ noise', even though, as we show in this section, their origins may be purely deterministic. An interesting feature of these signals is a lack of any characteristic temporal scale, known as 'scale-freeness', which most often reflects self-similarity (fractality) of the signal. For this reason the $1/f^b$ PSD is usually presumed to be a signature of complexity of the underlying system. Since its first observation by Johnson (1925), $1/f^b$ PSD has been detected in a wide class of systems concerning electronics, physics, biology, psychology and economics (Handel and Chung, 1993; Ward and Greenwood, 2007). The ubiquity and versatility of the '$1/f$ noise', as well as its origins, are not fully understood and should be considered one of the yet unresolved scientific puzzles.

It is worth noting that the PSD is a measure independent of the phase of the frequency components of the signal. Therefore different signals, possibly generated by different mechanisms, may yield the same PSD. Indeed, various explanations for the $1/f^b$ PSD of the neuronal recordings have been put forward. For example, Freeman (2000) postulated that this shape of the PSD of the EEG and MEG time series might arise due to 'multiple chaotic attractors with repetitive state transitions'. Recently, it has been suggested that the power law scaling of the PSDs of these recordings might follow from the low-pass filtering property of dendrites that conduct synapse-generated currents (Lindén et al., 2010), and/or from the fact that the signal generated by membrane currents prior to reaching the electrode, undergoes broadband $1/f$ filtering in the extracellular medium (Bédard et al., 2006; Bédard and Destexhe, 2009). Other scenarios rely on phenomena introduced earlier in this chapter, namely: criticality, chaos, noise, hierarchy of brain rhythms, and coexistence of many scales in the system. In what follows, we explore in more detail these hypotheses, focusing specially on the stochastic scenario employed in Chapters 3 and 5 of this Thesis.

Stochastic generation of $1/f^b$ power spectra and Ornstein-Uhlenbeck noise

Various stochastic processes have been shown to yield $1/f^b$ PSD. For example Davidsen and Schuster (2002) employed a first-passage time model, resembling a simplified driven spiking neuron with a threshold following the Brownian motion. Spike trains generated by this model yield a

PSD following $1/f^b$ over several decades, with b close to 1. Furthermore, multiplicative stochasticity in point processes (Kaulakys et al., 2005) and nonlinear stochastic differential equations (SDEs) (Ruseckas and Kaulakys, 2010) were shown to be capable of generating a $1/f^b$ PSD. In this Thesis we utilise stochastic processes that can be generated in a simpler way, e.g. from standard Gaussian noise (filtered by linear SDEs).

In general, one can classify stochastic time series according to their 'colour', which refers to their spectral composition or, equivalently, to their temporal correlation. In analogy to light, a noise that mixes all frequencies ('wavelengths' in the light analogy) equally and therefore yields a flat power spectrum ($1/f^b$, with $b = 0$) is called a 'white noise'. In neuroscience it is sometimes argued (Roberts and Robinson, 2012) that the brain processes and their rhythmic analogues are so complex (Engel et al., 2001), that none of them can be distinguished and in fact white noise is a decent approximation of the brain background activity. Indeed, a number of studies (Garnier et al., 2015; Lopes da Silva et al., 1974; Pons et al., 2010; Touboul et al., 2011; Victor et al., 2011) employed white noise for this purpose, as we also do in Chapter 4. Such approach has the advantage of simplicity and it is an appropriate technique for some applications, e.g. finding transfer functions. Nevertheless, it is clear that the experimental PSD obtained from neuronal macroscopic recordings are not flat (Buzsáki and Draguhn, 2004).

For example, experimental observations based on ECoG data exhibited the $1/f^b$ spectrum with b close to 2 (Freeman et al., 2000; He et al., 2010). Therefore one could argue that the 'red' noise, with its PSD $\sim 1/f^2$, is a better spectral representation of a spatially integrated synaptic brain activity as detected in this kind of measurements. As the red noise describes displacement in the Brownian motion, its values may wander away from baseline, which makes this noise physiologically implausible in this context. In order to deal with this difficulty we follow Uhlenbeck and Ornstein (1930) and introduce leaky integration, which reverts the mean of this noise to zero. In such case, we talk of the Ornstein-Uhlenbeck (OU) noise. The rate of the mean reversion is given by a parameter τ that we can freely change, thereby varying the spectral composition of the noise. For $\tau \to 0$,

the PSD of the noise tends to the flat PSD of the white noise, whereas for large values of τ (and f bounded away from zero) it tends to the PSD of the red noise. These properties follow from Equation (2.16) introduced in Chapter 2. Although in order to tune the b parameter freely one needs a superposition of a number of such noise sources (see next section), using a single source already allows to systematically vary the PSD, e.g. in order to study the consequences of using the white noise approximation. We adopt this approach in Chapters 3 and 5.

The Ornstein-Uhlenbeck noise can be considered a convenient approximation of the $1/f^b$ noise. For example, networks of spiking neurons have been shown to generate realistic $1/f^b$-like spectra when driven by OU noise (Sancristóbal et al., 2013). In Chapter 5 we show that the same effect occurs for networks of coupled neural masses. OU noise is often used in theoretical neuroscience, for example it has been associated with the integration of background synaptic activity acting upon a neuron (Destexhe and Rudolph, 2004). Recent studies of OU processes driving neural models have investigated the effects of coloured noise on temporal distributions of neuronal spiking (Braun et al., 2015; Silva and Vilela, 2015) and the generation of multimodal patterns of alpha activity (Freyer et al., 2011) Nevertheless, differences in neuronal dynamics driven by the OU and $1/f^b$ noises have been identified (Sobie et al., 2011).

Finally, let us point out that the $1/f^b$ PSD of neuronal recordings are unlikely to be caused exclusively by purely stochastic processes. If this was the case, then no structure in phase distribution of the Fourier components of the signal would be discernible. Such structure and cross-frequency dependencies involving phases has been observed He et al. (2010). These observations suggest that rhythms embedding can underlie another potential mechanism of the $1/f^b$ PSD generation. We introduce this mechanism in the following section and discuss cross-frequency effects thoroughly in Chapter 5.

Multiscale and rhythm embedding as origins of the $1/f^b$ power spectra

$1/f^b$ PSD can arise from a coexistence of many processes operating in different timescales in one system. For example, Hausdorff and Peng (1996) showed that $1/f^b$ PSDs can arise with a spectrum intermediate between the

limits of the white and red noises from a superposition of PSDs of a number of (stochastically driven) exponential relaxations with properly chosen amplitude and time constants (that determine the value of b). In the context of neuroscience this scenario has been examined by Miller et al. (2009), who suggested that the $1/f^b$ PSD follows from the separation of time constants of leak and synaptic currents. This multiscale explanation also finds support in computational modelling. Hutt and Frank (2005) showed that $1/f^b$ PSD can arise in a spatially extended neuronal model operating close to a bifurcation, due to a coexistence of many temporal modes, which in turn follow from delays and many spatial scales imposed by the coupling kernel.

The multiscale scenario can be considered not only in the context of decay processes, but also in the context of oscillations. This is so because slow rhythms of the brain yield more power than fast ones, since they arise from larger neuronal structures and therefore reflect the synchronous oscillations of a large number of sources (Buzsáki and Draguhn, 2004). In contrast, faster rhythms (e.g. gamma) arise due to more local circuitry (Bartos et al., 2007) and therefore have less power. This observation can be interpreted also in the context of the communication through coherence functionality (see Sections 1.4.1 and 1.4.6), which requires that slower (modulating) rhythms arise on wider brain areas, encompassing all neuronal populations engaged in communication conducted in higher (modulated) frequency ranges. These populations, although modulated by a common source, do not have to be synchronised, therefore they generate less power than the slower, modulating rhythms.

Furthermore, modulation itself reduces the power of faster modulated rhythms. Consideration of a simplified case when the slower (modulating) harmonic rhythm envelops the amplitude of the faster (modulated) one, shows that in stationary conditions, the total power of the faster rhythm is two times smaller than the total power of the slower one. A cascade of such rhythm embedding would entail a decay of the PSD with increasing frequency. As pointed out by He (2014) this scenario is unlikely to be the only reason for the $1/f^b$ shape of the PSDs generated by the brain. That

is because the narrow-band peaks appear and disappear on the $1/f^b$ background which lasts regardless to rhythmic oscillations.

Criticality as source of $1/f^b$ power spectra

Appearance of the $1/f^b$ PSD might be a signature of (self-organised) criticality. As mentioned in Section 1.4.4 critical states are characterised by diverging correlations (both spatial and temporal), which may extend to system's boundaries. To develop intuition about the meaning of the power spectrum at criticality, we note that due to the Wiener-Khinchin theorem, a constant correlation function results in a $1/f^b$ power spectrum, with $b = 1$ (Pruessner, 2012). Heavy-tailed correlation functions decaying according to power laws result in different values of b. Furthermore, high power in low frequencies can be linked to critical slowing down (see Section 1.4.4).

The original theory linking $1/f^b$ PSD with self-organised criticality (Bak et al., 1987) relies on dissipation of energy from low-frequency perturbations towards higher frequencies, realised in the spatially extended critical system. In fact, this theory, similarly to the 'multiscale scenario' discussed in the previous paragraph, involves a summation of spectra of processes spanning a wide range of temporal and spatial scales. It is the reason of appearance of this wide range of scales that should be attributed to self-organised criticality which in this case reflects the fact that a small perturbation may cause a large event.

Nevertheless, it is important to be aware of two things in this context. Firstly, distributions of sizes and durations of events (such as neuronal avalanches in the brain) are not the same as correlations of signals (such as the EEG/MEG recordings), although both may follow power laws yielding $1/f^b$ PSDs. Secondly, even though every self-organised critical system is expected to exhibit the $1/f^b$ PSD, the observation of this PSD alone is not sufficient to confirm self-organised criticality. One of the reasons for that, as discussed in this section, is that the $1/f^b$ PSD may arise from a multitude of phenomena other than self-organised criticality. Another reason is that spatially extended self-critical systems are expected to show fluctuations described by power laws in both time and space, whereas cases of systems showing temporal $1/f^b$ PSD but lacking power laws in spatial fluctuations are known (Davidsen and Schuster, 2000).

1.4.6 Brain networks

Recent years brought a rapid advancement of network science (Barabási, 2002), which formulated universal laws applicable also to brain networks. Moreover, progress in mesoscopic-scale non-invasive magnetic resonance imaging (MRI) techniques, such as diffusion tensor imaging and diffusion spectrum imaging (Daducci et al., 2014), allowed to infer large-scale *structural* brain networks, from the connectivity of white matter tracts. The complete map of structural connectivity of the nervous system, in analogy to the *genome*, is termed the *connectome* (Hagmann, 2005; Sporns et al., 2005). Measurements allowing to capture mesoscopic neuronal activity, e.g. fMRI and EEG, provide data from which *functional* and *effective* brain networks can be derived. This leads to the notion of functional connectome, which can be linked to the structural one by means of mesoscopic-scale modelling techniques, such as those employed in this Thesis. In what follows, we discuss these three types of brain networks and the link between them, provided by computational models.

Structural networks

Most studies of structural brain networks are focused on the connectivity of the cerebral cortex. The reason for this is that the cortex, compared to other brain structures, has exceptionally developed wiring (see Section 1.1.2). According to the 'integrated information theory' (Tononi and Koch, 2015), complexity of this wiring gives rise to consciousness. In general, the organisation of the cortical connectivity is considered to balance realisation of functional demands with wiring cost (Bullmore and Sporns, 2012). One of the primary demands is the aforementioned functional 'segregation-integration' (Tononi et al., 1994), which is crucial for effective brain functioning. Realisation of specific tasks requires local specialisation of neuronal tissue, which indeed is typical of the cerebral cortex (see Section 1.1). In order to quickly process these tasks, the tissue constituting a certain specialised domain needs to be internally strongly connected. On the other hand, realisation of complex tasks (e.g. driving a car), which involve different domains, requires communication across these domains and mediation of a congruent solution. This is achieved by a global

integration of locally processed specific sub-tasks (seeing the road, reading road signs, changing gears).

Fulfilment of the segregation-integration functionality combined with optimisation of the wiring cost leads to a specific network topology, resembling the small-world topology (Watts and Strogatz, 1998) that combines high local clustering with short global average path length. The small-worldness of neuronal structures has been observed in various spatial scales (Sporns and Zwi, 2004). Other, more recent studies suggest that the connectivity of the human cortex might follow rather a so-called 'large-world' topology (Hilgetag and Goulas, 2015), characterised by a hierarchical-modular structure. This large-scale connectome architecture, besides high clustering and low average path length (present in small-world networks) shows robustness via connections redundancy, existence of hubs (due to a certain degree of scale-freeness in topology, Heuvel and Sporns, 2013; Stam, 2014) and preferential connectivity between these hubs, so called 'rich clubs' (Heuvel and Sporns, 2011, 2013). Characteristics of the large-scale structural brain networks, attributed to scale-freeness and small-worldness, maximise entropy and multistability (Deco et al., 2012; Golos et al., 2015). Also the hierarchical-modular structure is believed to maximise dynamical complexity (Zamora-López et al., 2016), as well as it additionally bolstering fulfilment of the functional 'segregation-integration' demand (Sporns, 2013), supports occurrence of metastability (Shanahan, 2010), criticality (Kaiser, 2010; Wang and Zhou, 2012), Griffith phases (Muñoz et al., 2010), and chimera states (Shanahan, 2010; Villegas et al., 2014). Moreover, most of the above listed topological traits are also found in *functional networks* (Eguíluz et al., 2005), which we discuss in the next section.

Functional and effective networks

The distinction between structural and functional connections was mentioned already by Freeman (1975). Functional networks are derived from temporal synchronisation of neural activity in different brain areas. Stronger synchronisation between the two areas reflects a stronger link in the network, which, to some extent, reflects the structural connectivity. Nevertheless, the structural connectome is relatively invariant, whereas

the functional connectivity evolves in time through a variety of configurations, which presumably reflect different brain states (Park and Friston, 2013). This evolution is possible due to dynamical mechanisms modulating strength of functional connections (Bastos et al., 2015; Grothe et al., 2012). These mechanisms are not part of the structural connectivity, which, therefore, should not be considered the most important brain network. Since functional networks reflect coherence, their ongoing evolution due to the exploration of the dynamical repertoire can be understood as probing (and possibly maintaining) various possible CTC communication channels that can be used when the system (e.g. due to an external stimulus) converges to one of the attractors (Deco and Kringelbach, 2016).

Unlike structural networks, the functional networks are undirected by definition. Recent efforts aim at tracking the directionality of functional connections by analysing responses of the network to external stimulation (David, 2014). Traditionally, networks carrying information about direct influences between neuronal assemblies - *causality* of the system - are termed *effective* networks (Friston, 1994). They can be determined e.g. by means of Granger causality or Dynamic Causal Modelling (DCM) (Friston et al., 2003), which, to this end, uses mesoscopic-scale neuronal modelling and Bayesian inference.

Mesoscopic-scale modelling is used not only in DCM, but also in linking structure with function (Pons et al., 2010). This approach has shown that functional and structural large-scale networks match best when the dynamics of the neuronal model operate close to a bifurcation (Hlinka and Coombes, 2012). Slightly below the bifurcation the match between the simulated and the experimentally measured functional connectivities is also maximised (Deco et al., 2013). Under such conditions one can also infer structural connectivity from the functional one (Deco et al., 2014) or gain insight in brain dynamics by comparing response of the model to external perturbation with deep brain stimulation protocol data (Deco et al., 2015). The work presented in this Thesis focuses mostly on dynamics evinced in individual nodes of such modelled networks, as well as on interactions between pairs of nodes. In particular, in Chapter 4 we explore different

scenarios to satisfy the 'closeness-to-phase transition' demand, showing that they lead to dramatically different collective dynamics.

1.4.7 Dynamical traits of neuronal diseases

In the previous sections of Introduction we have introduced the dynamical traits of a healthy functioning brain. Deviations from these traits may be caused or may underlie, neurological disorders. In this section we briefly outline some exemplary diseases and their corresponding dynamical symptoms with reference to brain characteristics introduced in the preceding part of this Introduction. These dynamical aberrations detected in the brain functioning might serve as biomarkers facilitating diagnostic procedures. Moreover, understanding their governing mechanisms allows to simulate them *in silico*, allowing for drugs and treatments testing. Such theoretical and computational approach can be integrated with the experimental one (Coombes and Terry, 2012).

We have, for example, mentioned that in the properly functioning brain, balance between synchrony and asynchrony is finely tuned. It occurs that deviation from this state may be harmful for brain functioning; an excess of synchrony is linked to Parkinson's disease and epilepsy, while its deficit is related to disorders such as autism and schizophrenia (Uhlhaas and Singer, 2006). Increased nonlinearity has been suggested to characterise epilepsy (Breakspear et al., 2006). Also oscillatory patterns of the brain may be distorted by neurological diseases, which may affect existing rhythms and the associated brain functions. Such is the case for schizophrenia (Uhlhaas and Singer, 2013), and Alzheimer's and Parkinson's diseases, where aberrations of rhythmicity are presumably underlied by lesions of brain structure (Pons et al., 2010; Uhlhaas and Singer, 2006). Moreover, some diseases are characterised by the occurrence of aberrant rhythms, such as tremors in Parkinson's (Jankovic, 2008) and multiple sclerosis (Koch et al., 2007), and seizures in epilepsy (Kramer et al., 2012).

Likewise, arrhythmic processes may be impaired: deviations from the $1/f^b$ power spectrum of various measures related to brain functioning and human behaviour have been linked to malfunctions of motor control (Diniz et al., 2011). Also imbalance between excitation and inhibition has been associated with clinical symptoms, e.g. in animal models with autism (Lee

et al., 2016). This disease has also been linked to excessive neuronal accommodation, the lack of which may results in attention deficit hyperactivity disorder (Duch et al., 2013). Another example of dynamical aberration concerns multistability. Victor et al. (2011) observed that EEG recordings from patients who suffered brain injuries exhibit less alternations of patterns.

The abovementioned structural lesions may cause alterations to topological traits of brain networks such as small-world and scale-free patterns, hierarchical modularity, hubs and rich clubs in Alzheimers disease, multiple sclerosis, traumatic brain injury and epilepsy (Stam, 2014). Such alternations have been also found in schizophrenia, in both structural (Thanarajah et al., 2016) and functional networks (experimentally derived and computationally modelled, Cabral et al., 2013). Lesions of the brain structure might shift its dynamics away from the optimal point; theoretical and computational dynamical studies may help to diagnose such state and facilitate recovery (Deco et al., 2014). Deviations of brain dynamics from the critical point into the supercritical regime were assumed to underlie various malfunctions, e.g. a restricted repertoire of movements and hyper-reactive reactions to sensory stimulation in autistic patients (Shew and Plenz, 2013). Loss of self-organised criticality was found also during epileptic seizures by Meisel et al. (2012). A shift from an optimal regime, in which segregation-integration functionality is maximised, was observed in Parkinson's disease (Deco et al., 2015). In that case, modelling of deep brain stimulation revealed that this intervention shifts the dynamics towards the optimal regime.

In general, the design of therapeutic stimulation protocols can be significantly supported by dynamical modelling. Knowledge of the brain dynamics allows to theoretically and computationally study their response to external perturbations. Such study may, for example, reveal the optimal relative phase between signal and stimulation that leads to a desired effect, e.g. mitigation of illness symptoms. Mechanistic models of brain stimulation protocols are applicable in migraine, Parkinson's disease and epilepsy (Wang et al., 2015). This stimulative treatment and computational modelling is especially promising in the case of epilepsy (Soltesz and Staley,

2011). This disease motivates part of the research presented in this Thesis, therefore we introduce it in more detail in the following section.

1.5 EPILEPSY

Epilepsy is a chronic neurological disorder characterised by the recurrence of *seizures* - unpredictable disruptions of healthy brain functioning. These aberrant states are characterised by 'abnormal, excessive or synchronous neuronal activity in the brain' (Fisher et al., 2005) that can be bounded to a certain brain region (*focal seizure*) or can extend to the whole brain (*generalised seizure*). Transient impairments caused by seizures affect such brain functions as emotions, memory, sensory and motor control, cognition, and behaviour (Fisher et al., 2005), thereby heavily impeding quality of life. *Absence* and *tonic-clonic* seizures result in loss of consciousness which in the latter case is accompanied by alternating contractions and relaxations of skeletal muscles. Epilepsy affects $\sim$50 million people worldwide, out of which about 30% is resistant to pharmacological treatment (http://www.who.int/mediacentre/factsheets/fs999/en/).

The main method allowing to detect, track and monitor epileptic activity *in vivo* is via EEG that measures potentials of synaptic origins (see Section 1.2). Due to its low cost and non-invasiveness, extracranial EEG is the method of first choice, but due to its poor spatial resolution, localising epileptic foci is usually done with intracranial EEG, performed with electrode arrays implanted into the brain. On the other hand, high temporal resolution of EEG signals allows for discrimination and analysis of temporal epileptic patterns. In general, there is a variety of such characteristic epileptic patterns (Kramer and Cash, 2012), nevertheless in this Thesis we focus on a spiky one that captures some characteristics of 'spike-and-wave' (SW) discharges (Destexhe, 2007). Figure 1.4 shows a snippet of the EEG time course comprising high amplitude $\sim$3 Hz SWs. The abruptness of their occurrence and cessation brings epilepsy close to the theory of critical transitions (see Section 1.4.4). It is, however, not the only observation related to epilepsy that makes this disorder specially relevant for dynamical and computational modelling.

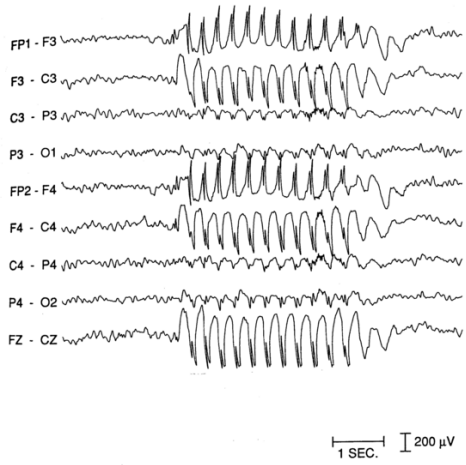

Figure 1.4: An exemplary multimodal EEG recording from an absence seizure (Suffczyński, 2000). Abbreviations on the left are standard symbols of EEG electrodes.

This modelling may aid alternative treatment for therapy-resistant patients. For example, *Vagus Nerve Stimulating* implants (Yuan and Silberstein, 2016) stimulate the brain in a presumably desynchronising manner that diminishes the risk of epilepsy recurrence. Tests are being also conducted for transcranial and deep brain stimulation (Stamoulis and Chang, 2012). In either case, the exact form of the stimulating signal might be crucial for the outcome (Fisher and Velasco, 2014). Optimising the applied pulse, e.g. in real time in a closed-loop setup (Berenyi et al., 2012), can be immensely supported by computational modelling (Milton et al., 2004; Taylor et al., 2014). The closed-loop solution can also be empowered by a model-inversion approach and the Kalman filter, which was shown to be effective in providing insight in epileptic dynamics from experimental observations (Freestone et al., 2014).

Computational approaches also led to a shift in our understanding of epilepsy, which is currently being thought of as a network-level disease, rather than merely a local pathology (Khambhati et al., 2014; Khambhati et al., 2016; Richardson, 2012; Terry et al., 2012; Van Diessen et al., 2013). Such approach can help to localise and eliminate large-scale brain network nodes crucial for the generation and spreading of seizures. In that direction, modelling has been shown to be a potentially effective aid for surgical

resections (Goodfellow et al., 2016; Hutchings et al., 2015). In Chapter 3 we focus on particular dynamical factors facilitating initiation and spreading of epilepsy, whereas in Chapter 4 we study potential mechanisms of seizure terminations.

Considering epilepsy a dynamical disorder (Milton and Jung, 2002; Milton, 2010) has led to development of a number of computational models reproducing various epileptic waveforms (Wendling et al., 2015). In particular, many characteristics of transitions between healthy and epileptic activity was explained on the ground of bifurcation theory (Breakspear et al., 2006; Kramer et al., 2012; Milanowski and Suffczyński, 2016; Touboul et al., 2011). Recent efforts are also being directed towards patient-specific connectome modelling (Jirsa et al., 2016). Finally, computational methods have been engaged in development of seizure prediction methods (Mormann et al., 2007) that since recently compete in an annual contest (Brinkmann et al., 2016).

1.6 AIM AND ORGANISATION OF THE THESIS

In this Thesis we focus on modelling temporal dynamics of mesoscopic brain processes, and on relating them to experimental data. In particular, we are interested in processes underlying the generation of specific temporal patterns in signals registered in EEG and fMRI recordings. In the case of EEG these patterns are epileptiform dynamics and inter-rhythmic interactions, and in the case of fMRI they concern the behaviour of the signal in the resting state (when brain stimulation is absent) and in the poststimulus period (when stimulation is present). We link the generation of EEG patterns to stochastic and harmonic driving of a mesoscopic-scale neuronal model. In particular, we concentrate on the effects arising from the finite temporal correlation of the driving stochastic process, which we model as an Ornstein-Uhlenbeck noise. In contrast with the commonly used white noise, this type of driving reproduces the $1/f^b$ spectral properties of the brain. We therefore predicate that this assumption also approximates better the background activity of the brain acting upon a modelled patch of tissue (e.g. a cortical column). This modelling is done by means of a mesoscopic neural mass model.

We therefore study a neuronal population as a dynamical system subject to temporally correlated noise and harmonic driving. We are interested in the effects that arise from the interplay between the characteristic timescales of the driving (temporal correlation of the noise, frequency of the harmonic signal) and the bifurcation structure of the model. We show that these effects recapitulate phenomena known from experimental EEG recordings, in particular initiation and termination of epileptic seizures, visually evoked epilepsy and increase of EEG power in a fast frequency band, occurring as a result of slow driving (cross-frequency transfer). Special attention is paid to effects arising due to coupling between neuronal populations: we introduce the concept of collective excitability and a mathematical method for finding the critical coupling strength at which a network of coupled dynamical elements (here neuronal models) loses stability. We also show how the coupling strength modulates behaviour of a system operating close to a transition (in our case a 'catastrophic' one).

This Thesis is organised in the following way. In Chapter 2 we introduce the history and mathematical formulation of neural mass models, focusing on an extended version of one such model (used later in this Thesis). Chapter 3 is devoted to the dynamics of a single module of the model. Therefore, connectivity is not considered; emphasis is put instead on driving this model with harmonic signals and Ornstein-Uhlenbeck noise. In Chapter 4 we extend the model to two coupled modules and study their interactions. In that case we simplify the driving stochastic process by modelling it with white noise, which allows us to extract collective phenomena without additionally considering their dependence on the noise correlation time. Having studied the dynamics of a single module and intermodular interactions, we move on to networks (of progressively increasing size) driven with harmonic signals and Ornstein-Uhlenbeck noise. This is done in Chapter 5, where we also extend our methods to spectral analysis.

This organisation of the Thesis is motivated by 'making things as simple as possible, but no simpler'[5]. We extend the complexity of the system

[5]The authorship of this maxim is traditionally assigned to Albert Einstein.

gradually, deepening chapter-by-chapter our comprehension of its dynamics. This apparently parsimonious approach is sufficient to propose explanations for a number of phenomena known to occur in the brain. One such phenomenon, discussed in Chapter 6, is not related to EEG recordings, but to fMRI. For this reason, in that chapter a model of the fMRI signal generation is introduced, studied and tested on experimentally collected data. Coupling this model with a neuronal model, such as the one used in the first chapters of this Thesis, should allow to relate computational simulations not only to EEG, but also to fMRI experimental data. In summary, the aim of this Thesis is to link particular experimental observations of brain activity to dynamical properties of models concerned with brain processes occurring in the mesoscopic scale.

CHAPTER 2

MODELLING MESOSCOPIC BRAIN DYNAMICS

Computational neuronal models may be used for various purposes. A neural network, for example, may serve for solving classification problems. Neural networks are loosely motivated by neuronal anatomy, but most often lack in biological fidelity. Other descriptions aim at researching some level of biological realism rather than computational capacities, with the goal of increasing our understanding how the brain works. Such is the case of neural mass models used in our work. It allows to compare results of computational simulations with experimental measurements, such as those obtained with EEG, MEG and fMRI. An agreement consistency between simulation and experiment allows to validate the model, to gain insight in biological processes and to make predictions. We do all of these in this Thesis.

Biologically inspired neuronal modelling may concern structures of various spatial scales, from the dendritic arbour to the whole cortex. The *population modelling* introduced in Section 1.3 focuses on describing collective activity of groups of neurons. These neurons share some specific features, e.g. a 'population of inhibitory neurons' gathers only inhibitory neurons and abstracts from their real phenotypes. The size of such population depends on the granularity of the model, but it is constrained by a sufficient degree of internal coherence. As mentioned in Section 1.1.3, experimental studies revealed groups of cortical neurons of highly correlated activity, so called *cortical columns*. These columns are therefore natural objects of modelling. The models that describe their activity can be done by interconnecting several neuronal populations contained within the purported column. This choice of granularity provides a correspondence to spatial scales typical of non-invasive neuroimaging techniques such as EEG, MEG and fMRI. Nevertheless, populations are not limited to the representation of cortical columns, e.g. increased synchrony caused by

an epileptic seizure may allow to approximate pyramidal neurons in a cortical area (in case of a focal seizure) or even in the whole brain (in case of the generalised seizure) with a single population (Breakspear et al., 2006).

There is a number of ways in which one can derive a mathematical description of the activity of a neuronal population. One can, for example, apply formally the *mean-field* approach to an ensemble of spiking neurons to obtain the Fokker-Planck equation describing their dynamics (Deco et al., 2008). A specific dynamical representation of the average state of the population (corresponding to the mean of the distribution) is the *neural mass model* (NMM). If this average state is space-dependent, we talk of a *neural field*. We do not elaborate on the latter approach, since in this Thesis we focus solely on temporal effects. Spatially extended systems can also be modelled by means of neural masses interconnected accordingly to anatomical networks (see Section 1.4.6). In what follows, we outline the evolution of the NMMs, focusing on the progress that led to the introduction of the Jansen-Rit model, extensively used in this Thesis. We also outline extensions to this model and recent progress in neural mass modelling.

2.1 HISTORICAL OVERVIEW OF NEURAL MASS MODELS

2.1.1 Foundations of neural mass models

The introduction of the concept of *neural masses* is often attributed to Freeman (1972a,b) and Lopes da Silva et al. (1974). Nevertheless, earlier works of Beurle (1956) and Griffith (1963, 1965) who considered spatially extended 'masses of cells having properties similar to the known properties of neurons' with exponentially decaying excitatory connections (Liley et al., 2012). Although these works can be considered cornerstones of *neural fields* (see above), they also paved the way to the formulation of models not including spatial dimension. Such was the model introduced by Wilson and Cowan (1972), which describes the dynamics of the proportion of neurons in the population firing per unit of time, thereby strengthening the notion of the *firing rate*.

Wilson-Cowan model

The Wilson-Cowan model comprises two inter- and self-connected neuronal point populations with refractory periods. One population comprises excitatory neurons and the other inhibitory ones. Inhibitory action was already considered by Freeman (1967), who linked it to damped and self-sustained oscillatory behaviour. The Wilson-Cowan model assumes that upon receiving an input a certain fraction of neurons in the population fires. This fraction is dependent on the strength of the excitation and on the distribution of firing thresholds in the population (described by a rate response function). Alternatively, one could assume that the threshold is the same for all neurons in the population, but the distribution of synapses (mediating the incoming signal) is not uniform. In either interpretation, for a unimodal bell-shaped distribution, the response function takes the shape of a sigmoid, bounded, in the case of the Wilson-Cowan model, to values between 0 and 1.

This model can be considered as a *rate model*, since it is only concerned with firing rates, i.e. it does not contain variables referring directly to electrophysiology. Nevertheless, the momentary level of excitation resulting from an external input is obtained here from a convolution of this input with an impulse response kernel function. This linear-time-invariant (LTI) approach would be no different from the way in which post synaptic potentials are computed in later developed models (*voltage models*), but Wilson and Cowan introduced an additional time coarse graining in order to simplify this convolution. They were also the first to employ the *phase plane analysis* to studies of mesoscopic neuronal dynamics, an approach that had been used earlier by FitzHugh (1961) for spiking neurons. This allowed Wilson and Cowan to identify limit cycles in their model. Significant parts of their work, e.g. inhibitory coupling, interpopulation connectivity, linear time-invariance, and the sigmoidal rate response function are present in neural mass models, although Wilson and Cowan did not call their model a 'neural mass'.

Approach of W.J. Freeman

The term 'neural mass' was arguably used first in the same year by Freeman (1972a,b) with a reference to 'tens or hundreds of millions of neurons'. Freeman advocated for studying these groups of neurons, which he saw relevant to electrophysiological measurements. In his book (Freeman, 1975) he introduces a comprehensive approach to neural mass modelling. The main strength of his approach is a combination of an abundance of experimental measurements with a tailored theory based on signal analysis. To prevent giving up biological fidelity for mathematical tractability, Freeman assumed that nonlinearities can be treated by a series of piece-wise linearisations. That allowed him to rely on the LTI systems theory and use its analytical techniques. Within this framework, Freeman modelled complex cortical structures (exceeding the simple topology of the Wilson-Cowan model) and fitted results to experiments dealing for instance with impulse responses of populations.

Interestingly, in Freeman's approach the connectivity within neural masses is based not on anatomical connections, but on functional ones, identified between neuronal 'sets'. These sets are hierarchically organised. For instance zero-level set describes a group of non-interacting neurons having same input and the same sign of output, and a first-level set comprises two zero-level sets, coupled either in an excitatory or inhibitory manner. The second-level set containing all four possible combinations of interactions is topologically equivalent to the Wilson-Cowan model. In general, in Freeman's approach, the dynamics of neural masses are governed by two conversions. The first one is an asymmetric sigmoidal 'wave-to-pulse' conversion, yielding the firing rate of a population resulting from certain postsynaptic potentials, and an inverse 'pulse-to-wave' conversion. As a result, the dynamics of the second-level set is described by four third-order linear differential equations. The order of equations caused that, unlike in earlier models, the maximal post synaptic potential (PSP) at the soma occurs with a realistic delay with respect to the arrival of the pulse at the synapse. As a result, Freeman was able to reproduce with great fidelity electrophysiological signals generated from the mammalian olfactory bulb

and prepyriform cortex. In the former case, the result led to conclusions about the role of chaos in the brain (reviewed in Section 1.4.2).

Approach of F.H.L. da Silva

A similar approach, also with realistic PSPs, was introduced by Lopes da Silva et al. (1974), who constructed a model of the EEG alpha rhythm, arising in the thalamus due to inhibitory feedback between thalamo-cortical relay neurons and inhibitory interneurons. Note that due to the universality of inhibitory feedback loops, the same network can also be used to model cortical activity. The model was computationally integrated on a lattice, and treated analytically in the reduced form of a simple circuit. In the former case, individual neurons were considered; in the latter, a sigmoidal rate function was adopted, following Wilson and Cowan (1972), to account for mass generation of spikes.

Similarly to Wilson and Cowan, and to Freeman, da Silva et al. linearised the simplified (lumped) version of the model, what allowed them to obtain an analytical expression for the transfer function - response to driving with white noise. This stochastic driving and a resulting stationary response were novel in comparison to earlier purely deterministic models, where decaying output activity would appear as a response to transient stimulation. In the later development of this model the PSPs were suggested to be described by *alpha* functions, instead of previously used sums of exponentials (Rotterdam et al., 1982). The inclusion of a population of excitatory interneurons was suggested by Lopes da Silva et al. (1976) and studied by Zetterberg et al. (1978), who noted the universality of this circuit and suggested its relevance to local cortical populations with pyramidal neurons. Twenty years later this model was slightly modified and popularised by Ben H. Jansen and colleagues.

2.1.2 Jansen-Rit model

The Jansen-Rit model was introduced to study visually evoked potentials (Jansen and Rit, 1995; Jansen et al., 1993). It comprises elements introduced in the aforementioned studies, i.e. a response function described with a slightly modified sigmoid, realistic PSPs described by alpha functions and

treated within the LTI framework, and a lumped circuit describing the interconnection of three types of neuronal populations. We provide a detailed description of the model and its mathematical formulation in Section 2.3. It is basically a slightly modified version of the models of da Silva and Zatterberg, additionally expressed in a differential form. The main contribution of Jansen and Rit was the introduction of intra-population connection strengths adequate to cortical anatomy known from other studies. Therefore, their description refers specifically to a cortical column, not to the thalamus, as it was originally proposed by Lopes da Silva et al. (1974).

Today's popularity of this model stems probably from its simplicity, combined with rich dynamics that include excitability, Hopf bifurcations, and bistability between two limit cycles (as shown extensively in this Thesis). One of these limit cycles, similarly to da Silva's model case, resembles healthy alpha oscillations, and the other one resembles unhealthy epileptic-like activity. The rich dynamics of this model were revealed in several studies. For example, Malagarriga et al. (2015b) used a network of interconnected and periodically driven Jansen-Rit modules in order to study how this network performs computational operations on various dynamical inputs. Chaos has been found in a system of two coupled Jansen-Rit modules (Huang et al., 2011) and in a single, periodically driven module (Spiegler et al., 2011), which may also display periodicity and quasi-periodicity (Malagarriga et al., 2015a).

2.1.3 Recent development and extensions

As mentioned in Section 1.3, NMMs are commonly used to model phenomena that affect the brain's EEG, such as the abovementioned visual stimuli and epilepsy. Other phenomena of this kind involve the effects of drugs and sleep.

Neural mass models in studies of epilepsy and other diseases

Neural mass models have been used to study various aspects of epilepsy, such as focal and generalised seizures, interictal activity, transition from healthy rhythms to seizures and spreading of the latter, epileptic networks, and various epileptiform temporal patterns (Wendling et al., 2015). In

some cases, the studies were performed on universal models. Such is the case of the thalamo-cortical model of Robinson et al. (2002), which is built on the familiar NMM principles: a sigmoidal rate response function and realistic PSPs modelled by exponentials. Bifurcation analysis revealed that depending on the parameter values, this model is capable of displaying several healthy and epileptic rhythms (Breakspear et al., 2006). This observation allowed to use this model to show that some symptoms related to tonic-clonic and absence seizures follow from properties of the corresponding bifurcations (Breakspear et al., 2006). Extending this model with basal ganglia allowed Albada and Robinson (2009) to study Parkinsonian states.

Another class of studies builds on the known NMMs in order to reproduce epileptic phenomena. For example, the model of Wendling et al. (2002) extends the Jansen-Rit model by one additional population of inhibitory interneurons characterised by slow dynamics. The same extension with different values of parameters was also introduced by Goodfellow et al. (2011). The model of Suffczyński et al. (2004) extends the model of da Silva; it comprises two modules representing cortex and thalamus, it concerns two timescales of inhibition, and it additionally considers calcium currents. This model was able to show spontaneous occurrence of epileptic spikes, as well as suggest a stimulation protocol leading to the disruption of seizures. The simple inclusion of timescales, different than originally proposed for the alpha rhythm generation, was also applied by Molaee-Ardekani et al. (2010), who in a Jansen-Rit-like model considered shorter timescales and reproduced fast oscillations of seizure onsets. Considering slow and fast scales in a cortical module of the Jansen-Rit, and introducing a thalamic module allowed Bhattacharya et al. (2011) to study alpha rhythms in Alzheimer's disease.

Spectral properties, evoked potentials and interactions between modules

A NMM based on da Silva's approach was used to study potential causes of event-related synchronisation (ERS) and desynchronisation (ERD) in

the alpha (Suffczyński et al., 2001), and beta and gamma bands (Grabska-Barwińska and Żygierewicz, 2006). David and Friston (2003) used two coupled generalised Jansen-Rit modules (enriched with populations of various kinetics) to study how changes in the model parameters (in particular delays and coupling strengths between the modules) affect its temporal and spectral properties. The authors found that these models upon parameter values change are capable of generating rhythms in a broad frequency range. In subsequent studies, David et al. (2004) focused on the functional connectivity (see Section 1.4.6) generated by this model and its event-related responses (David et al., 2005, 2006). Chakravarthy et al. (2009) used this model to study feedback control strategies for the suppression of seizures in the epileptic brain. Wang and Knösche (2013) implemented the Jansen-Rit description to model the laminar structure of the cortex. They also enriched the model with plasticity in order to study habituation effects as measured in the MEG recordings during auditory stimulation.

Networks of neural masses

Recently, studies of the interactions between a small number of coupled neural masses were extended to whole networks. For example, a regular lattice of interconnected Jansen-Rit modules additionally furnished with slow inhibition was utilised by Goodfellow et al. (2011) to study spatial spreading of epileptic activity. As mentioned in Section 1.5, recent studies consider epileptic neural masses arranged in realistic brain networks (Goodfellow et al., 2016; Hutchings et al., 2015). Similarly, a number of studies of large-scale brain networks (see Section 1.4.6) rely on neural masses. Babajani and Soltanian-Zadeh (2006) suggested to consider a neural mass as a model not of the whole cortical area, but as a model of a minicolumn (see Section 1.1.3). Coupling many such columns led to a model of a cortical voxel generating the fMRI signal. We devote Chapter 6 to a model of this signal generation, and we discuss driving it with fast rhythms, such as the alpha rhythm typical of the Jansen-Rit model.

A similar connectivity model was extended to large-scale brain network to study EEG spectra (Sotero et al., 2007), functional connectivity and synchronisation (Pons et al., 2010). They used interconnected Jansen-Rit

modules enriched with self-excitation of pyramidal neurons. There is a dichotomy in this methodology: intra-area connections are modelled with a spatially extended connectivity kernel (reflecting the heterogeneity of anatomical short-range cortical lateral connections), whereas discrete inter-area connections follow from brain imaging tractography data. Finally, Nguyen Trong et al. (2012) used a network of Jansen-Rit modules to model orientation selectivity of the visual cortex and to study the association between spontaneous and evoked activity. The last example establishes a link between NMMs and cognitive processes (as opposed to the simple generation of MEG/EEG/fMRI signals).

Models of sleep, drugs and anaesthesia

Sleep and anaesthetic drugs can influence directly excitability, and indirectly the neuronal oscillatory patterns observed in the EEG. This renders NMMs relevant to represent these brain states. For example, Weigenand et al. (2014) used an NMM to explain K-complexes and slow oscillations in the EEG patterns typical of NREM phase sleep. Transitions between different phases of sleep were studied on a spatially extended model by Steyn-Ross et al. (2005). Same authors focused on transitions induced by the anaesthetic drug propofol (Steyn-Ross et al., 1999). The effects induced by this drug were also investigated by Hindriks and Putten (2012), Hutt (2013) and Hashemi et al. (2015). Finally, Rowe et al. (2005) used the Robinson model to study drug effects in attention deficit hyperactivity disorder.

2.2 Principles, advantages and disadvantages of neural mass modelling

In this section we take a closer look at some assumptions underlying the NMMs. First, we focus on the LTI assumption and we examine when the shape of the PSPs resulting from an incoming spike can be approximated by the shape of change of the synaptic conductance. At the microscopic level the impulse response of the latter is often described by double exponentials, as can be derived formally from probabilistic considerations on the opening and closing of synaptic receptor channels (Dayan and Abbott, 2001). In a simplified approach, this conductance is described by the alpha

function. In case of a single neuron, the subthreshold membrane voltage V (here describing the PSP) can be expressed in a simplified way by a leaky integration with synaptic current (Dayan and Abbott, 2001):

$$\tau_m \frac{dV(t)}{dt} = E_{\mathrm{L}} - V(t) - r_{\mathrm{m}} g_{\mathrm{s}}(t)(V(t) - E_{\mathrm{s}}), \tag{2.1}$$

where τ_{m} is the membrane time constant, E_{L} is the rest potential, r_{m} is the membrane resistance and $g_{\mathrm{s}}(t)$ is the time-dependent synaptic conductance. Assuming infinitely fast membrane relaxation[1] $\tau_{\mathrm{m}} \to 0$ we obtain:

$$V(t) = \frac{E_{\mathrm{L}} + r_{\mathrm{m}} g_{\mathrm{s}}(t) E_{\mathrm{s}}}{1 + r_{\mathrm{m}} g_{\mathrm{s}}(t)}, \tag{2.2}$$

which shows that $V(t)$ does not change linearly with $g_{\mathrm{s}}(t)$. After considering only the first-order Taylor expansion around $r_{\mathrm{m}} g_{\mathrm{s}}(t) = 0$ we obtain:

$$V(t) = E_{\mathrm{L}} + r_{\mathrm{m}} g_{\mathrm{s}}(t)(E_{\mathrm{s}} - E_{\mathrm{L}}). \tag{2.3}$$

This equation shows that at rest $V(t)$ equals E_{L}, while the synaptic current adds to $V(t)$ the conductance-generated signal scaled by the difference between the rest and the synaptic reverse potentials. We therefore arrived to a solution fulfilling the LTI assumption with a kernel described by the scaled synaptic conductance response. In case of an incoming spike train, the resulting potential is obtained from a convolution of that kernel with the input. At the population level, when considering not the exact momentary, but rather temporally averaged potential (within a small interval comparable to the timescale of synaptic dynamics), convolution with a spike train changes to a convolution with the *firing rate* function, which describes number of spikes per this time interval[2]. Since all effects related to neuronal inputs are considered linear we can scale them up from the level of a single neuron to the level of a neuronal population. This allows to relate characteristics of a population to microscopic synaptic properties. At that level we talk of the *average* $V(t)$ in population and the *average* firing rate.

[1] This assumption is typical of NMMs. A model in which finite τ_{m} is considered is the model of Liley et al. (2002)

[2] For the formal derivation see e.g. Hutt (2015)

We illustrate these considerations with an example in which the impulse response of the synaptic conductance is given by the alpha function:

$$g_{\mathrm{s}}(t) = \Theta(t - t_0) \cdot (t - t_0) \frac{\bar{g}_{\mathrm{s}}}{\tau_{\mathrm{s}}} e^{-(t-t_0)/\tau_{\mathrm{s}}}, \tag{2.4}$$

where Θ is the Heaviside step function, t_0 is spike arrival time, τ_{s} is the synaptic characteristic timescale, and $\bar{g}$ is the characteristic amplitude. Figure 2.1 shows the temporal evolution of $V(t)$ upon spike arrival at $t = 0$ s, given by solutions of Equations (2.1)-(2.3) in blue, green, and red, respectively. In practise, temporal differences between the exact and the approximated solutions can be partially compensated by adjusting the PSP time constant(s). This is additionally justified, because in neural mass models we are interested in potentials occurring at the soma, and thus some delay should exist with respect to the synaptic activity. The assumptions we made to arrive to Equation (2.3) can be understood in the following way: membrane dynamics are much faster than synaptic conductance dynamics, and synaptic activity acts as if the membrane potential remained close to its resting state value E_{L}; the further it deviates from that value, the worse the approximation is. Indeed, Figure 2.1A shows that when these assumptions do not hold, the time course of the PSP as approximated by the synaptic conductance differs from the exact solution, whereas Figure 2.1B shows that the separation of τ_{s} and τ_{m} timescales and only a small variation from the resting state E_{L} (compare scales on Y axes in panels A and B) make all results consistent with each other.

It is worth noting that in our NMM, the amplitudes of the PSP impulse responses are smaller than 10 mV, and as a result the average membrane potentials of neuronal populations in the model do not deviate from the quiescence state by more than ~ 20 mV. This means that in practise they do not get close to E_{s}, where the approximation error is greatest. This approach is somehow familiar to that of the integrate-and-fire model, where subthreshold membrane potentials are considered only within a ~ 20 mV range, i.e. between the resting state (~ -70 mV) and the firing threshold (~ -50 mV). Nevertheless, as shown above, here an additional linear assumption is made, valid when the potential remains close to the steady state.

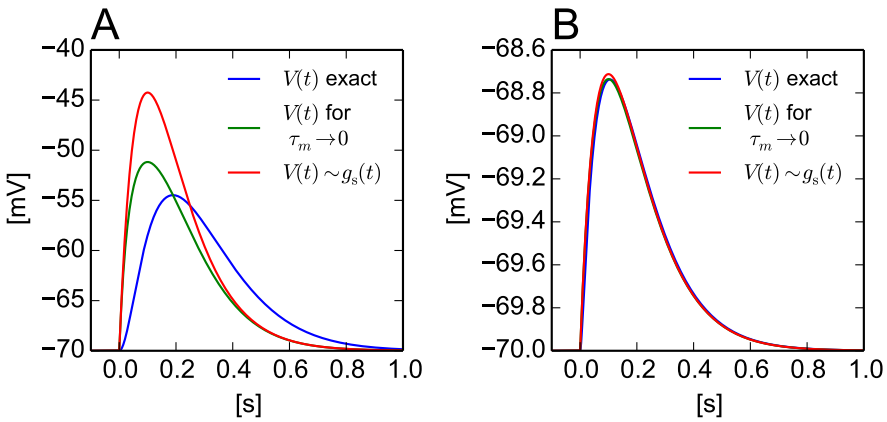

Figure 2.1: Time evolution of the post synaptic potential V for a single neuron. In both panels solutions to Equations (2.1)-(2.3) are shown in blue, green, and red, respectively. A spike arrives at $t_0 = 0$ and the synaptic conductance changes according to the alpha function (Equation (2.4)). Panel A corresponds to τ_{m}=100 ms, τ_{s}=100 ms, $r_{\mathrm{m}}\bar{g}_{\mathrm{s}}$=1. Panel B corresponds to τ_{m}=5 ms, τ_{s}=100 ms, $r_{\mathrm{m}}\bar{g}_{\mathrm{s}}$=0.05. E_{L} = -70 mV and E_{s}=0 mV.

In a nutshell, NMMs are useful in modelling activity of large groups of neurons, operating in a fairly and invariantly synchronous manner. This assumption is supported by the fact that sensory information incoming to the nervous system affects groups of neurons rather than individual neurons. Nevertheless, NMMs are not concerned with coherence of the neurons within the group. As explained in Section 1.3, they implicitly assume that coherence is high enough (to produce a detectable signal) and invariant. Nonetheless, change to this coherence is one of the possible explanations of the event-related changes to the EEG power spectra (Pfurtscheller and Lopes da Silva, 1999). A single neuronal population described with the NMM approach will inevitably fail to capture this behaviour. Only recently a 'next generation of neural mass models' that deals explicitly with intra-population synchrony was introduced by Coombes and Byrne (2016).

Large groups of neurons are responsible for generation of signals detected in non-invasive neuroimaging techniques, such as EEG, MEG and fMRI. For this reason results obtained with NMMs are often related to these measurements. The averaging description of the NMMs permits to describe macroscopic phenomena without detailing subtleties related to

individual neurons, e.g. their morphology or phenotype, which at the microscopic level may produce specific firing patterns. In this description, phenomena related to short timescales, e.g. correlations between spike trains, are averaged out. Also processes occurring in long timescales, for example synaptic plasticity, are not considered in NMMs. Furthermore, effects related to membrane dynamics and fluctuations around the mean activity of the population can not be studied within the NMM framework. The convenient assumption about linearity of all effects related to neuronal inputs comes for a price, e.g. negligence of active dendrites. On the other hand, an unquestionable advantage of NMMs is their simple formulation, which allows for mathematical tractability and numerical simulations of full-brain models. In what follows, we introduce the formulation of the NMM used in this Thesis.

2.3 Extended Jansen-Rit model

The results presented in this Thesis are obtained from a model comprising a number of coupled stochastically driven Jansen-Rit models of cortical columns. Therefore, our model does not account for realistic head geometry, nor for volume conduction and time delays. The latter is justified by the fact that neighbouring cortical columns are separated by a distance smaller than one millimetre. Since the speed of signal propagation in axons has a lower limit 0.1 m/s (Segev and Schneidman, 1999). The delay between neighbouring columns is smaller than milliseconds, which is at least one order of magnitude smaller than the characteristic timescales of the system. We study this model systematically, gradually increasing its complexity through this Thesis. In Chapter 3 we focus on dynamics generated by a single module (column), next, we study in Chapter 4 interactions between two modules, and finally, in Chapter 5 we consider an all-to-all connected network.

2.3.1 Model of a cortical column

The internal structure of a cortical column modelled with the Jansen-Rit approach comprises the following three neuronal assemblies: a population of pyramidal neurons, a population of excitatory interneurons and

a population of inhibitory interneurons. The model lacks self-excitation and self-inhibition of populations. Internal dynamics of the column are described with two transformations: the first one converts average presynaptic spiking activity (firing rate) to average somatory potential, and the second one transforms the resulting potential at the soma to a spiking rate. We discuss both transformations in what follows.

Firing rate → potential

This transformation assumes linearity and time-invariance (LTI). It is given by the following convolution:

$$y(t) = \int_{-\infty}^{t} h(t - t')s_{\text{in}}(t')\mathrm{d}t', \tag{2.5}$$

where $s_{\text{in}}(t)$ is a time-dependent average firing rate of spike trains incoming to a population, $y(t)$ is a postsynaptic membrane potential (PSP), and the $h(t)$ kernel describes a PSP response at the soma resulting from an impulse activation at the synapse. This kernel equals zero for $t < 0$ and otherwise is given by the following expression for excitatory and inhibitory connections:

$$h_e(t) = Aate^{-at}, \tag{2.6}$$

$$h_i(t) = Bbte^{-bt}, \tag{2.7}$$

where A and B are the maximum excitatory and inhibitory postsynaptic potentials, and a and b are constants shaping the excitatory and inhibitory PSPs time profiles, respectively. These constants follow from lumped contributions of all dilatory effects that include synaptic kinetics, dendritic signal propagation, and leak currents. For example, Labyt et al. (2006) interpret the value of a as a reciprocal of an average over AMPA and NMDA decay times. According to values used by Jansen et al. (1993), B is almost seven times greater than A, which can be partially explained by the perisomatic effect (see Section 1.1.2) exerted by inhibitory cells. Both kernels are shown in Figure 2.2A. Using Equation (2.6) one can express the transformation given by Equation (2.5) by the following differential form:

$$\frac{d^2y(t)}{dt^2} + 2a\frac{dy(t)}{dt} + a^2y(t) = Aa \cdot s_{\text{in}}(t), \tag{2.8}$$

Similarly, by using Equation (2.7) one can find a corresponding representation for inhibitory processing.

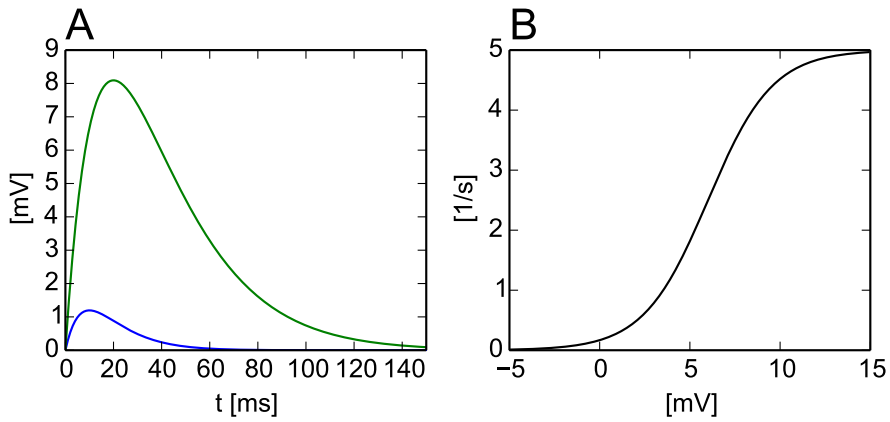

Figure 2.2: Two transformations fundamental to neural mass modelling. Panel A shows kernels generating excitatory (blue) and inhibitory (green) postsynaptic potentials (PSPs). Panel B shows the rate response function, which converts average somatic potentials to average firing rate.

Potential → firing rate

The second transformation, describes somatic conversion of the average PSP into an average firing rate. When the membrane potential rises above threshold in the neuronal soma, a spike is generated. NMMs do not implement the mechanisms of this generation, but rather describe it statistically at the population level. This transformation (previously referred to as a 'rate response function') is given by the following sigmoid function:

$$s_{\text{out}}(y) = \text{Sigm}(y) = \frac{2e_0}{1 + e^{r(\nu_0 - y)}}, \tag{2.9}$$

where $s_{\text{out}}(y)$ is average firing rate of spike trains, y is its average net PSP (in general, time dependent), $2e_0$ is the maximum firing rate, ν_0 is the PSP for which half maximum of the firing rate is reached, and r determines steepness (and thus nonlinearity) of this transformation. This sigmoid is depicted in Figure 2.2B.

2.3.2 Intracolumnar and intercolumnar connectivity

The two transformations described in the preceding section allow to model circuits of interconnected neuronal populations (cortical columns). A circuit corresponding to a Jansen-Rit cortical column is shown in Figure 2.3. The figure shows coloured representations (see caption for colour meanings) of neuronal populations and connections between them. Efferents and afferents (shown outside of the grey cylinder) couple columns into a network and drive them in a deterministic and stochastic manner. The black rectangles in Figure 2.3 stand for the transformations: somatory processing given by Equation (2.9) is denoted with 'Sigm', excitatory interactions between populations are marked with h_e and inhibitory ones with h_i, and multiplication by K refers to coupling strength between the columns (established between pyramidal populations). The constants $C_{1,2,3,4}$ reflect proportions of synaptic connections between populations, so they can be thought of as intra-population connection strengths. The dynamics of a network of columns described with the black circuit from Figure 2.3 are governed by the set of the following equations:

$$\begin{cases} \ddot{y}_0^i(t) + 2a\dot{y}_0^i(t) + a^2 y_0^i(t) = Aa\ \mathrm{Sigm}[y_1^i(t) - y_2^i(t)] & (2.10) \\ \ddot{y}_1^i(t) + 2a\dot{y}_1^i(t) + a^2 y_1^i(t) = Aa\{I_{\mathrm{ex}}^i(t) + C_2\ \mathrm{Sigm}[C_1 y_0^i(t)]\} & (2.11) \\ \ddot{y}_2^i(t) + 2b\dot{y}_2^i(t) + b^2 y_2^i(t) = Bb\{C_4\ \mathrm{Sigm}[C_3 y_0^i(t)]\} & (2.12) \end{cases}$$

When multiplied by C_1 or C_3, y_0^i gives an average excitatory PSP in column i that the population of pyramidal neurons induces on populations of excitatory and inhibitory interneurons, respectively. y_1^i is the average excitatory PSP in this column induced on the population of pyramidal neurons and y_2^i is the average inhibitory PSP on this population. Subsequently $y_1^i - y_2^i$ is a resultant average net PSP on this population, which, as explained in Section 1.2, is assumed to be proportional to the measured EEG. For simplicity we will drop the index i whenever the referenced variables apply to all columns. We set parameters of the neural mass model to typically used values as given in Jansen and Rit (1995): $e_0 = 2.5\ s^{-1}$, $v_0 = 6$ mV, $r = 0.56\ \mathrm{mV}^{-1}$, $A = 3.25$ mV, $B = 22$ mV, $a = 100\ \mathrm{s}^{-1}$, $b = 50\ \mathrm{s}^{-1}$, $C_1 = 135$, $C_2 = 108$, $C_3 = C_4 = 33.75$. In the following section we elaborate on the external input to a column, $I_{\mathrm{ex}}(t)$.

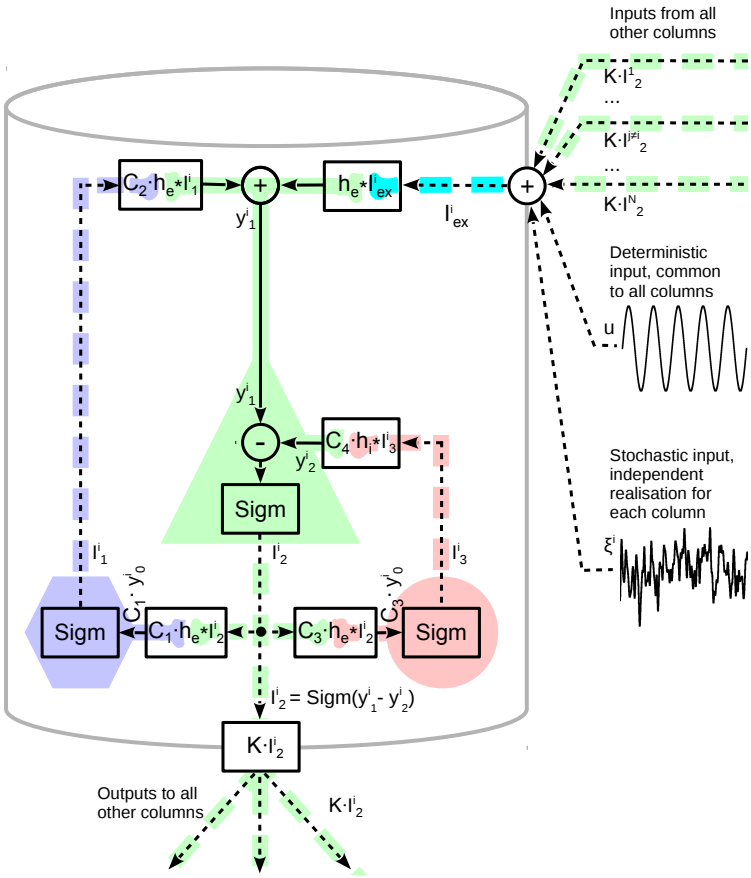

Figure 2.3: A scheme of one node of a network of Jansen-Rit cortical columns. The grey cylinder marks boundaries of one cortical column. A population of pyramidal neurons is marked with green, and populations of excitatory and inhibitory interneurons with blue and red, respectively. Somata are depicted with the triangle, hexagon and circle. Continuous lines stand for dendritic processing and dashed ones for axonal processing. The black circuit depicts an analytic description of the model. A dot means multiplication and a star operator denotes convolution. Outside of the grey cylinder are shown afferents and efferents of the cortical column. Cyan indicates a sum of external inputs from other columns in the network and from non-modelled sub-cortical and cortico-cortical structures, modelled in a lumped way with deterministic and stochastic components.

2.3.3 External input to cortical columns

The term $I^i_{\text{ex}}(t)$ in Equation 2.11 represents the external input to the i column, incoming to the population of pyramidal neurons and comprising the contribution from other columns in the network and lumped cortico-cortical and sub-cortical afferents. It is given by the following equation:

$$I^i_{\text{ex}}(t) = \xi^i(t) + p + u(t) + \frac{K}{N-1}\sum_{\substack{j=1 \\ j\neq i}}^{N} \text{Sigm}[y^j_1(t) - y^j_2(t)], \tag{2.13}$$

and it is expressed in s^{-1} since it refers to the firing rate. The coupling contribution term is not taken into account in the studies performed on one column ($N = 1$ in Chapter 3). The lumped afferents are modelled as a sum of a constant component p and zero-mean signals: stochastic $\xi^i(t)$ and harmonic $\tilde{A}\sin(\frac{2\pi}{T}t + \phi)$. The effect of $I_{\text{ex}}(t)$ on the dynamics of the model is one of the foci of this Thesis. In Chapter 3 we study the role that stochastic and rhythmic driving have on a single cortical column, in Chapter 4 we focus on interplay between noise and coupling between two connected columns, and in Chapter 5 we study a stochastically and periodically driven network of columns.

Constant input: bifurcation diagram

Previous studies have sought to understand the dynamics of the Jansen-Rit model by examining the effect of p as a bifurcation parameter for $N = 1$ (Grimbert and Faugeras, 2006; Jansen and Rit, 1995; Spiegler et al., 2011; Touboul et al., 2011). In Figure 2.4A we recreate with XPPAUT (Ermentrout, 2002) the results of Grimbert and Faugeras (2006), illustrating the invariant sets of the model of a single cortical column that exist for different, time invariant values of $I_{\text{ex}} = p$. To ease subsequent interpretations of the dynamics invoked by different choices of temporally varying $I_{\text{ex}}(t)$, we briefly review the different dynamic regimes that are possible in this model. Since we only discuss a single module here ($N = 1$), in what follows we omit the column's index in the superscript of state variables. Although in Figure 2.4A we plot a range of I_{ex} that includes negative values (region I in Figure 2.4A), we focus on positive values of I_{ex}, since only these are biologically plausible. The regime marked II in Figure 2.4A spans for

$-12.15\ \mathrm{s}^{-1} < p < 89.83\ \mathrm{s}^{-1}$. It is a bistable regime that contains two stable fixed points: a node (blue) and a focus (cyan). At $p = 89.83\ \mathrm{s}^{-1}$ the focus transitions to a limit cycle (green) in a supercritical Hopf bifurcation. This limit cycle has its characteristic frequency close to 10 Hz, and has therefore previously been used to model the alpha rhythm of the brain (henceforth referred to as 'alpha limit cycle'). Its time course is shown in Figure 2.4B.

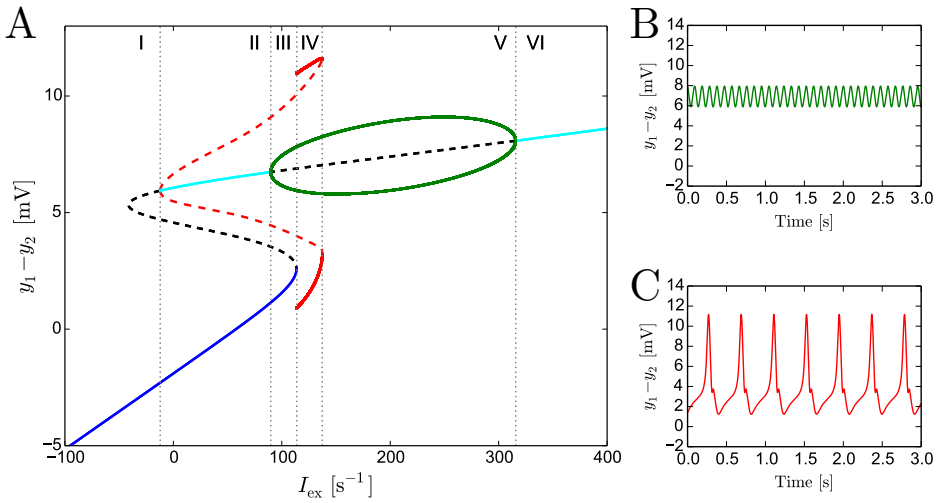

Figure 2.4: Bifurcation diagram of the Jansen-Rit model defined in Equations (2.10)-(2.12) for $N = 1$ (panel A) and time courses of limit cycles (panels B,C). Panel A shows a bifurcation diagram obtained for parameters of the model set to biologically plausible values proposed in Jansen and Rit (1995). The X axis shows external, constant input to the pyramidal population $I_{\mathrm{ex}} = p$. The Y axis shows net postsynaptic potential on this population: $y_1 - y_2$. Continuous (dashed) lines represent stable (unstable) solutions. Cyan and blue denote a node and a focus, respectively, and green and red indicate alpha and epileptiform limit cycles, respectively. Vertical, grey dotted lines divide the diagram to six regimes (denoted by roman numerals) of qualitatively distinct dynamical properties. Panels B and C show time courses corresponding to alpha and epileptic-like oscillations, respectively. They represent two stable solutions from the bistable regime IV, with $p = 120\ \mathrm{s}^{-1}$.

The area marked III is also bistable, however here the two stable solutions are the node (blue) and the alpha limit cycle (green). At $p = 113.58\ \mathrm{s}^{-1}$ the stable node ceases to exist in a saddle-node on invariant

circle (SNIC) bifurcation that creates a limit cycle reminiscent of epileptiform spikes, henceforth referred to as 'epileptiform limit cycle'. The amplitude of this cycle is shown as a continuous red line in Figure 2.4A and its time course is shown in Figure 2.4C. The frequency of this limit cycle ranges from 0 Hz at its creation ($p = 113.58$ s^{-1}) to ~ 5 Hz at its termination point ($p = 137.38$ s^{-1}). Region IV in Figure 2.4A denotes a bistable regime in which the epileptiform limit cycle coexists with the alpha limit cycle. Regime V starts at $p = 137.38$ s^{-1}, where the epileptiform limit cycle vanishes in a fold of limit cycles. In regime V the alpha limit cycle is the only stable solution. It ceases to exist in a supercritical Hopf bifurcation at $p = 315.70$ s^{-1}, where the last regime, marked with VI, starts. The focus (cyan) remains the only stable solution there.

With no coupling, p determines the average working point of the system in the landscape of dynamical regimes as shown in Figure 2.4A. In agreement with a number of studies suggesting that the brain operates close to a phase transition (see Sections 1.4.4 and 1.4.6) we set p close to one of the above mentioned bifurcations (exact values to be specified in each chapter). In particular, the value of p corresponding to the Hopf bifurcation characterised by the alpha rhythm, mimics 'healthy-like' activity, whereas values of p corresponding to the catastrophic-epileptic SNIC bifurcation correspond to aberrantly excitable settings modelling 'unhealthy-like' tissue and activity. We study both cases in Chapter 3, then we focus on 'unhealthy-like' settings in Chapter 4 and on 'healthy-like' settings in Chapter 5.

Time-dependent input: coupling and stochasticity

In physiological conditions, other components of I_{ex} perturb the system, so the input varies from p and the system does not remain permanently in one place on the bifurcation diagram presented in Figure 2.4A. Coupling between the columns is realised by feeding the output of the population of pyramidal neurons of the upstream column to the population of pyramidal neurons of the downstream column. This coupling signal is multiplied by the coupling strength K and normalised by the number of the afferent connections to a column. For every column this number equals $N-1$ in case of N columns in the network, since we consider only all-to-all connectivity.

This normalisation allowed us to study the dependence of the results on the system size N for a constant value of the coupling strength K (Chapter 5). Without that normalisation, increasing the number of columns N in all-to-all topology would ultimately lead to saturation due to excessive external driving.

The stochastic components, $\xi^i(t)$, are given either by white noise (Chapter 4) or by the Ornstein-Uhlenbeck (OU) process (Chapters 3 and 5) discussed in Section 1.4.5. In the former case $\xi^i(t) = \sqrt{2D}\xi^i_w(t)$, where $\xi^i_w(t)$ is a random variable representing Gaussian white noise with zero mean and correlation $\langle \xi^i_w(t)\xi^i_w(t')\rangle = \delta(t-t')$ and $\langle \xi^i_w(t)\xi^j_w(t')\rangle = 0$ for $i \neq j$. In the latter case $\xi^i(t) = \xi^i_{\text{ou}}(t)$, where $\xi^i_{\text{ou}}(t)$, is derived from the solution of the following linear stochastic differential equation:

$$\frac{d\xi^i_{\text{ou}}}{dt} = -\frac{\xi^i_{\text{ou}}}{\tau} + \frac{\sqrt{2D}}{\tau}\xi^i_w(t) \tag{2.14}$$

In the steady state, the OU noise has a Gaussian distribution of values characterised with the following standard deviation:

$$\sigma_{\text{ou}} = \sqrt{\frac{D}{\tau}} \tag{2.15}$$

The intensity of the noise can be defined as a product of its stationary variance (accounting for amplitudes of random fluctuations) and its correlation time (accounting for persistence of the fluctuations) (Laing and Lord, 2010). In the notation adopted here, the intensity defined in this way is given by D.

Finally, the power spectrum of the OU noise is given by the Lorentzian function:

$$S_{\text{ou}}(f) = \frac{2D}{1 + 4\pi^2\tau^2 f^2} \tag{2.16}$$

This equation shows that variations of the parameter τ modify the spectral composition of the noise, as mentioned in Section 1.4.5. These variations are illustrated in Figure 2.5, which visualises Equation (2.16) for three different values of τ: 1 s (red), 0.1 s (green), and 0.01 s (blue). In each case there is a cutoff frequency $f^* = (2\pi\tau)^{-1}$ for which scaling of the PSD changes from the white noise $2D$ (for $f \ll f^*$) to the red noise $2D/(2\pi\tau f)^2$ (for $f \gg f^*$), thus $\sim 1/f^b$ with $b = 0$ in the former, and $b = 2$ in the latter

case, as discussed in Section 1.4.5. In this Thesis we study how variations of noise parameters, in particular τ, affect dynamics of the driven system.

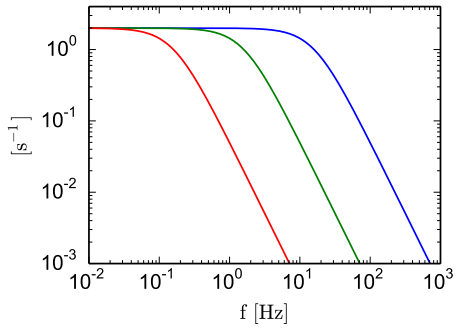

Figure 2.5: Lorentzian curves in log-log scale. The plots correspond to Equation (2.16) with $D = 1$ s^{-1}, and τ=1 s (red), 0.1 s (green) and 0.01 s (blue). Units on the Y axis follow from the units of D.

In summary, the model used in this Thesis describes the averaged activity of groups of neurons. The results obtained can be related to neuroimaging measurements such as EEG. The model itself is a network of all-to-all interconnected modules of Jansen-Rit neural masses. Each of these modules can exhibit in deterministic stationary conditions a repertoire of dynamics introduced in this chapter. In our model, however, the modules are driven by independent realisations of either white or Ornstein-Uhlenbeck noise, and by periodic and constant signals common to the whole network. These driving components are characterised by specific parameters. The results presented in the following chapters of this Thesis elucidate how values of these parameters, and the coupling strength of the network shape the dynamics exhibited by the model.

CHAPTER 3

NOISE-INDUCED EPILEPTIFORM DYNAMICS

3.1 INTRODUCTION

In this chapter we focus on the dynamics of an individual Jansen-Rit module driven by periodic signals and temporally correlated noise. We determine characteristics of the driving signals that elicit epileptic-like activity in the model. In the brain, epileptic symptoms are characterised by excessive synchrony arising on areas extending beyond individual cortical columns. The Jansen-Rit module studied here represents such an area. At this scale, deficits can be observed both in the dynamics of brain regions (Iannotti et al., 2016; Valentín et al., 2005) and the connections between them (O'Muircheartaigh et al., 2012). In this context, recent focus has been placed on the role that large-scale brain networks play in epilepsy (Kramer and Cash, 2012; Richardson, 2012; Spencer, 2002; Van Diessen et al., 2013). A fundamental, unanswered question in this context is how seizures emerge and spread in such networks (Goodfellow et al., 2016; Petkov et al., 2014; Terry et al., 2012). Mathematical models of brain dynamics can be helpful in studying the mechanisms underlying these phenomena (Lytton, 2008; Suffczyński et al., 2006; Wendling et al., 2015).

The nodes of a brain network are exposed to the surrounding activity generated by the interconnected nodes. In general, dynamics evinced by a single node might depend on the intrinsic properties of this node and on the incoming driving. In particular, driving by epileptiform rhythms might lead to generation of these rhythms, and as a consequence, to spreading of a seizure in the brain. Furthermore, emergent network dynamics might play a role in the generation of highly synchronous epileptic-like states (Goodfellow et al., 2011; Rothkegel and Lehnertz, 2011). Prior to studying these phenomena on networks, it is sensible to understand how the temporal properties of the driving signals interact with internal dynamical

properties of an isolated node in the context of generation of epileptiform activity.

Previous work has focused on the types of dynamics that could underpin transitions from healthy EEG to seizure EEG, such as changes in model parameters (bifurcations, Breakspear et al., 2006; Touboul et al., 2011), coexistence of healthy and abnormal states (bistability, Lopes da Silva et al., 2003), excitability (Baier et al., 2012) and intermittent behaviour (Goodfellow and Glendinning, 2013). The bifurcation route into seizures relies on a (relatively) slow timescale change in the brain that drives it into an alternate (pathological) state, whereas the bistability and excitability paradigms rely on a (fast) perturbation-induced transition from the healthy to pathological state. However, any of these scenarios can be assumed to occur amidst a backdrop of ongoing brain dynamics, which could additionally influence transitions into seizures. As discussed in Chapter 1, these dynamics involve a broadband (stochastic) activity and oscillations with well defined frequencies. In this chapter we use both these types of dynamics as input signals driving the Jansen-Rit neural mass model. In the context of epileptic-like dynamics, this model is characterised by both bistability and excitability (see Section 2.3). We therefore study a variety of possible scenarios leading to the occurrence of epileptiform dynamics in this model. These scenarios arise from an interplay between the non-trivial bifurcation structure of the model (see Figure 2.4A) and the temporal properties of the driving signals that stand for the external stimulation or the lumped background activity of the brain network.

Modelling studies of seizure onset typically lump the 'background' dynamics of the brain into stochastic fluctuations, which have most often been assumed to have a flat power spectrum (see Section 1.4.5). However, the background EEG activity of the brain is characterised with a $1/f^b$ shape (see Section 1.4.5), with prominent frequencies appearing concomitantly with different brain states (Buzsáki and Draguhn, 2004; Freeman et al., 2000; Niedermeyer and Silva, 2005). Some of these frequencies might play a role in the initiation of epileptiform activity. In particular, in humans an increase of power in the delta band has been observed in MEG (Gupta et al., 2011) and EEG (Sadleir et al., 2011) recordings preceding absence

seizures. Pathological slow rhythms can also be observed in interictal or preictal periods associated with focal epilepsies (Lee et al., 2000; Tao et al., 2011; Valentín et al., 2014). In animal models of epilepsy, electrophysiological recordings performed in the preictal phase have revealed an increase of power in the delta (Sitnikova and Luijtelaar, 2009), and delta and theta (Van Luijtelaar et al., 2011) bands. Furthermore, the most common type of reflex epilepsy (photosensitive epilepsy) is believed to depend on frequency of visual stimulation (Kasteleijn-Nolst Trenite, 2006).

The wealth of observations listed above, among many others, raise the need to better understand the response of neuronal populations to afferent rhythms and stochastic fluctuations with a variety of dynamics, including those that can be approximated by noise yielding a realistic $1/f^b$ power spectrum, and those that contain dominant rhythms observed in the epileptic brain. In Section 1.4.5 we discussed in detail the relation between relaxational processes and the $1/f^b$ PSD, and we introduced the Ornstein-Uhlenbeck (OU) noise, which we formulated mathematically in Section 2.3.3. In this chapter we study the effect of the OU noise and rhythmic driving on the generation of epileptiform dynamics in the Jansen-Rit model. We study this model in two paradigms: a 'healthy' scenario, when the average working point of the model is set at a certain distance from the epileptic excitability threshold, and an 'unhealthy' one, when this distance is reduced. In both cases we classify the dynamics of this model by assessing variations of the signal around its time-averaged value, thus distinguishing between 'healthy' and epileptiform dynamics.

3.2 Methods

We performed a series of simulations of the model introduced in Section 2.3 for a single Jansen-Rit module ($N = 1$) exposed to the Ornstein-Uhlenbeck (OU) noise with varying values of the correlation time τ and the stationary standard deviation σ_{ou}. Therefore, the additive stochastic component $\xi^i(t)$ in Equation (2.13) takes the form of $\xi^i_{ou}(t)$ given by Equation (2.14). Since in this chapter we only deal with a single column, in what follows we drop the i index.

3.2.1 'Healthy-like' and 'unhealthy-like' paradigms

The Jansen-Rit model and its variations are often used to simulate epileptic activity (see Section 2.1.3). In particular, in order to mimic the behaviour of unhealthy, seizure-generating patches of neuronal tissue (e.g. epileptic foci), variations to the model's parameters are introduced. In general, the occurrence of epileptic activity in this model is facilitated when excitation is increased and/or inhibition is decreased. For example, Grimbert and Faugeras (2006) observe more epileptic spikes in the model's output upon increasing the value of the ratio A/B. A similar effect is achieved by Goodfellow et al. (2016) by reducing B in Wendling's model. Here we introduce hyper-excitability by increasing the p parameter, which effectively shifts the average working point of the system towards the SNIC bifurcation, where the regime of epileptic behaviour begins. Our 'healthy-like' settings correspond to $p = 89$ s^{-1}, i.e. close (on average) to the Hopf bifurcation at $p = 89.83$ s^{-1}. This choice is motivated by the premise that the brain operates near a second-order phase transition or bifurcation (see Section 1.4.4). The 'unhealthy-like' settings correspond to $p = 113$ s^{-1}, the point just below the 'catastrophic' SNIC bifurcation at $p = 113.58$ s^{-1} (see Figure 2.4A). Note that the 'healthy' and epileptiform activity can be evinced by the model in both paradigms. We introduce the classification of these activities in what follows.

3.2.2 Classification of model dynamics

We are interested in classifying the dynamics of one cortical column according to the 'healthy' or 'epileptiform' behaviour described previously (Grimbert and Faugeras, 2006; Jansen and Rit, 1995; Spiegler et al., 2010; Touboul et al., 2011), which depends upon the parametrisation of the model and on the nature of its input I_{ex} (see Equation (2.13)). By considering the bifurcation diagram shown in Figure 2.4A, we define epileptiform dynamics as those corresponding to the epileptiform limit cycle (see Figure 2.4C), and healthy dynamics as any of the other regimes. The latter comprises either noise-driven fluctuations around the stable node, or oscillations with frequency close to 10 Hz (alpha oscillations, see Figure 2.4B)

due to the presence of, or proximity to, the limit cycle generated by the Hopf bifurcation.

Our classification of the output of the Jansen-Rit cortical column in these three categories is depicted in Figure 3.1. The classification is established via the following algorithm. First, a moving average of the model's output, $y_1 - y_2$, is computed with a sliding window of length 0.4 s. This window is long enough to sufficiently smooth out the signal (see Figure 3.1B) and thus allow for estimation of its variability (details below), and short enough to mark transitions between dynamical regimes with good temporal accuracy (see Figure 3.1A). Second, the root mean square ($\text{RMS}_{(y_1-y_2)}$) of the $y_1 - y_2$ signal around this mean is obtained. When this quantity is high, variations of the signal are rapid and/or have a high-amplitude, which are features of the epileptiform limit cycle. Therefore, we set a threshold $\text{Th}_\text{B} = 2.25$ mV (dashed line in Figure 3.1C) that establishes the value of $\text{RMS}_{(y_1-y_2)}$ above which a specific time point of the signal is classified as being in the epileptiform regime. Otherwise, we compare the smoothed $y_1 - y_2$ signal with the threshold value $\text{Th}_\text{A} = 5$ mV (dashed line in Figure 3.1B), which separates the focus from the node along the $y_1 - y_2$ axis (cf. Figure 2.4A). If the smoothed signal is greater than Th_A, we classify that data point as belonging to an alpha oscillation, while if it is smaller we classify it as part of a noisy fluctuation around the node. Note that this methodology can be applied for both deterministic and stochastic driving of the system (in the deterministic case we do not call the node dynamics 'stochastic'). The thresholds Th_A and Th_B and the window length have been set such that resulting classification complies with inspection by eye. The attractor-based classification method described above is adequate in our case, since our model attractors can be distinguished easily by amplitude. For other types of models, or for the analysis of experimental data, adding frequency information to aid the classification might be beneficial, although purely temporal classifications have been found to be sufficient in some cases (Kramer et al., 2012).

3.2.3 Spectral composition of the noise

In order to study how the frequency content of OU noise relates to traditionally defined EEG frequency bands (i.e. delta, theta, alpha, beta,

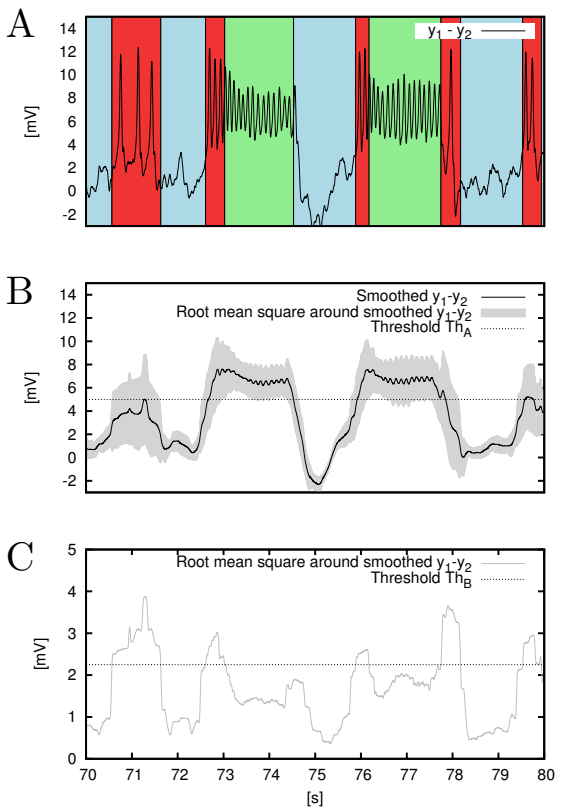

Figure 3.1: Methodology for the classification of the dynamics of a single column. Panel A shows $y_1 - y_2$ obtained from 10 seconds of stochastic simulation for $p = 89\,\mathrm{s}^{-1}$, $\tau = 10^{-0.5}$ s, $\sigma_{\mathrm{ou}} = 50\,\mathrm{s}^{-1}$. Background colours indicate the type of activity assigned with the classification algorithm: red stands for epileptiform dynamics, green for alpha oscillations, and blue for random fluctuations around the node. Panel B shows a smoothed version of the $y_1 - y_2$ signal from panel A, obtained with a running mean computed within a 0.4-second-long sliding window. The dashed line denotes the $\mathrm{Th_A} = 5$ mV threshold, which is used to discriminate between stochastic fluctuations around the node (smoothed $y_1 - y_2 \leq \mathrm{Th_A}$) and alpha oscillations (smoothed $y_1 - y_2 > \mathrm{Th_A}$). Grey marks the root mean square of $y_1 - y_2$ around its smoothed version ($\mathrm{RMS}_{(y_1-y_2)}$). This value is shown in panel C in grey along with the $\mathrm{Th_B} = 2.25$ mV threshold, which is used to identify epileptiform dynamics (when $\mathrm{RMS}_{(y_1-y_2)} > \mathrm{Th_B}$).

gamma), we quantify the fraction of the total spectral power of the noise (with correlation time τ) contained within each of the bands. We do it by integrating power spectrum of the noise (see Equation (2.16)) in the limits ($f_{\min}, f_{\max}$) delimiting particular frequency bands. As a result, for each band we obtain the following τ-dependent function:

$$E(\tau, f_{\min}, f_{\max}) = \frac{2}{P_{\text{tot}}} \cdot \int_{f_{\min}}^{f_{\max}} S_{\text{ou}}(f) df = \frac{2}{\pi} \arctan(2\pi\tau f) \Big|_{f_{\min}}^{f_{\max}} \tag{3.1}$$

where the normalisation factor P_{tot} yields the total power and equals $\int_{-\infty}^{\infty} S_{\text{OU}}(f) df = \frac{D}{\tau}$. The factor 2 in front of the integral follows from taking into account the power transmitted in both the positive and negative frequency bands.

3.2.4 Computational simulation

We integrated the system using the stochastic Heun scheme (Toral and Colet, 2014) with a time step equal to 10^{-4} s, and we stored every tenth point of the simulation. For each value of the noise correlation time τ and stationary standard deviation σ_{ou} we performed 10 simulations, each with different realisation of the noise (which was frozen for different values of τ, σ_{ou}) and we averaged the results. Each simulation was 111 seconds long. The first 10 seconds were discarded and one second buffered the sliding window. In the deterministic system, the model was simulated for 111 seconds, with 100 seconds of discarded transient and one second buffering the sliding window. This means that the effective time courses used in the deterministic analysis were each 10 seconds long, which corresponds to the longest period of the driving sinusoid that we utilised.

3.3 Results

3.3.1 Stochastic driving

Simulations of the model under different values of the correlation time τ of the driving OU noise reveal qualitatively different dynamics (Figure 3.2). For weakly correlated noise (low values of τ) stochastic fluctuations around the node predominate (Figure 3.2A). For intermediate

temporal correlations epileptiform rhythms are more often observed (Figure 3.2B), whilst at larger correlation times the model displays mainly stationary and alpha-oscillatory activities (Figure 3.2C). These results suggest that epileptiform dynamics are more readily observed for noise with intermediate correlation times. In order to systematically study this effect, simulations of the model were performed for different values of τ and standard deviation of the noise, σ_{ou}. For each simulation, we measured the fraction of the total time that the system spent in the epileptiform regime (Figure 3.2D). This time is obtained by means of a classification algorithm described above.

Figure 3.2D shows that for large enough values of the standard deviation σ_{ou}, epileptiform dynamics arise for an intermediate value of the noise correlation time. As σ_{ou} decreases, the interval of values of τ for which epileptiform dynamics predominates is shifted to larger values. The intensity D of OU noise, (described in Equation (2.15)) is overlaid in white dashed lines on Figure 3.2D. It can be seen that the onset of epileptiform dynamics for intermediate values of τ coincides with constant values of D. This means that in order to generate epileptiform dynamics, the noise generated by the OU process should have sufficient intensity, regardless of its power and correlation time. However, this simple relationship does not hold for $\tau \gtrsim 10^{-1.5}$ s. The system more often displays alpha oscillations for large correlation times ($\tau \gtrsim 10^{-0.5}$ s) than for small correlation times.

Figure 3.3 shows the fractions of time that the system spends in the three attractors of interest, i.e. the node (panels A and B), spiky behaviour (C and D) and alpha oscillations (E and F). This figure demonstrates both healthy-like (top row) and unhealthy-like (bottom row) settings with initial conditions set exactly to the node. This activity prevails for the whole simulation time in case of a healthy-like system driven with noise approaching the white noise limit $\tau \to 0$ (dark red region on the left of panel A) and noise with a small amplitude (dark red region on the bottom of panel A). The same noise, however, is able to excite the system in an unhealthy-like case, so that the node attractor is escaped (panel B). In a healthy-like case only more intense noise allows for this escape (panel A again) and for initiation of epileptic spikes (panel C).

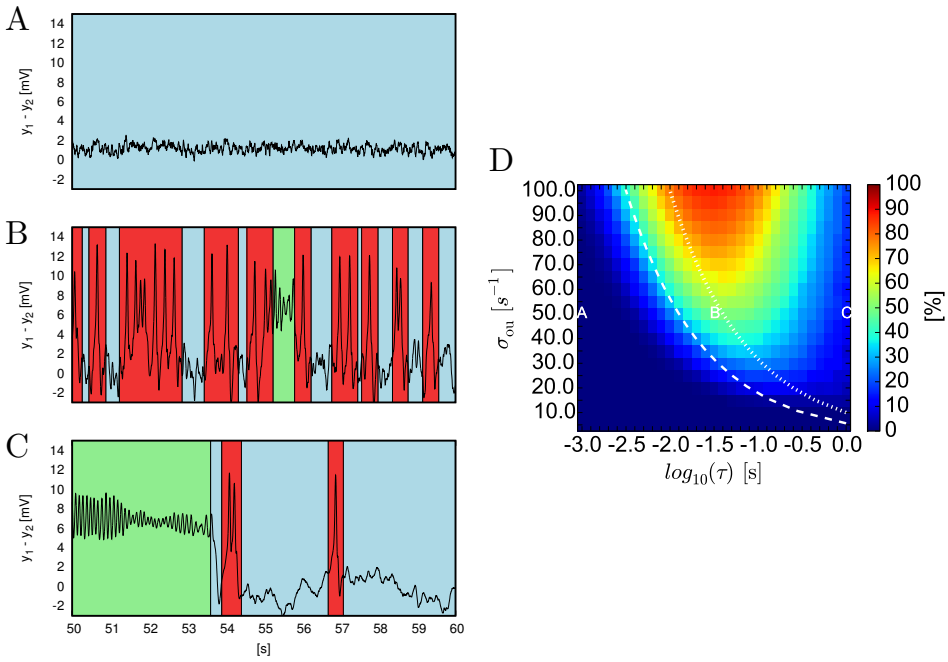

Figure 3.2: Response of the Jansen-Rit model to driving with the Ornstein-Uhlenbeck (OU) noise. The left panels of the figure show example outputs (time courses of $y_1 - y_2$) produced by the model under OU noise driving characterised with correlation time τ equal to 10^{-3} s (panel A), $10^{-1.5}$ s (panel B) and 10^{0} s (panel C). Background colours mark periods of random fluctuations around the node (blue), epileptiform dynamics (red) and alpha activity (green). In all these cases the stationary standard deviation of the noise σ_{ou} was equal to 50 s^{-1} and p was set to 89 s^{-1}. Panel D shows the fraction of time that the system spent in epileptiform dynamics as a function of the noise correlation time τ (varied along the X axis in logarithmic scale) and the noise stationary standard deviation σ_{ou} (varied along the Y axis). Locations of the letters A,B and C mark settings in which time traces shown in panels A,B and C were obtained. The white lines denote points of equal values of noise intensity D: the dashed line marks D=$\sqrt{1000}$ s^{-1} and the dotted one marks D = 100 s^{-1}. In all cases initial conditions corresponded exactly to the node.

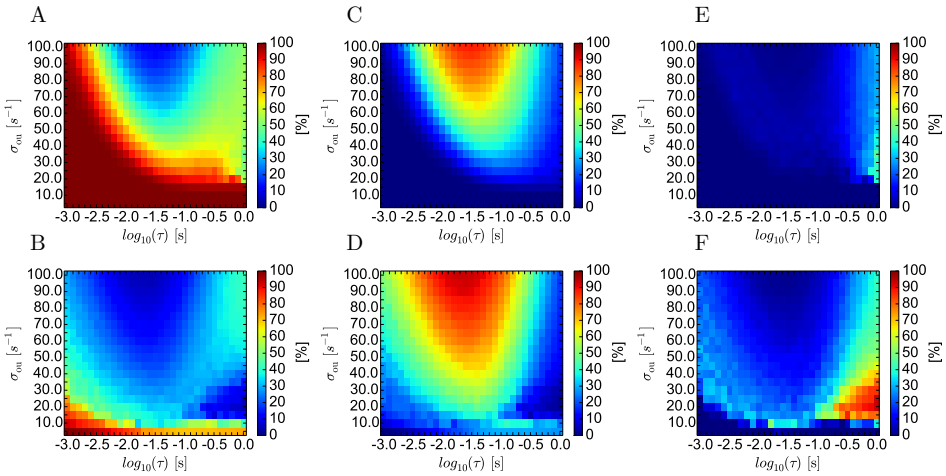

Figure 3.3: Fraction of time spent by the system in each of its attractors with initial conditions set at the node. Noisy oscillations around the node (panels A and B), epileptic-like spiking activity (panels C and D), and alpha oscillations (panels E and F) are shown as a function of autocorrelation time of the driving Ornstein-Uhlenbeck noise τ (varied along X axes) and stationary standard deviation of the noise σ_{ou} (varied along Y axes). The top row corresponds to a healthy-like situation (p=89 s^{-1}) and the bottom row corresponds to unhealthy-like, more excitable situation (p=113 s^{-1}). In all cases initial conditions were set exactly to the node.

Panels C (replotted for clarity from Figure 3.2D) and D show the fraction of the total time spent on epileptic spiking in a healthy-like and unhealthy-like conditions, respectively. These panels indicate that in both conditions the spiking fraction of time depends on the autocorrelation time of the driving noise τ, and that for high amplitudes of the driving noise this dependency has a maximum for $\tau \sim 10^{-1.5}$ s, which moves to the right with decreasing amplitude of the driving. Panels C and D indicate that for τ in a range close to that maximum, epileptic-like spiking activity is triggered more easily, i.e. with lower driving amplitudes than for other τ values. Simulating unhealthy-like state by increasing p (panel D) decreases the minimal value of the driving amplitude that elicits epileptic-like behaviour (compare panels C and D). This effect can be understood on the basis of the bifurcation diagram (Figure 2.4A): an increase of p translates to a smaller distance to the excitability threshold (dotted line between regimes III and IV in Figure 2.4A), thus a lower amplitude of the noise

is sufficient to trespass it. Similarly, the stripe on the bottom of panel D ($\tau \gtrsim 10^{-1.5}$ s, $\sigma_{\text{ou}} \lesssim 10$ s^{-1}) corresponds to noise amplitudes that are high enough to enter regime IV in Figure 2.4 (and provoke spiking), but not high enough to reach regime V, where the spiking attractor ceases to exist.

Figures 3.3C and D show that the ranges of parameter values (noise amplitude and autocorrelation time τ) producing epilepsy in the unhealthy-like case are larger than in the healthy-like case. However, Figure 3.3C also reveals that for sufficiently large amplitudes, healthy-like case may also evince and epileptic response. This result may impose a limit on physiologically feasible driving amplitudes. We assume that for such values of the driving amplitude, only occasional, isolated spikes occur in the healthy-like case (panel C), while the same driving in an unhealthy-like case elicits abundant spikes and periods of continuous epileptic activity (panel D). Occurrence of spikes in the healthy-like case can be interpreted as microseizures that do not develop into epileptic activity. Such microseizures were recorded in healthy subjects (Stead et al., 2010). In Chapter 5 we simulate a network of cortical columns and we discuss how the isolated spikes can be blended in the background activity, so that they are not discernible in the recorded EEG signal. The occurrence of spikes in an unhealthy-like case can be interpreted either as spontaneous epileptic seizures (when the driving stands for the background activity of the brain) or as reflex epilepsy (when the driving stands for external stimuli).

Panels E and F show the fraction of the total time that the system spent on alpha oscillations in the healthy-like and unhealthy-like cases, respectively. These panels indicate that the alpha activity occurs mostly for large values of the noise autocorrelation time τ. All results presented in Figure 3.3 have also been computed for initial conditions set to alpha activity. These results are shown in Figure 3.4, and demonstrate that all the effects discussed above remain for different initial conditions. In particular, low amplitude and low correlation time correspond to noise that is not able to relocate the system from the initial attractor (alpha oscillations).

In order to test the generalisability of these results, we performed equivalent simulations for the healthy-like system under alternative choices of temporal parameters a and b. The bifurcation diagrams and

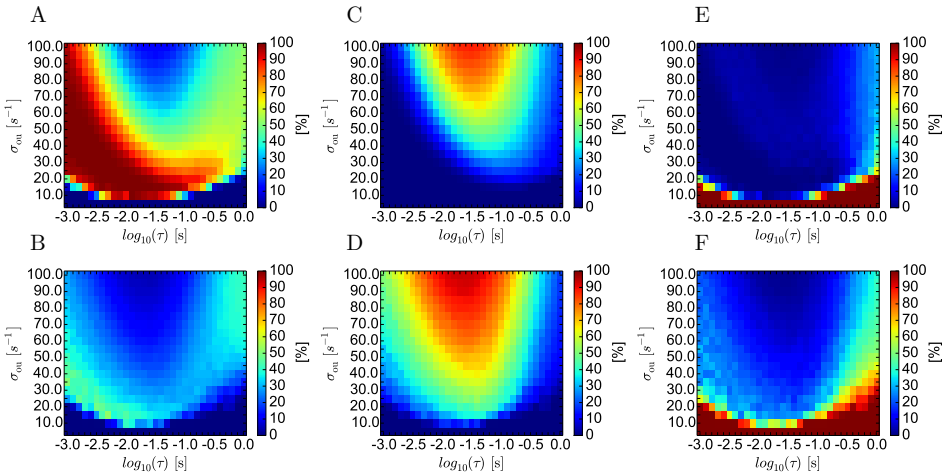

Figure 3.4: Fraction of time spent by the system in each of its attractors for initial conditions set at the focus (top row) and alpha limit cycle (bottom row). Noisy oscillations around the node (panels A and B), epileptic-like spiking activity (panels C and D), and alpha oscillations (panels E and F) are shown as a function of the autocorrelation time of the driving Ornstein-Uhlenbeck noise τ (varied along X axes) and the stationary standard deviation of the noise σ_{ou} (varied along Y axes). The top row corresponds to healthy-like conditions (p=89 s^{-1}) and the bottom row corresponds to unhealthy-like, more excitable conditions (p=113 s^{-1}). In the former case, the initial conditions were set exactly to the focus, and in the latter case, the initial conditions were set exactly to one of the points on the trajectory of alpha oscillations.

corresponding fractions of time spent in the spiky attractor are shown in Figure 3.5. Decreasing a from 100 s^{-1} to 95 s^{-1} (panels A, B) leads to the epileptic-like limit cycle beginning at a value of $I_{\text{ex}} = p$ (panel A) lower than in the standard settings (101.06 s^{-1} and 113.58 s^{-1}, respectively). As a consequence spiking occurs already for lower noise amplitudes (panel B). Moreover, in this case we observe an abundant occurrence of spikes for high τ values (panel B). This is due to the reduction of the bistable regime, i.e. to the fact that for the most part the epileptic limit cycle does not coexist with any other stable solution (again panel A). Similarly, the bistable regime is reduced when b is decreased to 45 s^{-1} (panel C), what again leads to the occurrence of spikes for high τ values (panel D). Moreover, in this case the spiking limit cycle exists for a range of $I_{\text{ex}} = p$ values wider (panel

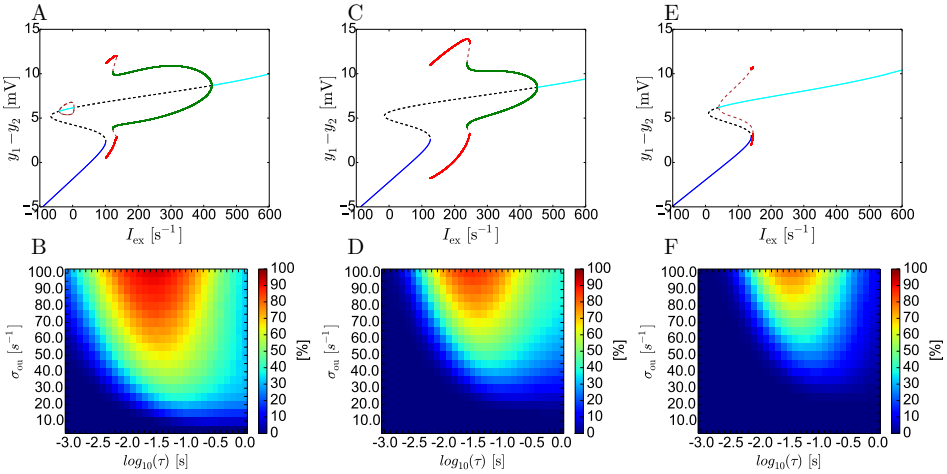

Figure 3.5: Bifurcation diagrams of the Jansen-Rit model (top row) and the corresponding fractions of time spent on epileptic spiking (bottom row) obtained for varied values of parameters a and b: $a = 95$ s^{-1}, $b = 50$ s^{-1} (panels A and B), $a = 100$ s^{-1}, $b = 45$ s^{-1} (panels C and D), and $a = 110$ s^{-1}, $b = 50$ s^{-1} (panel E and F). The X axes in the bifurcation diagrams show external, constant input to the pyramidal population $I_{\text{ex}} = p$. The Y axes in the bifurcation diagrams shows the net postsynaptic potential on this population: $y_1 - y_2$. Continuous (dashed) lines represent stable (unstable) solutions. Cyan and blue lines denote a node and a focus, respectively, and green and red lines indicate stable alpha and epileptiform limit cycles, respectively. Brown dashed line denotes unstable limit cycles. In panels B,D and F the autocorrelation time of the driving Ornstein-Uhlenbeck noise τ varies along the X axis, and the stationary standard deviation of the noise σ_{ou} varies along the Y axis. The results shown in these panels were obtained for $p = 89$ s^{-1} (healthy-like conditions).

C) than for the standard value $b = 50$ s^{-1} used above. The last case corresponds to increased $a = 110$ s^{-1} (panels E, F). Here, the regime of spiking oscillations is reduced and as a consequence epileptic-like activity is generally diminished in the system (panel F). Unlike the previous two cases, here this diminishing effect is also present for high τ values, due to bistability, which prevails between the spiky limit cycle and the focus, although the alpha attractor does not exist at all (again panel E). This leads to reduction of spiking activity for high τ values, similarly as in the default a, b values case. Finally, increasing b from 50 s^{-1} to 52.5 s^{-1} leads to the disappearance of the spiking attractor, therefore we did not study that case.

3.3.2 Relationship to brain rhythms

To relate these findings to underlying frequency components of brain rhythms we studied how OU processes with different correlation times distribute their power in different frequencies. In order to do this we used Equation (3.1) to quantify the fraction of power deposited by the noise (characterised with correlation time, τ) in a given frequency window ($f_{\text{min}}, f_{\text{max}}$). Evaluation of this function for f_{min} and f_{max} set according to boundaries of traditionally defined EEG frequency bands (delta, theta, alpha, beta, gamma) is shown in Figure 3.6. For each frequency band, the location of the maximum of the E function (Equation (3.1)) represents the value of noise correlation time τ that maximises spectral power of the noise within that band. Values of τ corresponding to these maxima are indicated with filled circles on the X axis of Figure 3.6. They demonstrate that the choice of noise correlation time $\tau = 10^{-1.55}$ s maximises spectral power in the theta band (cyan). Furthermore, $\tau = 10^{-1.25}$ s maximises spectral power in the delta band (magenta). Experimental studies suggest that enhancement of rhythms falling to these two bands may precede occurrence of epileptiform activity (Gupta et al., 2011; Sadleir et al., 2011; Sitnikova and Luijtelaar, 2009; Van Luijtelaar et al., 2011). We therefore combine delta and theta bands together and find that spectral power within this delta+theta band is maximised for $\tau = 10^{-1.4}$. As shown in the previous section (Figure 3.2), this value of τ coincides with correlation times of the driving noise for which epileptic spiking is most prevalent. Therefore, we speculate that rhythms around the theta band ($4 - 8$ Hz) or in the wider delta + theta band ($2 - 8$ Hz) are particularly prone to eliciting epileptiform dynamics in the model.

3.3.3 Periodic driving in the deterministic system

In order to test prediction made at the end of last section, we analysed the response of the system to harmonic driving $u(t) = \tilde{A}\sin(\frac{2\pi}{T}t + \phi)$. We systematically varied the amplitude $\tilde{A}$, period T and phase ϕ (with step $\pi/6$) of the harmonic driving, and quantified the dynamics of the model. We also verified how increasing of the system's excitability (thus mimicking the unhealthy-like conditions) affects the results. It has previously been

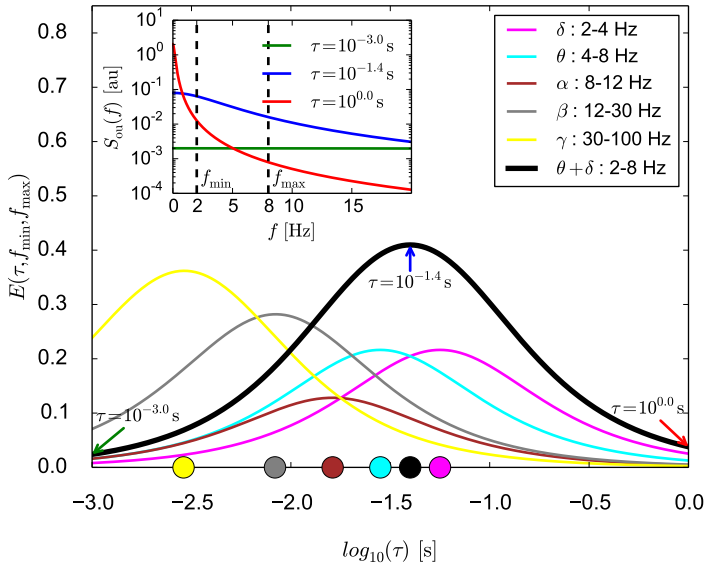

Figure 3.6: Distribution of spectral power in frequency bands of standard brain rhythms and dependence of location of maximum power on noise correlation time τ. Evaluation of the $E(\tau, f_{\text{min}}, f_{\text{max}})$ function (see Equation (3.1)) of an Ornstein-Uhlenbeck noise characterised with correlation time τ within a frequency range $(f_{\text{min}}, f_{\text{max}})$ is plotted for fixed frequency ranges that correspond to distinct brain rhythms: delta (2-4 Hz, magenta), theta (4-8 Hz, cyan), alpha (8-12 Hz, brown), beta (12-30 Hz, grey), gamma (30-100 Hz, yellow) and combined delta+theta ($2-8$ Hz, black). Units on the Y axis express fraction of the spectral power of the noise characterised with τ contained within the $f_{\text{min}}, f_{\text{max}}$ range. Correlation time of the noise τ varies along the X axis. The inset illustrates the meaning of $E(\tau, f_{\text{min}}, f_{\text{max}})$. It shows an example theoretical power spectrum of the Ornstein-Uhlenbeck noise calculated for $\tau = 10^{-3.0}$ s (green), $\tau = 10^{-1.4}$ s (blue) and $\tau = 10^{0}$ s (red). In each case the stationary variance σ^2_{ou} was set to an arbitrary value $1\ s^{-2}$. Dashed vertical lines mark the (f_{min},f_{min})= (2, 8) Hz range, for which the black plot shown in the main panel was derived from Equation (3.1). Green, blue and red arrows on the main plot indicate values of the $E(\tau, f_{\text{min}}, f_{\text{max}})$ function that correspond to these spectra. The value indicated by the blue arrow is highest (in this case it corresponds to the maximum), which follows from the fact that the area below the blue curve, limited by f_{min} and f_{max} in the inset is greater that area set by either red, or green curves. Filled circles on the X axis indicate values of τ corresponding to maxima of $E(\tau, f_{\text{min}}, f_{\text{max}})$: $\tau = 10^{-2.54}$s for gamma, $\tau = 10^{-2.08}$s for beta, $\tau = 10^{-1.79}$s for alpha, $\tau = 10^{-1.55}$s for theta, $\tau = 10^{-1.25}$s for delta, and $\tau = 10^{-1.4}$s for delta + theta.

shown that the Jansen-Rit model displays a variety of dynamics, caused by rhythmic driving, including periodicity, quasi-periodicity and chaos (Malagarriga et al., 2015a; Spiegler et al., 2011). In this case, however, we narrow our interest to whether the activity resembles epileptiform dynamics, alpha oscillations, or fluctuations around the node, and therefore apply the same classification algorithm as in the stochastic system (see Section 3.2). We focus on elucidating values of amplitude, frequency and phase for which healthy or epileptiform dynamics are observed.

Healthy-like paradigm

Figure 3.7 shows the presence of each of these dynamics for the healthy-like settings when the amplitude and period of the driving harmonic signal are varied. Panels A and B of this figure correspond to $\phi = 0$ and panel C corresponds to $\phi = \pi/2$. Alpha oscillations and the node solution are encoded with oblique stripes (top-right to bottom-left for the node and top-left to bottom-right for alpha) and epileptiform dynamics are encoded with grey. Panel A corresponds to initial conditions set exactly to the node, whereas panels B and C correspond to initial conditions exactly at the focus. The diagrams are divided in regimes denoted with lowercase letters. In case of panels A and B the regimes are additionally accentuated with black lines. Figure 3.7A demonstrates that for fast periodic driving ($T \lesssim 10^{-0.8}$ s), the initial node dynamics are preserved and epileptiform rhythms are not elicited even when the driving amplitude is large.

On the other hand, for very slow driving ($T > 10^{0.5}$ s) and sufficiently high amplitude ($\tilde{A} > 50$ s^{-1}), alpha oscillations dominate (regime 'd'). Similarly to the stochastic case, epileptiform dynamics prevail for intermediate periods of the driving and sufficiently large amplitude (regime 'a'). An exemplary time course corresponding to this case is shown in Figure 3.8A$_1$ (and the corresponding driving signal in Figure 3.8A$_2$). For initial conditions set to alpha oscillations, Figure 3.7B demonstrates that neither fast ($T \lesssim 10^{-1.2}$ s) nor slow driving, characterised with an amplitude not exceeding a limit value, causes transitions away from the initial dynamics. Similarly to the node initial conditions, intermediate values of T give rise to epileptiform dynamics (regime 'g'). In all cases, exclusively

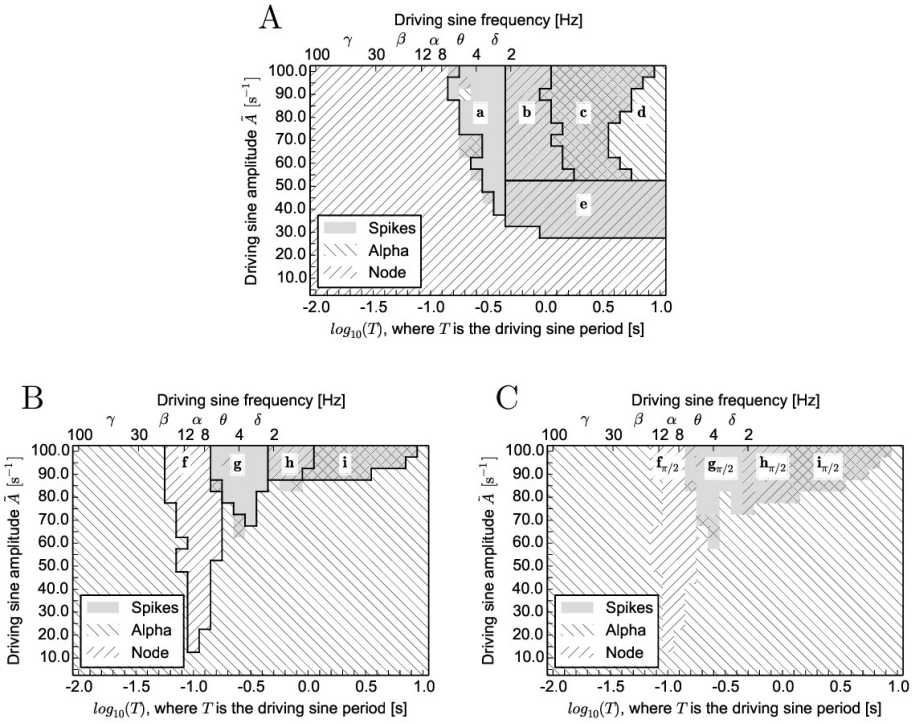

Figure 3.7: Phase diagrams showing the different dynamical regimes resulting from oscillatory driving with varying amplitude, period and phase obtained in the healthy-like paradigm. The response of the Jansen-Rit model under harmonic driving was classified as either a node (oblique stripes from top-right to bottom-left), alpha activity (oblique stripes from top-left to bottom-right), or epileptiform dynamics (grey). This classification was conducted for varying driving amplitude $\tilde{A}$, displayed on Y axes, and driving period T, displayed on X axes in logarithmic (bottom) and linear (top) scales. Ranges and names of typical brain rhythms are denoted on the linear scale. In general, different dynamical regimes might coexist, therefore patterns overlap. Panel A corresponds to initial conditions set exactly to the node, and panels B and C to initial conditions set exactly to alpha oscillations, specifically to the mean value between the maximum and minimum, on the upswing of the limit cycle. In all cases p=89 s^{-1} (healthy-like paradigm); $\phi = 0$ for panels A, B and $\phi = \pi/2$ for panel C. Black lines in panels A, B divide the diagram into distinct regimes, annotated with letters. Homologous regimes in panel C are denoted with the same letters as in panel B, with an additional $\pi/2$ in subscript (implying phase shift). See text for details.

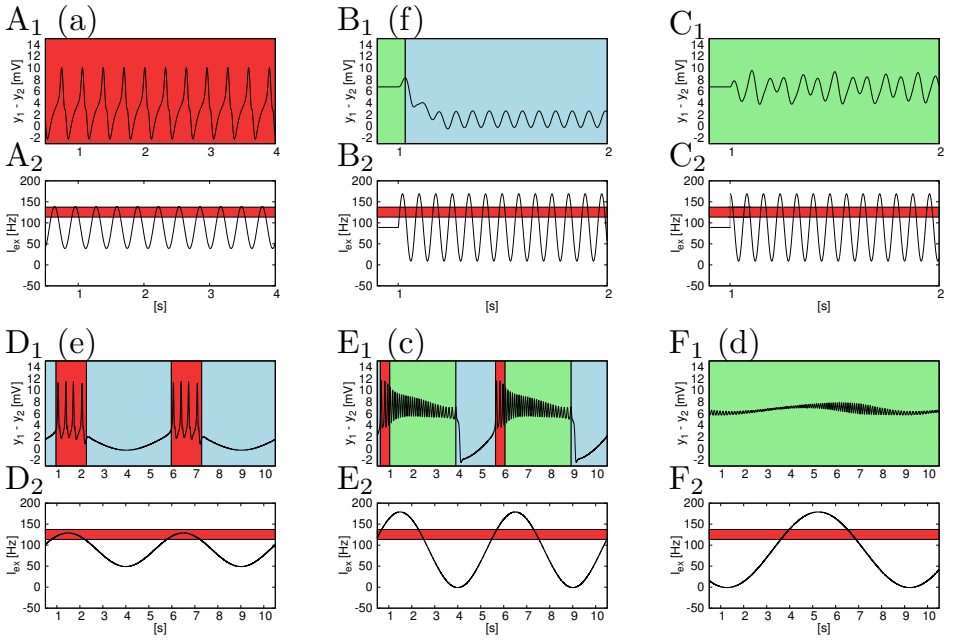

Figure 3.8: Time courses characteristic of various dynamics in the healthy-like paradigm. Panels with '1' in subscript show responses of the model, and panels with '2' in subscript show the corresponding driving signals. In the latter case the red stripes correspond to regime IV (epileptic spiking) from the bifurcation diagram (Figure 2.4). Lowercase letters indicate dynamical regimes from Figure 3.7, to which the presented time courses correspond. In case of panels B and C the onset of the driving signal was delayed by 1 s in order to better visualise the effect. Note that temporal scales on X axes differ. $\phi = 0$ for all panels, apart from panel C, where $\phi = \pi/2$. Panels A: $T = 10^{-0.5}$ s, $\tilde{A} = 50$ s^{-1}. Panels B, C: $T = 10^{-1.1}$ s, $\tilde{A} = 80$ s^{-1}. Panels D: $T = 10^{0.7}$ s, $\tilde{A} = 40$ s^{-1}. Panels E: $T = 10^{0.7}$ s, $\tilde{A} = 90$ s^{-1}. Panels F: $T = 10^{0.9}$ s, $\tilde{A} = 90$ s^{-1}.

epileptiform dynamics occur when driving frequencies correspond to either delta or theta rhythms, as expected from the analysis introduced in the previous section. Moreover, Figure 3.7A indicates that for lowest amplitudes of the driving, slower frequencies are able to elicit spiking than in the case of larger amplitudes. This observation can be linked to the drift of the maximum detected in the stochastic driving case (see again Figures 3.3C, 3.4C).

Driving with frequencies of ~ 10 Hz leads to a resonance effect, causing an escape from alpha oscillations to the node. This effect is present

in regime 'f' and the corresponding time course is shown in Figure 3.8B_1. This resonance results in long-term node dynamics. Panels A and B in Figure 3.7 were obtained for $\phi = 0$. We note that alternative choices of ϕ did not significantly alter the results of Figure 3.7A (only individual cells on the left boundary of regime 'a' varied for some phases). However, we did identify an effect of altering phase in that the resonance regime ('$f_{\pi/2}$' in Figure 3.7C) is slightly narrower when the driving sinusoid is shifted by the phase $\phi = +\frac{\pi}{2}$. An exemplary time course corresponding to $\phi = +\frac{\pi}{2}$ is shown in Figure 3.8C_1, where the driving harmonic signal was turned on[1] at $t = 1$ s. The phase shift chosen impedes the resonance. For other phase shifts this effect of resonance attenuation is not that prominent, or does not occur, but the lower boundaries of regimes 'g', 'h' and 'i' can be extended towards smaller values of $\tilde{A}$ for some non-zero phase shifts (see e.g. regimes '$g_{\pi/2}$', '$h_{\pi/2}$' and '$i_{\pi/2}$' in Figure 3.7C).

These effects, in particular the resonance attenuation, can be understood from the structure of the bifurcation diagram of the model (Grimbert and Faugeras, 2006) shown in Figure 2.4A. The fact that the focus branch, within the range of our interest, is monotonically increasing, means that introducing a slowly varying positive (negative) perturbation to I_{ex} (when the system is set to the focus) results in an increase (decrease) of the focus coordinates along the $y_1 - y_2$ axis. Consequently, a sudden positive (negative) jump of the driving signal followed by its slow decrease (increase), makes the phase point move in direction opposite to the driving. Such is the case of the discontinuous driving presented in Figure 3.7C_2, where a close to antiphase coupling between the driving and the response of the system (Figure 3.7C_1) annihilates the resonance.

The structure of the bifurcation diagram also explains other observed phenomena. For example, transient periods of intensive spiking (bursting), interleaved with periods of quiescence are observed when a slowly varying input periodically crosses the bifurcation and leads the system to

[1] This delayed turning on of the driving signal was applied only in these cases in order to better illustrate the resonance effect. In all cases presented in Figure 3.7 the driving signal was turned on at $t = 0$ s and a long transient was discarded, as explained in Section 3.2

alternate between regimes III and IV. In this case, the system switches between the node (denoted by blue in regime III in Figure 2.4A) and epileptiform spikes (continuous red in regime IV). These dynamics are represented in Figure 3.7 as combined spiking+node activity in regimes 'b', 'h' and '$h_{\pi/2}$'. In this case, although the driving amplitudes can be high enough to enter regime V, alpha oscillations are not observed, because the driving is too fast and the system does not have time to converge to these oscillations. Furthermore, regime 'e' in Figure 3.7A marks driving that is slow enough and characterised by amplitudes high enough to cross the excitability threshold (enter regime IV in Figure 2.4A) - thus eliciting bursts of spikes - but at the same time not large enough to enter regime V of alpha oscillations. Figure 3.8D_1 shows an exemplary bursting time course corresponding to this regime.

Slow driving with sufficiently high amplitude moves the system through all dynamic regimes and overshoots the epileptiform spiking regime to regime V, where alpha oscillations are the only existing dynamics. In this case, the system displays the effect of hysteresis. For the upswing of the driving sinusoid all three dynamical regimes are displayed: from the node in regimes II and III (blue in Figure 2.4A), through epileptiform dynamics in regime IV (continuous red in Figure 2.4A), to alpha oscillations in regime V (green in Figure 2.4A). During the downswing phase of the driving, however, the system remains in quasistatic conditions in the alpha attractor, so in the bistable regimes IV and III it exhibits alpha oscillations (green in Figure 2.4A) and in the bistable regime II it remains on the focus (cyan in Figure 2.4A). This hysteresis loop is closed when driving with a sufficiently high amplitude moves the system to, or sufficiently close, regime I, where the system relaxes to the node (blue in Figure 2.4A). This effect occurs in regimes 'c', 'i' and '$i_{\pi/2}$' combining all three types of dynamics. Figure 3.8E_1 shows an exemplary time course corresponding to regime 'c'.

For smaller driving frequencies the system remains in alpha oscillations and does not revert to the node (regime 'd'). A similar effect is observed for initial conditions set to the focus (Figures 3.7B,C). These effects explain

why stochastic driving with power concentrated in low frequencies promotes alpha oscillations of the system (as described in section 3.3.1). Figure 3.8F_1 shows how slow driving, characterised with a sufficiently high amplitude, pushes the system deeper into the alpha limit cycle, thereby increasing the amplitude of alpha oscillations. We note that these regimes are also physiologically relevant, since slow (0.25 Hz) driving has been shown to lead to an increased power in the alpha band (we elaborate on this case in Chapter 5) and bursting following a slow quasi-harmonic pattern may occur in the early ictal phase of seizures (Alarcon et al., 1995).

Unhealthy-like paradigm

Results obtained in unhealthy-like conditions are shown in Figure 3.9. Dynamics encoding is same as in the healthy-like case (Figure 3.7). Figure 3.9A corresponds to initial conditions set exactly to the node. Since health impairment is implemented here as an increase of p to $113\ \mathrm{s}^{-1}$, lower driving amplitudes (comparing to the healthy-like case where $p = 89\ \mathrm{s}^{-1}$) are needed to reach regimes IV and V in the bifurcation diagram (Figure 2.4A). Therefore, patterns corresponding to non-node dynamics are shifted downwards (towards lower amplitudes) for unhealthy-like conditions (Figure 3.9A) in comparison to healthy-like conditions (Figure 3.7A).

As a result, these two phase diagrams share similarities. We therefore mark some regimes in Figure 3.9A with lowercase letters corresponding to homologous regimes in Figure 3.7A. Here we add an additional star symbol signifying hyper-excitability. Indeed, most of the effects discussed for initial conditions set at the node in the healthy-like settings are also present in the unhealthy-like case. Those effects are: pure spiking (regime 'a*'), spiking interleaved with quiescence (regimes 'b*' and 'e*'), hysteresis (regime 'c*') and quasistatic dynamics (regime 'd*'). Regimes of the phase diagram corresponding to these effects have changed sizes in comparison to healthy-like conditions. This can also be explained by the shift of the average working point of the system, e.g. smaller driving amplitudes are needed to reach regime V, where only alpha oscillations are permitted. As a consequence, they occupy more space on the phase diagram (regime 'd*'), and conversely the regime where all three dynamics mix (regime 'c*') is diminished. Since the boundaries between regimes are more ragged in

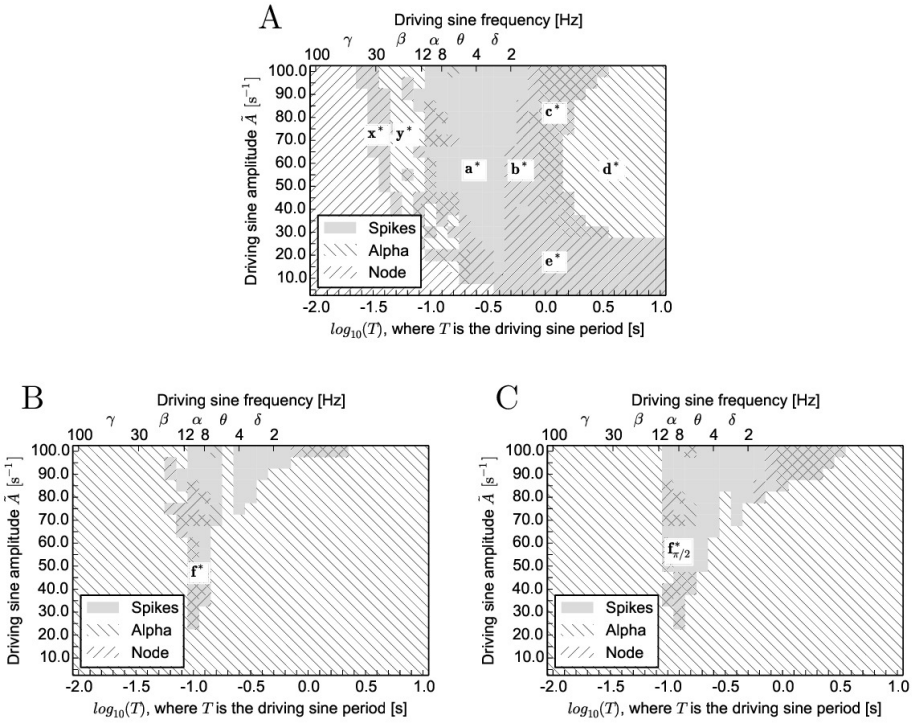

Figure 3.9: Phase diagrams showing the different dynamical regimes resulting from oscillatory driving with varying amplitude, period and phase obtained in the unhealthy-like paradigm. The response of the Jansen-Rit model under harmonic driving was classified as either a node (oblique stripes from top-right to bottom-left), alpha activity (oblique stripes from top-left to bottom-right), or epileptiform dynamics (grey). This classification was conducted for varying driving amplitude $\tilde{A}$, displayed on Y axes, and driving period T, displayed on X axes in logarithmic (bottom) and linear (top) scales. Ranges and names of typical brain rhythms are denoted on the linear scale. In general, different dynamical regimes might coexist, therefore patterns overlap. Panel A corresponds to initial conditions set exactly to the node, and panels B and C to initial conditions set exactly to alpha oscillations, specifically to the mean value between the maximum and minimum, on the upswing of the limit cycle. In all cases p=113 s^{-1} (unhealthy-like paradigm); $\phi = 0$ for panels A, B and $\phi = \pi/2$ for panel C. Regimes homologous to those from the healthy-like paradigm (Figure 3.7) are denoted with same letters as in that case, with an additional star meaning hyper-excitability. In panel C we use an additional '$\pi/2$' in subscript, implying phase shift by $\phi = \pi/2$. See text for details.

this case, we do not accentuate them with lines. Finally, we note that in this case, phase shifts of the driving signal introduced only variations of individual cells, not the general structure of the phase diagram.

On the other hand, some phenomena are present only in the unhealthy-like settings. For example, here epileptic spiking occurs already for faster driving rhythms (regime 'x*') which were not able to excite the healthy-like system, regardless of the value of the driving amplitude. We interpret it as one of the effects of operating close to a 'catastrophic transition' (see Section 1.4.4). An exemplary time course corresponding to regime 'x*' is shown in Figure 3.10A_1 (and the corresponding driving signal in Figure 3.10A_2). This time course shows two processes occurring in separate timescales: fast response to the driving and slow spiking. Similarly, alpha oscillations are already recognised in the unhealthy-like conditions for driving faster than in the healthy-like conditions (regime 'y*'). A time course corresponding to this behaviour is demonstrated in Figure 3.10B_1. It shows that the natural oscillations of the system get entrained by the driving signal, and therefore the evinced frequency exceeds the alpha rhythm[2] (~ 10 Hz). Also the epileptic-like oscillations can outpace their highest natural frequency due to the entrainment effect. This effect occurs in regime 'a*', for sufficiently high amplitude and the driving period $T = 10^{-0.7}$ s, which corresponds to frequency slightly above 5 Hz, whereas highest natural frequency of the epileptic-like limit cycle is ~ 4.65 Hz. This entrainment is illustrated in Figures 3.10$C_{1,2}$.

Figures 3.9B,C correspond to initial conditions set exactly to alpha oscillations, specifically to the mean between the maximum and the minimum, on the upswing of the limit cycle. Figure 3.9B shows that the previously introduced resonance effect occurring for driving frequencies around ~ 10 Hz is present also in the unhealthy-like conditions (regime f*). Nevertheless, in this case, the escape from the alpha attractor may be followed by all three dynamics types (time course in Figure 3.10D_1) or even exclusively by epileptic spiking (time course in Figure 3.10E_1). From EEG/MEG recordings it is known that alpha oscillations are particularly typical to the

[2]Note almost sixteen oscillations within one presented second of time course in Figure 3.10B. $16 \simeq 10^{-1.2}$, which is the driving frequency (in Hz).

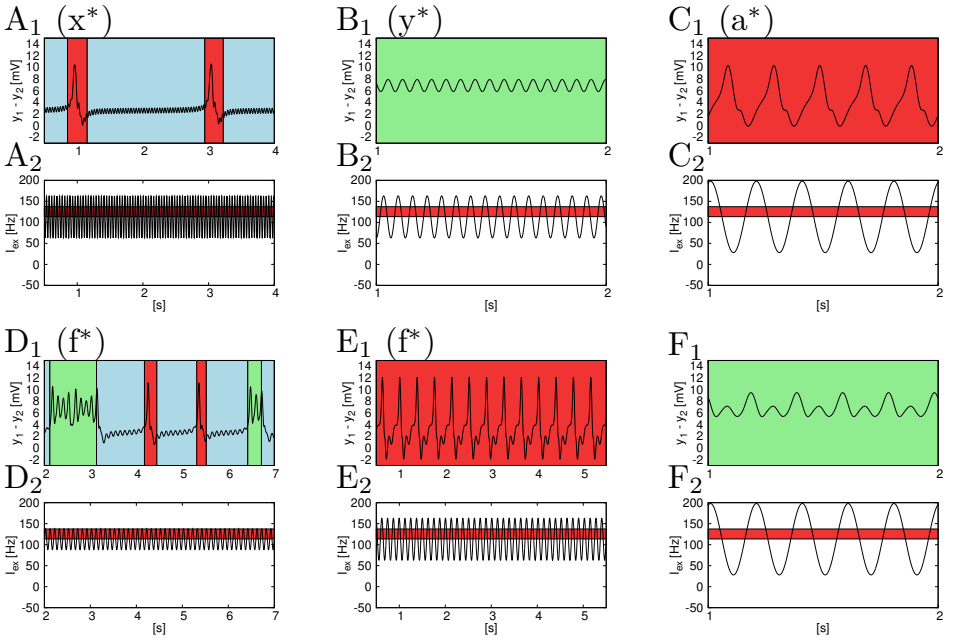

Figure 3.10: Time courses characteristic to various dynamics in the unhealthy-like paradigm. Panels with '1' in subscript show responses of the model, and panels with '2' in subscript show the corresponding driving signals. In the latter case the red stripes correspond to regime IV (epileptic spiking) from the bifurcation diagram. Lower case letters indicate dynamical regimes from Figure 3.9, to which the presented time courses correspond. Note that temporal scales on X axes differ. Panels in the top row correspond to initial conditions set exactly to the node. Panels in the bottom row correspond to initial conditions set to alpha oscillations, specifically to the mean value between the maximum and minimum, on the upswing of the limit cycle. Panels A: $T = 10^{-1.4}$ s, $\tilde{A} = 50$ s^{-1}. Panels B: $T = 10^{-1.2}$ s, $\tilde{A} = 50$ s^{-1}. Panels C: $T = 10^{-0.7}$ s, $\tilde{A} = 85$ s^{-1}. Panels D: $T = 10^{-0.9}$ s, $\tilde{A} = 25$ s^{-1}. Panels E: $T = 10^{-0.9}$ s, $\tilde{A} = 50$ s^{-1}. Panels F: $T = 10^{-0.7}$ s, $\tilde{A} = 85$ s^{-1}.

visual cortex, we therefore speculate that this resonance effect could be related to photosensitive epilepsy (Kasteleijn-Nolst Trenite, 2006) - induction of epileptic seizures by visual stimulation. We also note that when the alpha rhythm is added to the joint delta+theta wide frequency band considered in the spectral analysis introduced in Section 3.3.2, then the expected noise correlation time τ for which spiking is maximised is $10^{-1.5}$ s, thus consistent with the stochastic results presented in Section 3.3.1.

Finally, a stripe of pure alpha oscillations is found in Figure 3.9B for driving characterised with $T = 10^{-0.7}$ s $\simeq$ 5 Hz, which is the first subharmonic of the natural frequency of the system. As a result, due to the 1:2 phase coupling between the driving and the response (see time courses in Figures 3.10$F_{1,2}$), no escape from the alpha attractor occurs. In healthy-like conditions this 'subharmonic coupling' was also present for the same driving frequency, but only for a limited range of amplitudes (see again Figure 3.7B). Here it is observed for all amplitudes when $\phi \in \langle \pi, 2\pi \rangle$ and is still present, albeit diminished, for other ϕ values. A phase diagram corresponding to $\phi = \pi/2$ and showing attenuation of this effect for larger amplitudes is shown in Figure 3.9C. This figure also shows that the width of the resonance peak varies depending on ϕ and excitability of the system (compare regimes 'f', '$f_{\pi/2}$' in Figures 3.7B,C and 'f*', '$f^*_{\pi/2}$' in Figure 3.9B).

3.4 Discussion

In this chapter we investigated the effect of rhythmic driving and coloured noise on the generation of epileptiform dynamics in a single module of the Jansen-Rit neural mass model. We found that epileptiform dynamics are more readily elicited by noise with certain temporal correlations. By exploring the composition of Ornstein-Uhlenbeck noise in different frequency bands and driving of the model with sinusoidal rhythms, we discovered that simulated epileptiform discharges are more easily generated by rhythms in the delta and theta frequency bands. Moreover, we studied a hyper-excitable variation of the model, thereby mimicking unhealthy-like conditions wherein epileptic activity can be elicited more easily. In such conditions a wider range of driving frequencies, in particular alpha frequency, was found to generate epileptiform dynamics in the model. We

suggest that the local microcircuit interactions embodied by the model can give rise to emergent dynamics that leave it prone to generating epileptiform rhythms when bombarded by afferent spiking with particular rhythmic properties.

Experimental and clinical findings lend support to this hypothesis. Interictal focal slow activity in the delta or delta-theta bands has been shown to be present in a majority of invasive recordings from people with temporal lobe epilepsy, and it lateralises with regions of seizure onset (Valentín et al., 2014), in particular in neocortical temporal lobe epilepsy (Tao et al., 2011). Thus slow rhythms are associated with epileptic brain networks (Tao et al., 2011). Our modelling results lead us to hypothesise that such rhythms could also be the cause of onset of seizures in such networks. Indeed, slow rhythms are also observed in invasive recordings at seizure onset in focal epilepsies (Jiménez-Jiménez et al., 2015; Lee et al., 2000). Slow rhythms have also been observed in association with generalised epilepsies in both clinical and experimental data. Sitnikova and Luijtelaar (2009) observed an increase of delta activity prior to onset of spike-wave-discharges in the WAG/Rij rodent model and Van Luijtelaar et al. (2011) reported an increase of delta and theta rhythms in the preictal phase of brain activity in the same animal model. The frequency of the alpha rhythm has also been shown to be lower in people with epilepsy compared to control subjects (Larsson and Kostov, 2005).

Moreover, we found that in the hyper-excitable settings, driving with frequency ~ 10 Hz also leads to an epileptic response of the system. Depending on the choice of initial conditions, this effect can be related either to closeness to a 'catastrophic transition' or to resonance with a natural frequency of the system, which corresponds to the alpha rhythm. Since this rhythm is particularly associated with the visual cortex, we speculate that the observed resonance might manifest especially easily for visual stimulation. Indeed, such case was observed on mass scale in 1997 in Japan, when a flickering scene in a popular cartoon 'Pokèmon' led to nearly 700 children being brought to hospitals with a suspicion of epileptic seizures (Takahashi and Tsukahara, 1998). The flickering frequency was

determined to be $\sim$ 12 Hz, therefore within (a higher range of) the alpha band.

Our results indicate that periodic driving with frequencies coinciding with this band may lead to an escape from the alpha attractor[3]. This escape in the 'unhealthy-like', hyper-excitable system is followed by epileptic activity. Such resonance effect could also inflict a transition from the focus to the epileptic limit cycle in the aforementioned model of epilepsy of Breakspear et al. (2006). In that case, however, the frequency of the driving should correspond to the frequency of epileptic activity, whereas our results show that the driving might coincide with a frequency of a healthy attractor, which is escaped due to the resonance. Subsequently, epileptic activity of an arbitrary frequency may follow. This is possible due to the coexistence of limit cycles, absent in the approach of Breakspear et al. (2006) but highly likely to be universal in the brain (see Section 1.4). Finally, we showed that the resonance effect depends on the phase of the driving, which is consistent with computational studies of stimulation aimed at seizure abatement (Taylor et al., 2014). Nevertheless, we would not expect this phase-dependent resonance quenching to be detectable in experiments with visual stimulation, because of lack of globally coherent alpha oscillations.

Our results suggest a potential mechanism of propagation of abnormal dynamics in large-scale brain networks: a local network generating abnormal rhythms could induce the propagation of this activity in connected brain regions. The epileptic brain is increasingly being thought of and studied in terms of networks (Berg et al., 2010; Goodfellow et al., 2011; Naze et al., 2015; Petkov et al., 2014; Richardson, 2012; Sanz-Leon et al., 2015). Understanding seizure generation in networks is a difficult task since seizures represent emergent dynamical transitions due to both the underlying connectivity structure of the network and the intrinsic dynamics of individual nodes (Goodfellow et al., 2016; Terry et al., 2012). To simplify this situation, in our study we separated the intrinsic node and network effects, considering the effects of temporally structured afferent

[3]The alpha rhythm is modelled as narrow-band $\sim$ 10 Hz oscillations in the Jansen-Rit model, but in the brain it is found within the $8 - 12$ Hz range (see Section 1.4.1), thus the resonance effect could occur for a wider frequency band than in our simulation.

activity to a node. Our observations that certain rhythms preferably generate epileptiform dynamics arise from an interplay between the presence of different invariant sets (Figure 2.4A) and the timescale of fluctuations in I_{ex}. For example, on the node branch, close to the epileptiform limit cycle, slow variations in afferents can allow the epileptiform limit-cycle to appear and, if the amplitude of these fluctuations lies within a certain interval, the system can also converge to this attractor, therefore displaying epileptiform rhythms. By uncovering these phenomena in the deterministic system, we are able to better understand the ways in which stochastic fluctuations with power in certain frequencies could cause transitions in dynamics and ultimately lead to epileptiform activity.

In our study we used a set of parameters for the Jansen-Rit model that give rise to dynamics relevant to the study of healthy brain function such as the alpha rhythm as well as pathological dynamics (Jansen and Rit, 1995; Jansen et al., 1993; Wendling et al., 2000). Previous studies have used bifurcation analysis to demonstrate how the arrangement of invariant sets changes in parameter space (Spiegler et al., 2010; Touboul et al., 2011), and have studied the response of neural mass models to driving by rhythmic pulses (Spiegler et al., 2011) and white noise (Wendling et al., 2000). Our work advances on these previous studies by quantifying the effect that temporally correlated noise and rhythmic input have in terms of the generation of epileptiform spiking, which led us to hypothesise a role for low-frequency brain rhythms in the generation of seizures. We therefore demonstrated the importance of non-white noise in the context of bifurcations of neural mass models to uncover the mechanisms underlying brain (dys-)function. The chosen parameter set enabled us to study the effect that different afferent dynamics have on the generation of these dynamics, and we further demonstrated that variations in the arrangement of attractors did not affect the optimal timescale for induction of epileptiform dynamics. Bistability and a limited size of the epileptic regime in the bifurcation structure were shown to be crucial for attenuation of epileptic activity for very slow driving.

3.5 Summary and outlook

In this chapter we studied the response of a single Jansen-Rit module to stochastic and harmonic driving. In the former case, we showed the importance of temporal correlation of the driving noise. In the latter case, we demonstrated a spectrum of phenomena such as hysteresis, entrainment, (subharmonic) phase coupling, and resonance. Furthermore, we linked the two cases and showed how the deterministic driving, along with the bifurcation structure of the system, explains results obtained in the stochastic setup. Finally, we related these phenomena to clinical observations of epilepsy. Since the driving frequency which is most likely to elicit epileptic activity partially coincides with the natural frequency of spiking, future work could study spreading of epileptic activity on networks, where (pathological) activity generated by one node could spread to interconnected nodes. In Chapter 5 we show power spectra produced under the driving employed here, and in the next chapter we extend the model to two reciprocally coupled and stochastically driven modules, and we study their interactions. In particular, we focus on phenomena arising from an uncommon property of the Jansen-Rit model: coexistence of two limit cycles.

CHAPTER 4

COLLECTIVE EXCITABILITY AND NOISE

4.1 INTRODUCTION

Computational models in neuroscience rely on parameters derived from anatomy and physiology. As discussed in the 'Introduction' and 'Modelling mesoscopic brain dynamics' chapters, these models often discretize spatially extended neuronal tissue and introduce a 'coupling strength' that refers to the magnitude of interaction between nodes of a discretised mesh or network. In practical terms, this quantity is most often a multiplier of the output activity of an upstream node, before this output is fed to a downstream node. It is not clear, however, how to derive this coupling strength experimentally. For this reason, in computational models the coupling strength is often used as a scan parameter (Deco et al., 2013). Such variations of the coupling strength, with other parameters of an excitatory network kept constant, entail changes of the effective input received by the nodes. In such conditions it becomes unclear to what extent the changes of dynamical properties of the system emerge from inter-node interactions and to what extent they simply follow from the intra-node dynamics driven by an increased effective net input.

For example, Huang et al. (2011) find, in a system of two interconnected Jansen-Rit modules, that an increase of coupling strength at some point leads to vanishing of equilibria. Nevertheless, as discussed in Section 2.3.3, a similar effect occurs in case of a single Jansen-Rit module, i.e. in the absence of inter-module interaction, where an increase of a constant input leads to a Hopf and a saddle-node on invariant circle (SNIC) bifurcations (see Figure 2.4A), which result in the disappearance of the associated stable fixed points. We studied the behaviour of the Jansen-Rit model around these bifurcations in the previous chapter, where we saw that increasing the constant input p delivered to the model, as well as increasing the amplitude (in a certain range) of the driving signal, facilitates occurrence of

epileptic-like activity. It is a rather self-evident observation, confirmed also in studies of more than two modules (Goodfellow et al., 2016). Also in the context of epilepsy, Goodfellow et al. (2011) study the spreading of transient epileptic-like excitations on a lattice of interconnected Jansen-Rit modules (with additional slow inhibition). Those authors also examine the role of coupling between nodes of the network, observing that mixing of two oscillatory modes (see Section 2.3.3) gives rise to transient excitations. The authors do not, however, quantify the durations of these excitations, nor do they consider noise, which is ubiquitous in the nervous system (see Section 1.4.2).

Here we focus on the temporal properties of such transient excitations in a system of two coupled Jansen-Rit modules subject to white noise. These transients arise due to an aforementioned non-trivial feature of the Jansen-Rit model, namely the coexistence of two limit cycles (see Section 2.3.3), one of which displays quasiharmonic oscillations of frequency ~ 10 Hz, resembling alpha activity (see time course in Figure 2.4B), and the second of which displays spiky epileptic-like behaviour (see time course in Figure 2.4C). The interplay between these two dynamics is physiologically relevant: in the epileptic brain the spreading of seizures may be gradual, therefore both types of oscillatory modes may coexist and interact. The transient episodes do not occur due to slow changes of one of the system's parameters that would lead to hovering over the bifurcation (Baier et al., 2012; Lopes da Silva et al., 2003), but rather due to complex interactions between the two oscillatory modes. These interactions, in turn, are modulated by the coupling strength between the modules.

In this chapter we study the dynamical properties of these excitation episodes, by systematically varying the coupling strength between two reciprocally connected Jansen-Rit modules. In order to initiate excitations we subject the two modules to Gaussian white noise. In the previous chapter we emphasised the importance of temporal correlation of the driving noise, although we did it by means of the system that was previously thoroughly studied in the white noise setup (Aburn et al., 2012; Garnier et al., 2015; Jansen and Rit, 1995; Touboul et al., 2011). Here we introduce a novel setup, characterised by a compensated input, and we conduct the study

with a simplified, temporally uncorrelated driving. This methodology allows to ascertain those effects arising solely due to the introduced novelty.

In the presented approach, regardless of the value of the coupling strength, the system in the steady state is situated always equally far from the excitability threshold (the SNIC bifurcation). As we exclude a simple crossing through the bifurcation due to the increased net input, we can focus on effects arising from interconnectedness of two nodes of the large-scale cortical network. This interconnectedness gives rises to an excitable behaviour, and therefore we term it 'collective excitability'. We show a non-monotonous trend of the initiation rate of the excitation episodes as a function of the coupling strength, and we observe coupling-mediated synchronous terminations of these episodes, which bear resemblance to clinically observed epileptic activity (Schindler et al., 2007).

4.2 Methods

The system studied in this chapter is governed by Equations (2.10)-(2.12) with $N = 2$, $u(t) = 0$ and stochastic processes $\xi^i(t)$ given by independent realisations of Gaussian white noise with intensity D, i.e.: $\xi^i(t) = \sqrt{2D}\xi^i_w(t)$, where $\langle \xi^i_w(t)\xi^i_w(t')\rangle = \delta(t-t')$ and $\langle \xi^i_w(t)\xi^j_w(t')\rangle = 0$ for $i \neq j$. The parameter p is set in such a way that in the absence of noise and coupling, the system converges to the node (blue in regime III in Figure 2.4A). Increase of the coupling strength K leads to an increase of the input to each column, I^i_{ex}, given with Equation (2.13), what may lead to crossing a bifurcation point (entering regime IV in Figure 2.4A). In order to avoid it, we decrease the constant component p from Equation (2.13) in a way that keeps the system in the steady state equally far ($\Delta p = 1$ s^{-1}) from the excitability threshold (the SNIC bifurcation), regardless of the value of K. For a single Jansen-Rit module, the location of the excitability threshold could be read from the bifurcation diagram (Figure 2.4A). Nevertheless, here we deal with a system of two interconnected columns, and therefore, we need to perform a bifurcation analysis for the system with $N = 2$. This analysis is presented in the following section.

4.2.1 Codimension-1 bifurcation analysis

In order to localise the excitability threshold in the system governed by Equations (2.10)-(2.12) with $N = 2$, we performed a bifurcation analysis (Ermentrout, 2002) of the deterministic part of this system. We focused our attention on the location of the SNIC bifurcation, above which, in an uncoupled system, spans a regime of bistability between the two limit cycles (see Section 2.3.3). Figure 4.1 shows this SNIC bifurcation for three values of the coupling strength K along with the associated stable (continuous line) and unstable (dashed line) branches. In the numerical simulations presented in this chapter, for each value of K we chose p in such a way that the system in the absence of noise operates at a distance $\Delta p = 1$ s^{-1} below the excitability threshold (the SNIC bifurcation). For example: for K=0, the SNIC bifurcation occurs at $p_{\text{snic}} = 113.58$ s^{-1}, therefore we choose the constant part p of the input I_{ex} to be equal to $p = 112.58$ s^{-1}, whereas for $K = 10$, $p_{\text{snic}} = 107.3$ s^{-1}, thus we set p to 106.3 s^{-1}. Since the location of this SNIC bifurcation marks the onset of epileptic activity, it is of high importance in theoretical studies on epilepsy (see Section 1.4.7). Figures 4.1A-C demonstrate that for growing K, p_{snic} decreases. In order to find the exact course of this $K - p_{\text{snic}}$ dependency, in the following section we perform a codimension-2 bifurcation analysis. Moreover, we introduce an alternative method (from now on referred to as the 'derivative method') of tracking the location of a saddle-node bifurcation in a system of coupled modules.

4.2.2 Codimension-2 bifurcation analysis and the derivative method

Here we introduce a simple method of tracking a loss of stability due to a saddle-node (SN) bifurcation in a compound system. We also validate this method with a continuation analysis performed with XPPAUT (Ermentrout, 2002). Such a loss of stability might be of special importance, e.g. when due to the saddle node on invariant circle (SNIC) bifurcation it marks a 'catastrophic' (see Section 1.4.4) onset of an epileptic-like limit cycle. This is the case for the Jansen-Rit model utilised in this Thesis (see Section 2.3.3). The derivative method presented in what follows was developed and tested on that model.

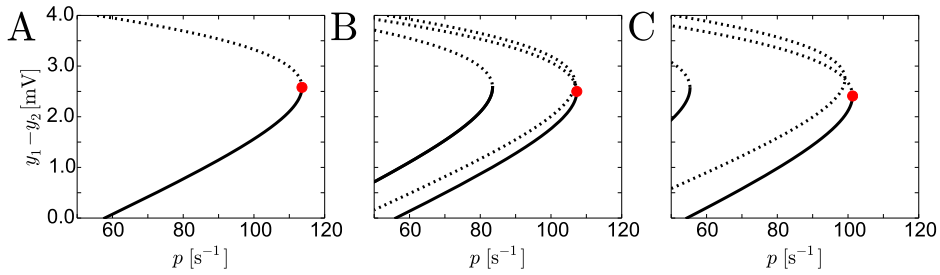

Figure 4.1: Bifurcation structure of the model around the SNIC bifurcation for the system of two coupled Jansen-Rit modules. The three panels A,B and C demonstrate invariant sets for the coupling strength K equal 0, 10 and 20, respectively. Continuous (dashed) lines mean stable (unstable) equilibria. The red dot marks location of the SNIC bifurcation. Panel A, showing uncoupled case, corresponds to a fragment of the bifurcation diagram presented in Figure 2.4A.

The solid line in Figure 4.1A shows a stable solution (a node) for two uncoupled Jansen-Rit columns exposed to external constant driving p. This system is described by the deterministic part of Equations (2.10)-(2.12) with $K = 0$, and has properties of one single column. When coupling between the two columns increases, however, the SNIC bifurcation moves to the left (compare the locations of the red dot in panels A-C in Figure 4.1). If p is kept constant within the stable branch (continuous line in Figure 4.1A), the distance between the working point of the system and the SNIC decreases as the coupling strength increases and the output of the system (read from the Y axis of Figure 4.1) increases. This output, however, entails a further increase of the input fed to the interconnected column, which again provokes an increase of its output, and a similar influence is exerted by the second column upon the first. This transient process continues updating I^i_{ex}. Existence of the steady state (understood as the stable node below the SNIC bifurcation) requires that I^i_{ex} is finite, thus updates to I^i_{ex} must decrease in time. In order to express this condition formally, let us define a coupling function $f_{\text{c}}(I_{\text{ex}})$, which multiplied by K converts the input I^i_{ex} delivered to column i into this column's output. For the steady state of a deterministic system with $N = 2$ and $u(t) = 0$, this coupling functions is given by (compare with the last term of Equation (2.13)):

$$f_{\text{c}}(I_{\text{ex}}) = \text{Sigm}[y_1^*(I_{\text{ex}}) - y_2^*(I_{\text{ex}})], \tag{4.1}$$

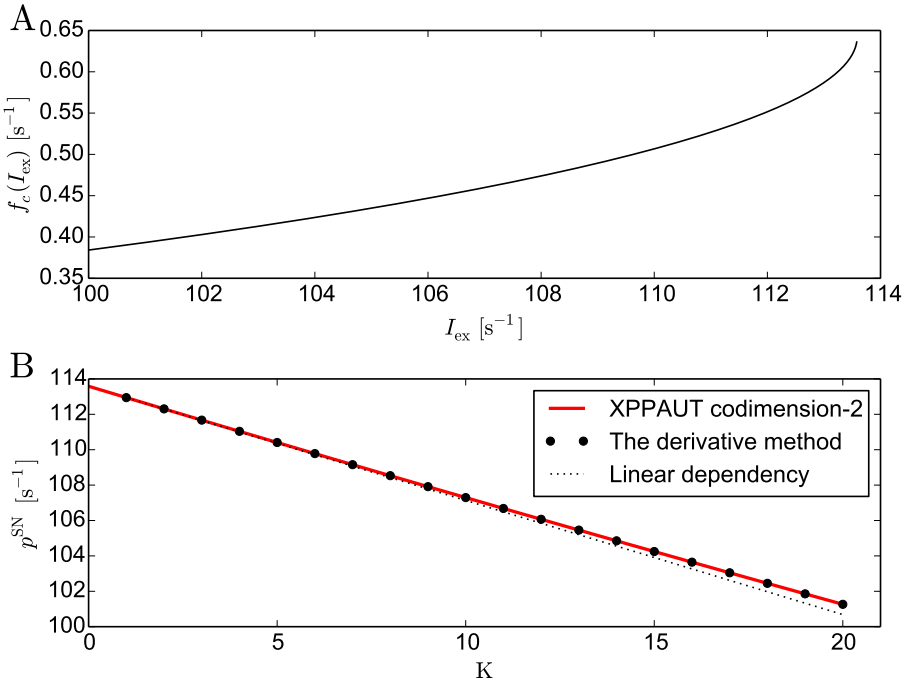

Figure 4.2: Panel A: coupling function characterising the interaction between two columns. Panel B: location of the saddle-node bifurcation in the system of two connected Jansen-Rit modules computed with XPPAUT (red line) and with the 'derivative method'. The approximated linear dependency is marked by the dotted line.

where $y^*_{1,2}(I_{\text{ex}})$ denotes the value of the $y_{1,2}$ state variables in the steady state corresponding to I_{ex} and to the stable branch associated with the SN bifurcation[1]. For analytical implicit expressions for $y^*_{1,2}(I_{\text{ex}})$ see e.g. Garnier et al. (2015) and Huang et al. (2011). The $f_{\text{c}}(I_{\text{ex}})$ function is shown in Figure 4.2A. By means of this function, we can rewrite Equation (2.13) and express I_{ex} in the steady state as a sum of external constant driving p and the coupling term:

$$I_{\text{ex}} = p + K f_{\text{c}}(I_{\text{ex}}) \tag{4.2}$$

[1]Due to the symmetry of the system, the introduced dependencies are valid for both columns. We therefore dropped for simplicity the index i from the subscripts of the I_{ex} and y state variables. Furthermore, since the described method does not require that the tracked bifurcation is a global SNIC, but in general it can be a saddle-node as well, we from now on will refer to this bifurcation with the 'SN' abbreviation.

A necessary condition for stability of the steady state of two coupled modules can be then written as:

$$K \left. \frac{df_c(x)}{dx} \right|_{x=I_{ex}} \leq 1 \tag{4.3}$$

If this condition is not fulfilled, a perturbation $\Delta I_{ex} > 0$ of the external driving entails an increase of the coupling term exceeding ΔI_{ex}, which for monotonically increasing f_c leads to divergence of I_{ex}. Thus, for monotonically increasing and differentiable f_c, and for $K > 0$ we expect the disappearance of the stable solution (SN bifurcation) at I_{ex}^{SN} such that:

$$\left. \frac{df_c(x)}{dx} \right|_{x=I_{ex}^{SN}} = \frac{1}{K} \tag{4.4}$$

from where Equation (4.2) allows to find the corresponding external driving p^{SN} (X coordinate of the bifurcation points, marked with red dots in Figure 4.1). Therefore, it is enough to know the coupling function f_c and its derivative in order to quickly find the location of the SN bifurcation for an arbitrary K. Finding this location allows us to set the constant driving of the system p to $p^{SN} - \Delta p$.

Figure 4.2B shows the location of the SN bifurcation of two coupled Jansen-Rit modules for increasing coupling, computed with the derivative method (black dots), along with the result of the codimension-2 analysis performed with XPPAUT (red line). In order to emphasise a slight deviation from the linear dependency, we plot it in a form approximating Equation (4.2) : $p^{SN} = -K f_c(p_{single}^{SN}) + p_{single}^{SN}$ (dotted line), where $p_{single}^{SN} \sim I_{ex}^{SN}$ is where the SN bifurcation occurs for a single Jansen-Rit module. In the reminder of this chapter, for a given value of K, the constant input p to the system is set $\Delta p = 1$ s^{-1} below the value read from the Y coordinate of the black dot from Figure 4.1 with its X coordinate value equal to K. For $K = 0$ we use the values known from the single column case.

This 'derivative method' is not indispensable for the results presented later in this chapter. In order to find settings of the $p - K$ values, we could engage only the XPPAUT codimension-2 analysis. Nevertheless, in this Thesis we introduced the 'derivative method' since it might be found useful when applied to networks of modules featuring saddle-node bifurcations. That is because by substituting K in Equations (4.2)-(4.4) by $K(N-1)$

one can find the location of the SN-driven stability loss in a fully bidirectionally coupled network of N Jansen-Rit modules (as the one studied in Chapter 5), without performing continuation analysis which might be demanding due to the high dimensionality of the corresponding system. As mentioned before, localising the SN-driven stability loss might be of high interest when it marks a 'catastrophic transition', like the transition to epileptic spiking set by the SNIC bifurcation in the Jansen-Rit model. Note that this method would not apply to instabilities arising from foci, because in that case, when relaxing to the focus the system transiently exceeds the steady state value and therefore we can not apply the simple reasoning of the one-sided I_{ex} convergence.

4.2.3 Classification of model dynamics

In order to study the temporal properties of transient excitation episodes, we use the classification algorithm illustrated in Figure 4.3 and described in what follows. Running averages within a sliding window of length $W = 0.5$ s are computed for output signals $y_1^i - y_2^i$ of both columns ($i \in \{1,2\}$). Spans of time course in which at least one of these averages was above the threshold $T = 5$ mV are considered excitation periods. For the values of W and T chosen, the result of the classification agrees with eye inspection and pure epileptic-like spikes are not considered excitation episodes. This is what we want, because we are interested in activity that can be transiently self-sustained and therefore can lead to longer excitation periods. To emphasise this exclusion of short pure spikes, from now on we use the term 'prolonged excitation transients' (or simply 'prolonged activity'). Figure 4.3 shows 10 second of simulation, generated by the model in the presence of white noise. The outputs of both columns are denoted by thin blue and black lines, and the corresponding running averages by the thick lines in the same colours. Whenever at least one of the running means crosses the threshold T (dashed line), the signal is considered prolonged activity. Note that the synchronous spiking of both columns occurring around $t = 49$ s is not considered prolonged activity, whereas the short episode appearing between $t = 43$ s and $t = 44$ s is considered as such.

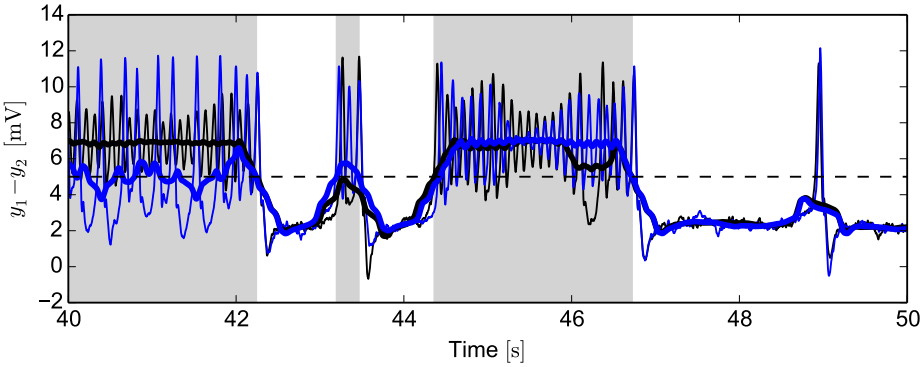

Figure 4.3: Classification of activity. The output signals of two columns are marked with thin black and blue lines. Running averages of these signals obtained with a sliding window of length 0.5 s are shown by thick black and blue lines. The threshold T is marked with a dashed line, and periods classified as prolonged activity are represented by the grey background. Here coupling strength is $K = 10$, the intensity of white noise is $D = 0.5\ \mathrm{s}^{-1}$, and p is adjusted to K according to the methodology introduced in text.

4.2.4 Computational simulation

We integrated the system with the stochastic Heun scheme. For each setting of D and K values we performed ten simulations 3601 s long (one second was used to buffer the sliding window), furnished with different realisations of stochastic processes, frozen for different parameters settings.

4.2.5 Averaging and computation of rates

In the 'Results' section we compute the initiation and termination rates of the prolonged excitation transients. The initiation rate is defined as the total number of prolonged excitation transients divided by the total duration of the steady state, whereas the termination rate is defined as the total number of terminations of prolonged excitation transients divided by their total duration. These quantities are not computed for each realisation of the noise separately, but rather within each set of parameters once for all realisations considered together. This procedure minimises effects related to the finite time of the simulation and at the same time involves various realisations of stochastic processes.

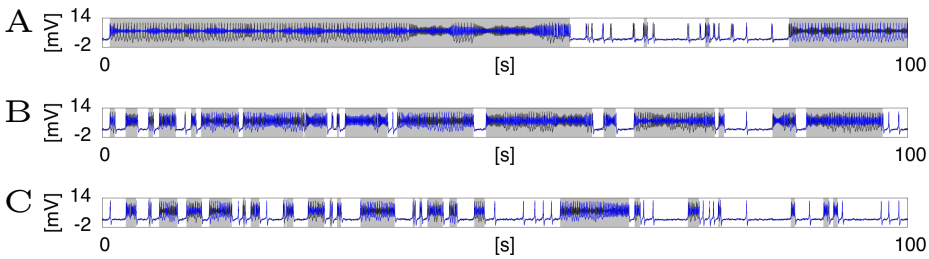

Figure 4.4: Exemplary time courses obtained for three different values of the coupling strength. 100 seconds of activity of the model is shown for $K = 5$ (A), $K = 10$ (B) and $K = 15$ (C). Periods classified as prolonged activity are represented by a grey background. In all cases the noise intensity D was set to 0.5 s^{-1}, and the system was operating $\Delta p = 1$ s^{-1} below the excitability threshold set by the SNIC bifurcation.

4.3 RESULTS

We studied the role of coupling in initiation and termination of prolonged excitation transients appearing in the system of two coupled Jansen-Rit modules operating close to ($\Delta p = 1$ s^{-1}) the excitability threshold and subject to white noise. Figure 4.4 demonstrates sample time courses obtained for three different values of coupling K and in the presence of noise characterised by intensity $D = 0.5$ s^{-1}. Durations of prolonged excitation transients (marked with the grey background) and steady state periods (white background) for different values of K show that the rates of initiation and termination of prolonged excitation transients depend on the coupling strength between the columns. In particular, for low coupling strength values (panel A, $K = 5$) the system does not change the state frequently, as for greater coupling strength values (panels B and C, $K = 10, 15$, respectively). In contrast, for intermediate values of K (panel B, $K = 10$) the system switches to the excited state most readily. Next, we studied these effects by systematically varying K and performing long simulations providing high statistics, as described in the 'Methods' section. This allowed us to estimate initiation and termination rates of prolonged excitation transients.

Figure 4.5 shows how the initiation and termination rates of prolonged excitation transients depend on the coupling strength K. The results are

presented for three different intensities of the noise: $D = 0.25$, 0.5 and $1\ \mathrm{s}^{-1}$ (blue, red and green, respectively). This figure demonstrates that for low values of K both the initiation and termination rates are relatively low, indicating rare transitions between steady and excited states. $K = 0$ corresponds to the case of two separated modules, and shows that in that case transitions between the states are rare. We already studied a comparable case in Chapter 3: an excitation event corresponds here to noise-induced transition from the node to the alpha limit cycle (from blue to green in regime III in Figure 2.4A) of at least one column, and a termination event corresponds to the opposite transition between those states. As can be read from Figure 4.5, this effect relies on sufficiently high intensity of the noise (green). For low noise intensity (blue) and low coupling K, the effect it is virtually absent, while it emerges for increasing K. This reliance on coupling between the modules is what we refer to as 'collectiveness' of excitability.

The increase of K leads to a moderate increase of termination rates and a rise of initiation rates, which reach a maximum for intermediate K ($K = 8$ for $D = 0.25\ \mathrm{s}^{-1}$, $K = 9$ for $D = 0.5\ \mathrm{s}^{-1}$ and $K = 10$ for $D = 1\ \mathrm{s}^{-1}$). For larger K values the initiation rates decay, whereas termination rates increase more rapidly. For large coupling the termination rate is basically independent on the noise intensity, showing that in that regime it is coupling, not noise, that plays a major role in the termination of activity. In other words, when K is high, in the excited state, the system is hardly susceptible to noise. The concurrence of a noise-dependent initiation and noise-independent termination is a typical behaviour of an excitable system (Lindner et al., 2004). In this system large enough coupling induces excitable behaviour at the level of two columns, which thus constitutes a collective effect. In the presented case, however, for $K < 15$, termination rate depends on noise intensity, which is illustrated by the separation of dotted lines in Figure 4.5.

Figure 4.6 shows the activity of the system around the termination of prolonged excitation transients. Figure 4.6A shows that for low coupling ($K = 5$). The termination of activity is unsynchronised between the two columns. In that regime the termination is partially inflicted by noise,

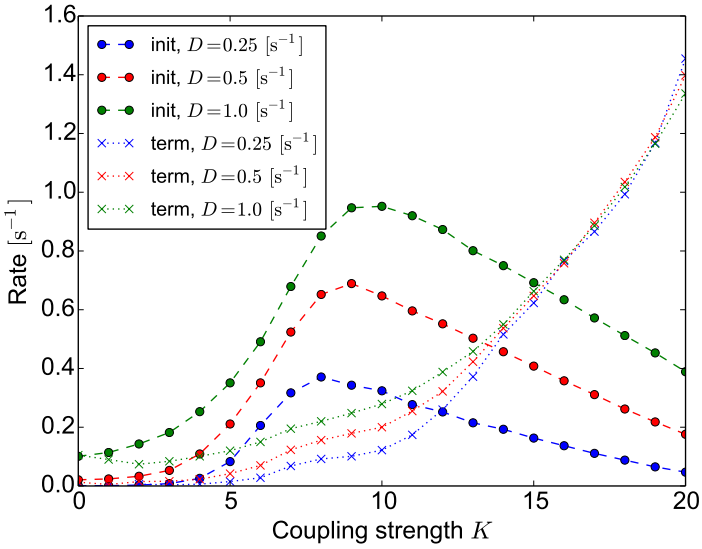

Figure 4.5: Dependence of the initiation and termination rates on coupling strength and noise intensity. Initiation ('init', dots) and termination ('term', crosses) rates for discrete values of the coupling strength K are shown for three different intensities of the driving noise: $D = 0.25$ s^{-1} (blue), $D = 0.5$ s^{-1} (red), $D = 1$ s^{-1} (green). Dashed and dotted lines are plotted to guide the eye. Note that for the lowest noise intensity ($D = 0.25$ s^{-1}) and two lowest coupling values ($K = 1, 2$) the initiation rate was too low to gather sufficient number of episodes allowing to measure termination rate. Therefore the two lowest points of termination rate for lowest noise intensity are considered outliers and are not plotted.

whereas for higher K it occurs rather due to synchronisation effects. Figure 4.6B shows how for high coupling ($K = 15$) the synchrony between the two columns gradually develops, until a simultaneous drop of activity terminates the excitation period. Although this gradual development of synchrony does not have to be present in every excitation transient, the synchronous termination is prevalent for higher coupling.

The dependence on K of this synchronous termination is shown in Figures 4.6C-E, where the black line represents the average over both columns and all excitation transients for the given coupling: $K = 5$ (panel C), $K = 10$ (panel D), $K = 15$ (panel E). The grey lines shown in these panels are 100 exemplary time courses of individual columns. They converge most strongly to the averaged time course (black line) after the termination ($t = 1$ s) in the case of strongest coupling (Figure 4.6E). Also in that case

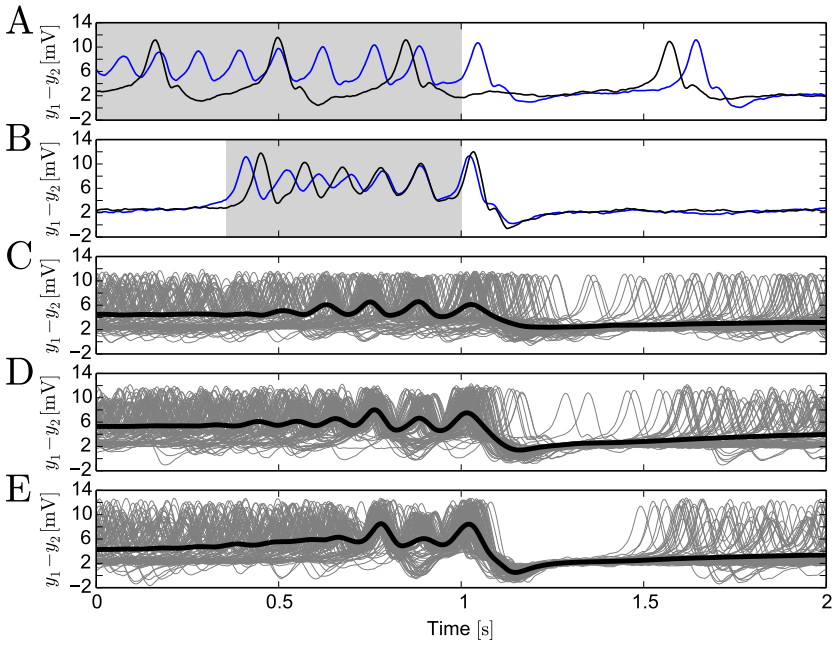

Figure 4.6: Terminations patterns of prolonged excitation transients. Panels A and B show exemplary time courses of two cortical columns (black and blue lines) for $K = 5$ and $K = 15$, respectively. Periods of prolonged excitation transients are marked with the grey background. Panels C, D, E show averaged time courses from both columns and from all prolonged excitation transients registered for $K = 5, 10, 15$, respectively. Grey lines in these panels are 100 exemplary time courses. In all cases the moment found by the classification algorithm as the point of excitation termination has been shifted to the middle of the plot (it corresponds to $t = 1$ s). The results were obtained for $D = 0.5\ \mathrm{s}^{-1}$. The thick lines in panels C, D, E were obtained from averaging $2.5 \cdot 10^3$, $11 \cdot 10^3$ and $18 \cdot 10^3$ individual time courses, respectively.

the kink typical to the refractory period of the Jansen-Rit model is most strongly pronounced (dip in the black line after $t = 1$ s). Greater coupling promotes this synchronous termination, which explains the faster appearance of synchronisation patterns for $K = 15$ (black line in Figure 4.6E) than for $K = 5$ (black line in Figure 4.6C), as well as the growth of the termination rate with K presented in Figure 4.5.

The trend of the initiation rate presented in Figure 4.5 with coupling also may be explained as follows. Low K values hamper recruitment between the columns: when one column spikes due to the stochastic perturbation, it is less likely to excite the other one, as long as K remains low. For larger K values, however, a spike in one column entails a significant perturbation applied to the other column, and allows it to also leave the steady state. If the coupling between the columns is strong enough, then both columns may display the same behaviour - they synchronously spike and simultaneously (and quickly) fall to the refractory period followed by the steady state (see again the isolated spike around $t = 49$ s in Figure 4.3). Intermediate K values, in contrast allow for the mixing of oscillatory modes; although the recruited column leaves the steady state, the columns do not fully synchronise and as a result at least one of them sustains activity by moving to the attractor of alpha oscillations that lack refractory period. These oscillations yield increased output that is fed to the other column, which can again go active after leaving the refractory period, and a prolonged excitatory activity may develop. This effect explains why the initiation rate peaks for an intermediate coupling in Figure 4.5. The location of the peak in Figure 4.5 varies for different noise intensities D, which can be explained by the fact that larger noise requires higher coupling strength for complete synchronisation.

4.4 DISCUSSION

In this chapter we studied the behaviour of a system of two reciprocally coupled Jansen-Rit modules operating slightly below the SNIC bifurcation and subject to white noise. We focused on characterising temporal properties of prolonged excitation transients as a function of coupling strength and noise intensity. These excitation transients occur in the system in an

abrupt way due to the proximity of the 'catastrophic transition' underlying the onset of relaxation oscillations. Coexistence of these oscillations with another, quasiharmonic limit cycle, facilitates the emergence of these excitation periods to long lasting activity. This activity, in turn, can abruptly terminate due to complete synchronisation of both modules in the refractory period of the relaxation oscillatory mode. We quantified the rates of transitions between the excited and steady states, and we showed that the excitability of the system depends non-monotonically on the coupling strength between the modules.

Excitability can be defined based on the amplitude of system's response to external stimulation. The magnitude of this amplitude depends on stimulation in a strongly nonlinear way: stimuli exceeding a certain threshold evoke a response characterised by an amplitude much greater than for stimuli not exceeding the threshold. Our definition of excitability is based not on amplitude, but rather on duration of system's response. We observed that for sufficiently strong coupling this duration (on average) does not depend on the driving noise intensity. Such behaviour is typical of excitability. In our system we identified another regime, characterised by weaker coupling, in which the duration of the response does depend on the driving noise. Note that according to our definition, the simultaneous spiking of both columns is too short to be considered an excitation event. Breaking of symmetry promotes excitations, and in our system it is provided by independent realisations of the noise acting upon the columns.

Similarly to Chapter 3, the findings presented here can be related to epilepsy. This disease is primarily characterised by excessive synchrony (see Section 1.5). Nevertheless, recently it has been observed that synchronisation might be increasing during development of seizures (Khambhati et al., 2014; Truccolo et al., 2011). It has been proposed that seizures imply synchronisation, and synchronisation leads to termination of seizures (Majumdar et al., 2014). Termination of seizures has been shown to exhibit signatures of a 'catastrophic transition' (Kramer et al., 2012). The synchronous termination, occurring due to simultaneous entering the refractory period,

has been hypothesised to be the scenario underlying a synchronous termination of seizures (Schindler et al., 2007). This behaviour and a 'catastrophic transition' are featured by our model.

Due to the excessive synchrony during seizures, a single neural mass may represent a large-scale cortical area or even the whole brain (Breakspear et al., 2006). Here we characterised a regime of high coupling in which the system is highly synchronous and therefore its activity could be approximated by the time course of a single module. Intermediate coupling gives rise to complex phenomena, absent when the columns interact weakly. It has been suggested that the healthy brain is most likely to operate in the intermediate coupling regime (Deco et al., 2013), where the emergence of complexity might empower computational capabilities. Our results do not necessarily have to describe epileptic dynamics: prolonged excitations contain periods in which both columns dwell in the alpha attractor.

4.5 SUMMARY AND OUTLOOK

In this chapter we focused on interactions between two coupled Jansen-Rit modules operating in bistable regimes. This bistability involved coexistence of two limit cycles, interactions of which gave rise to complex, long excitations. We quantified temporal properties of these excitations and showed that various settings of the system, with fixed distance to the 'catastrophic transition', lead to very different behaviours. In the previous chapter we showed that temporal correlation of the driving noise facilitates excitation in the Jansen-Rit neural mass model. The results presented here relate to that finding, because each column could be considered a low-pass filter that transforms the white noise presented here into temporally correlated output driving the interconnected column. A natural extension of our approach could address the effects of introducing temporal correlation of the noise in the presented methodology. In what follows we combine the effects studied so far, i.e. we consider a system compound of a number of columns driven by temporally correlated noise and harmonic signal. Moreover, we go beyond temporal analysis of the model's response, focusing on its spectral properties and relating them to experimental data.

CHAPTER 5

CROSS-FREQUENCY TRANSFER WITH STOCHASTIC DRIVING

5.1 INTRODUCTION

In this chapter we study the spectral properties of a system of coupled Jansen-Rit modules subject to driving with temporally correlated noise and a periodic signal. In particular, we are interested in reproducing two spectral phenomena characteristic to brain dynamics, namely the $1/f^b$ shape of the background EEG power spectrum (see Section 1.4.5) and cross-frequency interactions. The latter phenomenon is widespread in brain dynamics; it may involve various rhythms and may concern various configurations of coupling between amplitudes and/or phases of those rhythms (Jirsa and Müller, 2013). Here we are interested in the 'phase-to-amplitude' coupling that occurs when the phase of the slower rhythm modulates the amplitude of the faster rhythm. We introduced this mechanism in Section 1.4.1 and we mentioned one of its potential functions in the brain: facilitation of 'communication through coherence'. This phenomenon can also be considered a transfer of power between different frequency bands: the slow driving leads to periodic increases of power in the faster band. Indeed, such phenomena have been observed experimentally, for example transcranial stimulation of the brain at low frequencies (smaller than 1 Hz) has been seen to cause for instance an increase in oscillatory power at larger frequencies (5 Hz-10 Hz) (Marshall et al., 2006; Massimini et al., 2007).

Recently much emphasis has been placed on quantifying and characterising the transfer of spectral power across frequencies (known in what follows as cross-frequency coupling, Jirsa and Müller, 2013), and on identifying its functional roles in the brain (Canolty and Knight, 2010; Jensen and Colgin, 2007). In particular, power spectrum correlations have been

observed for instance between theta and gamma rhythms in the rat hippocampus during memory retrieval (Shirvalkar et al., 2010), between posterior gamma and frontal alpha/beta oscillations in the human brain during motor imagery tasks (Lange et al., 2008), and between the gamma and delta bands in different regions of the human visual cortex during a visual task (Bruns and Eckhorn, 2004). Phase coupling between delta and alpha bands has also been reported in human brains performing an orientation task (Isler et al., 2008). More common is the situation in which the oscillation power in a given frequency band is modulated by a second rhythm at lower frequency. Such cross-frequency coupling has been observed for instance between alpha and gamma activities in humans during rest (Osipova et al., 2008) and between theta and gamma oscillations in rats during learning (Tort et al., 2009). Other behavioural correlates of cross-frequency coupling have been found, associated for instance with reward coding (Cohen et al., 2009a) and decision making (Cohen et al., 2009b) in humans. Also, recent work has shown that cross-frequency coupling is modulated by behavioural tasks (Voytek et al., 2010). Cox et al. (2014) reported cross-frequency coupling between the phase of sleep spindles and the amplitude of higher frequency rhythms, in particular beta, recorded in EEG during sleep. This effect, in turn, was modulated in the frontal cortex by the phase of slow sleep oscillations.

Despite the large number of experimental studies pointing towards cross-frequency correlations, several difficulties arise when it comes to the interpretation of this phenomenon. As pointed out by Aru et al. (2015), the methodologies applied in a number of recent studies on cross-frequency coupling are not flawless and the results might have been over-interpreted. Therefore, further and stricter studies on the functional role of cross-frequency coupling are needed to confirm previous results. In particular, not all cross-frequency correlations are signatures of direct interaction between rhythms. And when they are, such correlations may be explained by different mechanisms, which may be grouped into two broad scenarios. In one scenario, two neuronal oscillators operating at two different rhythms might be coupled bidirectionally to each other. This coupling could mediate an interaction that would result in each of the oscillators

being affected in one way or another by the natural frequency of the other oscillator (Jirsa and Müller, 2013). When such bidirectional interaction occurs locally, it has been proposed to be mediated by the firing activity of the underlying neurons (Mazzoni et al., 2010). In such a way delta oscillations, for instance, control the level of local cortical excitability, which in turn modulates the excitatory-inhibitory balance that gives rise to the gamma rhythm (Mazzoni et al., 2011).

In a second, somewhat simpler scenario, cross-frequency correlations might arise due to unidirectional coupling, through which the spectral features of the driving neuronal population would be directly transferred to the driven population. When the same external stimulus is encoded by two different rhythms, cross-frequency correlations can appear as a result of that common unidirectional driving (Mazzoni et al., 2008). In some cases, however, the stimulus does not necessarily affect directly the neurons underlying one of the rhythms. This might be the case of recent experimental work by Bayer et al. (2011), who examined the effect of rocking on sleep in human subjects. In that study, healthy volunteers were asked to lie down on a rocking bed that oscillated slowly, at a frequency of 0.25 Hz. This periodic stimulation was seen to ease the transition from waking to sleep, and to increase the power of cortical oscillations (measured via EEG) in the alpha range. In this chapter we ask whether a cross-frequency transfer such as that reported by Bayer et al. (2011) can be the result of the low frequency input driving a mesoscopic broadband oscillator operating in the alpha range. To that end, we engage the Jansen-Rit model introduced in Chapter 2 and we subject it to driving with Ornstein-Uhlenbeck noise, which may be considered a simple approximation of a realistic '$1/f^b$' broadband brain activity (see Section 1.4.5).

5.2 Methods

We study the system of N coupled Jansen-Rit modules described by Equations (2.10)-(2.12), with stochastic components $\xi^i = \xi^i_{\text{ou}}$ given by Equation (2.14). Values of the rest of model parameters are specified in Table 5.1. We relate our computational findings to the EEG experimental measurements. Therefore, like previously, we are interested in analysing

Variable	Symbol	Value	Units
Number of columns	N	4, unless stated otherwise	-
Integration step	h	0.001	s
Noise intensity	D	350, unless stated otherwise	s^{-1}
Noise correlation time	τ	0.15, unless stated otherwise	s
Constant input component	p	75 for coupled system, 90 for uncoupled	s^{-1}
Coupling strength between the columns	K	15, unless stated otherwise	-
Driving sine signal frequency	f	0.25, unless stated otherwise	Hz
Driving sine signal amplitude	$\tilde{A}_0$	45, unless stated otherwise	s^{-1}
Driving sine signal phase	ϕ	0	-
Reshaped signal amplitude	$\tilde{A}'$	10.76	s^{-1}
Reshaped signal minimal frequency	f_{min}	0.05	Hz
Reshaped signal maximal frequency	f_{max}	4	Hz
Reshaped signal frequency step	f_{step}	0.05	Hz
Length of simulation	-	1010	s
Length of rejected transient	-	10	s

Table 5.1: Parameter values of the neural mass model. Parameters e_0, v_0, r, A, B, a, b, $C_{1,2,3,4}$ were set to plausible values as stated in Section 'Extended Jansen-Rit model'.

$y_1(t) - y_2(t)$, which is approximately proportional to the local EEG signal (see Sections 1.2 and 2.3). As mentioned in Sections 1.4.4 and 1.4.6, a number of studies stipulate that the brain operates slightly below a second-order phase transition or bifurcation. In the system utilised here, such working point can be found near one of the Hopf bifurcations discussed in Section 2.3.3. We already studied a single Jansen-Rit module driven by constant input in the vicinity of a Hopf bifurcation ($p = 89\ s^{-1}$). These settings corresponded to the 'healthy-like' paradigm introduced in Chapter 3. Here we follow that approach in the case of a system of coupled columns ($N > 1, K \neq 0$), where we require that the total input to a column, I_{ex}, not just the constant component p, is on average close to the bifurcation. This approach is similar to the one applied in Chapter 4, because of at least two reasons. Firstly, we support the study of a compound system with knowledge about the dynamics of its constitutive elements. Secondly, we estimate the total input delivered to one element. Nevertheless, here we

do it with respect to the averaged signal computed over the activity period, not solely with respect to the steady state (as we did in Chapter 4).

We set parameters of the external excitatory input such that its value averaged over time (and over columns in case of the network), $\langle I_{\text{ex}} \rangle \simeq 90$ s^{-1}, is located close to the first Hopf bifurcation point (separating regimes II and III in Figure 2.4A). The external input I_{ex}^i delivered to a cortical column contains in general constant, stochastic, and periodic components, as well as an input coming from all other columns. Only the constant component p and the contribution from the afferent columns have non-zero mean, and therefore determine $\langle I_{\text{ex}} \rangle$. Stochastic and periodic components have zero means, and even though they do not affect the average of the total input $\langle I_{\text{ex}} \rangle$, they do contribute to its variance.

5.2.1 Numerical methods

The model was integrated using the stochastic Heun integration method (Toral and Colet, 2014) with a time step equal to 0.001 s. In each run we simulated 1010 seconds of activity, discarding the first 10 seconds. We computed the power spectra by applying the Welch algorithm from the Matplotlib Python module, using a Hanning window. The length of each time segment was chosen to be 20 seconds, with an overlap between segments equal to 10 seconds.

5.3 Results

5.3.1 Spectral and temporal properties of a single column

We first studied the behaviour of a single cortical column receiving an input $p = 90$ s^{-1}, systematically varying the parameters of the Ornstein-Uhlenbeck noise, namely its noise intensity D (varied in a range from 0.1 s^{-1} to 1000 s^{-1}) and correlation time τ (varied in a range from 0.001 s to 10 s). We obtained the power spectrum in each case and compared it with the one reported in the experiments of Bayer et al. (2011) (see Figure 5.1A). Our goal here was to choose the noise parameters for which the computational result reproduced the experimental characteristics, namely an $1/f^b$ shape with an embedded peak in the alpha band. Figure 5.1B shows three power spectra obtained from the model driven by noisy inputs with the

same variance but different intensities and correlation times. We found that the experimental characteristics were qualitatively best reproduced for $\tau = 0.15$ s and $D = 350$ s^{-1} (see Figure 5.1A and 5.1B). Our result is robust for a range of D and τ values, provided that $\tau \lesssim 0.2$ s. Beyond that region, the power spectrum at low frequencies ($\lesssim 2$ Hz) becomes noticeably steeper than at higher frequencies (red trace in Figure 5.1B), which is not the case for experimental data. Moreover, for these large τ values the alpha peak becomes too prominent, whereas in the opposite limit it decreases as the correlation time τ is reduced (blue trace in Figure 5.1B), becoming significantly smaller (with respect to the $1/f^b$ background) than in experimental data for $\tau < 0.15$ s.

This dependence of the signal spectrum on the noise characteristics can be explained on the basis of the results presented in Chapter 3 in the following way: the system operates on average close to the Hopf bifurcation, where the limit cycle regime begins. This regime is explored transiently by the system due to the stochastic driving. The duration of the episodes in which the system stays in the oscillatory regime is dictated by the correlation time of the noise. Small τ implies rapid changes of the input to the system, which does not have time to relax to the limit cycle regime, and alpha oscillations do not occur. In contrast, for relatively large τ, the input changes in a more smooth manner and the system has time to relax and exhibit alpha oscillations, which contribute to the alpha peak in the power spectrum. The noise intensity D plays a role too, because for a given τ it affects how deep the system can go into the limit cycle regime. The broadband shape of the power spectrum roughly follows the shape of the spectrum of the noise, which depends on the control parameter τ. This effect is noticeable specially for low frequencies, and originates in the regime which in deterministic conditions corresponds to a node, where the system follows the noisy driving, and thus yields power spectra similar to that of the Ornstein-Uhlenbeck noise. In this way, the combined effect of different dynamics gives rise to a realistic power spectrum. Albeit similar to the '$1/f^b$' signature of criticality (see Section 1.4.5) the effect described here does not rely on critical behaviour.

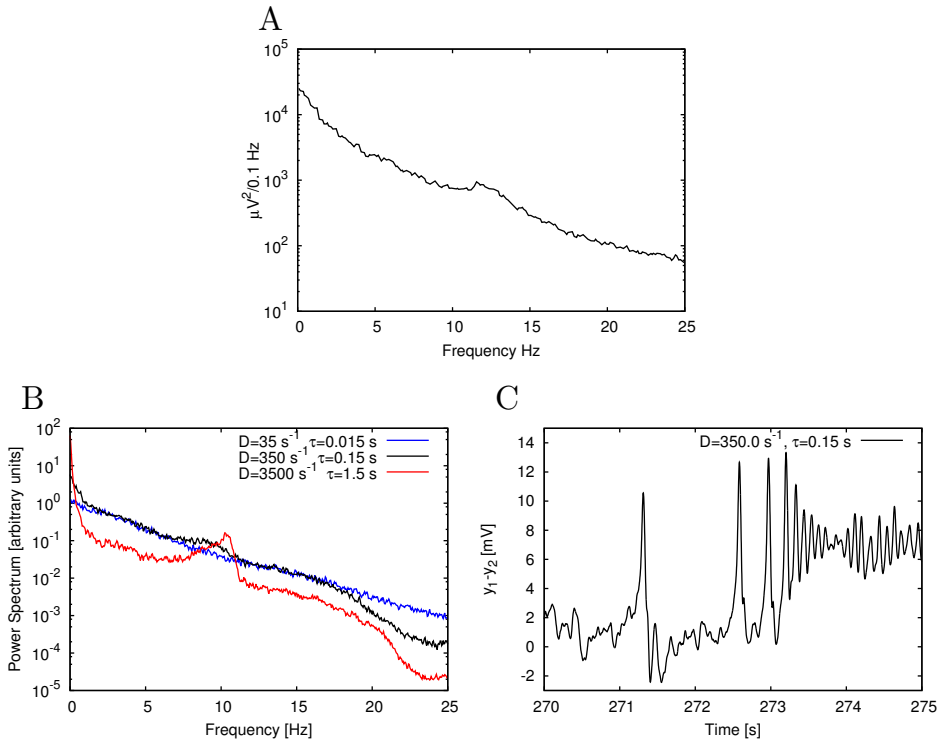

Figure 5.1: Comparison of experimental and computational power spectra. Panel A shows experimental data extracted from Figure 1D of Bayer et al. (2011). Panel B shows power spectra obtained for three different noise sets of D and τ values while variance of the noise is the same for each case. The black line corresponds to the time series shown in panel C, the red line to conditions when the correlation time τ is increased tenfold and the blue one when it is ten times decreased. Panel C shows the time trace obtained from the Jansen-Rit model of a single cortical column with an input consisting of two parts: a constant component equal to $90\ \mathrm{s}^{-1}$ and a stochastic one determined by Ornstein-Uhlenbeck noise with intensity $D = 350\ \mathrm{s}^{-1}$ and correlation time $\tau = 0.15$ s. Three distinct types of dynamics are apparent: the dynamics begin with a noisy behaviour based on the fixed point, then spiky dynamics show up and finally the time trace ends with alpha oscillations.

The correlation time τ dictated by synaptic effects is conjectured to be of the order of 10 ms (Mazzoni et al., 2008; Sancristóbal et al., 2013) rather than 100 ms. In our case, however, noise stands for background activity arising from collective effects at the mesoscopic scale. Note also that in the computational results shown in Figure 5.1B the alpha peak is shifted toward lower frequencies with respect to experimental results shown in panel A. The location of the peak could have been shifted by changing parameters of the model, however we chose to perform the analysis with the original set of parameters proposed by Jansen and Rit (1995), in order to maintain coherence with the previous chapters of this Thesis and other studies that adopted that set of parameters.

Although the power spectrum obtained with these noise parameters (black in Figure 5.1B) reproduces qualitatively the experimental results (Figure 5.1A), its corresponding temporal evolution exhibits a strong spiky behaviour (Figure 5.1C), which is far from what is typically observed in experimental EEG recordings of healthy subjects. Indeed, in Chapter 3 we showed that noise with parameters used here (corresponding to $\sigma_{\text{ou}} \simeq 50$ s^{-1} and $\tau \simeq 10^{-0.8}$ s) elicits a considerable amount of spikes in a single Jansen-Rit column. We also showed, that an adequate change of noise parameters would suppress the spiky dynamics. However, in that case the spectral match between experimental and computational data would be lost. We therefore conclude that the behaviour of a single column is not able to recapitulate realistically both the temporal and spectral characteristics of the experimental observations at the same time. For this reason we extended our model to several coupled columns.

5.3.2 Coupled cortical columns

The signals measured in experimental EEG recordings do not arise from a single cortical column, but from an aggregate of columns. In order to take this into account we extended our model to represent multiple coupled columns. As a simplifying assumption, we consider that the signal registered by an electrode is an average of the signals generated by individual columns in the probed area. We refer to this signal as $y_1 - y_2$, with no i indexes in subscripts. As explained in Section 2.3, the model considers only excitatory connections between populations of pyramidal neurons

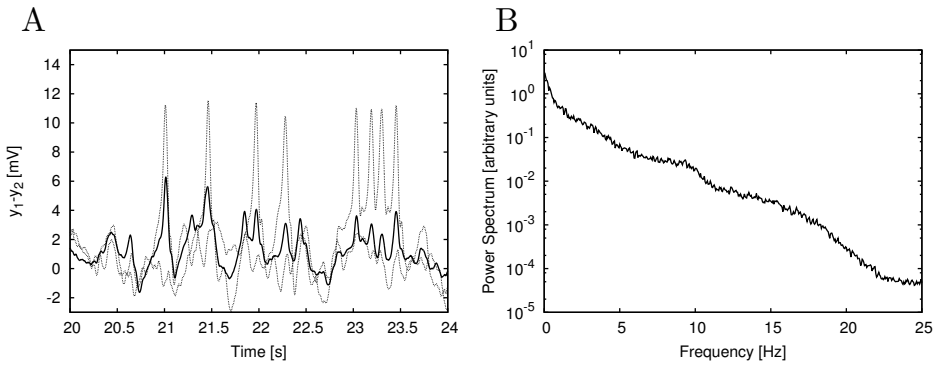

Figure 5.2: Effect of signal averaging. Panels A and B show a typical time trace and power spectrum, respectively, analogous to panels B and C of Figure 5.1, but obtained from the model of four columns coupled in an all-to-all bidirectional manner. The coupling strength constant K was set to 15 and the constant component of input, p, to 75 s^{-1}. Panel A shows time traces of two individual columns (dashed lines) and the average signal of all four columns (solid line). Averaging attenuates individual spikes, but does not affect the power spectrum substantially (as shown in panel B).

residing in different cortical columns. Therefore, there are two new parameters with respect to the single-column case: the number of columns N and the coupling strength K. Our aim was to test our cross-frequency transfer hypothesis in a simple model, therefore for a start we considered only $N = 4$ cortical columns coupled in a simple all-to-all manner with equally strong connections. Already for four coupled columns, individual spikes in the temporal domain are substantially attenuated due to averaging (Figure 5.2A), rendering time traces that qualitatively resemble EEG signals. On the other hand, the power spectrum of the averaged signal still resembles the experimental one (Figure 5.2B). This approach finds support in experiments; so-called 'microseizures' –spiky, epileptic-like activity that may be detected only in a very fine spatial scale (~ 1 mm electrode array resolution, 40 μm electrode size)– have been observed experimentally by Stead et al. (2010), not only in epileptic subjects, but also sporadically in healthy ones.

The coupling contribution to each column was normalised by the number of afferent columns ($N - 1$ for our all-to-all connectivity topology, as expressed in Equation (2.13)). This normalisation allowed us to study the

dependence of the results on the system size N for a constant value of the coupling strength K. Without it, increasing the number of columns N in all-to-all topology would ultimately lead to saturation due to excessive external driving. Increasing the number of columns to $N = 100$ showed that the spectrum remains qualitatively consistent with the experimental one independently of the system size.

We next studied how robust the behaviour shown in Figure 5.2 above is with respect to changes in the constant input and coupling strength. To vary those parameters it is necessary to take into account the fact that the input into a cortical column from other columns is implicitly dependent on p, which has the same value for all columns and determines the dynamical regime in which the columns operate. In order to keep the effective total input $\langle I_{\text{ex}} \rangle$ close to 90 s^{-1}, the coupling strength K needs to be compensated by reducing the input constant component p below 90 s^{-1}. Taking this into consideration, we ran a series of simulations for $N = 4$ columns varying both the constant input component p and the coupling strength K. For each condition we averaged the inputs coming from the coupling terms over time and over all columns. In this manner we obtained the mean contribution of inter-column coupling to the input of a column. Adding this value to the constant input p gives the average total input acting upon a column, $\langle I_{\text{ex}} \rangle$. We varied the coupling strength in the range $0 < K < 70$, and in each case we chose the constant input component within the range 50 s$^{-1} < p < 90$ s^{-1} in such a way that the average external input to each column $\langle I_{\text{ex}} \rangle$ was close to 90 s^{-1}, in accordance with our assumption regarding proximity to the bifurcation point.

In these conditions we found dependence of the average of the coupling input on coupling strength K close to linear. Note that this result resembles the $p - K$ dependency presented in Figure 4.2. Moreover, we found that the coefficient of variation (defined as the ratio of the standard deviation to the mean) of this input was close to unity, which indicates that not only its average, but also its standard deviation grows linearly with K. This can be explained by two effects. First, higher synchronisation causes in-sync spiking that weakens the effect of averaging between the columns.

Second, these periods of high activity alternate with periods of low activity when due to the lower value of p the columns operate effectively in the fixed point regime. In the whole parameter range that fulfils the condition $\langle I_{\text{ex}} \rangle \sim 90$ s^{-1}, the temporal behaviour and power spectrum resembled the experimentally observed one. With that caveat, our results are robust not only with respect to the parameters of the Ornstein-Uhlenbeck noise and the system size, but also with respect to the constant input and coupling strength. The simulations described below correspond to $K = 15$ and $p = 75$ s^{-1}.

5.3.3 Effect of an oscillatory input

In the experimental study performed by Bayer et al. (2011) on human subjects, volunteers were placed on a bed that was swung at a frequency 0.25 Hz. In our model we represent the stimulus associated with this movement as a harmonic driving. EEG data was recorded from the Fz electrode during the N2 sleep phase of the subjects for two conditions: swinging (bed in motion) and stationary (bed still). The experiment showed that swinging facilitates the transition from the awake state to sleep, and that it enhances the EEG power of both slow and alpha oscillations (see Figure 5.3A). According to the experimental setup the bed motion is harmonic, thus we started with mimicking swinging by applying to each column in our model an oscillatory component $u(t) = \tilde{A}\sin(2\pi f t + \phi)$, with $f = 0.25$ Hz and $\phi = 0$. We set the driving amplitude $\tilde{A} = \tilde{A}_0 = 45$ s^{-1}, and left all other parameters unchanged with respect to the stationary conditions described in the previous section.

A typical power spectrum of the signal obtained from the model with harmonic driving is presented in Figure 5.3B. The figure shows that the power spectrum obtained in the swinging condition (driving with a simple sine, blue) indeed enhances the stationary spectrum (black) in both the alpha band and for the frequency corresponding to the driving. Figure 5.4A shows a typical time course obtained in the swinging condition (thick black line). This figure shows that both the instantaneous amplitude of the alpha oscillations and the average value of the signal are modulated by the driving signal. The mechanism underlying both these effects originates in the bifurcation structure of the model (see Figure 2.4A), and was first

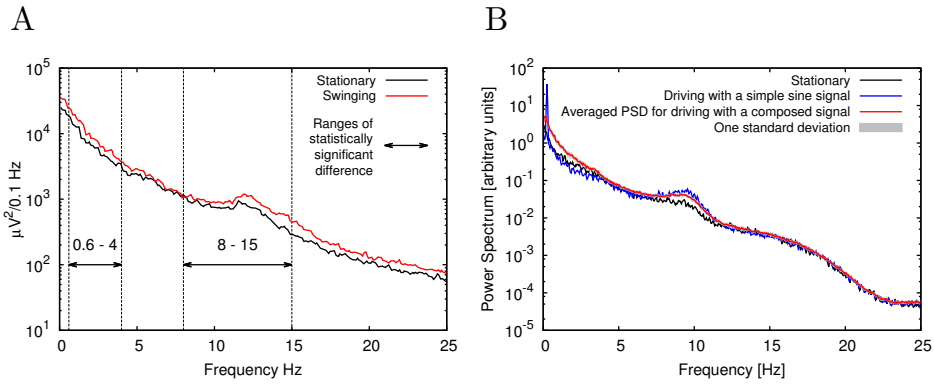

Figure 5.3: Effect of low-frequency driving. Panel A shows experimental EEG power spectra published by Bayer et al. (2011) (Figure 1D of that article), recorded from the Fz electrode in N2 sleep phase for both stationary (black line) and swinging (red line) conditions. Bayer et al. (2011) performed paired 2-tailed t-tests and found statistically significant increase in power in the ranges denoted here with horizontal arrows. In these ranges they found p-value to be $p < 0.05$, except for the frequency range 1 Hz - 2 Hz, where $p < 0.005$. Panel B shows power spectra obtained from the model in the periodically driven case (blue line) compared with the absence of driving (black line) and with the case of driving with the reshaped signal (red). This signal comprises sinusoid ingredients with varying frequencies, amplitudes and random phases (see text for details). Grey marks one standard deviation of distribution of power spectra obtained for different values of phases in the reshaped signal. In all cases we used four all-to-all connected columns subject to Ornstein-Uhlenbeck noise with intensity $D = 350\ \mathrm{s}^{-1}$ and correlation time $\tau = 0.15$ s. In the case of sinusoidal driving, the input had amplitude $\tilde{A} = 45\ \mathrm{s}^{-1}$ and frequency $f = 0.25$ Hz. The columns were coupled with coupling strength $K = 15$.

reported by Tsodyks et al. (1997) for the case of gamma-theta coupling in a Wilson-Cowan model. Recent works described this effect in a modified Wilson-Cowan model (Onslow et al., 2014) and in a modified Jansen-Rit model (Sotero, 2016). We now examine in detail this mechanism for our case.

In stationary conditions, the system explores all of the dynamics determined in Chapter 3: stochastically driven oscillations around the node, (stochastically driven) alpha oscillations and spiky behaviour. Similarly to the case presented in Chapter 3, this exploration arises as a consequence of the conjunction of two factors. The first factor is the proximity and coexistence of different dynamical regimes in the vicinity of the chosen

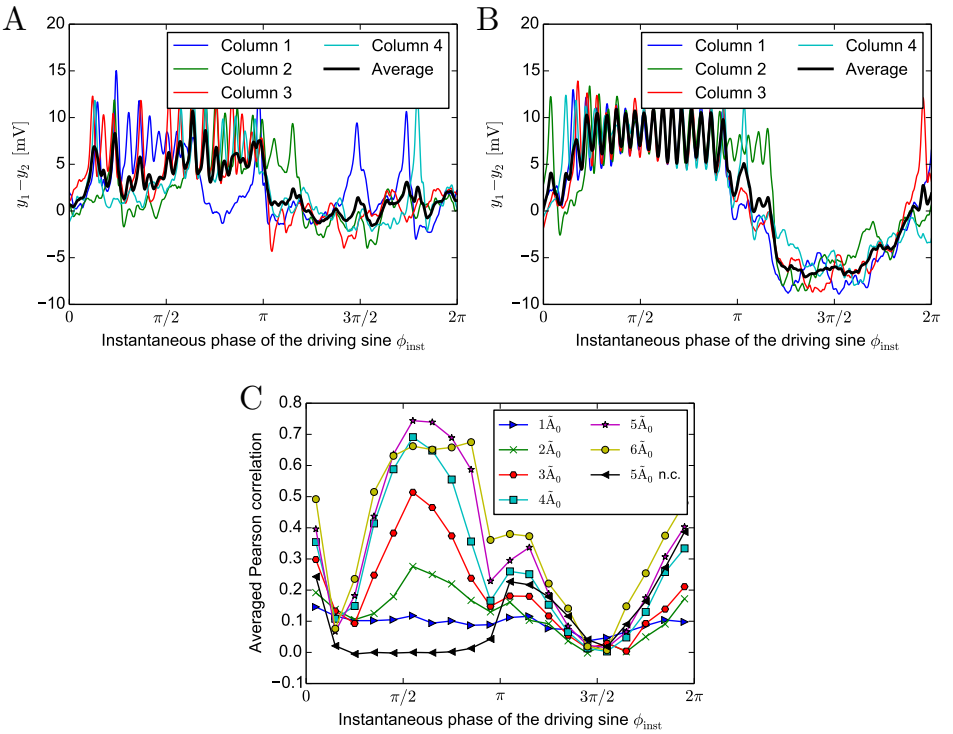

Figure 5.4: Time courses in the driven system and synchronisation effects. Panels A and B show time courses of all four columns (coloured lines) and the averaged signal (thick black line). The amplitude of the driving was set to $A_0 = \tilde{A}_0 = 45$ s^{-1} (panel A) and to $A_0 = 5\tilde{A}_0 = 225$ s^{-1} (panel B). Panel C shows averaged values of the Pearson correlation coefficient computed as a function of instantaneous phase of the driving sine for six values of the amplitude of the driving signal $\tilde{A} = \{1\tilde{A}_0, 2\tilde{A}_0, ..., 6\tilde{A}_0\}$. The lines are plotted to guide the eye. All data in all panels, apart from the black triangles in panel C, were obtained for the coupled system with $K = 15$ and $p = 75$ s^{-1}. In the uncoupled case ('n.c.' - no coupling) $p = 90$ s^{-1}. In all cases the system was driven with a sine signal with frequency 0.25 Hz. See text for details.

input value $\langle I_{ex} \rangle = 90$ s^{-1} (see bifurcation diagram in Figure 2.4A). The second factor is stochastic driving, which enforces alternations between these regimes. For the noise parameters chosen here, $D = 350$ s^{-1} and $\tau = 0.15 \simeq 10^{-0.8}$ s, the variance of the Ornstein-Uhlenbeck noise is $\simeq 48$ s^{-1}, which effectively means that the system may reach regimes II-V shown in Figure 2.4A. As we demonstrated in Chapter 3, for these settings of the noise, and corresponding settings of I_{ex}, the long-term behaviour of the system with $N = 1$ is independent of the choice of initial conditions and all three dynamics are displayed (with most rare alpha oscillations).

In the presence of oscillatory driving this situation changes and a number of factors contribute to an overall increase of power in the alpha band (again blue vs. black in Figure 5.3B). Firstly, the amplitude of alpha oscillations is smaller in the direct vicinity of the Hopf bifurcation ($I_{ex} \gtrsim 90$ s^{-1}) than for greater I_{ex} values, determined by the driving signal amplitude. The averaged time course of all columns showed in black in Figure 5.4A indeed indicates that the alpha oscillations are superimposed to the oscillatory signal during the positive half of the driving cycle, i.e. when the instantaneous phase $\phi_{inst} \in (0, \pi)$. During the negative half of the cycle the system moves further away from the oscillatory regimes and it may dwell in one of the random fixed point regimes (it is mostly the node). Consequently, less spiky behaviour is observed, which results in a slight decrease of power in $0 - 5$ Hz frequency band that corresponds to spiking (Grimbert and Faugeras, 2006). This decrease is shown in Figure 5.3B and in all panels of Figure 5.5. Figure 5.4B also shows that the system is much less prone to noise in the limit cycle regime (positive half of the sine) that in the node regime (negative half of the sine).

Another factor boosting power in the alpha band is the fact that in regime V (see again Figure 2.4A), i.e. for $I_{ex} > 137.38$ s^{-1}, alpha oscillations become the only allowed dynamics, so flipping between different regimes ceases to occur. This results not only in an increased alpha activity of each individual column, but also in an increase of synchronisation between the columns. For sufficiently high driving amplitude, columns go through transient in-phase synchronisation periods, where the averaged amplitude of their alpha oscillations is greater than in the periods of unsynchronised

alpha activity. These synchronisation periods may occur for only some, or for all columns in the system, they may be terminated by noise and then may reappear due to coupling between the columns. A few peaks, which emerge due to synchronisation between the columns during the positive half of the driving sine are shown in black in Figure 5.4A. For the chosen value of the driving amplitude $\tilde{A}_0 = 45$ s^{-1} these synchronisation episodes are irregular and not prevalent. It is due to the fact that $\tilde{A}_0$ sets the maximal value of the deterministic part of the input to $\simeq 135$ s^{-1}, which coincides with the starting point of the purely alpha regime at 137.38 s^{-1}. This regime may still be explored due to noise, but under these conditions the system operates at best on the edge of resonance (Battaglia and Hansel, 2011; Kang et al., 2010).

To the contrary, for higher driving amplitudes, synchronisation develops fully, enhancing further power increase in the alpha band. This effect is presented in Figure 5.4B, where the driving amplitude is set to $\tilde{A} = 5\tilde{A}_0 = 225$ s^{-1}, therefore to a value that allows to reach to 315 s^{-1}, thus to the end of the alpha limit cycle (end of regime V at 315.70 s^{-1} in Figure 2.4A). As a consequence during almost whole positive half of the driving sine all columns oscillate with the alpha frequency in a synchronous manner. Therefore, not only dynamics of each individual column, but also collective effects contribute to the increase of power in the alpha band. Next, we perform a systematic study of those effects.

In order to quantify the correlation between columns we used the Pearson correlation coefficient, which quantifies the amount of linear dependence between two signals. Time courses (1000 s long after discarded transients) corresponding to driving with amplitudes $\tilde{A} = \{1\tilde{A}_0, 2\tilde{A}_0, ..., 6\tilde{A}_0\}$ were cut to slices of durations equal to a full period of the driving signal (4 s), and each slice was then divided to 20 intervals, in which the Pearson coefficients were computed. The result for each driving amplitude is a vector of 20 averages over all columns and all slices. We show this result as a function of the instantaneous phase ϕ_{inst} in Figure 5.4C. In order to maintain the clarity of the plot we do not show error bars. The standard deviations of the distributions of Pearson coefficients values within each

interval never exceed 0.35, and due to high statistics the standard error of the mean is minimal in all cases.

The black triangles in Figure 5.4C correspond to the uncoupled system (with $K = 0, p = 90\ \mathrm{s}^{-1}$), and show no correlation for the most part of the positive half of the driving sine. The non-zero correlation corresponding to the negative half of the driving signal can be explained by the fact that for small and decreasing I_{ex}, in the bistable regime II (see Figure 2.4A), all columns tend to converge to, and follow, the node (blue). As a result, their time courses are correlated. This effect is also present in the coupled systems, and it can be seen in Figure 5.4B, where in spite of stochastic fluctuations all signals have a decreasing tendency for $\phi_{\mathrm{inst}} \in (\pi, 3/2\,\pi)$. At the end of this interval the common drive along the node branch slows down to zero, and noisy fluctuations dominate the dynamics and diminish the correlation, which recovers on the way back along the node branch during the driving upswing. The dip in correlation observed at $\phi_{\mathrm{inst}} = \pi/5$ corresponds to a regime in which the columns may already spike or oscillate, but synchronisation is not yet established (see Figure 5.4B again). Synchronisation emerges optimally around $\phi_{\mathrm{inst}} = \pi/2$, where driving through the regime V of alpha oscillations slows down to zero, and complete synchronisation is achieved most easily. This effect does not apply to the case of amplitude $\tilde{A} = 6\tilde{A}_0$, which can be explained by the fact that this value of the amplitude allows to overshoot the alpha limit cycle (regime V in Figure 2.4A) and enter the focus dynamics (regime VI), where noise affects the system more strongly than in the limit cycle regime, and synchronisation is partially lost. In what follows we explore how the changes of $\tilde{A}$ affect the power spectrum.

Impact of variations of $\tilde{A}, N$ and f on the power spectrum

The effect of variations of the driving signal amplitude on the power spectrum is shown in Figure 5.5A, with red indicating an *increase* in power and blue representing a *decrease* with respect to the stationary conditions. This figure shows that the power increase in the alpha band is robust with respect to the driving amplitude, provided its value is large enough. The slight increase in the frequency that responds maximally, observed for

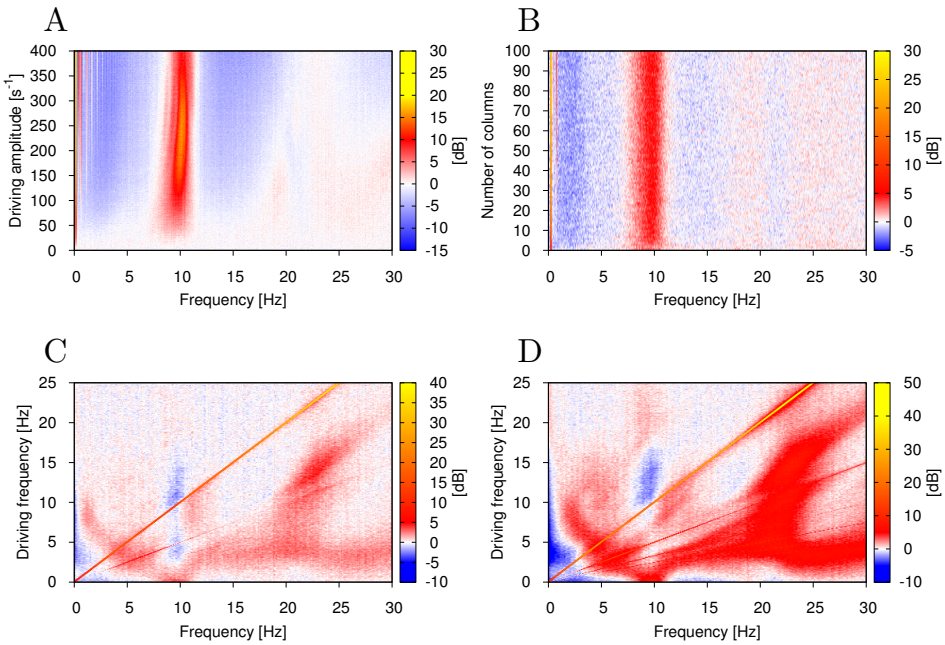

Figure 5.5: Relative change of the power spectrum with respect to stationary conditions as the function of the amplitude $\tilde{A}$ (panel A), number of columns N (panel B) and frequency f (panels C and D). Colour represents the relative change of the power spectrum expressed in dB, as defined by $10\log_{10}(\mathrm{PSD}_{\mathrm{driven}}/\mathrm{PSD}_{\mathrm{stat}})$, where $\mathrm{PSD}_{\mathrm{driven}}$ is the power spectrum in the presence of driving and $\mathrm{PSD}_{\mathrm{stat}}$ is the power spectrum in its absence. In panels A,C and D the number of columns was $N = 4$, in panels B,C and D the driving amplitude $\tilde{A}$ was fixed to $45\ \mathrm{s}^{-1}$, and in panels A and B the driving frequency was fixed to 0.25 Hz. Again, the analysis was performed on a system of all-to-all connected Jansen-Rit models of cortical columns in the presence of Ornstein-Uhlenbeck noise with intensity $D = 350\ \mathrm{s}^{-1}$ and correlation time $\tau = 0.15$ s. The coupling strength between the modules is $K = 15$.

large amplitude values, might be understood from the fact that the frequency of the limit cycle exhibited by the neural mass model increases slightly for increasing input to the columns (Spiegler et al., 2010).

Next, we studied the impact of the system size on the observed effect. The result shown in Figure 5.5B indicates that under the chosen conditions (oscillatory driving with amplitude $\tilde{A} = \tilde{A}_0 = 45\ \mathrm{s}^{-1}$ and frequency $f = 0.25$ Hz) the results are robust with respect to the system size. The only noticeable difference is the gain of power in low frequencies, which can be

explained by the fact that with an increase of N, the averaging procedure diminished fluctuations around the mean, which roughly follows the driving signal regardless to N. This leads to an increase of relative power at f.

Finally, we examined the response of the model with $N = 4$ columns to driving with a large span of signal frequencies, ranging from values much smaller than its intrinsic alpha frequency (as we have been discussing so far) all the way to much larger frequencies (up to 25 Hz). The results, shown in Figure 5.5C, reveal that an increase in alpha occurs only for low-enough driving frequencies ($f \lesssim 2$ Hz). As the driving frequency increases, the initial response at alpha splits and leads to increase of power at frequencies smaller and larger than alpha. Interestingly, at this point the alpha band undergoes a decrease, rather than an increase, in power. The low-frequency power ($\lesssim 0.5$ Hz) is also reduced for a wide range of driving frequencies. The response is dominated by a straight diagonal line corresponding to 1:1 response to the driving frequency, and by its first harmonic. This strong 1:1 response means that in the case of harmonic driving every injected frequency is transferred by the system. The same study performed for $\tilde{A} = 2\tilde{A}_0 = 90$ s^{-1} (Figure 5.5D) showed that the changes to the power spectrum are robust with respect to the driving amplitude, although for stronger signals higher harmonics show up and relative changes in the power spectrum are enhanced and widened. Also, the relative decrease of power in the alpha band occurs for driving frequencies faster than in the case presented in Figure 5.5C.

Driving with a reshaped signal

The experiment also showed a statistically significant increase of power for low frequencies. The increase is also observed in the model, but is much more centred (peaked) at the driving frequency (0.25 Hz) than in the experiment, where it is much smoother, probably due to reshaping of the low-frequency harmonic signal by sensory, thalamic and/or thalamocortical processing. In order to test whether driving with the processed signal also leads to an increase of power in the alpha band, in the next step we

injected into the system a reshaped signal of the form:

$$u_{\text{reshaped}}(t) = \tilde{A}' \sum_{n=n_{\min}}^{n_{\max}} 10^{-\frac{n \cdot f_{\text{step}} - f_{\min}}{f_{\max} - f_{\min}}} \sin[2\pi(n f_{\text{step}} t + X_n)] \tag{5.1}$$

where $n_{\min} = f_{\min}/f_{\text{step}}$, $n_{\max} = f_{\max}/f_{\text{step}}$, $f_{\min} = 0.05$ Hz is the minimal frequency of the driving, $f_{\max} = 4$ Hz is the maximal one, f_{step} was set to 0.05 Hz and X_n is a random number in the range $\langle 0, 1)$. This formula describes a signal composed of a sum of sines with frequencies from $f_{\min}$ to $f_{\max}$ taken every f_{step}, with exponentially decaying amplitudes and with randomly distributed phases. The choice of $f_{\max}$ has been dictated by the upper limit of the frequency interval in which Bayer et al. (2011) observed a significant increase of power. The amplitude $\tilde{A}' = 10.76$ s was set so that this composed signal delivered the same power to the model as the previously used simple sine signal with amplitude $\tilde{A} = 45$ s. We performed 10 full simulations for different distributions of random phases and averaged the power spectra obtained. The resulting averaged spectrum along with one standard deviation of the power spectrum distribution is shown in Figure 5.3B. This figure shows that driving with the reshaped signal reproduces the experimental results better than driving with a simple sine: the increase in the alpha band is present regardless of the randomisation of phases, and instead of a decrease of power for low frequencies (as observed in the simple sine driving case), an increase (similar to the experimental result) is observed. This increase in low frequencies is possible due to the aforementioned capability of the system of transferring power in a broad range of driving frequencies.

5.4 Discussion

We studied a minimal model that gives rise to broadband oscillations in the alpha frequency band. The model consists of a small number of cortical columns coupled in an all-to-all configuration. These columns received background signal from the rest of the brain in the form of a temporally correlated Ornstein-Uhlenbeck noise. We showed that the resulting power spectrum of synaptic activity qualitatively resembles experimental recordings: it follows a characteristic $1/f^b$-like profile with an embedded peak in

the alpha band. Future work could examine driving with other stochastic signals, which can recapitulate a $1/f^b$ power spectrum more accurately (see Section 1.4.5). Our results suggest that due to the system's capability of transferring power in a broad range of frequencies, such approach would also lead to a realistic response. This capability follows from the bifurcation structure of the model, in particular from the monotonically increasing stable node branch, which provides that, as long as the system remains in its basin of attraction, an increase of the external driving leads to an increase of the model's output.

Furthermore, for the set of parameters chosen, the bifurcation structure of the model features a limit cycle behaviour characterised by a well-defined alpha frequency (David and Friston, 2003), which in the power spectrum appear superimposed to the $1/f^b$ profile. On the other hand, generating this profile entails - in agreement with what we showed in Chapter 3 - that the neural mass model operates also in a spiking regime, which differs from the characteristic dynamics observed in the EEG of healthy subjects. This type of macroscopic measurement, however, reflects the behaviour of multiple coupled columns, and we showed that when this situation is considered in our model the spiking behaviour disappears due to averaging, rendering signals which recapitulate the experimentally observed EEG while maintaining the broad power spectrum. This does not have to always be the case: as we discussed in Chapter 4, excessively high coupling in the system leads to synchronous spiking, which would not be smeared out by the averaging procedure.

Furthermore, we have examined the effect of low-frequency driving with a simple sine signal and a composed one, showing a cross-frequency transfer through which these driving signals increase the power not only of low-frequency rhythms, but also of the alpha activity. The result qualitatively reproduces the experimental observations of Bayer et al. (2011) on the effect of rocking on alpha activity and sleep, and is robust with respect to the choice of model parameters. We showed that the increase of power in the alpha band results from both an enhancement of the alpha activity of individual cortical columns and collective synchronisation effects. These effects, in turn, are dependent on dynamical regime, as well

as on a balance between coupling and stochasticity, which here allowed for development of synchronisation of alpha oscillations, but not epileptic spiking. We also note a parallel of this scenario to mechanisms explaining event-related synchronisation (David et al., 2005; Pfurtscheller and Lopes da Silva, 1999). Our results suggest that certain types of cross-frequency transfer in the brain can be simply the result of passive driving of a broad-band neuronal oscillator, which brings this effect close to the vast body of work dealing with the driving and synchronisation of chaotic oscillators (Anishchenko et al., 2007; Boccaletti et al., 2002; Pikovsky et al., 2001).

Interestingly, a systematic analysis shows that the frequency transfer only occurs towards the intrinsic frequency of the oscillator (alpha) when the driving frequency is low; as it increases, the response shifts to both lower and higher frequencies, and the power in the alpha band decreases instead of increasing. We note that the range of driving frequencies, for which this phenomenon occurs, approximately corresponds to rhythms which cause the resonance effect reported in Chapter 3. This effect leads to attenuation of alpha oscillations in the system. Furthermore, the results presented here allow us to predict that driving faster than the one already tested experimentally should lead to a decrease of power in the alpha band. Testing this prediction experimentally in the setup used by Bayer et al. (2011) is not feasible due to high driving frequencies and potential discomfort of subjects. Alternative tests, e.g. by means of visual stimulation, could be potentially harmful, because in susceptible subjects they could elicit epileptic attacks (as discussed in Chapter 3). Taken together, our results indicate that a relatively simple oscillation-generation mechanism in neuronal populations has a strongly nontrivial response to periodic driving, providing a rich scenario to interpret a variety of cross-frequency phenomena in the brain.

5.5 Summary and outlook

In this chapter we extended the Jansen-Rit model to a number of globally coupled modules and we engaged spectral analysis in order to characterise the model's response to stochastic and periodic driving. We therefore extended and complemented results presented in previous chapters. We

demonstrated that a network of coupled neural masses subject to temporally correlated noise exhibits a well-defined rhythm (in the alpha range) embedded in a broadband spectral background similar to what is observed experimentally. We also showed that this broadband oscillator reacts to periodic driving at a frequency much lower than its natural frequency, by increasing its activity at the latter in agreement with experimental observations. We suggested a generic mechanism that might underlie cross-frequency interactions. This mechanism relies on the bifurcation properties of the model and it is enhanced by collective effects, namely by coupling-mediated synchronisation between individual columns. Future studies could focus on impact of delivering noise to populations of interneurons, as well as consider different stochastic processes and multiplicative noise.

This chapter concludes the first part of this Thesis, i.e. our study of the impact that coupling, stochasticity and periodic driving have on dynamics of the Jansen-Rit model. So far we were relating our theoretical findings to phenomena observed in the EEG recordings; in what follows we turn to modelling another macroscopic method of brain imaging - functional magnetic resonance.

CHAPTER 6

BOLD SIGNAL MODELLING

6.1 INTRODUCTION

Large-scale brain dynamics are often studied by means of EEG recordings. This methodology is particularly common due to its high temporal accuracy (practically limited only by the hardware sampling frequency) combined with its low price, non-invasiveness and simplicity of application. In this Thesis we have been interested so far in modelling various dynamical phenomena observed in EEG recordings. These recordings, however, are limited to probing outer brain structures (the cerebral cortex) and have a relatively poor spatial resolution (> 1 cm, Bojak and Breakspear, 2015) which limits our understanding of the full spatiotemporal organisation of the brain. To address these limitations, the functional magnetic resonance (fMRI) is often applied in neuroscience (Logothetis, 2003) due to its good coverage of the whole brain via its spatial resolution (> 0.5 mm, Bojak and Breakspear, 2015) is often applied in neuroscience . On the other hand, this technique exhibits a relatively low temporal resolution (> 1 s, Bojak and Breakspear, 2015), and therefore can be considered somehow complementary to the EEG.

Given the abovementioned limitations of the two techniques, a powerful approach is therefore based on simultaneous EEG/fMRI measurements. We deal with such combined data in this chapter. In order to model brain activity as registered in the EEG recordings, in the previous chapters we employed the Jansen-Rit neural mass model (see Chapter 2). However, the neuronal activity generated by such model can not be related to the fMRI signal in a straightforward manner. The reason for this is that the method does not directly register activity of the neurons, but rather the consequences of haemodynamic and metabolic processes affected by, and modulating, this activity. Therefore, in order to relate the simulated neuronal activity to the fMRI signal, one needs a model of these processes. In

this chapter we discuss this type of modelling, focusing in particular on their capability to reproduce poststimulus behaviour of the signal and on their applicability to modelling the resting state.

6.1.1 Basics of BOLD signal generation and detection

Increased local neuronal activity entails increased metabolism in the brain, which involves more oxygen usage. According to Buxton and Frank (1997) a moderate rise of the net consumption of oxygen (cerebral metabolic rate of oxygen - CMRO2) requires a larger than proportional increase of oxygen delivery and thus increased blood flow, because rise of blood flow itself entails a drop of oxygen extraction efficacy. As a result, counterintuitively, venous blood becomes locally more oxygenated or, in other words, local concentration of deoxygenated haemoglobin (deoxyhaemoglobin) in the blood drops. Deoxygenated haemoglobin, unlike the oxygenated one, has paramagnetic properties and therefore a change of its concentration alters magnetic susceptibility of the blood. The MRI signal caused by the change of deoxyhaemoglobin content is called Blood Oxygenation Level Dependent (BOLD) signal. A decrease of deoxyhaemoglobin content implies an increase of the BOLD signal, which is usually delayed by about 2 s with respect to stimulus (Logothetis, 2003).

It was observed, however, that the typical BOLD response resulting from a transient stimulus is not entirely positive, but rather starts and ends with negative values. They are often referred to as 'initial dip' and 'post-stimulus undershoot' (see Figure 6.1). There is currently no agreement about the origin of these two features of the BOLD signal. The initial dip is subtle and not always registered; the undershoot is more prominent and therefore has been the subject of several experimental and theoretical studies (Buxton, 2012). These studies are important for understanding the mechanisms underlying the BOLD response, which in turn would allow to infer neuronal activity from the fMRI recordings (Heeger and Ress, 2002).

6.1.2 Modelling the poststimulus undershoot: the Balloon Model

One of the first mathematical models of the poststimulus phenomenon assumes that the undershoot originates in the delayed high oxygen extraction needed to restore oxygen in the tissue after the stimulus has ceased,

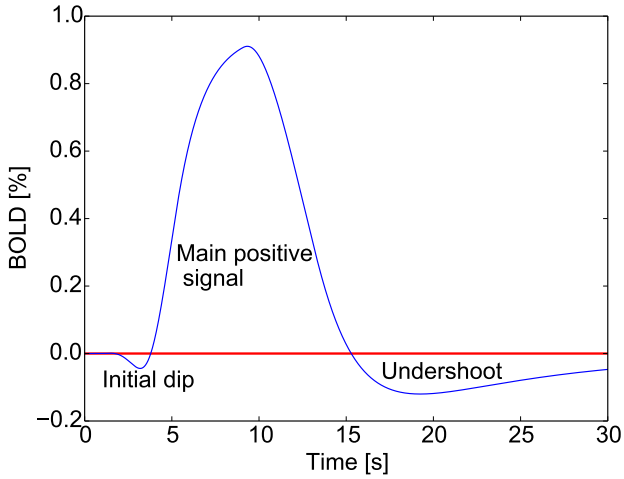

Figure 6.1: A typical shape of a stimulus-induced BOLD (blue) response deviation from baseline (red). This figure does not depict experimentally collected data; it is a sketch illustrating a typical time course of the BOLD response to transient stimulation.

and blood flow and volume have already returned to baseline (Davis et al., 1998). Another scenario is based on the observation of Mandeville et al. (1996, 1998), who noted that changes of blood flow are not tightly coupled temporally to changes in the volume of the venous compartment in the somatosensory cortex of rats. The blood flow was found to evolve on a fast timescale, whereas the volume evolved on both: a fast and a slow timescale. Experimental studies of Grubb et al. (1974) had previously shown that the relative changes of these two quantities are related by a power law. Mandeville et al. (1996, 1998) generalised this relation (from now on referred to as 'Grubb's relation') to transient states, in which, in particular, the value of the exponent varies. This result prompted Buxton et al. (1998) to formulate a model, which explains the BOLD signal poststimulus undershoot by means of a delayed elevation of volume of

the venous compartment, when the CMRO2 and the blood flow have already returned to baseline. This results in reduced clearance of deoxyhaemoglobin and consequently in an undershoot of the BOLD signal. Buxton et al. (1998) modelled this temporal decoupling by increasing nonlinearity in the Grubb's relation and, due to the slow inflation/deflation of the venous compartment, they called their model a 'Balloon Model'.

Shortly afterwards, Mandeville et al. (1999) formulated their own mathematical model describing the dynamics of capillary and venous compliance responding to blood pressure. They built on the Windkessel theory[1] and arrived to a formulation that was consistent with Grubb's relation in the steady state, but which was in general non-stationary. Similarly to Buxton et al. (1998) they recognised the delayed blood volume elevation as a potential explanation of the BOLD signal undershoot effect. Next, Friston et al. (2000) used the considerations of Mandeville et al. (1999) in order to modify the Balloon Model of Buxton et al. (1998). Friston et al. (2000) restored the stationary Grubb's relation and, as a consequence, their approach does not take into account the transient decoupling between blood flow and volume (which was the main motivation for the Balloon Model and the possible origin of the poststimulus undershoot). In order to be able to test their model on data from fMRI stimulation protocols, Friston et al. (2000) additionally introduced a transformation converting this stimulation to blood flow ('neurovascular model' from now on). Friston et al. (2000) were the first to use the combined term 'Balloon-Windkessel', and this is how we refer in this chapter to their version of the model. When referring to both models we will use the term 'haemodynamic model'.

6.1.3 Poststimulus overshoot

Recently, Mullinger et al. (2013) reported that the undershoot is not always present in the BOLD signal, but may be replaced by an overshoot. Furthermore, Mullinger et al. (2013) observed that the poststimulus behaviour of the BOLD signal is modulated by the EEG power of the mu rhythm[2]

[1] Windkessel (German: 'air chamber') - a theory, proposed in 1899 by Otto Frank, who performed experiments with water passing through a leather bag and described its dynamics mathematically.

[2] The mu rhythm falls into the alpha band, but it has a different origin than the alpha rhythm: it is associated with voluntary movement and is found only over the motor cortex.

registered in the $8 - 13$ Hz frequency band. In particular, higher power of poststimulus event-related synchronisation (PERS) of the mu rhythm implies a poststimulus undershoot of the BOLD signal, whereas lower power of PERS of the mu rhythm implies an *overshoot*. This result shows that the poststimulus shape of the BOLD signal is not only related to the dynamics of the venous compartment and to metabolism (as considered in the approaches discussed above) but rather also involves some aspects of neuronal activity. Mullinger et al. (2013) employed the model of Davis et al. (1998) in order to estimate CMRO2 from experimentally measured blood flow and BOLD. The results obtained contradict with the scenario suggested for the Balloon Model, so Mullinger et al. (2013) conclude that the interpretation of the undershoot provided by this model is not fully correct. They do not, however, implement this model themselves, thus they do not test directly how well it reproduces their experimental data. Here we complement their work and implement the Balloon Model and the Balloon-Windkessel Models, and we test these models on experimental data involving both the poststimulus undershoot and overshoot.

6.1.4 Modelling the resting state fMRI

The effects mentioned above appear as a result of stimulation, which alters neuronal activity (and hence haemodynamics and metabolism). Nevertheless, a state lacking any stimulation - the 'resting state' - has been shown in numerous studies to be very informative about brain dynamics (Deco et al., 2013). For this reason, recording and modelling of the fMRI signal in this state is of high interest. Since spatial resolution of these recordings (> 0.5 mm, Bojak and Breakspear, 2015) corresponds to the mesoscopic scale neuronal structures (see Section 1.1.3), it is natural to employ neuronal population models, such as the neural mass models introduced in Chapter 2, to mimic the neuronal activity that can later be transformed into the BOLD signal. In order to perform this transformation, in practise one needs first to convert neuronal activity to the resulting blood flow, which is then transformed into the BOLD signal. The chain of operations illustrating the whole process is shown in Figure 6.2. In that scheme, the modelling of stimulation is marked as optional (in parentheses) because it does not apply to the steady state. The output of the neuronal model is

fed into a neurovascular model, which converts it to blood flow. This, in turn, can be an input to the haemodynamic model, which gives the BOLD signal.

Although a number of more sophisticated models have recently been proposed (see Buxton, 2012) and although they account for some physiological effects better than the Balloon-Windkessel Model, it is still precisely this model that is until today widely used by the neuronal modelling community (in particular, in the resting state context). Given that the haemodynamic model was designed to capture effects arising in the steady state, due to a clearly distinguishable stimulation, it might not be straightforward to employ this model's methodology to mimic this background itself. In this chapter we examine some consequences of using the Balloon and the Balloon-Windkessel Models in the resting state context, together with neuronal models (such as the Jansen-Rit model introduced in Chapter 2).

6.2 MODELS AND METHODS

We now introduce in detail the model components constituting the transformation pipeline shown in Figure 6.2. We do not discuss neuronal models, as they can be implemented in multiple ways, one of which (neural mass modelling) was explored in Chapter 2. In order to introduce the pipeline components more clearly, we start from the output (the BOLD signal) and progress with the description backwards along the pipeline.

6.2.1 Balloon and Balloon-Windkessel models

In the reminder of this chapter we consider both the 'Balloon Model' introduced by Buxton et al. (1998), and the 'Balloon-Windkessel Model' proposed by Friston et al. (2000). If not stated explicitly otherwise, our discussion applies to both models. All parameter values and state variables of the two models are listed in Table 6.1. They are both nonlinear input-state-output models; they are not time-invariant, which means that they account for the fact that a response to a stimulus depends on their current state. The 'balloon' represents a venous compartment and can be interpreted as a representation of one voxel of the fMRI image. We now discuss this model in detail.

Parameter	Meaning	Units	Balloon	Balloon-Windkessel
$V_0^\dagger$	Volume of blood that is intravascular in the steady state	ml	NS	
V_0	Fraction of blood that is intravascular in the steady state.	-	0.01	0.02
Q_0	Deoxyhaemoglobin content in the steady state	NS	NS	
E_0	Oxygen extraction rate in the steady state	-	0.4	0.34
k_1	Constant derived from earlier studies. Its value was estimated for magnetic field $B_0 = 1.5\ T$ and TE=40 ms.	-	$\simeq 7E_0$	
k_2	Constant derived from earlier studies	-	$\simeq 2$	
k_3	Constant derived from earlier studies	-	$\simeq 2E_0 - 0.2$	
L_0	Flow rate of blood in the steady state	ml/s	NS	
τ_0	Blood transition time through venous compartment in the steady state = $V_0^\dagger / L_0$	s	2	0.98
α	Venous compartment 'balloon' stiffness parameter	-	≤ 0.5	0.33
State variable	**Meaning**	**Units**	**Balloon**	**Balloon-Windkessel**
$V(t)^\dagger$	Volume of blood that is intravascular in general	ml		
$V(t)$	Fraction of blood that is intravascular in general	-		
$Q(t)$	Deoxyhaemoglobin content in general	NS		
$E(t)$	$E(t) = E(l_{\text{in}}(t))$ Oxygen extraction rate in general	-		
$L_{\text{in}}(t)$	Flow rate of the blood incoming to the vascular balloon	ml/s		
$L_{\text{out}}(V)$	Flow rate of the blood outgoing from the vascular balloon	ml/s		
CMRO_2	Relative cerebral metabolic rate of oxygen	-	$l_{\text{in}}(v(t)) \cdot E(t)$	
$l_{\text{in}}(v)$	Relative flow rate of the blood incoming to the vascular balloon with respect to the steady state	-	L_{in}/L_0	
$l_{\text{out}}(v)$	Relative flow rate of the blood outgoing from the vascular balloon with respect to the steady state	-	L_{out}/L_0	
$v(t)$	Volume of the intravascular blood (the balloon) relative to the steady state	-	$V(t)/V_0 = V(t)^\dagger / V_0^\dagger$	
$q(t)$	Deoxyhaemoglobin content relative to the steady state	-	$Q(t)/Q_0$	

Table 6.1: Parameter values and state variables of the Balloon and the Balloon-Windkessel models as specified by Buxton and Frank (1997) and Friston et al. (2000), respectively. '-' means that the variable or parameter is dimensionless. All symbols with subscript '0' refer to the lower steady state. Variables denoted with lowercase symbols stand for the values relative to this state. In order to avoid confusion between relative and absolute volume, we here distinguish the latter with a dagger. 'NS' stands for 'Not Specified'.

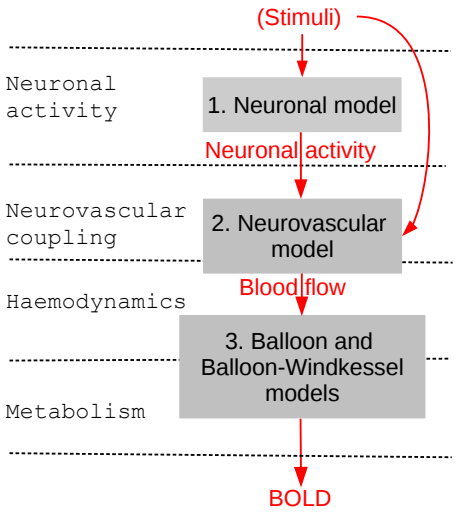

Figure 6.2: Chain of transformations performed in consecutive steps of the workflow pipeline. The grey boxes stand for models of different processes and the red, annotated arrows stand for their input/output signals. Dashed horizontal lines separate domains of classes of physiological processes. Simulating neuronal activity is optional; in a simplified case the neuronal model is not included in the pipeline, and some characteristics of the stimulation applied to subjects (e.g. its intensity or frequency) serves directly as an input to the neurovascular model. This simplified path is illustrated here with the curved arrow. If the neuronal model is present, it may generate resting state activity (no stimuli) or it may be externally perturbed.

The BOLD signal

Buxton et al. (1998) obtained the following formula for the BOLD signal by combining earlier numerical studies (references 21-25 from Buxton et al., 1998) and assuming small deviations from equilibrium:

$$\mathrm{BOLD}(t) = V_0 \left[k_1(1 - q(t)) + k_2 \left(1 - \frac{q}{v}\right) + k_3(1 - v(t)) \right], \tag{6.1}$$

where $v(t)$ is a normalised variable equal to $V(t)/V_0$, with V_0 being the fraction of blood that is intravascular in the steady state, and $V(t)$ denoting the change of this fraction over time. An increase of $v(t)$ corresponds to inflation of the vascular 'balloon', which is assumed here to be the main contributor to the change of the overall blood volume. Similarly, the model assumes that all the deoxyhaemoglobin remains in the venous

compartments. $q(t) = Q(t)/Q_0$ stands for the relative change in the deoxyhaemoglobin content with respect to the steady state. Subscript naught indicates variables referring to the steady state, in which the relative values, denoted by lowercase variables (e.g. $v(t)$, $q(t)$), equal 1. k_1, k_2, k_3 are dimensionless constants taken from earlier works (see references 23 and 25 from Buxton et al., 1998) and set accordingly to the specific settings of the fMRI magnet.

Dynamics of the venous compartment - the balloon

In steady state, blood delivery to the venous balloon (blood input flow) $L_{\text{in}}(t)$ equals blood output flow $L_{\text{out}}(t)$, and they both equal L_0. Therefore, in that state the relative quantities: $l_{\text{in}}(t) = L_{\text{in}}(t)/L_0$ and $l_{\text{out}} = L_{\text{out}}(t)/L_0$ are both equal to 1. When blood delivery exceeds blood outflow, the venous balloon inflates. $l_{\text{out}}(t)$ in turn, gets amplified by pressure caused by the inflated balloon. This quantity is an input (in general time-dependent) to the model, and the output flow, l_{out}, is one of the model's state variables that is a function solely of the venous compartment volume $v(t)$ (denoted in this relation 'v' for readability). Grubb et al. (1974) found experimentally that the latter function in the steady state follows:

$$l_{\text{out}}(v) = v^{1/\alpha}, \tag{6.2}$$

where α is a constant exponent describing the stiffness of the balloon, estimated by Grubb et al. (1974) to 0.38.

Additionally, Buxton et al. (1998) took into account experimental results of Mandeville et al. (1996, 1999), from which it follows that the tight temporal coupling between $v(t)$ and $l_{\text{out}}(v)$ is transiently lost during periods of rapid changes of the state variables. Buxton et al. (1998) modified Grubb's formula in a way that complies with Equation (6.2) in two limit steady states: in the absence of stimulation and during long, constant stimulation that results in a steady, maximal increase of blood flow. In the former case (from now on referred to as the 'lower steady state') $l_{\text{out}} = 1$ by definition. For the latter case (from now on referred to as the 'higher steady state'), both Buxton et al. (1998) and Mandeville et al. (1996, 1999) observed an increase of blood flow up to 70% with respect to the lower steady state, therefore $l_{\text{out,h}} = 1.7$ (output blood flow in the high steady state). Buxton

et al. (1998) suggested that in between the two limits the new $l_{\text{out}} = f(v)$ relation[3] should have increased nonlinearity, in order to account for the temporal decoupling between $l_{\text{out}}(v)$ and $v(t)$. This approach is alternative to the explicit non-stationarity introduced by Mandeville et al. (1999). Here, the relation in fact remains stationary, but due to the increased nonlinearity, there is a regime in which small changes of volume are needed to significantly affect the flow. During deflation it results in an apparent lag of the volume behind the flow, and it mimics decoupling of these two quantities.

Buxton et al. (1998) do not specify the exact formula governing the relation $l_{\text{out}} = f(v)$ used in their article. Since this formula is needed to examine their approach, we propose it in the following form, which generalises Grubb's relation:

$$l_{\text{out}}(v) = a \cdot v^{1/\alpha} + b. \tag{6.3}$$

Taking into account the steady state constraints imposed by Buxton et al. (1998) leads to the following values of coefficients a and b:

$$\begin{cases} a = \dfrac{l_{\text{out,h}} - 1}{v_h^{1/\alpha} - 1} & (6.4) \\ b = 1 - a, & (6.5) \end{cases}$$

where $l_{\text{out,h}} = 1.7$ is the relative flow in the high steady state and $v_h = \sqrt{l_{\text{out,h}}} \simeq 1.3$ is the relative volume in that state. These values assure fulfilment of the boundary constraints, thus compliance with Equation (6.2) in the lower ($l_{\text{out,l}} = v_l = 1$) and higher ($l_{\text{out,h}} = 1.7,\ v_h = \sqrt{1.7}$) steady states for α equal to the reference value 0.5. At the same time, through variations of the α parameter, Equation (6.3) allows to alter the nonlinearity of the relation $l_{\text{out}} = f(v)$, affecting the system's behaviour in between the steady states. We therefore propose a concrete implementation of the temporal decoupling as suggested by Buxton et al. (1998). In the Balloon-Windkessel Model, Friston et al. (2000) used a power law (Equation (6.2)) and by fitting experimental data they estimated the exponent α to be equal to 0.33. This value is relatively close to the value observed by Grubb et al.

[3] 'f' means simply 'a function' here.

(1974) ($\alpha = 0.38$) and to the asymptotic steady state value predicted by Mandeville et al. (1999) ($\alpha = 0.36$).

In order to complete the description of the balloon dynamics, we specify one more relation, concerned with the rate of change of the relative volume of the venous balloon. It is dictated by mass conservation and the resulting balance between the input and output flows, and is given by the following formula:

$$\frac{dv}{dt} = \frac{1}{\tau_0}[l_{\text{in}}(t) - l_{\text{out}}(v)] \tag{6.6}$$

where τ_0 determines the rate of change of the volume.

Dynamics of metabolic processes

According to Buxton et al. (1998), the rate of change of the normalised deoxyhaemoglobin content is given by:

$$\frac{dq}{dt} = \frac{1}{\tau_0}\left[l_{\text{in}}(t)\frac{E(l_{\text{in}}(t))}{E_0} - l_{\text{out}}(v)\frac{q(t)}{v(t)}\right] \tag{6.7}$$

Here E_0 is the rate of oxygen extraction in the lower steady state, and $E(l_{\text{in}}(t))$ is this rate in an arbitrary state. This rate is given by a nonlinear formula, which couples metabolism and flow (for readability we drop time dependence of l_{in}):

$$E(l_{\text{in}}) = 1 - (1 - E_0)^{1/l_{\text{in}}}. \tag{6.8}$$

This formula follows from the microscopic oxygen transport model developed earlier by the authors of the Balloon Model (Buxton and Frank, 1997). In brief: when blood passes through capillaries faster, then the probability of oxygen uptake decreases. The oxygen limitation model adopted here (Buxton and Frank, 1997) assumes that (1) all oxygen that passes from capillaries to tissue is metabolised (there is no oxygen reservoir in tissue), and (2) no capillary recruitment is possible (all capillaries are perfused all the time). From these assumptions it follows that the increased demand for oxygen can be satisfied only by increased blood flow. Higher blood velocity entails reduced blood passage time through capillaries, and thus reduction of oxygen uptake probability, which in macroscopic terms translates to a reduction of oxygen extraction efficiency as expressed in Equation (6.8).

Parameter	Meaning	Units	Value
ϵ	Efficacy of the 'neuronal activity $\rightarrow$ blood flow' reaction	s^{-1}	0.54
τ_s	Time constant of the signal decay	s	1.54
τ_f	Time constant of the autoregulatory feedback of blood flow	s^2	2.46
Variable	**Meaning**	**Units**	
$s(t)$	Flow inducing signal (vasodilatory signal)	s^{-1}	
$n(t)$	Neuronal activity indicator	s^{-1}	

Table 6.2: Parameters and variables of the neurovascular model (Friston et al., 2000). Units and the value of ϵ correspond to the approach adopted by Friston et al. (2000), who considered the rate of stimulus presentation $n(t)$ as an input to the model.

6.2.2 Neurovascular model

Friston et al. (2000) proposed a linear neurovascular model that couples neuronal activity with the cerebral blood flow in the following way:

$$\begin{cases} \dot{l}_{\text{in}}(t) = s(t) & (6.9) \\ \dot{s}(t) \quad = \epsilon n(t) - s(t)/\tau_s - (l_{\text{in}(t)} - 1)/\tau_f, & (6.10) \end{cases}$$

where $l_{\text{in}}(t)$ has the same meaning (incoming blood flow) as in the Balloon and Balloon-Windkessel models. τ_s and τ_f are time constants (see table 6.2), $s(t)$ is some flow-inducing signal (vasodilatory signal), and $n(t)$ is an input proportional to neuronal activity. Friston et al. (2000) did not relate this input strictly to neuronal physiology, but assumed instead that the neuronal activity is in general linearly proportional to the rate of stimulus presentation $n(t)$, which is known in experiments. The coefficient of this proportionality is given by ϵ. In general, the input $n(t)$ can come from the output of a neuronal model, such as the Jansen-Rit model employed in earlier chapters of this Thesis. Such approach relies on the correspondence of spatial scales considered in the two modelling domains (neuronal and haemodynamic). The assumption mentioned above about linearity of neurovascular coupling was later supported by experimental evidence (Logothetis, 2003).

Equations (6.9)-(6.10) can be put together and expressed in a compact form:

$$\ddot{l}_{\text{in}}(t) + \dot{l}_{\text{in}}(t)/\tau_s + (l_{\text{in}}(t) - 1)/\tau_f = \epsilon\, n(t) \tag{6.11}$$

This is a formula governing a driven damped harmonic oscillator, which in an undriven case has a steady state at $l_{\text{in}} = 1$. From this equation, similarly to Friston et al. (2000) and Bojak and Breakspear (2015), we derive the damping coefficient ζ, the natural frequency f_0, and the resonant frequency f_r. Since our result for f_r slightly differs from those published earlier, we examined them in detail and found that Friston et al. (2000) in fact specify the natural frequency of the oscillator, although they refer to it as the 'resonance frequency', and Bojak and Breakspear (2015) specify a different value of the resonant frequency (0.088 Hz instead of 0.07 Hz). In order to clarify the characteristics of this oscillator, we list them in Table 6.3. The oscillator is found to be (significantly) underdamped, what introduces a rebound that yields an undershoot of the relative cerebral blood flow l_{in}.

Table 6.3 also shows that the natural and resonant frequencies of the oscillator are of the order of 0.1 Hz. Next, we estimate the amplitude of the response of this oscillator under driving with frequencies such as those generated by the neuronal model used in previous chapters of this Thesis. We assume that the driving is harmonic, has an amplitude A and angular frequency ω, and we consider the resulting formula for amplitude of forced oscillations, $A/\sqrt{(\omega^2 - \omega_0^2)^2 + (2\zeta\omega\omega_0)^2}$, in two limits: when $\omega = \omega_0$ and when $\omega \gg \omega_0$. In the first case, with $\zeta = 1/2$ (like here, see Table 6.3), the amplitude of the resulting oscillations is A/ω_0^2. In the second case, the amplitude of these oscillations can be approximated by A/ω^2. The second case applies to the Jansen-Rit model, which we utilised in the previous chapters of this Thesis. This model exhibits oscillations, characterised with a natural frequency $f^{\text{JR}} \sim 10$ Hz, thus $\sim 10^2$ times greater than the natural frequency of the neurovascular model discussed here. As a result, the amplitude of oscillations elicited by a driving at this frequency is reduced by the factor of $\sim 10^4$ with respect to slow driving close f_0.

Variable	Meaning	Formula	Units	Value
ω_0	Angular natural frequency	$1/\sqrt{\tau_f}$	Hz	0.64
f_0	Ordinary natural frequency	$\omega_0/2\pi$	Hz	0.1
ζ	Damping coefficient	$\frac{1}{2}\sqrt{\tau_f}/\tau_s$	-	0.51
f_r	Ordinary resonant frequency	$\omega_0\sqrt{1-2\zeta^2}/2\pi$	Hz	0.07

Table 6.3: Characteristics of the neurovascular model (Friston et al., 2000).

6.2.3 Scaling of the neuronal activity input signal

The Balloon and the Balloon-Windkessel models were developed to model evoked potentials: deviations of the BOLD signal from baseline. The question arises, however, how should these models be used in case of the resting state, where no clear distinction between (lower) steady states and stimulus application periods can be made. Furthermore, since neuronal activity may be quantified in general by different physical or physiological quantities, (e.g. firing rate, LFP or EEG potential) it may be expressed in different units, with different magnitudes, etc. For this reason, driving the neurovascular model (Friston et al., 2000) with this signal should be preceded by a transformation converting it to a suitable format and magnitude that allows to match it to this model. For example, in order to assure that the signal varies around zero, one can subtract the mean from the whole neuronal activity time series (Bojak, 2014). Furthermore, although it is not clear how various aspects of neuronal activity map onto the haemodynamic response, it is clear that the resulting increase of the cerebral blood has physiological limits. In order to guarantee this, Bojak and Breakspear (2015) proposed to set $\epsilon = \omega_0^2\zeta/A$, where A is the amplitude of the driving. When the driving is harmonic, this choice limits the resulting amplitude of the relative blood flow to $1/\sqrt{2} \sim 0.71$. We note the consistency between this limitation and experimental observations of the maximal blood flow ($\sim 70\%$, see above). We employ this scaling in Section 6.3.2.

6.2.4 Experimental data

We test the models described above on experimental data shared with us by Mullinger et al. (2013). A detailed description of the experimental procedure can be found in their publication. Here, we stress that these data include blood flow (measured with the arterial spin-labelling technique) and the BOLD signal. This allows us to examine separately components '2' and '3' from Figure 6.2. Moreover, a simultaneous EEG recording was performed and the collected blood flow and BOLD signal data were divided into four groups according to the power of EEG PERS of the mu rhythm ($8 - 13$ Hz). The first group corresponds to the lowest quartile of power ($0\% - 25\%$), the second group to the median quartile ($37.5\% - 62.5\%$), the third group to the highest quartile ($75\% - 100\%$), and the fourth group to the data corresponding to these three quartiles. According to Mullinger et al. (2013), the EEG PERS power in the mu band correlates with the poststimulus behaviour of the BOLD signal, therefore this signal from the first (third) group is characterised with a poststimulus overshoot (undershoot). We model signals from distinct groups separately, referring to them as 'PERS group I-IV'.

The EEG, fMRI and the blood flow measurements were performed simultaneously via the following protocol: 10 seconds of median nerve stimulation followed by 20 seconds of rest (see Figure 6.4B), repeated 40 times for each of the 11 subjects. The power of PERS was measured in the first 10 seconds of rest. For each subject the BOLD and the blood flow time series were averaged over trials within each quartile. Baselines were calculated independently for each subject as the mean value of the last 6 s of signal within each trial. As a result, 11 time series of BOLD data and 11 time series of blood flow data - each corresponding to one subject and each 30 s long - were obtained in each PERS group. Hardware sampling of the BOLD and CBF data was 2.6 s, which was then oversampled to 0.1 s. Dr Karen Mullinger provided us data in this form and then we averaged them over the subjects to get the mean value and standard error of the mean of the BOLD and blood flow data.

6.2.5 Numerical methods

In order to integrate the model we used the SciPy method `scipy.integrate.odeint()`, wrapping a FORTRAN `LSODA` routine from `ODEPACK` library. We used a constant 0.001 s long integration time step.

6.3 RESULTS

In this section we study the differences between the Balloon Model (Buxton et al., 1998, additionally furnished with the relation $l_{\text{out}} = f(v)$ introduced by us) and the Balloon-Windkessel Model (Friston et al., 2000). In particular we explore the relevance to the post stimulus behaviour of the BOLD signal of the dependence of $l_{\text{out}}(v)$ and of the value of the stiffness parameter α . Then we focus on the neurovascular model, in particular on the effect of its input signal transformation and on its relevance in reproducing experimentally measured blood flow. Finally, we test the Balloon and the Balloon-Windkessel models on experimental data.

6.3.1 Modelling the poststimulus undershoot

Here we compare the dynamics of the Balloon (Buxton and Frank, 1997) and the Balloon-Windkessel (Friston et al., 2000) models, and in particular we focus on the mechanisms generating the post-stimulus undershoot. The former model is furnished with the $l_{\text{out}} = f(v)$ relation as proposed by Buxton and Frank (1997) using the concrete form proposed by us (see Equation (6.3)). The latter model involves the Grubb's relation (see Equation (6.2)). In order to disentangle the effects following from the choice of the relation $l_{\text{out}} = f(v)$ from the effects following from the choice of parameter values, we test each model on its own parameter set and on the set of the other model[4]. Both sets of parameters are listed in Table 6.1.

Figure 6.3 shows chosen state variables of the Balloon and Balloon-Windkessel models: relative blood flow input (l_{in}) and output (l_{out}), venous compartment volume (v), and the BOLD signal. l_{in} follows a trapezoidal function, identical to the one used by Buxton et al. (1998): it has a

[4]In general swapping parameter values between two different representations might lead to unrealistic results. Therefore such two cases presented here should be understood only as studies of the dynamical properties of the models.

minimum at 1, a maximum at 1.7, 4 s of raise, 4 s of plateau, and 4 s of decay. The top panels correspond to the case in which $l_{\text{out}}(v) = a \cdot v^{1/\alpha} + b$ (the Balloon Model) with a and b values following from Equations (6.4) and (6.5), respectively. The bottom panels correspond to the case in which $l_{\text{out}}(v) = v^{1/\alpha}$ (the Balloon-Windkessel Model). The panels on the left correspond to the set of parameters proposed by Buxton et al. (1998) for the Balloon Model, and the panels on the right to the set of parameters proposed by Friston et al. (2000) for the Balloon-Windkessel Model (see Table 6.1 for both parameter sets). In the former case, the value of the stiffness parameter $\alpha = 0.066$ is suggested by us in a way that provides increased nonlinearity, as described by Buxton and Frank (1997). Each panel in Figure 6.3 includes an inset showing the relation $l_{\text{out}} = f(v)$ within the range concerned by the simulation.

The BOLD signal exhibits an undershoot observed only in the case shown in Figure 6.3A, i.e. for parameter values and the relation $l_{\text{out}} = f(v)$ corresponding to the Balloon Model. This reproduces the result of Buxton et al. (1998), and since we have here an expression for the relation $l_{\text{out}} = f(v)$, we can additionally analyse the mechanism of the undershoot effect. Returning of the input blood flow (green) to the lower steady state ($t = 13$ s, $l_{\text{in}} = 1$) entails that also $E(l_{\text{in}}) = 1$ (see Equation (6.7)). Therefore, Equation (6.7) reduces to: $\frac{dq}{dt} = \frac{1}{\tau_0}[1 - q(t)\frac{l_{\text{out}}(v)}{v(t)}]$, which has a fixed point $g^* = v/l_{\text{out}}$. From Equation (6.1) it follows that the BOLD signal is negative approximately when $q > 1$, so one can expect an undershoot of BOLD when $q^* > 1$, and thus $v > l_{\text{out}}$. This is the aforementioned delayed (with respect to blood flow) elevation of the balloon volume and this explains why the BOLD undershoot depends on the relation $l_{\text{out}} = f(v)$. The inset in panel 6.3A shows this relation along with the $1 : 1$ reference line (dotted), which highlights the existence of a regime where $v > l_{\text{out}}$. We find numerically that this regime exists for $v \in (1, 1.2)$. Continuous increase of v from the lower steady state (at $v = 1$) requires passing through that regime, which results in a characteristic dip in the BOLD signal at the beginning of the time course (blue in Figure 6.3, around $t = 4$ s).

Next, we found the limit value of the α parameter, above which the undershoot does not occur. It is given by the solution of the following

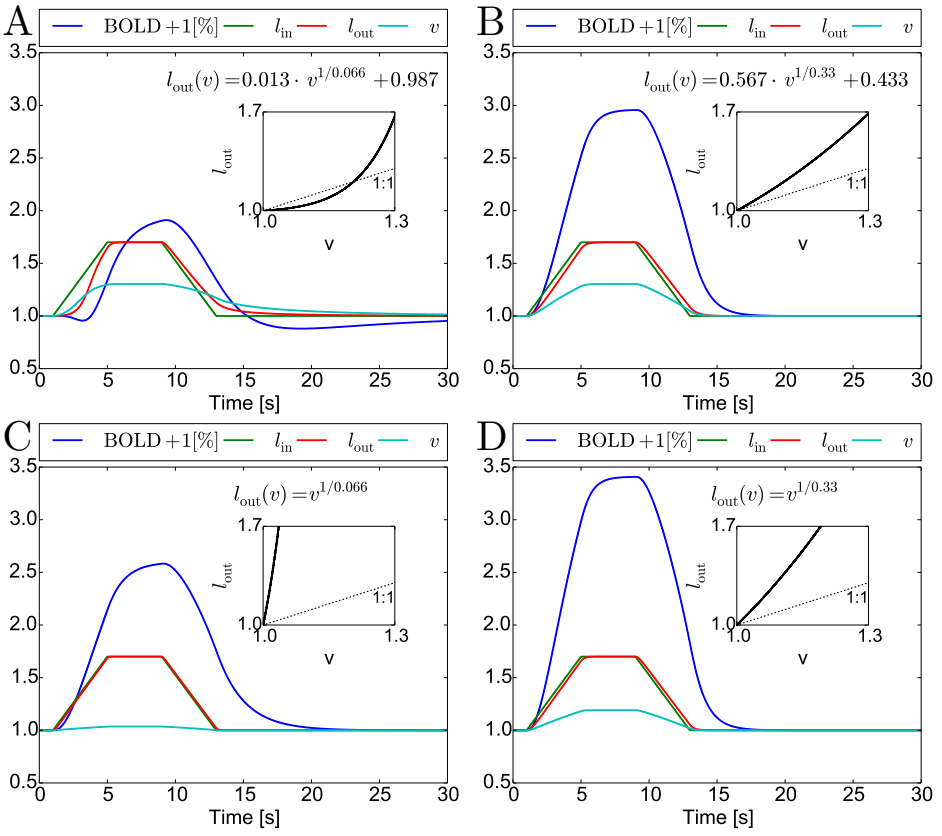

Figure 6.3: Dynamics of the Balloon and the Balloon-Windkessel models. Time evolution of the relative input (green) and output (red) blood flows, as well as volume (cyan) and the BOLD signal (blue) are shown for four different settings. Panels A and B correspond to the Balloon Model (Buxton and Frank, 1997) with the relation $l_{\text{out}} = f(v)$ given by Equation (6.5). Panels C and D correspond to the Balloon-Windkessel Model (Friston et al., 2000). Parameter values were set according to Table 6.1. Panels A and C correspond to the parameter set of the Balloon Model (with $\alpha = 0.066$), and panels B and D to the parameter set of the Balloon Model-Windkessel Model. In all cases the relation $l_{\text{out}} = f(v)$ is explicitly given and plotted in insets. Note that in order to highlight the correlation between all time traces, the BOLD signal was shifted upwards by 1. For all cases the relative input blood flow (green) follows a trapezoidal function (see text for details).

equation:

$$\left.\frac{dl_{\text{out}}(v)}{dv}\right|_{v=1} = 1 \tag{6.12}$$

where $l_{\text{out}}(v)$ is given by Equation (6.3) with values of the coefficients $a(\alpha)$ and $b(\alpha)$ following from Equations (6.4) and (6.5), respectively. Solving Equation (6.12) is straightforward and yields $a(\alpha_{\text{limit}}) = \alpha_{\text{limit}}$, from where we numerically find $\alpha_{\text{limit}} \simeq 0.156$. By integrating the Balloon Model we verified that no undershoot is present for $\alpha > \alpha_{\text{limit}}$. Indeed, Figure 6.3B shows that changing the parameter set to the one with $\alpha = 0.33$ does not yield the undershoot. Figures 6.3C,D show that for the two values of alpha used here, the undershoot is not present when $l_{\text{out}}(v)$ simply equals $v^{1/\alpha}$. This is related to the lack of a regime where $v > l_{\text{out}}$ (see insets to both these panels).

6.3.2 Neurovascular model

In this section we present the result of transforming neuronal activity to blood flow within the neurovascular model (Friston et al., 2000). We compare the results obtained with the previously published experimental data (Mullinger et al., 2013). Additionally we test the scaling of the input, which is performed in the resting state, where no clear stimulus can be distinguished.

Figure 6.4A shows the response (blood flow) of the neurovascular model to harmonic driving at the model's resonant frequency (f_r = 0.07 Hz, see Table 6.3). The unscaled signal (blue) is given by: $A\sin(2\pi f_r) + B$, where A and B were set to arbitrary values 1.5 and 0.5, respectively. The green line shows the same signal after removal of the mean and after scaling by $A/\omega_0^2\zeta$, as discussed in Section 6.2.3. This scaling assures that the relative blood flow does not increase over the limit value. For the value of ζ slightly rounded to $1/2$ (corresponding to our case) we found analytically that this limit value is $1 + 1/\sqrt{3} \simeq 1.58$. Indeed, after a long transient is discarded, the relative blood flow (red line in panel Figure 6.4A) reaches its maximal value at ~ 1.58. The minimal value of this signal, however, is ~ 0.42, which means significant relative variations of blood flow. The experimental data presented in panel Figure 6.4B (red, green, blue, and cyan lines for four PERS groups) indicate that these variations are significantly

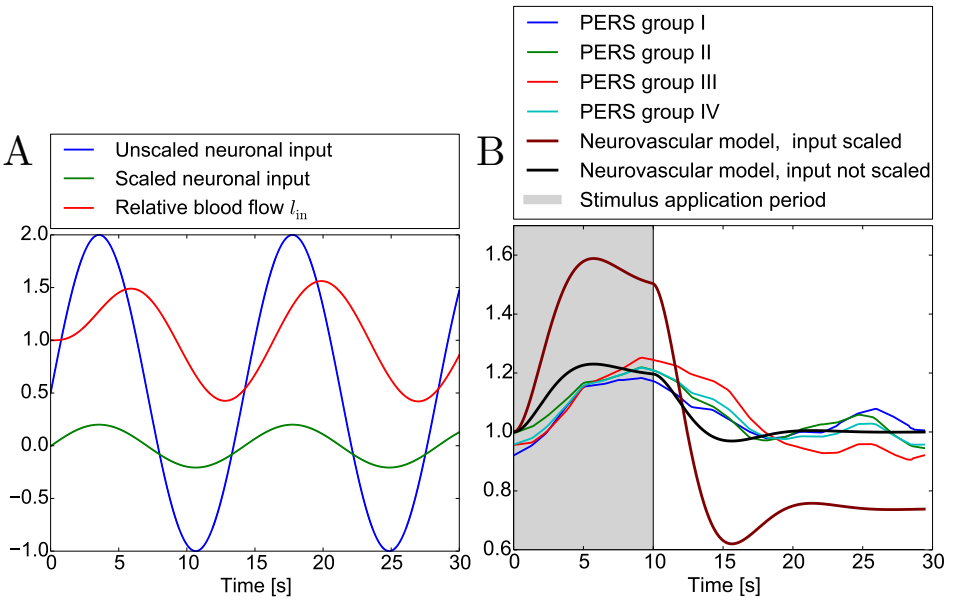

Figure 6.4: Dynamics of the neurovascular model (Friston et al., 2000). Panel A shows the effect of driving this model with a shifted and scaled harmonic input signal (green) characterised with the resonant frequency of the model (~ 0.07 Hz). The raw input signal, represented here by the shifted sinusoid (blue), can be in general an arbitrary time course (e.g. output from a neuronal model). After shifting and scaling, this signal (green) drives the neurovascular model, yielding blood flow (red). Panel B shows changes to blood flow resulting from 10 s of stimulation (grey). This panel shows both experimental and simulated data. The former are divided in four PERS groups: group I (blue), group II (green), group III (red), and group IV (cyan). The latter ones are obtained from the neurovascular model stimulated with a 10 seconds-long step function characterised by an amplitude 0.15. The choice of 10 s follows from the duration of stimulation during experiment. Panel B shows the resulting blood flow, computed from the unscaled (black) and scaled (maroon) input.

smaller (approximately between 0.9 and 1.2) even when stimulation is applied, therefore we suggest that the model should not allow for exceeding these values in the absence of stimulation (the resting state).

Apart from experimental data, Figure 6.4B shows the blood flow obtained from the neurovascular model driven with a step function, which represents stimulation. Consistently with the experimental protocol, this

function has non-zero values for the first 10 seconds of each trial. The figure shows the result corresponding to driving with an unscaled step function, with an arbitrary amplitude 0.15 (black) and a result corresponding to the same step function scaled accordingly to the procedure described above (maroon). The PERS groups I, II, III, and IV are shown in blue, green, red, and cyan, respectively. The results shown in Figure 6.4B indicate that the simulated time course evolves faster than the experimental one. They also show that the rebound effect of the neurovascular model yields deviations from baseline smaller than the observed in the experimental data and that could not fit the overshoot (blue line).

Furthermore, Figure 6.4B shows how the scaling of the input signal affects the blood flow baseline (lower steady state), which is shifted downwards (maroon, for $t \in (25, 30)$). This shift demonstrates how the scaling of the input signal adopted for the need of modelling the resting state affects the results obtained for the stimulation protocol. The amplitude of the driving, that is 0.15, was set in such a way that the resulting blood flow would have an amplitude corresponding to the experimental one. The scaled signal, however, is not biased with this arbitrary choice and yields a blood flow signal significantly exceeding the experimental one. It is a consequence of the fact that in this case the scaling in fact increases, rather than decreases the amplitude. As a result the simulated relative increase of blood flow is three times larger than the experimental one.

6.3.3 Simulating the BOLD signal from experimentally measured blood flow

In this section we simulate the BOLD signal from experimentally measured blood flows (presented in Figure 6.4B), which following other studies (Kamrani, 2012), we consider input to the haemodynamic models. We perform eight simulations, corresponding to all combinations between the four PERS groups of data and the two models: (Balloon and the Balloon-Windkessel). In the former case we used the relation $l_{\text{out}} = f(v)$ in the form specified in Equation (6.3) with $\alpha = \alpha_{\text{limit}} = 0.156$ (which entails $a = \alpha_{\text{limit}}$ and $b = 1 - \alpha_{\text{limit}}$). We increase the value of the α parameter (with respect to $\alpha = 0.066$ used in Section 6.3.1), in order to allow for entering the regime where $l_{\text{out}} > v$ and thereby allowing a positive BOLD signal generation. As

discussed in Section 6.3.1, for $\alpha = 0.066$ this regime is not reached for blood flow < 1.2, which is the case for virtually all data that we use here (see Figure 6.4B). The rest of parameter values follow from Table 6.2. The results obtained, along with the experimental data, are presented in Figure 6.5.

The experimental BOLD signal in Figure 6.5 (black line, with standard error of the mean in grey), is shown along with the simulated one from the Balloon (blue) and the Balloon-Windkessel (green) models, in four panels corresponding to PERS group I (panel A), II (panel B), III (panel C), and IV (panel D). Figure 6.5 shows that deviations of the BOLD signal generated with the Balloon Model (blue) from the baseline (the lower steady state) are suppressed in comparison to the experimental data. For none of the PERS groups an undershoot effect is observed (in agreement with our expectation) and a very small overshoot is detected for the PERS group I. Moreover, poststimulus differences in driving blood flows (red, green, blue, cyan for $t > 10$ s in Figure 6.4B) are not captured by the model and all four BOLD signals produced look alike (compare blue in Figures 6.5A-D). We also note that for the Balloon Model case, the simulated signal slightly lags behind the experimental one.

The BOLD signals obtained from the Balloon-Windkessel Model (green) show a qualitative consistency with the experimental data for all PERS groups. All these signals, as well as the experimental ones (black) follow the time courses of blood flow presented in Figure 6.4B. In general, the shape, amplitude and time alignment of the simulated signal corresponds well to the experimental data. Nevertheless, the simulated signal on panels A, C and D starts with a dip, not present in the experimental BOLD. It is a reminiscence of the low values of blood flow (< 1) at the beginning of the trials (see red, blue and cyan lines around $t = 0$ s in Figure 6.4B). We conclude that this dip is a consequence of the baseline-finding procedure.

6.4 DISCUSSION

Several studies were presented in this chapter. We analysed theoretically the poststimulus behaviour of the BOLD signal. We proposed the implementation of a concept put forward by Buxton et al. (1998), and showed that it renders the Balloon Model capable of yielding the poststimulus

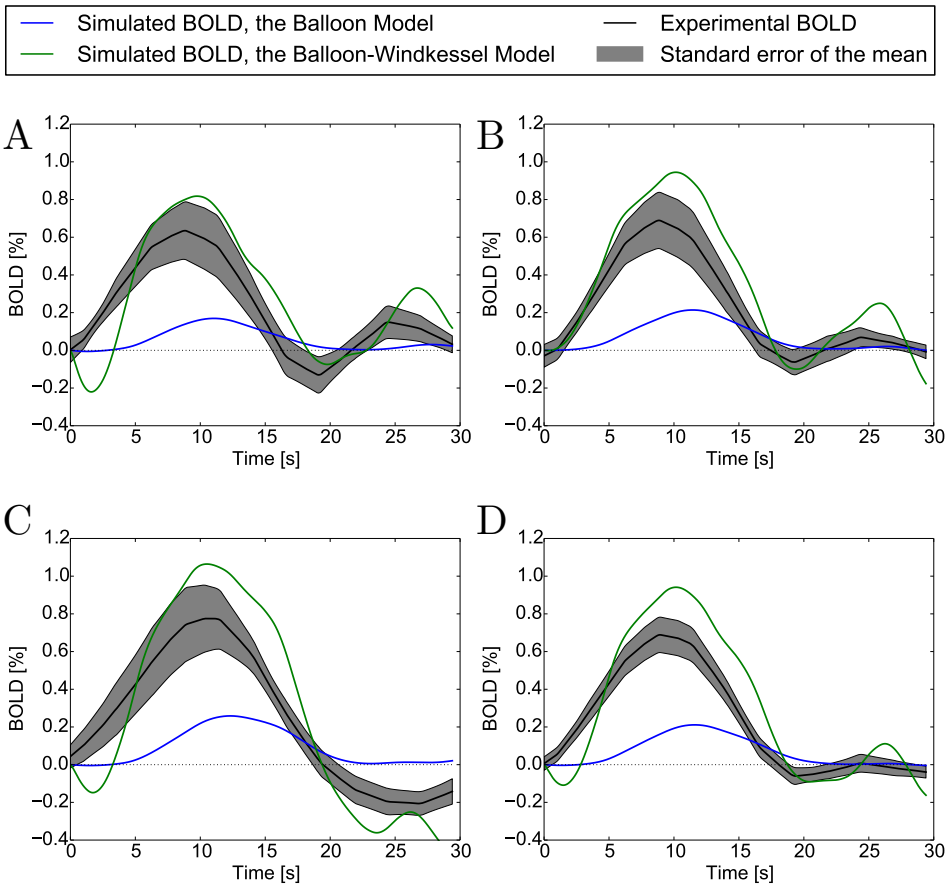

Figure 6.5: Experimental and simulated BOLD signals. The experimental signal is shown in black, with standard error of mean in grey. The simulated signal was generated with the Balloon (blue) and the Balloon-Windkessel (green) models separately in four different PERS groups: I (panel A), II (panel B), III (panel C) and IV (panel D). In the case of the Balloon Model, the relation $l_{\text{out}}(v) = 0.156 \cdot v^{1/0.156} + 0.844$ was used and in case of the Balloon-Windkessel Model the relation $l_{\text{out}}(v) = v^{0.33}$ was used.

BOLD undershoot even if the cerebral blood flow does not drop below the baseline. This is due to the delayed elevation of the venous compartment volume with respect to the output blood flow. We explained this mechanism quantitatively and determined conditions under which it occurs. From these conditions it follows that for our choice of the value of $\alpha = 0.066$ (which allows to reproduce the results of Buxton et al., 1998), and for the relative blood flow remaining below 1.2, the BOLD signal takes exclusively negative values. Interestingly, the experimentally measured relative blood flow that we analysed here, hardly ever exceeds 1.2. For this reason, we increased the value of the coefficient α in tests of the Balloon Model on experimental data. We thereby suppressed the BOLD signal undershoot generation mechanism based on the delayed elevation of the compartment volume, when blood flow has already returned to baseline, and we focused on another possible mechanism: a simple following of blood flow by the BOLD signal. Furthermore, we explained why the undershoot caused by the delayed elevation of volume is absent in the Balloon-Windkessel Model (Friston et al., 2000). This is not obvious, because this model is usually coupled with the neurovascular model (also discussed here), which yields a rebound (a drop below baseline due to damping) of blood flow. This, in turn, due to simple following of blood flow by the BOLD signal, entails its undershoot produced by the Balloon-Windkessel Model. Nevertheless, in this case the mechanism of the undershoot is very different than in the delayed elevation scenario.

The experimental data that we used exhibit an undershoot of the BOLD signal, whenever an undershoot in the corresponding blood flow time course is present. This suggests that the Balloon-Windkessel model might be (partially) valid. Our results show that indeed this model is able to reproduce both the poststimulus under- and overshoot, given that it is driven by an undershooting or overshooting blood flow, respectively. On the other hand, the Balloon-Windkessel Model neglects temporal decoupling between the venous compartment volume and the blood flow, although it is known to occur Mandeville et al. (1996, 1998) and might be contributing to the undershoot of the BOLD signal. We found that the Balloon Model with our implementation of the relation $l_{\text{out}} = f(v)$ does

not reproduce the BOLD signal from experimental blood flow as well as the Balloon-Windkessel Model. This relation is simplified and does not faithfully corresponding to the experimental observations Mandeville et al. (1996, 1998), in which case it would be expected to exhibit hysteresis, with blood flow increasing and decreasing rapidly and with blood volume catching up slowly.

We also examined the neurovascular model of Friston et al. (2000). We showed that it has strong low-pass filtering properties which would strongly attenuate relatively fast oscillations generated by a model such as the Jansen-Rit module, utilised earlier in this Thesis. We noted that additional dependence on neuronal activity needs to be introduced in this model in order to render it capable of reproducing both over- and undershooting poststimulus BOLD behaviour. Furthermore, we argued that the widely used Balloon-Windkessel Model, coupled with the neurovascular model, might not be accurate in generating physiologically plausible behaviour for the resting state. This is understandable, because originally these models were considering the resting state a flat baseline from which (positive) prominent deviations arise due to stimulation. Modelling subtle, in particular negative, fluctuations around the baseline was not an objective of the model. Nevertheless, although a number of more sophisticated models have been recently proposed (see review, Buxton, 2012) and although they account for some physiological effects better than the Balloon-Windkessel Model, it is still precisely this model that is until today used in the neuronal modelling community, also in the context of the resting state (Cabral et al., 2013). For example, the Balloon-Windkessel Model is part of The Virtual Brain (http://thevirtualbrain.org) software package and it is used in Dynamic Causal Modelling (Havlicek et al., 2015).

The Balloon-Windkessel Model might still be sufficient in some applications to modelling of brain dynamics, when it converts neuronal activity to the BOLD signal, which can later be compared with experimental fMRI recordings. Very often in such cases one is interested not in absolute values of these signals, but rather in correlations between signals from different brain areas (see 'functional connectivity' in Section 1.4.6). In the case of linear correlations, such as the Pearson correlation, scaling and shifting of

signals does not affect the result. It is the low-pass filtering property of the haemodynamic and neurovascular models that plays a crucial role in this kind of analysis, since it limits the bandwidth of the simulated signal to frequencies typical of fMRI recordings. In the future it would be interesting to compare simulated signals and functional connectivities obtained from the Balloon-Windkessel Model and from a simple spectral low-pass filter.

Nevertheless, from the physiological perspective, it is crucial not only to obtain secondary relative quantities such as correlations, but to model biological processes accurately. Comprehending these processes would allow to infer neuronal activity from registered fMRI BOLD signals. Currently it is not known how neuronal activity maps onto the BOLD signal. In particular, different aspects of neuronal activity may be driving haemodynamic and metabolic processes (Buxton, 2012; Mullinger et al., 2013). For these reasons we see a need to bridge physiological modelling (focused around metabolism and haemodynamics) with neuronal modelling. This would allow to obtain more insight from experimental data and exploit computational models more richly.

6.5 SUMMARY AND OUTLOOK

In this chapter we broadened the scope of interest of this Thesis to include large scale-dynamics qualified from fMRI recordings. We studied dynamical properties of models devised to simulate the BOLD signal and related physiological quantities. In particular we focused on the Balloon (Buxton and Frank, 1997) and the Balloon-Windkessel (Friston et al., 2000) models, and on the neurovascular model (Friston et al., 2000). Similarly to authors of these models, in order to study local phenomena, we considered a single vascular compartment (a voxel), although efforts to model inter-voxel interactions have already been made (Drysdale et al., 2010). We quantitatively analysed the poststimulus behaviour of the BOLD signal and brought up issues related to modelling the resting state as registered in fMRI recordings. We conjectured that for some applications of the haemodynamic models (in particular related to neuronal dynamics) a high level of biological fidelity is not indispensable to obtain realistic results. At the

same time, progress in the field of haemodynamic modelling would also empower studies of the neuronal dynamics.

CHAPTER 7

CONCLUSIONS AND PERSPECTIVES

7.1 SUMMARY OF FINDINGS

Neuronal dynamics span a wide range of temporal and spatial scales, rendering the brain a uniquely complex system. The aim of this Thesis was to study temporal properties of brain processes occurring in the mesoscopic spatial scale, i.e. processes generated by neuronal assemblies, rather than by individual neurons. We were particularly interested in advancing the understanding of the role that temporally correlated noise plays in shaping the mesoscopic-scale neuronal dynamics. We consider this issue specially relevant, because current studies of these dynamics have for the most part been concerned with temporally uncorrelated white noise (Garnier et al., 2015; Lopes da Silva et al., 1974; Petkov et al., 2014; Roberts and Robinson, 2012; Touboul et al., 2011; Victor et al., 2011) characterised by a flat power spectrum. However, it is known that EEG recordings yield a background shape of their power spectra that follows a '$1/f^b$' dependence on the frequency f. We therefore examined the question of the significance of the spectral composition of the background (stochastic) activity affecting a neuronal population. In order to disentangle effects related to different frequencies of this background activity, we systematically studied the response of the neuronal model to harmonic driving of varying frequency and amplitude. Our findings following from this procedure were related to particular experimental observations of brain dynamics, as registered in the EEG recordings in both healthy and unhealthy subjects.

We specifically focused on effects related to epilepsy. This neurological disorder affects millions of people worldwide, severely impairing their quality of life. Around 30% of epileptic patients (http://www.who.int/mediacentre/factsheets/fs999/en/) are resistant to pharmacological treatment and need alternative means of medical care.

One of the approaches towards the development of alternative therapies involves considering epilepsy a *dynamic disease* (Milton, 2010) and analysing it in the framework of nonlinear dynamics theory. We took that approach in this Thesis, by employing the Jansen-Rit nonlinear neuronal model, which is capable of recapitulating both healthy and epileptic brain dynamics. We studied the dynamics of this model in the context of three types of external driving: (1) stochastic, (2) harmonic, and (3) internal, the latter arising from the coupling between distinct neuronal populations (modules). We developed our framework methodically, starting from studies of a single Jansen-Rit module in Chapter 3, moving on to two coupled modules in Chapter 4 and finally focusing on a network of such modules in Chapter 5.

We related our theoretical findings to a number of phenomena found experimentally in the human brain. Those phenomena include initiation and termination of epileptic activity, visually induced seizures and increase of power in a high frequency band due to sensory stimulation in a low frequency band. In Chapter 6 we extended the scope of the modelled mesoscopic brain processes from neuronal activity to the haemodynamic and metabolic process that underlie the BOLD signal, as registered in the fMRI recordings. Accurate models of these processes allow to compare neuronal activity (e.g. simulated with models such as the Jansen-Rit model) with those recordings. Our work is, therefore, organised around dynamical properties of mesoscopic-scale models of brain activity and on their relation to experimental observations. In what follows we summarise the main findings presented in each chapter of this Thesis.

Conclusions from Chapter 3

Dynamics of a stochastically and harmonically driven neural mass model. In that chapter we focused on the dynamics of an individual Jansen-Rit module driven by harmonic signals and by Ornstein-Uhlenbeck noise. We found that epileptiform dynamics in this model are most easily initiated by noise characterised by certain temporal correlations. Our analysis revealed that these correlations maximise spectral power in combined alpha, delta and theta frequency bands. By introducing harmonic driving to the system, we showed that rhythms from this wide band indeed elicit

epileptiform dynamics in the model. Our findings are supported by clinical observations: indeed, an increase of power in delta and theta bands was observed prior to initiation of epileptic seizures (Gupta et al., 2011; Sadleir et al., 2011). We also found that although driving with a rhythm of frequency ~ 10 Hz leads to a resonance with the natural frequency of the model, it is 'harmless' with respect to evoking epileptic activity in the model. Nevertheless, this activity was elicited when the excitability of the system was increased, what we consider a model of an 'unhealthy-like', potentially epileptogenic neuronal tissue. Since the resonance frequency corresponds to the alpha rhythm, which is most prevalent over the visual cortex, we related the epileptogenic resonance to photosensitive epilepsy, which is known to occur in susceptible subjects, in particular, for stimulation falling into the alpha band (Takahashi and Tsukahara, 1998). All the effects observed were explained as interplays between the specific driving frequencies and the bifurcation structure of the model. We therefore showed the importance of coloured (temporally correlated) noise in the context of dynamical modelling of brain (dys-)function.

Conclusions from Chapter 4

Interactions between two reciprocally coupled neural masses: collective excitability. In Chapter 4 we extended our model to two coupled neural masses stimulated with white noise. We explored a rare feature of this neural mass model: the coexistence of two limit cycles. Their noise-initiated mutual interactions lead to long excitation transients. We showed that the initiation rate of these transients depends in a non-monotonic way on the coupling strength between the modules. For low coupling, transient noise-induced activations of one module are less likely to initiate activity in the other module, thus the initiation rate remains low. To the contrary, for high coupling the modules tend to fully synchronise, what excludes mixing of two distinct oscillatory modes. It is the intermediate coupling strength that promotes appearance of prolonged activity episodes. These episodes terminate due to simultaneous falling into refractory period; such scenario has been conjectured to underlie synchronous termination of epileptic seizures (Schindler et al., 2007). In summary, we quantitatively showed how oscillatory multistability leads to appearance of complex temporal patterns in a

relatively simple neuronal model. Moreover, in that chapter we introduced a simple and fast method of finding loss of stability in a bidirectionally all-to-all coupled network of dynamical systems featuring saddle-node bifurcation.

Conclusions from Chapter 5

Cross-frequency transfer in a stochastically driven mesoscopic neuronal model. In that chapter we found that a network of Jansen-Rit modules driven by temporally correlated noise yields realistic power spectra characterised by a '$1/f^b$' background (without relying on critical phenomena) with an embedded alpha peak. The peak grows when the network is driven by a slow rhythm. This result reproduces an experimental observation of Bayer et al. (2011). By analysing the bifurcation structure of the Jansen-Rit module we proposed a mechanism underlying this observation. We suggested that it relies on both the dynamical properties of a single module and collective synchronisation effects between the modules. Our results allowed to predict that for faster driving frequencies this increase of power in the alpha band would be substituted by a decrease.

Conclusions from Chapter 6

BOLD signal modelling. In that chapter we performed dynamical analysis of mechanisms potentially leading to a poststimulus undershoot in the BOLD fMRI signal. We tested two implementations of the Balloon Model (one of which is called 'Balloon-Windkessel Model') and showed that they involve different mechanisms responsible for the generation of the undershoot. According to the current state of knowledge (Buxton, 2012) both mechanisms could be significant. Moreover, by running the models on experimental data we demonstrated that the Balloon-Windkessel Model can reproduce both the poststimulus under- and overshoot of the BOLD signal, given that the flow of cerebral blood is also under- or overshooting, respectively. Finally, we examined the characteristics of a neurovascular model commonly used to couple neuronal activity with haemodynamics. In particular we considered the consequences of modelling the resting state, and

we concluded that the models we tested might be sufficient for some applications (e.g. modelling linear functional correlations between brain regions, as those measured by the fMRI recordings). Further development is needed in order to account for the role of neuronal activity in the generation of the BOLD signal.

7.2 Discussion

This Thesis started with a comprehensive 'Introduction' that put our research in a wider context of theoretical neuroscience. In all chapters that are concerned with neuronal dynamics (Chapters 3-5) we worked under the hypothesis that the brain operates close to a phase transition or bifurcation (Section 1.4.4, 'Criticality and the verge of transition'). In Chapters 3 and 5 we set our model parameters according to this hypothesis. Indeed, the results we obtained were in agreement with experimental findings, and the mechanism we suggested as their potential explanation relies on closeness to a Hopf bifurcation. Therefore, the scenario we considered goes along the lines of the hypothesis. Nevertheless, this scenario neither requires nor entails that the brain operates close to a strictly understood (self-organised) critical state (Chialvo et al., 2008). We also demonstrated that a '$1/f^b$'-like power spectrum (Section 1.4.5, '$1/f^b$ power spectra'), often considered a signature of critical phenomena, can be generated by a mesoscopic neuronal model driven by temporally correlated noise. Moreover, in Chapters 3 and 5 we focused on a 'catastrophic transition' in order to model unhealthy-like (epileptic) brain dynamics. In this case the impairment was modelled as moving the system further away from the Hopf bifurcation and setting it closer to the 'catastrophic' saddle-node on invariant circle bifurcation.

We also focused on brain rhythmicity (Section 1.4.1, 'Rhythms of the brain') and interactions between rhythms from distinct frequency bands. In Chapter 5 we proposed a minimalistic model of cross-frequency transfer of power. Indeed, the same mechanism has been suggested to underlie the phase-to-amplitude coupling in other mesoscopic neuronal models (Onslow et al., 2014). Our results on rhythmic driving (Chapters 3 and 5) revealed a number of phenomena evoked in the model for certain driving

amplitudes, frequencies and phases. This puts our research in the context of brain stimulation of both healthy Ngo et al. (2013), Spiegler et al. (2011), and Summerson et al. (2015) and epileptic subjects (Durand, 2009; Kasteleijn-Nolst Trenite, 2006). In the former case, we were able to make the prediction that an increase of driving frequency above the one that had been tested experimentally (Bayer et al., 2011), would lead to an effect opposite to the one observed experimentally. In the latter case, epileptogenic rhythms that we identified can be attributed either to intrinsic brain activity or to external stimulation. From the dynamical perspective, these two situations may be very different, because external stimulation is highly likely to be characterised with a well-defined phase (such was the case of Takahashi and Tsukahara, 1998), which may lead to entrainment and excessive synchronisation of neuronal activity in distinct brain sites, and consequently to a seizure.

A substantial part of the Introduction (Section 1.1.3, 'Cortical columns') was devoted to the discussion of the putative anatomical structures modelled by population (neural mass) models. Taking it together with the considerations about the internal synchrony of the modelled populations (Section 1.3, 'Population modelling') leads to the conclusion that population modelling is not limited to a single spatial scale of the modelled structure. In Chapter 4 we demonstrated that reciprocally coupled instances of a neuronal model tend to behave like one system when the coupling is strong. Therefore, here we conclude that their activity could be approximated by just one instance of the model. Indeed, neural masses have been used to model structures ranging from minicolumns (Babajani and Soltanian-Zadeh, 2006) to whole brain areas (or even to the whole brain when synchrony is high due to epilepsy, Breakspear et al., 2006). We note, however, that in the latter case effects related to delays might play a role (Coombes and Laing, 2009).

Comparison of the results presented in Chapters 3 and 5 reveals that the value of the noise correlation time that was found to generate most realistic power spectrum falls within the range of values that entail generation of epileptic spikes. Nevertheless, in the former case our model involves a network of neural masses and individual spikes are smeared

out in the background signal generated by the network. This is possible as long as coupling between the network elements is not excessive. If it is, as we demonstrated in Chapter 4, a full synchronisation of the coupled elements may enhance the spikes and impair the smearing. On the other hand, increased synchrony -typical to epilepsy- allows us to approximate the activity of a number of synchronised neural masses with the activity of only one neural mass model. In this context, the approach adopted by us in Chapter 3 can be considered such reduction.

When neural masses model cortical columns, local patches of neuronal tissue, or brain areas, are often organised into networks accounting for larger, complex brain structures (Section 1.4.6, 'Brain networks'). Our results concern also such networks. We introduced a method of localising the loss of stability of a neuronal network via a saddle-node bifurcation. This method is limited to all-to-all coupled networks; nevertheless its applicability may be wider than it seems, because the dynamics of all-to-all connected networks was shown to approximate the dynamics of random graphs, when exposed to Ornstein-Uhlenbeck noise (Torcini and Angulo-Garcia, 2014). We showed how interactions between two isolated network nodes (modelled as neural masses) lead to occurrence of complex transients (Chapter 4), and how synchronisation in networks leads to buildup of peaks in the power spectrum (Chapter 5).

We note a parallel from the latter scenario to event-related potentials and synchronisation (Pfurtscheller and Lopes da Silva, 1999). Nevertheless, as discussed in Chapter 2, 'Modelling mesoscopic brain dynamics', traditional neural mass models can only account for interpopulation (in contrary to intrapopulation) synchrony. Furthermore, our analysis of the limitations of neural mass models presented in that chapter also showed that these models assume that the average membrane potential is close to the steady state, which might not be, in general, the case for abrupt evoked potentials. Although neural mass models were shown successful in modelling some effects related to event-related (de)synchronisation (Grabska-Barwińska and Żygierewicz, 2006; Suffczyński et al., 2001), and evoked (David et al., 2005) and induced (David et al., 2006) potentials, we would expect that they have limited capabilities in this field.

Also our research on haemodynamic processes and modelling the BOLD signal presented in Chapter 6 could be related to closeness to a phase transition and to the dynamics of neuronal networks. Slow timescales characterising these processes filter out fast rhythms of the neuronal dynamics and as a result they relatively magnify slow processes, which are likely to be enhanced in the vicinity of a phase transition (see 'critical slowing down' in Sections 1.4.5 and 1.4.4), and they may also follow from emergent network dynamics. Therefore, BOLD modelling might be helpful in determining certain aspects of neural dynamics and (functional) connectivity (Cabral et al., 2013). A natural continuation of the work presented here is coupling the Jansen-Rit model with the Balloon-Windkessel Model and constructing a network of neural masses interconnected according to the connectome. Such two-level model would allow to compare simulated signals with experimentally collected fMRI recordings. Our results from such comparison are preliminary and were not included in this Thesis.

Finally, noise was a common theme present in most of this Thesis. We used both white and temporally correlated Ornstein-Uhlenbeck noise. By driving a mesoscopic neuronal model with the latter, we emphasised the importance of temporal correlations in generating rich neuronal dynamics, and we explored a potential scenario leading to one of scenarios of generation of a '$1/f^b$' power spectra (see Section 1.4.5, '$1/f^b$ power spectra'). Our research on the dynamical properties of a stochastically driven neuronal model contributes to the vast body of work on stochasticity in theoretical neuroscience (Laing and Lord, 2010). In particular, our identification of the level of noise autocorrelation time that maximises certain effects could be related to stochastic resonance (Gluckman et al., 1996), in which maximisation of a particular quantity (e.g. signal-to-noise ratio) is obtained via tuning of the noise characteristics.

We suggest that future work could elaborate on the way noise is delivered to the neuronal model. In particular, populations of interneurons could also be subject to stochastic driving. Furthermore, intrinsic noise could be considered; it would more faithfully account for stochasticity in neuronal interactions and it could itself lead to a '$1/f^b$' power spectrum

(Kaulakys et al., 2005). Finite correlations between noise realisations delivered to distinct neuronal modules could also be taken into account. Firstly, they would be motivated by experimental observations (see Mochol et al., 2015, and references from therein) and secondly they could alter our results, in which noise had mostly a destructive impact on synchronisation and was competing with coupling in this respect. To the contrary, correlated stochastic driving would be expected to promote synchrony. Furthermore, it would also be natural to promote the stochastic process used in Chapter 4 from white noise to a temporally correlated one. Finally, a number of Ornstein-Uhlenbeck noise sources could be combined in order to generate a signal more faithfully recapitulating a '$1/f^b$' shape of the power spectrum (Hausdorff and Peng, 1996). We speculate that effects presented in this Thesis would hold also for such linearly composed signals.

In the future it will be important to study the effects of coloured noise in a variety of different models, such as extensions to the neural mass model (Goodfellow et al., 2011; Wendling et al., 2002) that can generate alternative dynamics. Furthermore, future development of our work could combine approaches presented here in Chapters 3 and 5, and could examine explicitly the dynamics of networks of neural masses in order to investigate conditions for the propagation or restriction of epileptiform activity. Our studies on rhythms driving epileptiform dynamics could be extended to searching for stimulation protocols that are likely to *terminate*, but not *initiate* a seizure. There is an ongoing increase in interest in this stream of research in both theoretical (Jiruska et al., 2010; Wang et al., 2015) and experimental (Berenyi et al., 2012) studies. In particular, recent results (Taylor et al., 2014) emphasise the importance of taking into account the phase of the ongoing (epileptic) brain activity in these stimulation protocols. Indeed, results presented in Chapter 3 revealed that for some conditions, the model's response depends on the driving signal phase.

In this Thesis we demonstrated a number of phenomena occurring in models of brain dynamics at the mesoscopic scale, and explained them qualitatively on the ground of dynamical systems theory. In particular, we focused on effects arising from stochasticity, coupling and bifurcations of a specific neural mass model. Although this model (Jansen and Rit, 1995)

has been in use for over two decades now, we found novel physiological relevance of its properties, which we hope, due to the model's popularity, will be of interest to many.

APPENDIX

PUBLICATIONS AND PRESENTATIONS

Publications

1. M. Jedynak, A. J. Pons, J. Garcia-Ojalvo, M. Goodfellow (2016). "Temporally correlated fluctuations drive epileptiform dynamics". In: *NeuroImage* 16;146:188-196. doi:10.1016/j.neuroimage.2016.11.034.

2. M. Jedynak, A. J. Pons, J. Garcia-Ojalvo (2015). "Cross-frequency transfer in a stochastically driven mesoscopic neuronal model". In: *Frontiers in Computational Neuroscience* 9, 14. doi:10.3389/fncom.2015.00014.

3. M. Jedynak, A. J. Pons, J. Garcia-Ojalvo "Collective excitability and noise in a mesoscopic neuronal model". Manuscript in preparation.

Talks

1. "Identification of epileptogenic rhythms in a mesoscopic neuronal model". *ICANN Conference on Artificial Neural Networks*, 2016 IX 6-9, Barcelona, Spain.

2. "Colored noise as a driver of epileptiform dynamics in a mesoscopic neuronal model". *XXXVI Dynamics Days*, 2016 VI 6-10, Corfu, Greece.

3. "Noise induced effects and synchronization in mesoscopic brain dynamics". *Donders Discussions*, 2015 X 5-6, Nijmegen, the Netherlands.

4. "Brain research in the mesoscopic scale". *3rd Jornada d'Investigadors Predoctorals Interdisciplinaria*, 2015 II 5, Barcelona, Spain.

5. "Mesoscopic brain activity in the presence of stochastic and periodic inputs". *The Brain: Criticality, Dynamics, Networks and Function*, 2013 IX 2-6, Capri, Italy.

Poster presentations

1. "Stimulus induced resonance in a neural mass model driven with a temporally correlated noise". *International Conference on System Level Approaches to Neural Engineering*, 2015 IX 21-23, Barcelona, Spain.

2. "Stimulus induced resonance in a neural mass model driven with a temporally correlated noise". *CNS 2015 Meeting*, 2015 VII 18-23, Prague, Czech Republic.

3. "Cross-frequency transfer in a mesoscopic model of the brain with noisy oscillatory input". *IV Summer School on Statistical Physics of Complex and Small Systems*, 2014 IX 8-19, Mallorca, Spain.

4. "Cross-frequency transfer in a mesoscopic model of the brain with noisy oscillatory input". *Meeting of the Catalan Network for the Study of Complex Systems*, 2014-VI-19, Barcelona, Spain.

5. "Cross-frequency transfer in a mesoscopic model of the brain with noisy oscillatory input". *Barcelona Computational and Systems Neuroscience Meeting*, 2014 VI 16-17, Barcelona, Spain.

6. "Cross-frequency transfer in a mesoscopic model of the brain with noisy oscillatory input". *NETT Florence workshop Dynamics of Neural Circuits*, 2014 III 17-20, Florence, Italy.

7. "Mesoscopic brain activity in the presence of stochastic and periodic inputs". *Donders Discussion*, 31 X–1 XI 2013, Nijmegen, the Netherlands.

8. "Mesoscopic brain activity in the presence of stochastic and periodic inputs". *Brain Modes 2013: Criticality, connectivity, and neural masses*, 2-3 XII 2013, Amsterdam, the Netherlands.

BIBLIOGRAPHY

Abbott, L. F. and S. B. Nelson (2000). "Synaptic plasticity: Taming the beast". In: *Nat. Neurosci.* 3.November, pp. 1178–1183.

Abrams, D. M., R. Mirollo, S. H. Strogatz, and D. A. Wiley (2008). "Solvable model for chimera states of coupled oscillators". In: *Physical Review Letters* 101.8, pp. 1–4.

Aburn, M. J., C. A. Holmes, J. A. Roberts, T. W. Boonstra, and M. Breakspear (2012). "Critical fluctuations in cortical models near instability." In: *Frontiers in physiology* 3.August, p. 331.

Alarcon, G., C. D. Binnie, R. D. Elwes, and C. E. Polkey (1995). "Power spectrum and intracranial EEG patterns at seizure onset in partial epilepsy." In: *Electroencephalography and clinical neurophysiology* 94, pp. 326–337.

Albada, S. J. van and P. A. Robinson (2009). "Mean-field modeling of the basal ganglia-thalamocortical system. I. Firing rates in healthy and parkinsonian states". In: *Journal of Theoretical Biology* 257.4, pp. 642–663.

Andreae, L. C. and J. Burrone (2015). "Spontaneous Neurotransmitter Release Shapes Dendritic Arbors via Long-Range Activation of NMDA Receptors". In: *Cell Reports* 10.6, pp. 873–882.

Anishchenko, V., V. Astakhov, A. Neiman, T. Vadivasova, and L. Schimansky-Geier (2007). *Nonlinear Dynamics of Chaotic and Stochastic Systems: Tutorial and Modern Developments*. Springer Series in Synergetics. Springer Berlin Heidelberg.

Aru, J., J. Aru, V. Priesemann, M. Wibral, L. Lana, G. Pipa, W. Singer, and R. Vicente (2015). "Untangling cross-frequency coupling in neuroscience." In: *Current opinion in neurobiology* 31C, pp. 51–61.

Atay, F. M. and A. Hutt (2006). "Neural Fields with Distributed Transmission Speeds and Long-Range Feedback Delays". In: *SIAM Journal on Applied Dynamical Systems* 5.4, pp. 670–698.

Azevedo, F. A. C., L. R. B. Carvalho, L. T. Grinberg, J. M. Farfel, R. E. L. Ferretti, R. E. P. Leite, W. J. Filho, R. Lent, and S. Herculano-Houzel

(2009). "Equal numbers of neuronal and nonneuronal cells make the human brain an isometrically scaled-up primate brain". In: *Journal of Comparative Neurology* 513.5, pp. 532–541.

Babajani, A. and H. Soltanian-Zadeh (2006). "Integrated MEG/EEG and fMRI model based on neural masses." In: *IEEE transactions on biomedical engineering* 53.9, pp. 1794–801.

Babiloni, C., F. Vecchio, A. Bultrini, G. Luca Romani, and P. M. Rossini (2005). "Pre- and Poststimulus Alpha Rhythms Are Related to Conscious Visual Perception: A High-Resolution EEG Study". In: *Cerebral Cortex* 16.12, pp. 1690–1700.

Babiloni, C., C. Del Percio, L. Arendt-Nielsen, A. Soricelli, G. L. Romani, P. M. Rossini, and P. Capotosto (2014). "Cortical EEG alpha rhythms reflect task-specific somatosensory and motor interactions in humans". In: *Clinical Neurophysiology* 125.10, pp. 1936–1945.

Babloyantz, A., J. Salazar, and C. Nicolis (1985). "Evidence of chaotic dynamics of brain activity during the sleep cycle". In: *Physics Letters A* 111.3, pp. 152–156.

Baier, G., M. Goodfellow, P. N. Taylor, Y. Wang, and D. J. Garry (2012). "The importance of modeling epileptic seizure dynamics as spatio-temporal patterns." In: *Frontiers in physiology* 3.July, p. 281.

Bak, P. (1996). *How nature works: the science of self-organized criticality*. Copernicus.

Bak, P. and D. R. Chialvo (2001). "Adaptive learning by extremal dynamics and negative feedback". In: *Physical Review E* 63.3, p. 031912.

Bak, P., C. Tang, and K. Wiesenfeld (1987). "Self-organized criticality: An explanation of the 1/f noise". In: *Physical Review Letters* 59.4, pp. 381–384.

Barabási, A.-L. (2002). *Linked: The New Science of Networks*. Perseus Pub.

Barardi, A., B. Sancristóbal, and J. Garcia-Ojalvo (2014). "Phase-Coherence Transitions and Communication in the Gamma Range between Delay-Coupled Neuronal Populations". In: *PLoS Computational Biology* 10.7.

Bartos, M., I. Vida, and P. Jonas (2007). "Synaptic mechanisms of synchronized gamma oscillations in inhibitory interneuron networks". In: *Nature Reviews Neuroscience* 8.1, pp. 45–56.

Bastos, A. M., J. Vezoli, and P. Fries (2015). "Communication through coherence with inter-areal delays". In: *Current Opinion in Neurobiology* 31, pp. 173–180.

Battaglia, D. and D. Hansel (2011). "Synchronous chaos and broad band gamma rhythm in a minimal multi-layer model of primary visual cortex." In: *PLoS computational biology* 7.10, e1002176.

Bayer, L., I. Constantinescu, S. Perrig, J. Vienne, P.-P. Vidal, M. Mühlethaler, and S. Schwartz (2011). "Rocking synchronizes brain waves during a short nap." In: *Current biology : CB* 21.12, R461–2.

Baar, E., C. Baar-Eroglu, S. Karaka, and M. Schürmann (2001). "Gamma, alpha, delta, and theta oscillations govern cognitive processes". In: *International Journal of Psychophysiology* 39.2-3, pp. 241–248.

Bédard, C., H. Kröger, and A. Destexhe (2006). "Does the 1/f Frequency Scaling of Brain Signals Reflect Self-Organized Critical States?" In: *Physical Review Letters* 97.11, p. 118102.

Bédard, C. and A. Destexhe (2009). "Macroscopic models of local field potentials and the apparent 1/f noise in brain activity". In: *Biophysical Journal* 96.7, pp. 2589–2603.

Beggs, J. M. and D. Plenz (2003). "Neuronal avalanches in neocortical circuits." In: *The Journal of neuroscience : the official journal of the Society for Neuroscience* 23.35, pp. 11167–77.

Beggs, J. M. and N. Timme (2012). "Being Critical of Criticality in the Brain". In: *Frontiers in Physiology* 3.June, pp. 1–14.

Benayoun, M., J. D. Cowan, W. van Drongelen, and E. Wallace (2010). "Avalanches in a stochastic model of spiking neurons". In: *PLoS Computational Biology* 6.7, p. 21.

Berenyi, a., M. Belluscio, D. Mao, and G. Buzsaki (2012). "Closed-Loop Control of Epilepsy by Transcranial Electrical Stimulation". In: *Science* 337.6095, pp. 735–737.

Berg, A. T. et al. (2010). "Revised terminology and concepts for organization of seizures and epilepsies: Report of the ILAE Commission on Classification and Terminology, 2005-2009". In: *Epilepsia* 51.4, pp. 676–685.

Berger, H. (1933). "Über das Elektrenkephalogramm des Menschen". In: *Archiv für Psychiatrie und Nervenkrankheiten* 99.1, pp. 555–574.

Beurle, R. L. (1956). "Properties of a Mass of Cells Capable of Regenerating Pulses". In: *Philosophical Transactions of the Royal Society B: Biological Sciences* 240.669, pp. 55–94.

Bhattacharya, B. S., D. Coyle, and L. P. Maguire (2011). "A thalamo-cortico-thalamic neural mass model to study alpha rhythms in Alzheimer's disease". In: *Neural Networks* 24.6, pp. 631–645.

Boccaletti, S., J. Kurths, G. Osipov, D. L. Valladares, and C. S. Zhou (2002). "The synchronization of chaotic systems". In: *Physics Reports* 366, pp. 1–101.

Bojak, I. (2014). Personal communication.

Bojak, I. and M. Breakspear (2015). "Neuroimaging, Neural Population Models for". In: *Encyclopedia of Computational Neuroscience*. New York, NY: Springer New York, pp. 1919–1944.

Bojak, I., T. F. Oostendorp, A. T. Reid, and R. Kötter (2010). "Connecting mean field models of neural activity to EEG and fMRI data." In: *Brain topography* 23.2, pp. 139–49.

Bonachela, J., S. de Franciscis, J. J. Torres, and M. Muñoz (2010). "Self-organization without conservation: are neuronal avalanches generically critical?" In: *Journal of Statistical Mechanics: Theory and Experiment* 2010.02, P02015.

Bonjean, M., T. Baker, M. Bazhenov, S. Cash, E. Halgren, and T. Sejnowski (2012). "Interactions between core and matrix thalamocortical projections in human sleep spindle synchronization." In: *The Journal of neuroscience : the official journal of the Society for Neuroscience* 32.15, pp. 5250–63.

Botcharova, M., S. F. Farmer, and L. Berthouze (2012). "Power-law distribution of phase-locking intervals does not imply critical interaction". In: *Physical Review E - Statistical, Nonlinear, and Soft Matter Physics* 86.5, pp. 1–13.

Braun, W., P. C. Matthews, and R. Thul (2015). "First-passage times in integrate-and-fire neurons with stochastic thresholds". In: *Physical Review E* 91.5, pp. 1–7.

Breakspear, M., J. A. Roberts, J. R. Terry, S. Rodrigues, N. Mahant, and P. A. Robinson (2006). "A unifying explanation of primary generalized seizures through nonlinear brain modeling and bifurcation analysis." In: *Cerebral cortex (New York, N.Y. : 1991)* 16.9, pp. 1296–313.

Brinkmann, B. H. et al. (2016). "Crowdsourcing reproducible seizure forecasting in human and canine epilepsy". In: pp. 1713–1722.

Bruns, A. and R. Eckhorn (2004). "Task-related coupling from high- to low-frequency signals among visual cortical areas in human subdural recordings". In: *International Journal of Psychophysiology* 51.2, pp. 97–116.

Bullmore, E. T. and O. Sporns (2012). "The economy of brain network organization." In: *Nature reviews. Neuroscience* 13.5, pp. 336–49.

Bullock, T. H., M. C. Mcclune, J. Z. Achimowicz, V. J. Iragui-Madoz, R. B. Duckrow, and S. S. Spencer (1995). "EEG coherence has structure in the millimeter domain: subdural and hippocampal recordings from epileptic patients". In: *Electroencephalography and Clinical Neurophysiology* 95.3, pp. 161–177.

Buxhoeveden, D. P. and M. F. Casanova (2002). "The minicolumn hypothesis in neuroscience." In: *Brain : a journal of neurology* 125.Pt 5, pp. 935–51.

Buxton, R. B. and L. R. Frank (1997). "A model for the coupling between cerebral blood flow and oxygen metabolism during neural stimulation." In: *Journal of Cerebral Blood Flow and Metabolism* 17, pp. 64–72.

Buxton, R. B. (2012). "Dynamic models of BOLD contrast". In: *NeuroImage* 62.2, pp. 953–961.

Buxton, R. B., E. C. Wong, and L. R. Frank (1998). "Dynamics of blood flow and oxygenation changes during brain activation: the balloon model." In: *Magnetic resonance in medicine : official journal of the Society of Magnetic Resonance in Medicine / Society of Magnetic Resonance in Medicine* 39.6, pp. 855–64.

Buzsáki, G. (2006). *Rhythms of the Brain*. Oxford University Press.

Buzsáki, G. and A. Draguhn (2004). "Neuronal oscillations in cortical networks." In: *Science (New York, N.Y.)* 304.5679, pp. 1926–9.

Buzsáki, G. and E. I. Moser (2013). "Memory, navigation and theta rhythm in the hippocampal-entorhinal system". In: *Nature Neuroscience* 16.2, pp. 130–138.

Buzsáki, G., C. Anastassiou, and C. Koch (2012). "The origin of extracellular fields and currents–EEG, ECoG, LFP and spikes." In: *Nature reviews. Neuroscience* 13.6, pp. 407–20.

Buzsáki, G., N. Logothetis, and W. Singer (2013). "Scaling brain size, keeping timing: evolutionary preservation of brain rhythms." In: *Neuron* 80.3, pp. 751–64.

Cabral, J., H. M. Fernandes, T. J. Van Hartevelt, A. C. James, M. L. Kringelbach, and G. Deco (2013). "Structural connectivity in schizophrenia and its impact on the dynamics of spontaneous functional networks." In: *Chaos (Woodbury, N.Y.)* 23.4, p. 046111.

Cannon, J., M. M. McCarthy, S. Lee, J. Lee, C. Börgers, M. A. Whittington, and N. Kopell (2014). "Neurosystems: brain rhythms and cognitive processing". In: *European Journal of Neuroscience* 39.5, pp. 705–719.

Canolty, R. T. and R. T. Knight (2010). "The functional role of cross-frequency coupling." In: *Trends in cognitive sciences* 14.11, pp. 506–15.

Chakravarthy, N., S. Sabesan, K. Tsakalis, and L. Iasemidis (2009). "Controlling epileptic seizures in a neural mass model". In: *Journal of Combinatorial Optimization* 17.1, pp. 98–116.

Chialvo, D. R., A. Longtin, and J. Müller-Gerking (1997). "Stochastic resonance in models of neuronal ensembles". In: *Physical Review E* 55.2, pp. 1798–1808.

Chialvo, D. R., P. Balenzuela, D. Fraiman, L. M. Ricciardi, A. Buonocore, and E. Pirozzi (2008). "The Brain: What is Critical About It?" In: *AIP Conference Proceedings*. Vol. 1028. AIP, pp. 28–45.

Cohen, M. X., N. Axmacher, D. Lenartz, C. E. Elger, V. Sturm, and T. E. Schlaepfer (2009a). "Good vibrations: cross-frequency coupling in the human nucleus accumbens during reward processing." In: *Journal of cognitive neuroscience* 21.5, pp. 875–89.

Cohen, M. X., C. E. Elger, and J. Fell (2009b). "Oscillatory activity and phase-amplitude coupling in the human medial frontal cortex during decision making." In: *Journal of cognitive neuroscience* 21.2, pp. 390–402.

Collins, J. J., C. C. Chow, a Capela, and T. T. Imhoff (1996a). "Aperiodic stochastic resonance". In: *Physical Review E* 54.5, pp. 5575–5584.

Collins, J. J., T. T. Imhoff, and P. Grigg (1996b). "Noise-enhanced information transmission in rat SA1 cutaneous mechanoreceptors via aperiodic stochastic resonance." In: *Journal of neurophysiology* 76.1, pp. 642–5.

Compte, A., M. V. Sanchez-Vives, D. A. McCormick, and X.-J. Wang (2003). "Cellular and network mechanisms of slow oscillatory activity (<1 Hz) and wave propagations in a cortical network model." In: *Journal of neurophysiology* 89.5, pp. 2707–25.

Coombes, S. and Á. Byrne (2016). "Next generation neural mass models".

Coombes, S. and C. Laing (2009). "Delays in activity-based neural networks". In: *Philosophical Transactions of the Royal Society A: Mathematical, Physical and Engineering Sciences* 367.1891, pp. 1117–1129.

Coombes, S. and J. R. Terry (2012). "The dynamics of neurological disease: Integrating computational, experimental and clinical neuroscience". In: *European Journal of Neuroscience* 36.2, pp. 2118–2120.

Costa, N. M. da and K. A. C. Martin (2010). "Whose Cortical Column Would that Be?" In: *Frontiers in neuroanatomy* 4.May, p. 16.

Cox, R., J. van Driel, M. de Boer, and L. M. Talamini (2014). "Slow Oscillations during Sleep Coordinate Interregional Communication in Cortical Networks". In: *Journal of Neuroscience* 34.50, pp. 16890–16901.

Daducci, A. et al. (2014). "Quantitative comparison of reconstruction methods for intra-voxel fiber recovery from diffusion MRI". In: *IEEE Transactions on Medical Imaging* 33.2, pp. 384–399.

David, O. (2014). *Functional Brain Tractography Project*.

David, O. and K. J. Friston (2003). "A neural mass model for MEG/EEG:coupling and neuronal dynamics". In: *NeuroImage* 20.3, pp. 1743–1755.

David, O., D. Cosmelli, and K. J. Friston (2004). "Evaluation of different measures of functional connectivity using a neural mass model". In: *NeuroImage* 21.2, pp. 659–673.

David, O., L. Harrison, and K. J. Friston (2005). "Modelling event-related responses in the brain." In: *NeuroImage* 25.3, pp. 756–70.

David, O., J. M. Kilner, and K. J. Friston (2006). "Mechanisms of evoked and induced responses in MEG/EEG". In: *NeuroImage* 31.4, pp. 1580–1591.

Davidsen, J. and H. G. Schuster (2000). "$1/f^{\alpha}$ noise from self-organized critical models with uniform driving". In: *Physical Review E* 62.5, pp. 6111–6115.

Davidsen, J. and H. G. Schuster (2002). "Simple model for $1/f^{\alpha}$ noise". In: *Physical Review E* 65.2, p. 026120.

Davis, T., K. Kwong, R. Weisskoff, and B. Rosen (1998). "Calibrated functional MRI: Mapping the dynamics of oxidative metabolism". In: *Proceedings of the National Academy of Sciences* 95 (4), pp. 1834–1839.

Dayan, P. and L. Abbott (2001). *Theoretical Neuroscience: Computational and Mathematical Modeling of Neural Systems*. Computational Neuroscience Series. Massachusetts Institute of Technology Press.

Deco, G., A. R. McIntosh, K. Shen, R. M. Hutchison, R. S. Menon, S. Everling, P. Hagmann, and V. K. Jirsa (2014). "Identification of Optimal Structural Connectivity Using Functional Connectivity and Neural Modeling". In: *Journal of Neuroscience* 34.23, pp. 7910–7916.

Deco, G. and M. L. Kringelbach (2016). "Metastability and Coherence: Extending the Communication through Coherence Hypothesis Using A Whole-Brain Computational Perspective". In: *Trends in Neurosciences* 39.3, pp. 125–135.

Deco, G., V. K. Jirsa, P. a. Robinson, M. Breakspear, and K. Friston (2008). "The dynamic brain: from spiking neurons to neural masses and cortical fields." In: *PLoS computational biology* 4.8, e1000092.

Deco, G., V. Jirsa, a. R. McIntosh, O. Sporns, and R. Kötter (2009). "Key role of coupling, delay, and noise in resting brain fluctuations." In: *Proceedings of the National Academy of Sciences of the United States of America* 106.25, pp. 10302–7.

Deco, G., M. Senden, and V. Jirsa (2012). "How anatomy shapes dynamics: a semi-analytical study of the brain at rest by a simple spin model". In: *Frontiers in Computational Neuroscience* 6.September, pp. 1–7.

Deco, G., V. K. Jirsa, and A. R. McIntosh (2013). "Resting brains never rest: computational insights into potential cognitive architectures." In: *Trends in neurosciences* 36.5, pp. 268–74.

Deco, G., G. Tononi, M. Boly, and M. L. Kringelbach (2015). "Rethinking segregation and integration: contributions of whole-brain modelling." In: *Nature reviews. Neuroscience* 16.7, pp. 430–439.

DeFelipe, J. and I. Fariñas (1992). "The pyramidal neuron of the cerebral cortex: morphological and chemical characteristics of the synaptic inputs". In: *Prog Neurobiol* 39.6, pp. 563–607.

DeFelipe, J., L. Alonso-Nanclares, and J. I. Arellano (2002). "Microstructure of the neocortex: Compariv aspects". In: *J Neurocytology* 31.2002, pp. 299–316.

Dehghani, N., C. Bédard, S. S. Cash, E. Halgren, and A. Destexhe (2010). "Comparative power spectral analysis of simultaneous elecroencephalographic and magnetoencephalographic recordings in humans suggests non-resistive extracellular media". In: *Journal of Computational Neuroscience* 29.3, pp. 405–421.

Dehghani, N., N. G. Hatsopoulos, Z. D. Haga, R. A. Parker, B. Greger, E. Halgren, S. S. Cash, and A. Destexhe (2012). "Avalanche Analysis from Multielectrode Ensemble Recordings in Cat, Monkey, and Human Cerebral Cortex during Wakefulness and Sleep". In: *Frontiers in Physiology* 3.August, pp. 1–18.

Destexhe, A. (2007). "Spike-and-wave oscillations". In: 2.2, p. 1402.

Destexhe, A. and M. Rudolph (2004). "Extracting information from the power spectrum of synaptic noise." In: *Journal of computational neuroscience* 17.3, pp. 327–45.

Dijk, H. van, J.-M. Schoffelen, R. Oostenveld, and O. Jensen (2008). "Prestimulus Oscillatory Activity in the Alpha Band Predicts Visual Discrimination Ability". In: *Journal of Neuroscience* 28.8, pp. 1816–1823.

Diniz, A., M. L. Wijnants, K. Torre, J. Barreiros, N. Crato, A. M. T. Bosman, F. Hasselman, R. F. A. Cox, G. C. Van Orden, and D. Delignières (2011). "Contemporary theories of 1/f noise in motor control". In: *Human Movement Science* 30.5, pp. 889–905.

Douglas, R. J. and K. A. Martin (1991). "A functional microcircuit for cat visual cortex". In: *The Journal of physiology* 440.1, pp. 735–769.

Drysdale, P. M., J. P. Huber, P. a. Robinson, and K. M. Aquino (2010). "Spatiotemporal BOLD dynamics from a poroelastic hemodynamic model." In: *Journal of theoretical biology* 265.4, pp. 524–534.

Duch, W., K. Dobosz, and D. Mikołajewski (2013). "Autism and ADHD - Two ends of the same spectrum?" In: *Lecture Notes in Computer Science (including subseries Lecture Notes in Artificial Intelligence and Lecture Notes in Bioinformatics)* 8226 LNCS.PART 1, pp. 623–630.

Durand, D. M. (2009). "Control of seizure activity by electrical stimulation: Effect of frequency". In: *Proceedings of the 31st Annual International Conference of the IEEE Engineering in Medicine and Biology Society: Engineering the Future of Biomedicine, EMBC 2009*, p. 2375.

Eddy, S. R. (2004). "What is Bayesian statistics?" In: *Nature biotechnology* 22.9, pp. 1177–1178.

Eguíluz, V. M., D. R. Chialvo, G. a. Cecchi, M. Baliki, and a. V. Apkarian (2005). "Scale-Free Brain Functional Networks". In: *Physical Review Letters* 94.1, p. 018102.

El Boustani, S., O. Marre, S. Béhuret, P. Baudot, P. Yger, T. Bal, A. Destexhe, and Y. Frégnac (2009). "Network-state modulation of power-law frequency-scaling in visual cortical neurons". In: *PLoS Computational Biology* 5.9.

Engel, A. K., P. Fries, and W. Singer (2001). "Dynamic predictions: Oscillations and synchrony in topdown processing". In: *Nature Reviews Neuroscience* 2.10, pp. 704–716.

Ermentrout, B. (2002). *Simulating, analyzing, and animating dynamical systems : a guide to XPPAUT for researchers and students*. Philadelphia, Society for Industrial and Applied Mathematics.

Ermentrout, G. B., R. F. Galán, and N. N. Urban (2008). "Reliability, synchrony and noise". In: *Trends in Neurosciences* 31.8, pp. 428–434.

Faisal, A. A., L. P. J. Selen, and D. M. Wolpert (2008). "Noise in the nervous system". In: *Nature Reviews Neuroscience* 9.4, pp. 292–303.

Fisher, R. S. and A. L. Velasco (2014). "Electrical brain stimulation for epilepsy." In: *Nature reviews. Neurology* 10.5, pp. 261–70.

Fisher, R. S., W. Van Emde Boas, W. Blume, C. Elger, P. Genton, P. Lee, and J. Engel (2005). "Epileptic seizures and epilepsy: Definitions proposed by the International League Against Epilepsy (ILAE) and the International Bureau for Epilepsy (IBE)". In: *Epilepsia* 46.4, pp. 470–472.

FitzHugh, R. (1961). "Impulses and Physiological States in Theoretical Models of Nerve Membrane". In: *Biophysical Journal* 1.6, pp. 445–466.

Fox, M. D. and M. E. Raichle (2007). "Spontaneous fluctuations in brain activity observed with functional magnetic resonance imaging". In: *Nat Rev Neurosci* 8.9, pp. 700–711.

Freeman, W. J. (1967). "Analysis of function of cerebral cortex by use of control systems theory". In: *The Logistics Review* 3, pp. 5–40.

Freeman, W. J. (1972a). "Linear analysis of the dynamics of neural masses." In: *Annual review of biophysics and bioengineering* 1, pp. 225–56.

Freeman, W. J. (1972b). "Waves, pulses, and the theory of neural masses." In: *Progress in theoretical biology* 2.1.

Freeman, W. J. (1975). *Mass action in the nervous system*.

Freeman, W. J. (2000). "A proposed name for aperiodic brain activity: stochastic chaos". In: *Neural Networks* 13.1, pp. 11–13.

Freeman, W. J. and J. Zhai (2009). "Simulated power spectral density (PSD) of background electrocorticogram (ECoG)". In: *Cognitive Neurodynamics* 3.1, pp. 97–103.

Freeman, W. J., L. J. Rogers, M. D. Holmes, and D. L. Silbergeld (2000). "Spatial spectral analysis of human electrocorticograms including the alpha and gamma bands." In: *Journal of neuroscience methods* 95.2, pp. 111–121.

Freestone, D. R., P. J. Karoly, D. NeÅiÄ, P. Aram, M. J. Cook, and D. B. Grayden (2014). "Estimation of effective connectivity via data-driven neural modeling". In: *Frontiers in Neuroscience* 8.November, pp. 1–20.

Freyer, F., J. A. Roberts, R. Becker, P. A. Robinson, P. Ritter, and M. Breakspear (2011). "Biophysical Mechanisms of Multistability in Resting-State Cortical Rhythms". In: *The Journal of Neuroscience* 31.17, pp. 6353–6361.

Fries, P. (2005). "A mechanism for cognitive dynamics: Neuronal communication through neuronal coherence". In: *Trends in Cognitive Sciences* 9.10, pp. 474–480.

Fries, P. (2009). "Neuronal Gamma-Band Synchronization as a Fundamental Process in Cortical Computation". In: *Annual Review of Neuroscience* 32.1, pp. 209–224.

Friston, K. J., A Mechelli, R Turner, and C. J. Price (2000). "Nonlinear responses in fMRI: the Balloon model, Volterra kernels, and other hemodynamics." In: *NeuroImage* 12.4, pp. 466–77.

Friston, K. J. (1994). "Functional and effective connectivity in neuroimaging: A synthesis". In: *Human Brain Mapping* 2.1-2, pp. 56–78.

Friston, K., L. Harrison, and W. Penny (2003). "Dynamic causal modelling". In: *NeuroImage* 19.4, pp. 1273–1302.

Gai, Y., B. Doiron, and J. Rinzel (2010). "Slope-based stochastic resonance: How noise enables phasic neurons to encode slow signals". In: *PLoS Computational Biology* 6.6, pp. 1–22.

Garnier, A., A. Vidal, C. Huneau, and H. Benali (2015). "A neural mass model with direct and indirect excitatory feedback loops: identification of bifurcations and temporal dynamics." In: *Neural computation* 27.2, pp. 329–64.

Ghosh, A., Y. Rho, A. R. McIntosh, R. Kötter, and V. K. Jirsa (2008). "Noise during Rest Enables the Exploration of the Brain's Dynamic Repertoire". In: *PLoS Computational Biology* 4.10. Ed. by K. J. Friston, e1000196.

Gluckman, B. J., T. I. Netoff, E. J. Neel, W. L. Ditto, M. L. Spano, and S. J. Schiff (1996). "Stochastic Resonance in a Neuronal Network from Mammalian Brain". In: *Physical Review Letters* 77.19, pp. 4098–4101.

Golos, M., V. Jirsa, and E. Daucé (2015). "Multistability in Large Scale Models of Brain Activity". In: *PLoS Computational Biology* 11.12, pp. 1–32.

Goodfellow, M., C. Rummel, E. Abela, M. P. Richardson, K. Schindler, and J. R. Terry (2016). "Estimation of brain network ictogenicity predicts outcome from epilepsy surgery". In: *Scientific Reports* 6.0, p. 29215.

Goodfellow, M. and P. Glendinning (2013). "Mechanisms of intermittent state transitions in a coupled heterogeneous oscillator model of epilepsy." In: *Journal of mathematical neuroscience* 3.1, p. 17.

Goodfellow, M., K. Schindler, and G. Baier (2011). "Intermittent spike-wave dynamics in a heterogeneous, spatially extended neural mass model." In: *NeuroImage* 55.3, pp. 920–32.

Grabska-Barwińska, A. and J. Żygierewicz (2006). "A model of event-related EEG synchronization changes in beta and gamma frequency bands". In: *Journal of Theoretical Biology* 238.4, pp. 901–913.

Griffith, J. S. (1963). "A field theory of neural nets: I. Derivation of field equations." In: *Bulletin of Mathematical Biophysics* 25.1957, pp. 111–120.

Griffith, J. S. (1965). "A field theory of neural nets: II. Properties of the field equations". In: *Bulletin of Mathematical Biophysics* 27.1, pp. 187–195.

Grimbert, F. and O. Faugeras (2006). "Bifurcation analysis of Jansen's neural mass model." In: *Neural computation* 18.12, pp. 3052–68.

Grothe, I., S. D. Neitzel, S. Mandon, and A. K. Kreiter (2012). "Switching Neuronal Inputs by Differential Modulations of Gamma-Band Phase-Coherence". In: *Journal of Neuroscience* 32.46, pp. 16172–16180.

Grubb, R. L. J., Raichle M. E., and T.-P. M. M. Eichling J. O. (1974). "The effects of changes in PaCO_2 on cerebral blood volume, blood flow, and vascular mean transit time". In: *Stroke* 5.5, pp. 603–609.

Gupta, D., P. Ossenblok, and G. van Luijtelaar (2011). "Space-time network connectivity and cortical activations preceding spike wave discharges in human absence epilepsy: a MEG study". In: *Med Biol Eng Comput* 49.5, pp. 555–565.

Hagmann, P. (2005). "From diffusion MRI to brain connectomics". eng. PhD thesis. Lausanne: STI - School of Engineering.

Haimovici, A., E. Tagliazucchi, P. Balenzuela, and D. R. Chialvo (2013). "Brain Organization into Resting State Networks Emerges at Criticality on a Model of the Human Connectome". In: *Physical Review Letters* 110.17, p. 178101.

Handel, P. and A. Chung (1993). "Noise in physical systems and 1/f fluctuations". In: New York, NY (United States); AIP.

Harmony, T. (2013). "The functional significance of delta oscillations in cognitive processing". In: *Frontiers in Integrative Neuroscience* 7.December, p. 83.

Harmony, T., T. Fernández, J. Silva, J. Bosch, P. Valdés, A. Fernández-Bouzas, L. Galán, E. Aubert, and D. Rodríguez (1999). "Do specific EEG frequencies indicate different processes during mental calculation?" In: *Neuroscience Letters* 266.1, pp. 25–28.

Hashemi, M., A. Hutt, and J. Sleigh (2015). "How the cortico-thalamic feedback affects the EEG power spectrum over frontal and occipital regions during propofol-induced sedation". In: *Journal of Computational Neuroscience* 39.2, pp. 155–179.

Hausdorff, J. and C.-K. Peng (1996). "Multiscaled randomness: A possible source of 1/f noise in biology". In: *Physical Review E* 54.2, pp. 2154–2157.

Havlicek, M., A. Roebroeck, K. Friston, A. Gardumi, D. Ivanov, and K. Uludag (2015). "Physiologically informed dynamic causal modeling of fMRI data". In: *NeuroImage* 122, pp. 355–372.

Hayes, S., C. Grebogi, and E. Ott (1993). "Communicating with chaos". In: *Physical Review Letters* 70.20, pp. 3031–3034.

He, B. J. (2011). "Scale-Free Properties of the Functional Magnetic Resonance Imaging Signal during Rest and Task". In: *Journal of Neuroscience* 31.39, pp. 13786–13795.

He, B. J. (2014). "Scale-free brain activity: past, present, and future". In: *Trends in Cognitive Sciences* 18.9, pp. 480–487.

He, B. J., J. M. Zempel, A. Z. Snyder, and M. E. Raichle (2010). "The temporal structures and functional significance of scale-free brain activity". In: *Neuron* 66.3, pp. 353–369.

Heeger, D. J. and D. Ress (2002). "WHAT DOES fMRI TELL US ABOUT NEURONAL ACTIVITY?" In: *Nature Reviews Neuroscience* 3.2, pp. 142–151.

Herculano-Houzel, S. (2011). "Scaling of brain metabolism with a fixed energy budget per neuron: Implications for neuronal activity, plasticity and evolution". In: *PLoS ONE* 6.3.

Hesse, J. and T. Gross (2014). "Self-organized criticality as a fundamental property of neural systems". In: *Frontiers in Systems Neuroscience* 8.September, p. 166.

Heuvel, M. P. van den and O. Sporns (2011). "Rich-Club Organization of the Human Connectome". In: *Journal of Neuroscience* 31.44, pp. 15775–15786.

Heuvel, M. P. van den and O. Sporns (2013). "Network hubs in the human brain". In: *Trends in Cognitive Sciences* 17.12, pp. 683–696.

Hilgetag, C. C. and A. Goulas (2015). “Is the brain really a small-world network?” In: *Brain Structure and Function*.

Hindriks, R. and M. J. A. M. van Putten (2012). “Meanfield modeling of propofol-induced changes in spontaneous EEG rhythms”. In: *NeuroImage* 60.4, pp. 2323–2334.

Hlinka, J. and S. Coombes (2012). “Using computational models to relate structural and functional brain connectivity.” In: *The European journal of neuroscience* 36.2, pp. 2137–45.

Hodgkin, A. L. and A. F. Huxley (1990). “A quantitative description of membrane current and its application to conduction and excitation in nerve”. In: *Bulletin of Mathematical Biology* 52.1-2, pp. 25–71.

Hofman, M. A. (1988). “Size and shape of the cerebral cortex in mammals. II. The cortical volume.” In: *Brain, behavior and evolution* 32.1, pp. 17–26.

Huang, G., D. Zhang, J. Meng, and X. Zhu (2011). “Interactions between two neural populations: A mechanism of chaos and oscillation in neural mass model”. In: *Neurocomputing* 74.6, pp. 1026–1034.

Hubel, D. H. and T. N. Wiesel (1963). “Shape and arrangement of columns in cat’s striate cortex”. In: *The Journal of physiology* 165.3, pp. 559–568.

Hubel, D. H. and T. N. Wiesel (1974). “Sequence regularity and geometry of orientation columns in the monkey striate cortex.” In: *The Journal of comparative neurology* 158.3, pp. 267–293.

Hubel, D. H. and T. N. Wiesel (1977). “Functional architecture of macaque monkey visual cortex”. In: *Proceedings of the Royal Society of London. Series B* 198, pp. 1–59.

Hutcheon, B. and Y. Yarom (2000). “Resonance, oscillation and the intrinsic frequency preferences of neurons”. In: *Trends in Neurosciences* 23.5, pp. 216–222.

Hutchings, F., C. E. Han, S. S. Keller, B. Weber, P. N. Taylor, and M. Kaiser (2015). “Predicting Surgery Targets in Temporal Lobe Epilepsy through Structural Connectome Based Simulations”. In: *PLoS Computational Biology* 11.12, pp. 1–24.

Hutt, A. and T. D. Frank (2005). “Critical Fluctuations and 1/fα-Activity of Neural Fields Involving Transmission Delays”. In: *Acta Physica Polonica A* 108.2005, pp. 1021–1040.

Hutt, A. (2013). "The anesthetic propofol shifts the frequency of maximum spectral power in EEG during general anesthesia: analytical insights from a linear model". In: *Frontiers in Computational Neuroscience* 7.February, pp. 1–10.

Hutt, A. (2015). "Neural Fields Tutorial". In: CNS Meeting in Prague.

Iannotti, G. R. et al. (2016). "Epileptic networks are strongly connected with and without the effects of interictal discharges". In: *Epilepsia*, pp. 1–11.

Isler, J. R., P. G. Grieve, D Czernochowski, R. I. Stark, and D. Friedman (2008). "Cross-frequency phase coupling of brain rhythms during the orienting response." In: *Brain research* 1232, pp. 163–72.

Jankovic, J. (2008). "Parkinson's disease: clinical features and diagnosis". In: *Journal of Neurology, Neurosurgery & Psychiatry* 79.4, pp. 368–376.

Jansen, B. H. and V. G. Rit (1995). "Electroencephalogram and visual evoked potential generation in a mathematical model of coupled cortical columns". In: *Biological Cybernetics* 73.4, pp. 357–366.

Jansen, B. H., G. Zouridakis, and M. E. Brandt (1993). "A neurophysiologically-based mathematical model of flash visual evoked potentials". In: *Biological Cybernetics* 68.3, pp. 275–283.

Jensen, O. and L. L. Colgin (2007). "Cross-frequency coupling between neuronal oscillations." In: *Trends in cognitive sciences* 11.7, pp. 267–9.

Jensen, O., J. Kaiser, and J.-P. Lachaux (2007). "Human gamma-frequency oscillations associated with attention and memory". In: *Trends in Neurosciences* 30.7, pp. 317–324.

Jiménez-Jiménez, D. et al. (2015). "Prognostic value of intracranial seizure onset patterns for surgical outcome of the treatment of epilepsy". In: *Clinical Neurophysiology* 126.2, pp. 257 –267.

Jirsa, V. and V. Müller (2013). "Cross-frequency coupling in real and virtual brain networks." In: *Frontiers in computational neuroscience* 7.July, p. 78.

Jirsa, V. et al. (2016). "The Virtual Epileptic Patient: Individualized whole-brain models of epilepsy spread". In: *NeuroImage*.

Jiruska, P., A. D. Powell, J. K. Deans, and J. G. Jefferys (2010). "Effects of direct brain stimulation depend on seizure dynamics". In: *Epilepsia* 51.SUPPL. 3, pp. 93–97.

Johnson, J. B. (1925). "The Schottky Effect in Low Frequency Circuits". In: *Phys. Rev.* 26 (1), pp. 71–85.

Jones, E. G. (1998). "Viewpoint: The core and matrix of thalamic organization". In: *Neuroscience* 85.2, pp. 331–345.

Kaczmarek, L. K. and A Babloyantz (1977). "Spatiotemporal patterns in epileptic seizures". In: *Biol.Cybern.* 26, pp. 199–208.

Kærn, M., T. C. Elston, W. J. Blake, and J. J. Collins (2005). "Stochasticity in gene expression: from theories to phenotypes". In: *Nature Reviews Genetics* 6.6, pp. 451–464.

Kaiser, M. (2010). "Optimal hierarchical modular topologies for producing limited sustained activation of neural networks". In: *Frontiers in Neuroinformatics* 4.May, p. 8.

Kalman, R. E. (1960). "A New Approach to Linear Filtering and Prediction Problems". In: *Journal of Basic Engineering* 82.1, p. 35.

Kamrani, E. (2012). "Efficient hemodynamic states stimulation using fNIRS data with the extended Kalman filter and bifurcation analysis of balloon model". In: *Journal of Biomedical Science and Engineering* 05.11, pp. 609–628.

Kang, K., M. Shelley, J. A. Henrie, and R. Shapley (2010). "LFP spectral peaks in V1 cortex: network resonance and cortico-cortical feedback." In: *Journal of computational neuroscience* 29.3, pp. 495–507.

Karlsen, A. S. and B. Pakkenberg (2011). "Total numbers of neurons and glial cells in cortex and basal ganglia of aged brains with down syndrome-a stereological study". In: *Cerebral Cortex* 21.11, pp. 2519–2524.

Kasteleijn-Nolst Trenite, D. G. A. (2006). "Photosensitivity, visually sensitive seizures and epilepsies". In: *Epilepsy Research* 70.SUPPL.1, pp. 269–279.

Kaulakys, B., V. Gontis, and M. Alaburda (2005). "Point process model of 1/f noise vs a sum of Lorentzians". In: *Physical Review E - Statistical, Nonlinear, and Soft Matter Physics* 71.5, pp. 1–11.

Khakh, B. S. and K. D. McCarthy (2015). "Astrocyte calcium signaling: From observations to functions and the challenges therein". In: *Cold Spring Harbor Perspectives in Biology* 7.4, pp. 1–18.

Khambhati, A., B. Litt, and D. S. Bassett (2014). "Dynamic network drivers of seizure generation, propagation and termination in human epilepsy". In: *Proceedings of the National Academy of Sciences of the United States of America* 104.51, p. 7.

Khambhati, A. N., K. A. Davis, T. H. Lucas, B. Litt, and D. S. Bassett (2016). "Virtual Cortical Resection Reveals Push-Pull Network Control Preceding Seizure Evolution". In: *Neuron* 91.5, pp. 1170–1182.

Kitzbichler, M. G., M. L. Smith, S. R. Christensen, and E. Bullmore (2009). "Broadband Criticality of Human Brain Network Synchronization". In: *PLoS Computational Biology* 5.3. Ed. by T. Behrens, e1000314.

Klimesch, W. (1999). "EEG alpha and theta oscillations reflect cognitive and memory performance: a review and analysis". In: *Brain Research Reviews* 29.2-3, pp. 169–195.

Klimesch, W. (2012). "Alpha-band oscillations, attention, and controlled access to stored information". In: *Trends in Cognitive Sciences* 16.12, pp. 606–617.

Knill, D. C. and A. Pouget (2004). "The Bayesian brain: the role of uncertainty in neural coding and computation". In: *Trends in Neurosciences* 27.12, pp. 712–719.

Koch, M., J. Mostert, D. Heersema, and J. De Keyser (2007). "Tremor in multiple sclerosis". In: *Journal of Neurology* 254.2, pp. 133–145.

Kramer, M. a. and S. S. Cash (2012). "Epilepsy as a Disorder of Cortical Network Organization". In: *The Neuroscientist* 18.4, pp. 360–372.

Kramer, M. a. et al. (2012). "Human seizures self-terminate across spatial scales via a critical transition". In: *Proceedings of the National Academy of Sciences* 109.51, pp. 21116–21121.

Labyt, E., L. Uva, M. D. Curtis, and F. Wendling (2006). "Realistic Modeling of Entorhinal Cortex Field Potentials and Interpretation of Epileptic Activity in the Guinea Pig Isolated Brain Preparation". In: pp. 363–377.

Laing, C. and J. Lord (2010). *Stochastic Methods in Neuroscience*. Oxford University Press.

Lam, Y. W. and S. M. Sherman (2010). "Functional organization of the somatosensory cortical layer 6 feedback to the thalamus". In: *Cerebral Cortex* 20.1, pp. 13–24.

Lange, F. P. de, O. Jensen, M. Bauer, and I. Toni (2008). "Interactions between posterior gamma and frontal alpha/beta oscillations during imagined actions." In: *Frontiers in human neuroscience* 2.August, p. 7.

Larsson, P. G. and H. Kostov (2005). "Lower frequency variability in the alpha activity in EEG among patients with epilepsy". In: *Clinical Neurophysiology* 116.11, pp. 2701–2706.

Lee, E., J. Lee, and E. Kim (2016). "Excitation/Inhibition Imbalance in Animal Models of Autism Spectrum Disorders". In: *Biological Psychiatry* 6, pp. 1–10.

Lee, S.-A., D. D. Spencer, and S. S. Spencer (2000). "Intracranial EEG Seizure-Onset Patterns in Neocortical Epilepsy". In: *Epilepsia* 41.3, pp. 297–307.

Liley, D., I. Bojak, M. P. Dafilis, L. V. Veen, F. Frascoli, and B. L. Foster (2010). *Modeling Phase Transitions in the Brain*. Ed. by D. A. Steyn-Ross and M. Steyn-Ross. 126. New York, NY: Springer New York, pp. 117–145.

Liley, D. T. J., P. J. Cadusch, and M. P. Dafilis (2002). "A spatially continuous mean field theory of electrocortical activity." In: *Network (Bristol, England)* 13.1, pp. 67–113.

Liley, D. T. J., B. L. Foster, and I. Bojak (2012). "Co-operative Populations of Neurons: Mean Field Models of Mesoscopic Brain Activity". In: *Computational Systems Neurobiology*. Dordrecht: Springer Netherlands, pp. 317–364.

Lindén, H., K. H. Pettersen, and G. T. Einevoll (2010). "Intrinsic dendritic filtering gives low-pass power spectra of local field potentials". In: *Journal of Computational Neuroscience* 29.3, pp. 423–444.

Lindner, B., J. García-Ojalvo, A. Neiman, and L. Schimansky-Geier (2004). "Effects of noise in excitable systems". In: *Physics Reports* 392, pp. 321–424.

Lindner, J. F., B. K. Meadows, W. L. Ditto, M. E. Inchiosa, and A. R. Bulsara (1995). "Array enhanced stochastic resonance and spatiotemporal synchronization". In: *Physical Review Letters* 75.1, pp. 3–6.

Linkenkaer-Hansen, K., V. V. Nikouline, J. M. Palva, and R. J. Ilmoniemi (2001). "Long-range temporal correlations and scaling behavior in human brain oscillations." In: *The Journal of neuroscience : the official journal of the Society for Neuroscience* 21.4, pp. 1370–7.

Logothetis, N. K. (2003). "The underpinnings of the BOLD functional magnetic resonance imaging signal." In: *The Journal of neuroscience : the official journal of the Society for Neuroscience* 23.10, pp. 3963–71.

Longtin, A. (1993). "Stochastic resonance in neuron models". In: *Journal of Statistical Physics* 70.1-2, pp. 309–327.

Lopes da Silva, F. H., A. Hoeks, H. Smits, and L. H. Zetterberg (1974). "Model of brain rhythmic activity". In: *Kybernetik* 15.1, pp. 27–37.

Lopes da Silva, F. H., A. van Rotterdam, P. Barts, E. van Heusden, and W. Burr (1976). "Models of Neuronal Populations: The Basic Mechanisms of Rhythmicity". In: *Progress in Brain Research* 45.C, pp. 281–308.

Lopes da Silva, F. H., W. Blanes, S. N. Kalitzin, J. Parra, P. Suffczynski, and D. N. Velis (2003). "Dynamical diseases of brain systems: different routes to epileptic seizures." In: *IEEE transactions on bio-medical engineering* 50.5, pp. 540–8.

Lorente de No, R. (1938). "Architectonics and structure of the cerebral cortex". In: *Physiology of the nervous system*, pp. 291–330.

Lytton, W. W. (2008). "Computer modelling of epilepsy." In: *Nature reviews. Neuroscience* 9.8, pp. 626–637.

Ma, W. J., J. M. Beck, P. E. Latham, and A. Pouget (2006). "Bayesian inference with probabilistic population codes." In: *Nature Neuroscience* 9.11, pp. 1432–8.

Majumdar, K., P. D. Prasad, and S. Verma (2014). "Synchronization implies seizure or seizure implies synchronization?" In: *Brain Topography* 27.1, pp. 112–122.

Malagarriga, D., A. E. P. Villa, J. Garcia-Ojalvo, and A. J. Pons (2015a). "Mesoscopic Segregation of Excitation and Inhibition in a Brain Network Model". In: *PLoS Computational Biology* 11.2, pp. 1–21.

Malagarriga, D., M. a. García-Vellisca, A. E. P. Villa, J. M. Buldú, J. García-Ojalvo, and A. J. Pons (2015b). "Synchronization-based computation

through networks of coupled oscillators". In: *Frontiers in Computational Neuroscience* 9.August, pp. 1–13.

Mandeville, J. B. et al. (1996). "CBV functional imaging in rat brain using iron oxide agent at steady state concentration". In: *Proc. ISMRM 4th Annual Meeting, New York* 666, p. 292.

Mandeville, J. B., J. J. A. Marota, B. E. Kosofsky, J. R. Keltner, R. Wcissleder, B. R. Rosen, and R. M. Weisskoff (1998). "Dynamic functional imaging of relative cerebral blood volume during rat forepaw stimulation". In: *Magnetic Resononance in Medicine* 39, pp. 615–624.

Mandeville, J. B., J. J. Marota, C Ayata, G Zaharchuk, M. a. Moskowitz, B. R. Rosen, and R. M. Weisskoff (1999). "Evidence of a cerebrovascular postarteriole windkessel with delayed compliance." In: *Journal of cerebral blood flow and metabolism : official journal of the International Society of Cerebral Blood Flow and Metabolism* 19.6, pp. 679–689.

Marieb, E. and K. Hoehn (2007). *Human Anatomy and Physiology*. Pearson Education.

Marković, D. and C. Gros (2013). "Power laws and self-organized criticality in theory and nature". In: *Physics Reports*.

Markram, H. (2006). "The blue brain project." In: *Nature reviews. Neuroscience* 7.2, pp. 153–60.

Markram, H., M. Toledo-Rodriguez, Y. Wang, A. Gupta, G. Silberberg, and C. Wu (2004). "Interneurons of the neocortical inhibitory system." In: *Nature reviews. Neuroscience* 5.10, pp. 793–807.

Marshall, L., H. Helgadóttir, M. Mölle, and J. Born (2006). "Boosting slow oscillations during sleep potentiates memory." In: *Nature* 444.7119, pp. 610–3.

Massimini, M., F. Ferrarelli, S. K. Esser, B. A. Riedner, R. Huber, M. Murphy, M. J. Peterson, and G. Tononi (2007). "Triggering sleep slow waves by transcranial magnetic stimulation." In: *Proceedings of the National Academy of Sciences of the United States of America* 104.20, pp. 8496–501.

Mazziotta, J. C., A. W. Toga, A. Evans, P. Fox, and J. Lancaster (1995). *A probabilistic atlas of the human brain: theory and rationale for its development. The International Consortium for Brain Mapping (ICBM).*

Mazzoni, A., S. Panzeri, N. K. Logothetis, and N. Brunel (2008). "Encoding of naturalistic stimuli by local field potential spectra in networks of excitatory and inhibitory neurons." In: *PLoS computational biology* 4.12, e1000239.

Mazzoni, A., K. Whittingstall, N. Brunel, N. K. Logothetis, and S. Panzeri (2010). "Understanding the relationships between spike rate and delta/gamma frequency bands of LFPs and EEGs using a local cortical network model." In: *NeuroImage* 52.3, pp. 956–72.

Mazzoni, A., N. Brunel, S. Cavallari, N. K. Logothetis, and S. Panzeri (2011). "Cortical dynamics during naturalistic sensory stimulations: experiments and models." In: *Journal of physiology, Paris* 105.1-3, pp. 2–15.

McDonnell, M. D. and D. Abbott (2009). "What Is Stochastic Resonance? Definitions, Misconceptions, Debates, and Its Relevance to Biology". In: *PLoS Computational Biology* 5.5. Ed. by K. J. Friston, e1000348.

McDonnell, M. D. and L. M. Ward (2011). "The benefits of noise in neural systems: bridging theory and experiment". In: *Nature Reviews Neuroscience* 12.7, pp. 415–426.

McDonnell, M. D., J. H. Goldwyn, and B. Lindner (2016). "Editorial : Neuronal Stochastic Variability : Influences on Spiking Dynamics and Network Activity". In: 10.April, pp. 1–3.

Meisel, C., A. Storch, S. Hallmeyer-Elgner, E. Bullmore, and T. Gross (2012). "Failure of adaptive self-organized criticality during epileptic seizure attacks". In: *PLoS Computational Biology* 8.1.

Meyer, G. (1987). "Forms and spatial arrangement of neurons in the primary motor cortex of man". In: *J. Comp. Neurol.* 262.3, pp. 402–428.

Milanowski, P. and P. Suffczyński (2016). "Seizures Start without Common Signatures of Critical Transition". In: *International Journal of Neural Systems* 26.8, p. 1650053.

Miller, K. J., L. B. Sorensen, J. G. Ojemann, and M. Den Nijs (2009). "Power-law scaling in the brain surface electric potential". In: *PLoS Computational Biology* 5.12.

Millman, D., S. Mihalas, A. Kirkwood, and E. Niebur (2010). "Self-organized criticality occurs in non-conservative neuronal networks during up' states". In: *Nature Physics* 6.10, pp. 801–805.

Milstein, J., F. Mormann, I. Fried, and C. Koch (2009). "Neuronal shot noise and Brownian 1/f2 behavior in the local field potential." In: *PloS one* 4.2, e4338.

Milton, J. and P. Jung (2002). *Epilepsy as a Dynamic Disease*. Biological and Medical Physics, Biomedical Engineering. Springer.

Milton, J. G., J Foss, J. D. Hunter, and J. L. Cabrera (2004). "Controlling neurological disease at the edge of instability". In: *Quantitative Neuroscience: Models, Algorithms, Diagnostics, and Therapeutic Applications* 2, pp. 117–143.

Milton, J. G. (2010). "Epilepsy as a dynamic disease: A tutorial of the past with an eye to the future". In: *Epilepsy and Behavior* 18.1-2, pp. 33–44.

Mochol, G., A. Hermoso-Mendizabal, S. Sakata, K. D. Harris, and J. de la Rocha (2015). "Stochastic transitions into silence cause noise correlations in cortical circuits". In: *Proceedings of the National Academy of Sciences*, p. 201410509.

Molaee-Ardekani, B., P. Benquet, F. Bartolomei, and F. Wendling (2010). "Computational modeling of high-frequency oscillations at the onset of neocortical partial seizures: From 'altered structure' to 'dysfunction'". In: *NeuroImage* 52.3, pp. 1109–1122.

Mormann, F., R. G. Andrzejak, C. E. Elger, and K. Lehnertz (2007). "Seizure prediction: The long and winding road". In: *Brain* 130.2, pp. 314–333.

Moss, F. (2004). "Stochastic resonance and sensory information processing: a tutorial and review of application". In: *Clinical Neurophysiology* 115.2, pp. 267–281.

Mountcastle, V. B. (1957). "Modality and topographic properties of single neurons of cat's somatic sensory cortex." In: *Journal of neurophysiology* 20.4, pp. 408–34.

Mountcastle, V. B. (1997). "The columnar organization of the neocortex". In: *Brain* 120.4, pp. 701–722.

Mullinger, K. J., S. D. Mayhew, A. P. Bagshaw, R. Bowtell, and S. T. Francis (2013). "Poststimulus undershoots in cerebral blood flow and BOLD fMRI responses are modulated by poststimulus neuronal activity". In: *Proceedings of the National Academy of Sciences* 110.33, pp. 13636–13641.

Muñoz, M. A., R. Juhász, C. Castellano, and G. Ódor (2010). "Griffiths phases on complex networks". In: *Physical Review Letters* 105.12, pp. 1–4.

Narayanan, R. T., R. Egger, A. S. Johnson, H. D. Mansvelder, B. Sakmann, C. P. de Kock, and M. Oberlaender (2015). "Beyond Columnar Organization: Cell Type- and Target Layer-Specific Principles of Horizontal Axon Projection Patterns in Rat Vibrissal Cortex". In: *Cerebral Cortex* 25.11, pp. 4450–4468.

Naze, S., C. Bernard, and V. Jirsa (2015). "Computational Modeling of Seizure Dynamics Using Coupled Neuronal Networks: Factors Shaping Epileptiform Activity". In: *PLOS Computational Biology* 11.5, e1004209.

Ngo, H.-V. V., T. Martinetz, J. Born, and M. Mölle (2013). "Auditory closed-loop stimulation of the sleep slow oscillation enhances memory." In: *Neuron* 78.3, pp. 545–53.

Nguyen Trong, M., I. Bojak, and T. R. Knösche (2012). "Associating spontaneous with evoked activity in a neural mass model of visual cortex." In: *NeuroImage* 66C, pp. 80–87.

Niedermeyer, E. and F. H. Lopes da Silva (2005). *Electroencephalography: basic principles, clinical applications, and related fields*. 5th ed. Philadelphia: Lippincott Williams and Wilkins.

Nunez, P. and R. Srinivasan (2006). *Electric Fields of the Brain: The Neurophysics of EEG*. Oxford University Press.

O'Muircheartaigh, J., C. Vollmar, G. J. Barker, V. Kumari, M. R. Symms, P. Thompson, J. S. Duncan, M. J. Koepp, and M. P. Richardson (2012). "Abnormal thalamocortical structural and functional connectivity in juvenile myoclonic epilepsy". In: *Brain* 135.12, pp. 3635–3644.

Onslow, A. C. E., M. W. Jones, and R. Bogacz (2014). "A canonical circuit for generating phase-amplitude coupling". In: *PLoS ONE* 9.8.

Osipova, D., A. Takashima, R. Oostenveld, G. Fernandez, E. Maris, and O. Jensen (2006). "Theta and Gamma Oscillations Predict Encoding and Retrieval of Declarative Memory". In: *Journal of Neuroscience* 26.28, pp. 7523–7531.

Osipova, D., D. Hermes, and O. Jensen (2008). "Gamma power is phase-locked to posterior alpha activity." In: *PloS one* 3.12, e3990.

Padmanabhan, K. and N. N. Urban (2010). "Intrinsic biophysical diversity decorrelates neuronal firing while increasing information content". In: *Nature Neuroscience* 13.10, pp. 1276–1282.

Pakkenberg, B., D. Pelvig, L. Marner, M. J. Bundgaard, H. J. G. Gundersen, J. R. Nyengaard, and L. Regeur (2003). "Aging and the human neocortex". In: *Experimental Gerontology* 38.1-2, pp. 95–99.

Pang, R., B. J. Lansdell, and A. L. Fairhall (2016). "Dimensionality reduction in neuroscience". In: *Current Biology* 26.14, pp. 1–5.

Park, H.-J. and K. Friston (2013). "Structural and functional brain networks: from connections to cognition." In: *Science (New York, N.Y.)* 342.6158, p. 1238411.

Petermann, T., T. C. Thiagarajan, M. A. Lebedev, M. A. L. Nicolelis, D. R. Chialvo, and D. Plenz (2009). "Spontaneous cortical activity in awake monkeys composed of neuronal avalanches". In: *Proceedings of the National Academy of Sciences* 106.37, pp. 15921–15926.

Petkov, G., M. Goodfellow, M. P. Richardson, and J. R. Terry (2014). "A Critical Role for Network Structure in Seizure Onset: A Computational Modeling Approach". English. In: *Frontiers in Neurology* 5.

Pfurtscheller, G. and F. H. Lopes da Silva (1999). "Event-related EEG / MEG synchronization and desynchronization : basic principles". In: *Clinical Neurophysiology* 110, pp. 1842–1857.

Pfurtscheller, G., C. Neuper, C. Andrew, and G. Edlinger (1997). "Foot and hand area mu rhythms". In: *International Journal of Psychophysiology* 26.1-3, pp. 121–135.

Pfurtscheller, G., C. Neuper, C. Brunner, and F. L. da Silva (2005). "Beta rebound after different types of motor imagery in man". In: *Neuroscience Letters* 378.3, pp. 156–159.

Pikovsky, A., M. Rosenblum, and J. Kurths (2001). *Synchronization: a universal concept in nonlinear sciences*. Cambridge University Press.

Pikovsky, A. S. and J. Kurths (1997). "Coherence Resonance in a Noise-Driven Excitable System". In: *Physical Review Letters* 78.5, pp. 775–778.

Plenz, D. (2013). "The Critical Brain". In: *Physics* 6, p. 47.

Pons, A. J., J. L. Cantero, M. Atienza, and J. Garcia-Ojalvo (2010). "Relating structural and functional anomalous connectivity in the aging brain via neural mass modeling." In: *NeuroImage* 52.3, pp. 848–61.

Priesemann, V., M. Wibral, M. Valderrama, R. Pröpper, M. Le Van Quyen, T. Geisel, J. Triesch, D. Nikolić, and M. H. J. Munk (2014). "Spike avalanches in vivo suggest a driven, slightly subcritical brain state." In: *Frontiers in systems neuroscience* 8.June, p. 108.

Pruessner, G. (2012). *Self-Organised Criticality*.

Rabinovich, M. and H. Abarbanel (1998). "The role of chaos in neural systems". In: *Neuroscience* 87.1, pp. 5–14.

Rajan, K., L. F. Abbott, and H. Sompolinsky (2010). "Stimulus-dependent suppression of chaos in recurrent neural networks". In: *Physical Review E - Statistical, Nonlinear, and Soft Matter Physics* 82.1, pp. 1–5.

Ray, W. and H. Cole (1985). "EEG alpha activity reflects attentional demands, and beta activity reflects emotional and cognitive processes". In: *Science* 228.4700, pp. 750–752.

Richardson, M. P. (2012). "Large scale brain models of epilepsy: dynamics meets connectomics." In: *Journal of neurology, neurosurgery, and psychiatry* 83.12, pp. 1238–48.

Rilling, J. K. and T. R. Insel (1999). "The primate neocortex in comparative perspective using magnetic resonance imaging". In: *J Hum Evol* 37.2, pp. 191–223.

Roberts, J. A. and P. A. Robinson (2012). "Quantitative theory of driven nonlinear brain dynamics". In: *NeuroImage* 62.3, pp. 1947–1955.

Robinson, P. A., C. J. Rennie, and D. L. Rowe (2002). "Dynamics of large-scale brain activity in normal arousal states and epileptic seizures". In: *Physical Review E - Statistical, Nonlinear, and Soft Matter Physics* 65.4, pp. 1–9.

Robinson, P. A., C. J. Rennie, and J. J. Wright (2006). "Propagation and stability of waves of electrical activity in the cerebral cortex". In: 56.1, pp. 826–840.

Rockland, K. S. and N. Ichinohe (2004). "Some thoughts on cortical minicolumns". In: *Experimental Brain Research* 158.3, pp. 265–277.

Rockland, K. S. and D. N. Pandya (1979). "Laminar origins and terminations of cortical connections of the occipital lobe in the rhesus monkey". In: *Brain Research* 179.1, pp. 3–20.

Rothkegel, A. and K. Lehnertz (2011). "Recurrent events of synchrony in complex networks of pulse-coupled oscillators". In: *EPL (Europhysics Letters)* 95.3, p. 38001.

Rotterdam, A. van, F. H. Lopes da Silva, J. van den Ende, M. A. Viergever, and A. J. Hermans (1982). "A model of the spatial-temporal characteristics of the alpha rhythm". In: *Bulletin of Mathematical Biology* 44.2, pp. 283–305.

Rowe, D. L., P. A. Robinson, and E. Gordon (2005). "Stimulant drug action in attention deficit hyperactivity disorder (ADHD): Inference of neurophysiological mechanisms via quantitative modelling". In: *Clinical Neurophysiology* 116.2, pp. 324–335.

Rubio-Garrido, P., F. Pérez-De-Manzo, C. Porrero, M. J. Galazo, and F. Clascá (2009). "Thalamic input to distal apical dendrites in neocortical layer 1 is massive and highly convergent". In: *Cerebral Cortex* 19.10, pp. 2380–2395.

Ruseckas, J. and B. Kaulakys (2010). "1/f Noise From Nonlinear Stochastic Differential Equations". In: *Physical Review E - Statistical, Nonlinear, and Soft Matter Physics* 81.3, pp. 1–7.

Sadleir, L. G., K. Farrell, S. Smith, M. B. Connolly, and I. E. Scheffer (2011). "Electroclinical features of absence seizures in sleep". In: *Epilepsy Research* 93.2-3, pp. 216–220.

San Miguel, M. and R. Toral (1997). "Stochastic Effects in Physical Systems". In: p. 93.

Sancristóbal, B., R. Vicente, J. M. Sancho, and J. Garcia-Ojalvo (2013). "Emergent bimodal firing patterns implement different encoding strategies during gamma-band oscillations." In: *Frontiers in computational neuroscience* 7.March, p. 18.

Sancristóbal, B., B. Rebollo, P. Boada, M. V. Sanchez-Vives, and J. Garcia-Ojalvo (2016). "Collective stochastic coherence in recurrent neuronal networks". In: *Nature Physics* May, pp. 1–8.

Sanz-Leon, P., S. A. Knock, A. Spiegler, and V. K. Jirsa (2015). "Mathematical framework for large-scale brain network modeling in The Virtual Brain". In: *NeuroImage* 111, pp. 385–430.

Sapienza, L., P. A. Moro, and I Roma (2000). "Chaos or noise: Dif culties of a distinction". In: *Physical Review E* 62.1, pp. 427–437.

Sarpeshkar, R. (1998). "Analog versus digital: extrapolating from electronics to neurobiology." In: *Neural computation* 10.7, pp. 1601–1638.

Scheffer, M. (2009). *Critical Transitions in Nature and Society*. Princeton studies in complexity. Princeton University Press.

Scheffer, M., S. Carpenter, J. A. Foley, C. Folke, and B. Walker (2001). "Catastrophic shifts in ecosystems." In: *Nature* 413.6856, pp. 591–6.

Scheffer, M., J. Bascompte, W. A. Brock, V. Brovkin, S. R. Carpenter, V. Dakos, H. Held, E. H. van Nes, M. Rietkerk, and G. Sugihara (2009). "Early-warning signals for critical transitions." In: *Nature* 461.7260, pp. 53–59.

Schiff, S. J., K Jerger, D. H. Duong, T Chang, M. L. Spano, and W. L. Ditto (1994). "Controlling chaos in the brain." In: *Nature* 370.6491, pp. 615–620.

Schindler, K., C. E. Elger, and K. Lehnertz (2007). "Increasing synchronization may promote seizure termination: Evidence from status epilepticus". In: *Clinical Neurophysiology* 118.9, pp. 1955–1968.

Schöll, E. and H. G. Schuster (2008). *Handbook of chaos control*. John Wiley & Sons.

Segev, I. and E. Schneidman (1999). "Axons as computing devices: basic insights gained from models." In: *Journal of physiology, Paris* 93.4, pp. 263–70.

Shanahan, M. (2010). "Metastable chimera states in community-structured oscillator networks". In: *Chaos* 20.1.

Shepherd, G. M. and G. Sten (2010). *Handbook of Brain Microcircuits*. Oxford University Press.

Shew, W. L. and D. Plenz (2013). "The Functional Benefits of Criticality in the Cortex". In: *The Neuroscientist* 19.1, pp. 88–100.

Shirvalkar, P. R., P. R. Rapp, and M. L. Shapiro (2010). "Bidirectional changes to hippocampal theta-gamma comodulation predict memory

for recent spatial episodes." In: *Proceedings of the National Academy of Sciences of the United States of America* 107.15, pp. 7054–9.

Shriki, O., J. Alstott, F. Carver, T. Holroyd, R. N. a. Henson, M. L. Smith, R. Coppola, E. Bullmore, and D. Plenz (2013). "Neuronal Avalanches in the Resting MEG of the Human Brain". In: *Journal of Neuroscience* 33.16, pp. 7079–7090.

Silva, L. A. da and R. D. Vilela (2015). "Colored noise and memory effects on formal spiking neuron models". In: *Physical Review E* 91.6, p. 062702.

Sitnikova, E. and G. van Luijtelaar (2009). "Electroencephalographic precursors of spike-wave discharges in a genetic rat model of absence epilepsy: Power spectrum and coherence EEG analyses". In: *Epilepsy Research* 84.2-3, pp. 159–171.

Skarda, C. A. and W. J. Freeman (1987). "How brains make chaos in order to make sense of the world". In: *Behavioral and Brain Sciences* 10.02, p. 161.

Slutzky, M. W., P. Cvitanovic, and D. J. Mogul (2001). "Deterministic chaos and noise in three in vitro hippocampal models of epilepsy." In: *Annals of biomedical engineering* 29.7, pp. 607–18.

Slutzky, M. W., P. Cvitanovic, and D. J. Mogul (2002). "Identification of determinism in noisy neuronal systems". In: *Journal of Neuroscience Methods* 118.2, pp. 153–161.

Slutzky, M. W., P. Cvitanovic, and D. J. Mogul (2003). "Manipulating epileptiform bursting in the rat hippocampus using chaos control and adaptive techniques." In: *IEEE transactions on bio-medical engineering* 50.5, pp. 559–570.

Sobie, C., A. Babul, and R. De Sousa (2011). "Neuron dynamics in the presence of 1/f noise". In: *Physical Review E - Statistical, Nonlinear, and Soft Matter Physics* 83.5, pp. 1–11.

Soltesz, I. and K. Staley (2011). *Computational Neuroscience in Epilepsy*. Elsevier Science.

Sompolinsky, H., A. Crisanti, and H. J. Sommers (1988). "Chaos in Random Neural Networks". In: *Physical Review Letters* 61.3, pp. 259–262.

Sotero, R. C. (2016). "Topology, Cross-Frequency, and Same-Frequency Band Interactions Shape the Generation of Phase-Amplitude Coupling

in a Neural Mass Model of a Cortical Column". In: *PLoS Computational Biology* 12.11, pp. 1–29.

Sotero, R. C., N. J. Trujillo-Barreto, Y. Iturria-Medina, F. Carbonell, and J. C. Jimenez (2007). "Realistically coupled neural mass models can generate EEG rhythms." In: *Neural computation* 19.2, pp. 478–512.

Spencer, S. S. (2002). "Neural networks in human epilepsy: evidence of and implications for treatment." In: *Epilepsia* 43.3, pp. 219–27.

Spiegler, A., S. J. Kiebel, F. M. Atay, and T. R. Knösche (2010). "Bifurcation analysis of neural mass models: Impact of extrinsic inputs and dendritic time constants." In: *NeuroImage* 52.3, pp. 1041–58.

Spiegler, A., T. R. Knösche, K. Schwab, J. Haueisen, and F. M. Atay (2011). "Modeling brain resonance phenomena using a neural mass model." In: *PLoS computational biology* 7.12, e1002298.

Sporns, O. (2013). "Network attributes for segregation and integration in the human brain". In: *Current Opinion in Neurobiology* 23.2, pp. 162–171.

Sporns, O. and J. D. Zwi (2004). "The small world of the cerebral cortex." In: *Neuroinformatics* 2.2, pp. 145–162.

Sporns, O., G. Tononi, and R. Kötter (2005). "The human connectome: A structural description of the human brain". In: *PLoS Computational Biology* 1.4, pp. 0245–0251.

Spruston, N. (2008). "Pyramidal neurons: dendritic structure and synaptic integration." In: *Nature reviews. Neuroscience* 9.3, pp. 206–221.

Stam, C. J. (2014). "Modern network science of neurological disorders". In: *Nature Reviews Neuroscience* 15.10, pp. 683–695.

Stamoulis, C. and B. S. Chang (2012). "Modeling Non-Invasive Neurostimulation in Epilepsy as Stochastic Interference in Brain Networks". In: *Changes* 29.6, pp. 997–1003.

Stead, M., M. Bower, B. H. Brinkmann, K. Lee, W. R. Marsh, F. B. Meyer, B. Litt, J. Van Gompel, and G. a. Worrell (2010). "Microseizures and the spatiotemporal scales of human partial epilepsy." In: *Brain : a journal of neurology* 133.9, pp. 2789–97.

Steriade, M. and R. McCarley (2005). *Brain Control of Wakefulness and Sleep*. Springer.

Steyn-Ross, D. A., M. L. Steyn-Ross, J. W. Sleigh, M. T. Wilson, I. P. Gillies, and J. J. Wright (2005). "The sleep cycle modelled as a cortical phase transition". In: *Journal of Biological Physics* 31.3-4, pp. 547–569.

Steyn-Ross, M. L., D. a. Steyn-Ross, J. W. Sleigh, and D. T. Liley (1999). "Theoretical electroencephalogram stationary spectrum for a white-noise-driven cortex: evidence for a general anesthetic-induced phase transition." In: *Physical review. E, Statistical physics, plasmas, fluids, and related interdisciplinary topics* 60.6 Pt B, pp. 7299–7311.

Stocks, N. (2000). "Suprathreshold stochastic resonance in multilevel threshold systems". In: *Physical review letters* 84.11, pp. 2310–3.

Suffczyński, P., S. Kalitzin, and F. Lopes Da Silva (2004). "Dynamics of non-convulsive epileptic phenomena modeled by a bistable neuronal network". In: *Neuroscience* 126.2, pp. 467–484.

Suffczyński, P. (2000). "Neural dynamics underlying brain thalamic oscillations investigated with computational models". PhD dissertation. Institute of Experimental Physics, Department of Physics, Warsaw University.

Suffczyński, P., S. Kalitzin, G. Pfurtscheller, and F. H. Lopes Da Silva (2001). "Computational model of thalamo-cortical networks: Dynamical control of alpha rhythms in relation to focal attention". In: *International Journal of Psychophysiology* 43.1, pp. 25–40.

Suffczyński, P., F. Wendung, J. J. Bellanger, and F. H. L. Da Silva (2006). "Some insights into computational models of (patho)physiological brain activity". In: *Proceedings of the IEEE* 94.4, pp. 784–804.

Summerson, S. R., B. Aazhang, and C. Kemere (2015). "Investigating irregularly patterned deep brain stimulation signal design using biophysical models". In: *Frontiers in Computational Neuroscience* 9.June, pp. 1–10.

Takahashi, T. and Y. Tsukahara (1998). "Pocket Monster incident and low luminance visual stimuli: Special reference to deep red flicker stimulation". In: *Pediatrics International* 40.6, pp. 631–637.

Tang, Y., J. R. Nyengaard, D. M. G. De Groot, and H. J. G. Gundersen (2001). "Total regional and global number of synapses in the human brain neocortex". In: *Synapse* 41.3, pp. 258–273.

Tao, J. X., X. J. Chen, M. Baldwin, I. Yung, S. Rose, D. Frim, S. Hawes-Ebersole, and J. S. Ebersole (2011). "Interictal regional delta slowing is an EEG marker of epileptic network in temporal lobe epilepsy". In: *Epilepsia* 52.3, pp. 467–476.

Taylor, P. N., Y. Wang, G. Marc, D. Justin, M. Friederike, S. Ulrich, and B. Gerold (2014). "A computational study of stimulus driven epileptic seizure abatement". In: *PLoS ONE* 9.12, pp. 1–26.

Terry, J. R., O. Benjamin, and M. P. Richardson (2012). "Seizure generation: The role of nodes and networks". In: *Epilepsia* 53.9, pp. 166–169.

Tessone, C. J., C. R. Mirasso, R. Toral, and J. D. Gunton (2006). "Diversity-Induced Resonance". In: *Physical Review Letters* 97.19, p. 194101.

Tetzlaff, C., S. Okujeni, U. Egert, F. Wörgötter, and M. Butz (2010). "Self-organized criticality in developing neuronal networks". In: *PLoS Computational Biology* 6.12.

Thanarajah, S. E., C. E. Han, A. Rotarska-Jagiela, W. Singer, R. Deichmann, K. Maurer, M. Kaiser, and P. J. Uhlhaas (2016). "Abnormal connectional fingerprint in schizophrenia: A novel network analysis of diffusion tensor imaging data". In: *Frontiers in Psychiatry* 7.JUN, pp. 1–10.

Todorov, E. and M. I. Jordan (2002). "Optimal feedback control as a theory of motor coordination". In: *Nature Neuroscience* 5.11, pp. 1226–1235.

Tononi, G., O. Sporns, and G. M. Edelman (1994). "A measure for brain complexity: relating functional segregation and integration in the nervous system." In: *Proceedings of the National Academy of Sciences of the United States of America* 91.11, pp. 5033–7.

Tononi, G. and C. Koch (2015). "Consciousness: here, there and everywhere?" In: *Philosophical Transactions of the Royal Society B: Biological Sciences* 370.1668, pp. 20140167–20140167.

Toral, R. and P. Colet (2014). *Stochastic Numerical Methods: An Introduction for Students and Scientists*. Physics Textbook. Wiley.

Torcini, A. and D. Angulo-Garcia (2014). "Diluted neural networks : deterministic versus stochastic evolution". In: Dd.

Tort, A. B. L., R. W. Komorowski, J. R. Manns, N. J. Kopell, and H. Eichenbaum (2009). "Theta-gamma coupling increases during the learning of

item-context associations." In: *Proceedings of the National Academy of Sciences of the United States of America* 106.49, pp. 20942–7.

Touboul, J. and A. Destexhe (2010). "Can power-law scaling and neuronal avalanches arise from stochastic dynamics?" In: *PLoS ONE* 5.2.

Touboul, J., F. Wendling, P. Chauvel, and O. Faugeras (2011). "Neural Mass Activity, Bifurcations, and Epilepsy". In: *Neural computation* 23.12, pp. 3232–86.

Truccolo, W., J. a. Donoghue, L. R. Hochberg, E. N. Eskandar, J. R. Madsen, W. S. Anderson, E. N. Brown, E. Halgren, and S. S. Cash (2011). "Single-neuron dynamics in human focal epilepsy." In: *Nature neuroscience* 14.5, pp. 635–41.

Tsodyks, M. V., W. E. Skaggs, T. J. Sejnowski, and B. L. Mcnaughton (1997). "Paradoxical effects of external modulation of inhibitory interneurons". In: *Journal of Neuroscience* 17.11, pp. 4382–4388.

Uhlenbeck, G. E. and L. S. Ornstein (1930). "On the Theory of the Brownian Motion". In: *Physical Review* 36.5, pp. 823–841.

Uhlhaas, P. J. and W. Singer (2006). "Neural Synchrony in Brain Disorders: Relevance for Cognitive Dysfunctions and Pathophysiology". In: *Neuron* 52.1, pp. 155–168.

Uhlhaas, P. J. and W. Singer (2013). "High-frequency oscillations and the neurobiology of schizophrenia". In: *Dialogues in Clinical Neuroscience* 15.3, pp. 301–313.

U.S. National Library of Medicine (2001-2015). *The Visible Human Project*. 8600 Rockville Pike, Bethesda, MD 20894.

Valentín, A., G. Alarcón, M. Honavar, J. J. García Seoane, R. P. Selway, C. E. Polkey, and C. D. Binnie (2005). "Single pulse electrical stimulation for identification of structural abnormalities and prediction of seizure outcome after epilepsy surgery: a prospective study." In: *Lancet neurology* 4.11, pp. 718–26.

Valentín, A., G. Alarcón, S. F. Barrington, J. J. García Seoane, M. C. Martín-Miguel, R. P. Selway, and M. Koutroumanidis (2014). "Interictal estimation of intracranial seizure onset in temporal lobe epilepsy". In: *Clinical Neurophysiology* 125.2, pp. 231–238.

Valverde, S., S. Ohse, M. Turalska, B. J. West, and J. Garcia-Ojalvo (2015). "Structural determinants of criticality in biological networks." In: *Frontiers in physiology* 6.May, p. 127.

Van Diessen, E., S. J. H. Diederen, K. P. J. Braun, F. E. Jansen, and C. J. Stam (2013). "Functional and structural brain networks in epilepsy: What have we learned?" In: *Epilepsia* 54.11, pp. 1855–1865.

Van Luijtelaar, G., A. Hramov, E. Sitnikova, and A. Koronovskii (2011). "Spike-wave discharges in WAG/Rij rats are preceded by delta and theta precursor activity in cortex and thalamus". In: *Clinical Neurophysiology* 122.4, pp. 687–695.

Vicente, R., L. L. Gollo, C. R. Mirasso, I. Fischer, and G. Pipa (2008). "Dynamical relaying can yield zero time lag neuronal synchrony despite long conduction delays". In: *Proceedings of the National Academy of Sciences* 105.44, pp. 17157–17162.

Victor, J. D., J. D. Drover, M. M. Conte, and N. D. Schiff (2011). "Mean-field modeling of thalamocortical dynamics and a model-driven approach to EEG analysis." In: *Proceedings of the National Academy of Sciences of the United States of America* 108 Suppl, pp. 15631–8.

Villegas, P., P. Moretti, and M. a. Muñoz (2014). "Frustrated hierarchical synchronization and emergent complexity in the human connectome network". In: *Scientific Reports* 4.

Voytek, B., R. T. Canolty, A. Shestyuk, N. E. Crone, J. Parvizi, and R. T. Knight (2010). "Shifts in gamma phase-amplitude coupling frequency from theta to alpha over posterior cortex during visual tasks." In: *Frontiers in human neuroscience* 4.October, p. 191.

Vreeswijk, C. van and H. Sompolinsky (1996). "Chaos in Neuronal Networks with Balanced Excitatory and Inhibitory Activity". In: *Science* 274.5293, pp. 1724–1726.

Wang, P. and T. R. Knösche (2013). "A realistic neural mass model of the cortex with laminar-specific connections and synaptic plasticity - evaluation with auditory habituation." In: *PloS one* 8.10, e77876.

Wang, S.-J. and C. Zhou (2012). "Hierarchical modular structure enhances the robustness of self-organized criticality in neural networks". In: *New Journal of Physics* 14.2, p. 023005.

Wang, Y., F. Hutchings, and M. Kaiser (2015). *Computational modeling of neurostimulation in brain diseases*. 1st ed. Vol. 222. Elsevier B.V., pp. 191–228.

Ward, L. and P. Greenwood (2007). "1/f noise". In: *Scholarpedia*.

Watts, D. J. and S. H. Strogatz (1998). "Collective dynamics of'small-world' networks". In: *Nature* 393.6684, pp. 440–442.

Weigenand, A., M. Schellenberger Costa, H. V. V. Ngo, J. C. Claussen, and T. Martinetz (2014). "Characterization of K-Complexes and Slow Wave Activity in a Neural Mass Model". In: *PLoS Computational Biology* 10.11.

Wendling, F., J. J. Bellanger, F. Bartolomei, and P. Chauvel (2000). "Relevance of nonlinear lumped-parameter models in the analysis of depth-EEG epileptic signals." In: *Biological cybernetics* 83.4, pp. 367–78.

Wendling, F., F. Bartolomei, J. J. Bellanger, and P. Chauvel (2002). "Epileptic fast activity can be explained by a model of impaired GABAergic dendritic inhibition". In: *European Journal of Neuroscience* 15.9, pp. 1499–1508.

Wendling, F., P. Benquet, F. Bartolomei, and V. Jirsa (2015). "Computational models of epileptiform activity". In: *Journal of Neuroscience Methods*, pp. 1–19.

Wiesenfeld, K. (1991). "Amplification by globally coupled arrays: Coherence and symmetry". In: *Physical Review A* 44.6, pp. 3543–3551.

Wilson, H. R. and J. D. Cowan (1972). "Excitatory and inhibitory interactions in localized populations of model neurons." In: *Biophysical journal* 12.1, pp. 1–24.

Woolsey, T. A. and H. Van der Loos (1970). "The structural organization of layer IV in the somatosensory region (S I) of mouse cerebral cortex. The description of a cortical field composed of discrete cytoarchitectonic units". In: *Brain Research* 17.2, pp. 205–242.

Yuan, H. and S. D. Silberstein (2016). "Vagus Nerve and Vagus Nerve Stimulation, a Comprehensive Review: Part III". In: *Headache* 56.3, pp. 479–490.

Zamora-López, G., Y. Chen, G. Deco, M. L. Kringelbach, and C. Zhou (2016). "Functional complexity emerging from anatomical constraints in the brain: the significance of network modularity and rich-clubs". In: *Scientific Reports* 6.November, p. 38424.

Zetterberg, L. H., L Kristiansson, and K Mossberg (1978). "Performance of a model for a local neuron population." In: *Biological cybernetics* 31.1, pp. 15–26.

Zilles, K. and K. Amunts (2010). "Centenary of Brodmann's map conception and fate". In: *Nature Reviews Neuroscience* 11.2, pp. 139–145.